IMPROVED HVAC ENERGY THROUGHPUT MEASURING SYSTEM

A B RAINE

PhD

2015

IMPROVED HVAC ENERGY THROUGHPUT MEASURING SYSTEM

ANDREW BRIAN RAINE

A thesis submitted in partial fulfilment

of the requirements of the University of Northumbria at Newcastle for the degree of Doctor of Philosophy

Research undertaken in the Faculty of Mechanical and Construction Engineering

September 2015

Abstract

Currently heating, ventilation and air conditioning (HVAC) systems are difficult and costly to monitor for energy efficiency performance and reliability. As buildings evolve, they will require higher levels of insulation and air tightness which will require ventilation systems to provide the minimum number of air changes and reduced energy usage by recovering heat from the air before it is expelled. This will necessitate the need for monitoring of the operating performance of these systems so that air quality or building energy efficiency is not detrimentally affected.

A typical duct airflow monitoring device uses a pressure differential method to determine the airflow rate but they are fragile, expensive and create an additional pressure loss. The monitoring of airflow rates can indicate problems in the design, installation and operation of a HVAC system. One of the possible alternatives to using pressure differential type devices such as Pitot tube/arrays, orifice plates and Venturis is to use an ultrasonic flow rate sensor, but historically their high cost has restricted their use in HVAC systems.

This project has looked at improving on existing measuring systems by developing an ultrasonic in-duct flowmeter system to measure the mean airflow, temperature and humidity of a ventilation duct so that a comparative energy level can be accurately deduced.

A proof of concept in-duct ultrasonic airflow monitoring device has been developed and has obtained results within ±3.5% RMS of a Venturi airflow measuring device.

Matlab code for a Monte Carlo acoustic ray/particle tracing ultrasonic flowmeter simulation has been developed to study the effects of non-ideal installation scenarios. The fully developed centreline computational fluid dynamics (CFD) mean flow velocity to duct total mean flow velocity error can be up to 13%. Analysis of the CFD data for various duct scenarios has shown that this could be reduced to below 5% by using a transducer offset of approximately ±0.25 duct diameters or widths from the centreline at distances as close as one duct hydraulic diameter from an upstream disturbance, such as caused by a bend.

Acknowledgements

I would like to express my sincere gratitude to Prof Sean Danaher, who was my original principal supervisor, for giving me the opportunity to carry out this research and his advice on Matlab programming. I would like to thank my first supervisor Prof Chris Underwood for coming up with the research question, which was to find an improved way of measuring HVAC ventilation system energy throughput and for providing support with equipment requests and proofreading my documentation. I would like to thank my second supervisor Dr. Nauman Aslam for taking over the role of my principal supervisor and providing excellent support, especially with my first academic paper submission, which was very successful.

I would like to thank Northumbria University for providing studentship support funding and the necessary equipment and laboratory time.

I wish to thank my partner Fiona Burton and my son Jamie Raine for all their love and support in this endeavour.

Table of Contents

Table of Main Document Figures

List of Tables

Glossary of abbreviations and acronyms

AC	Alternating Current
AFG	Arbitrary Function Generator
AHU	Air Handling Unit
AMCA	Air Movement and Control Association
ANSYS	Analysis System - a finite element analysis software
ASHRAE	American Society of Heating, Refrigerating and Air-Conditioning Engineers
AWG	Arbitrary Waveform Generator
bbl	Oil barrel, a unit of volume, 42 US gallons or about 159 litres
CFD	Computational Fluid Dynamics
CH	Channel
CMUT	Capacitive Micro-machined Ultrasonic Transducer
COMSOL	A finite element analysis software previously called FEMLAB
COP	Coefficient of Performance
COPD	Obstructive Pulmonary Disease
CSV	Comma-Separated Values
CUTs	Capacitive Ultrasonic Transducers
DAC	Digital to Analogue Converter
DB	Dry Bulb
DC	Direct Current
DG	Discontinuous Galerkin
DOF	Degrees of Freedom
DSP	Digital Signal Processing
EHP	Electric Heat Pump
FDTD	Finite-Difference Time-Domain
FEA	Finite Element Analysis
FEM	Finite Element Method

GHP	Gas Heat Pump
GPU	Graphical Processing Unit
HAP	Household Air Pollution
HIRM	Helmholtz Integral Ray-trace Method
HVAC	Heating, Ventilation, and Air Conditioning
IC	Integrated Circuit
ITTD	Inverse Transit Time Difference
LTI	Linear Time Invariant
PCB	Printed Circuit Board
PIC	Registered trademark of Microchip Technology Inc. used on processors
RCP	Royal College of Physicians
RH	Relative Humidity
RMS	Root Mean Square
RS232	Electronic Industries Association (EIA) standard RS-232-C
RTD	Resistor Temperature Device
SPL	Sound Pressure Level
SSR	Solid-State Relay
SST	Shear Stress Transport
TDC	Time to Digital Converter
TOF	Time of Flight
USB	Universal Serial Bus
VI	LabVIEW Virtual Instrument
VRF	Variable Refrigerant Flow
WB	Wet Bulb
WHO	World Health Organisation
XLR	Cannon X series connector, locking with rubber insulation

Glossary of symbols

Symbol	Description	SI units
c	Speed of sound	m/s
D	Diameter of duct	m
Dh	Hydraulic diameters	m
f_0	Transducer centre frequency	Hz
L	Acoustic path length	m
t	Air temperature in degrees	°
t_{t0}	Transit time of acoustic signal in zero flow state	s
U_m	Mean airflow inlet velocity	m/s
U_{DTTM}	Airflow velocity using phase shift or differential transit time	m/s
U_{TTM}	Airflow velocity using transit time method	m/s
U_{upper}	Typical maximum design air velocity speed	m/s
Z	Transducer separation distance with reference to duct axis	m
Z_{max}	Maximum transducer horizontal separation for airflow	m
Δt_{max}	Typical maximum time of flight difference	s
Δt_{TR}	Differential transit time of the contra-propagating acoustic	s
t_{TRij}	Transit time of the acoustic signals between transducers	s
θ	Angle in degrees between acoustic path and the duct wall	°
t_{n1}	First negative going zero crossing point time, ∴ 2nd is t_{n2}	s
t_{p1}	First positive going zero crossing point time, ∴ 2nd is t_{p2}	s
t_{c1dn}	First downwind cycle midpoint time, ∴ 2nd = t_{c2dn}	s
t_{c1up}	First upwind cycle midpoint time, ∴ 2nd = t_{c2up}	s
c	Density	kg/m^3
ΔP	Pressure differential	Pa
v	Airflow velocity	m/s
γ	Specific humidity ratio of M_w to (M_w+M_{da}).	Ratio
M_w	Mass of water vapour in sample	kg
M_{da}	Mass of dry air in sample	kg
$\%RH$	Percentage relative humidity	%

Chapter 1.

INTRODUCTION

This introductory chapter provides an overview of the thesis and includes these topics:

1.1 Background and Rationale for this Research

1.1.1 Project motivation

At the beginning of this project in 2012, UK domestic and industrial energy costs had been increasing rapidly since about 2004 as shown in Figure 1.1 below. For example UK industrial fuel prices had increased by 118% [1] (p. 37) in the 10 year period from 2004.

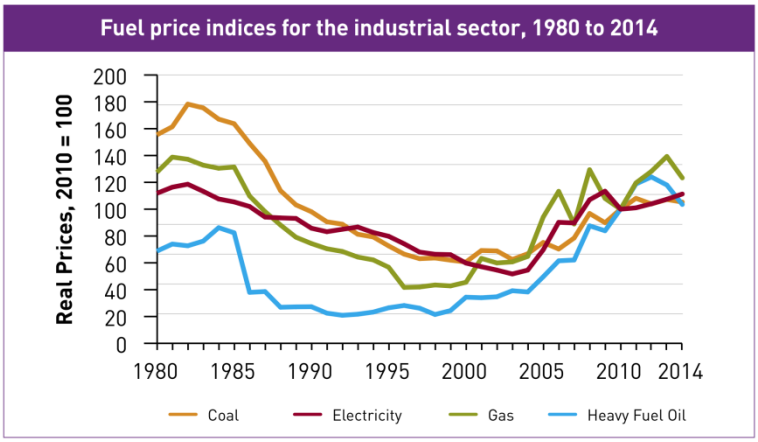

Figure 1.1. UK National Statistics; Fuel price indices for the industrial sector, 1980 to 2014.
(Source: UK energy in brief 2015,[2] (p. 37))

Currently, as of May 2016 the price of Brent crude oil in $ per barrel (bbl) has dropped rapidly from $109 in 2013 to below $50. It is said that most fuel prices are linked to the price of crude oil [1] (p. 37). Currently the data collected for 2014 [1] (p. 37) shows that electricity prices have risen by 4% and gas prices have fallen by 11% compared to the previous year. This demonstrates that oil and energy prices

can fluctuate rapidly and therefore it would be beneficial in the future to reduce our dependency on imported fuels, where possible.

There is no device currently available to measure HVAC energy throughput at a reasonable cost [3], [4]. This has been highlighted by research into electric and gas heat pumps (EHP/GHP) that the rated coefficient of performance (COP), Equation (1.1), does not represent the actual values found in a system installed in a building.

$$COP_{=} \frac{Quantity\ of\ heat\ exchanged\ by\ the\ indoor\ units}{Electric\ power\ \ consumption\ by\ Indoor\ and\ \ outdoor\ units} \quad (1.1)$$

In research by Ichikawa *et al.* [5] on a building, they found that the actual summer COP was 1.74 which was considerably lower than the rated COP of 2.57. The problem was found to be that the air conditioning system EHP capacity was overrated and was not operating efficiently because most of the time it was operating below 30% of its maximum operating load.

The UK government renewable heat incentive supports air to water heat pumps but does not support air to air heat pumps because there is no adequate metering of usable heat [6] (p. 40-41). They have not found a way of measuring the amount of direct air heating, as they have found for water and steam. They want to ensure that they have the right strategy for supporting air to air source heat pumps because a large number are already installed for cooling (air conditioning) purposes.

The impact on rising cost of fossil fuels and the global community awareness of the environmental effects of increasing levels of greenhouse gases have incentivised innovation in the renewable energy generation and conservation sector. Domestic and industrial property owners are now becoming more likely to consider fitting energy-saving options and renewable energy generation systems as it becomes more viable because of the shorter payback times, which can be due to the following factors; rising cost of energy, lowering cost of implementation and the introduction of government incentive schemes.

The monitoring of airflow rates, air temperatures and humidity at inlets and outlets can indicate problems in the design, installation and operation of a HVAC system. Problems that can cause performance degradation of a ventilation system [7–9] are listed in Table 1.1 below.

Table 1.1 Typical HVAC system problems.

Design	Installation	In service
a) Inadequate fan motors	a) Dampers incorrectly set	a) Blocked Air filters
b) Unsuitable duct sizes	b) Fans incorrectly balanced	b) Inlet fan fault
c) Incorrect sizing of AHU	c) Design incorrectly implemented	c) Air leaks in the duct system
		d) Ventilation outlets unbalanced

Currently HVAC (Heating, Ventilation, and Air Conditioning) systems are difficult and costly to monitor for energy efficiency performance and reliability. A typical duct airflow monitoring device uses a pressure differential method to determine the airflow. According to Yu *et al.* [10] they are fragile, expensive and add an additional pressure loss, but also their sensitivity is reduced with the reduction in airflow velocity. As buildings evolve, higher levels of insulation and air tightness are being specified which is requiring the installation of ventilation systems to provide the minimum number of air changes and also reduce energy usage by recovering the heat or cooling energy from the air before it is expelled. In the future this will necessitate the need for monitoring of the operating performance of these systems so that air quality or building energy efficiency [7], [8] is not detrimentally affected. The World Health Organisation (WHO) has stated that "globally, 4.3 million deaths were attributed to household air pollution (HAP) in 2012" of which 99,000 are in Europe [11]. The main medical conditions which are affected by indoor air pollution are stroke, ischaemic heart disease, chronic obstructive pulmonary disease (COPD), lower respiratory disease and lung cancer. Chemicals such as formaldehyde, which can be omitted by furniture and other materials, can irritate the lungs. Also particulates and nitrogen oxide from heating and cooking appliances can damage the lungs or heart and increase a person's sensitivity to allergens already in the home. It is suggested by the Royal College of Physicians (RCP) in their 2016 report called "Every breath we take: the lifelong impact of air pollution" that possible solutions to this problem is maintenance of good ventilation and reducing pollution sources which could be done by introducing emission standards/limits [12] (p.26).

Traditional airflow monitoring devices such as Pitot tube/arrays, orifice plate and Venturi tube use the differential pressure technique. The main drawbacks of these types of devices are the high cost, reduced sensitivity with reduced airflow speed and maintenance needed to clean the pressure sensing probes and tubes. The

high cost is mainly due to the high precision diaphragms required to measure the pressure differential to a sufficiently high enough sensitivity. The sensitivity can be low because the air pressure differential produced at the probe tubes is proportional to the square of the airflow velocity travelling parallel to the tube and, thus, rapidly diminishes as the air velocity reduces.

This project will investigate and develop a device which can monitor the main duct airflow parameters and therefore give an indication of the amount of energy being transferred through the ventilation system.

1.2 Primary Aims and Objectives of the Study

1.2.1 Aims of the project

The project aim is to develop a sensor to cost effectively measure accurately, conveniently and quickly the amount of energy transfer through a ventilation duct. The amount of energy transfer will be measured by using three parameters, which are the mean airflow, temperature and humidity.

1.2.2 Objectives

1) Develop a sensor that can measure the approximate mass airflow in a circular or square duct by using ultrasonic flowmeter techniques.
2) Integrate into objective number 1 a temperature sensor and humidity sensor.
3) Develop the instrument required by objective 1 and 2 that incorporates techniques and solutions which facilitates the low-cost manufacture of the device.

1.3 Original Contribution of Research

As a result of this research study, the author has made the following original contributions to knowledge.

1) Designed and tested a ventilation duct airflow measurement device for round or square ducting using an ultrasonic differential transit time method with the following features.
   a) Transducers are mounted together on the same side of the round or square duct so that the critical distance between the transducers cannot be altered so reducing errors caused by incorrect installation and making the installation simpler.

b) Square wave pulses are used which are less costly to produce than a sinusoidal burst waveform because a digital to analogue converter (DAC) is not required.
c) Anti-phase transmit pulse is used to reduce transducer ringing, which reduces minimum duct diameter distance and allows increased sensor update rate.
d) Receiver signal processing complexity is reduced by using a selection of zero crossing points at a time window determined from the duct airflow temperature.

2) Developed a MATLAB 3D acoustic in-duct flowmeter Monte Carlo ray/particle tracing simulation program which can simulate a reflective path acoustic flowmeters in a square or round duct and the effects of a three-dimensional flow profile on the transducers received acoustic signal.
3) Using the CFD data of square or round duct airflow after a bend. Analysed the mean flow across the centre line at various distances from the bend to calculate the percentage error compared to the total mean flow of the duct.
4) Provided a solution to the large centreline flow measurement errors in square and round ducts of up to 20% after a bend by offsetting the measurement from the centreline by 0.25 duct widths or diameters, which reduces the error to <4% for all duct scenarios analysed.

1.3.1 Publication

The following paper cited below was produced by the author and reports on a low-cost ventilation duct airflow measurement device [13] using an ultrasonic differential transit time method which is the main part of this thesis:

A. Raine, N. Aslam, C. Underwood, and S. Danaher,
"Development of an Ultrasonic Airflow Measurement Device for Ducted Air,"
Sensors, vol. 15, no. 5, pp. 10705–10722, May 2015
[Online]. Available: http://dx.doi.org/10.3390/s150510705

1.4 Outline of the Thesis

This thesis is organized as follows:

Chapter 2 is a literature review of the state-of-the-art in acoustic airflow rate measurement devices for ventilation followed by an overview of ultrasonic flowmeter simulation methods and relevant research.

Chapter 3 first explains a method for calculating HVAC energy throughput where there is no change in water vapour mass content of the air. After that a second method for calculating HVAC energy throughput is described for when there is a change in water vapour mass content. An overview of ventilation sensor technologies used to measure the required parameters for these calculations, such as air flow rate, temperature and humidity is presented.

Chapter 4 gives an overview of the HVAC energy throughput development system and instrument which involved the following:

a) Ultrasonic duct airflow measurement system.
b) Lab HVAC unit and Venturi.
c) Duct dry bulb and wet bulb temperature measurement system.
d) Capacitive humidity sensor network.
e) Signal processing method used to calculate the differential transit time.

Chapter 5 explains the experimental setup for testing the instrument in a circular and square duct and the results are presented for the instrument against a Venturi flowmeter in varying flow rates and air temperatures.

Chapter 6 describes instrument simulation and application case studies in scenarios to answer questions on how close to a disturbance such as a bend, the device as it is, can be fitted. A solution is proposed to reduce measurement errors and results are evaluated. Also a Matlab Monte Carlo particle simulation program that simulates acoustic flowmeter in round and square ducts is described.

Chapter 7, conclusions and future improvements are discussed.

Chapter 2.

LITERATURE REVIEW

In this chapter:

The first subsection of this literature review provides a description of state-of-the-art in ventilation and gas acoustic flow rate measurement devices. The second subsection gives an overview of research into ultrasonic flowmeter simulation methods which is important for predicting the flow meter operating performance in various installation scenarios.

2.1 Acoustic Ventilation Airflow Measurement Devices

In 1994 an ultrasonic duct airflow measurement device was proposed by Bragg and Lynnworth [14] from Panametrics Inc. (Waltham, MA, USA) which used a single port solution consisting of two transducers on a single circular flange, using O-rings to reduce acoustic crosstalk. Figure 2.1 shows a representation of this device fitted to a square duct.

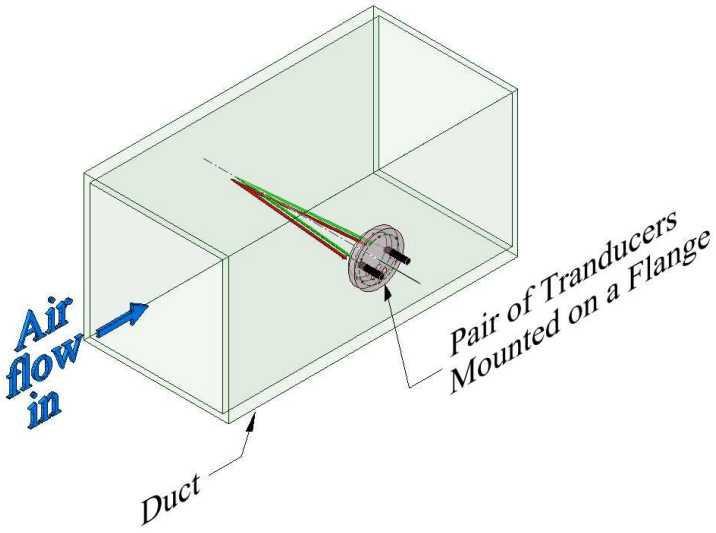

Figure 2.1. One port ultrasonic flow sensor for air, proposed by Bragg and Lynnworth.

A reflective path was used and it was suggested that optional sensors such as pressure, temperature and relative humidity could be combined with this unit. A single port device has the advantage that it is much easier to install than a two port

device and that the effects of the flow swirl can be eliminated due to the reflective path. It is actually suggested in this paper that if the device is rotated by 90°, It can be used to measure the actual amount of airflow swirl in the duct.

In the same year that Bragg and Lynnworth proposed the one port ultrasonic flow sensor for air, a patent was filed by Strauss *et al.* [15] which described a solution for measuring HVAC air velocity by using a contra propagating pulsed phase method. A strengthening structure as shown in Figure 2.2a is used in this design to minimize duct wall vibrations which they report can cause about 20 to 30% phase measurement variation when measuring a steady air velocity. In an alternative design of this invention a reflective path design and a duct internal supports sleeve is shown in Figure 2.2b.

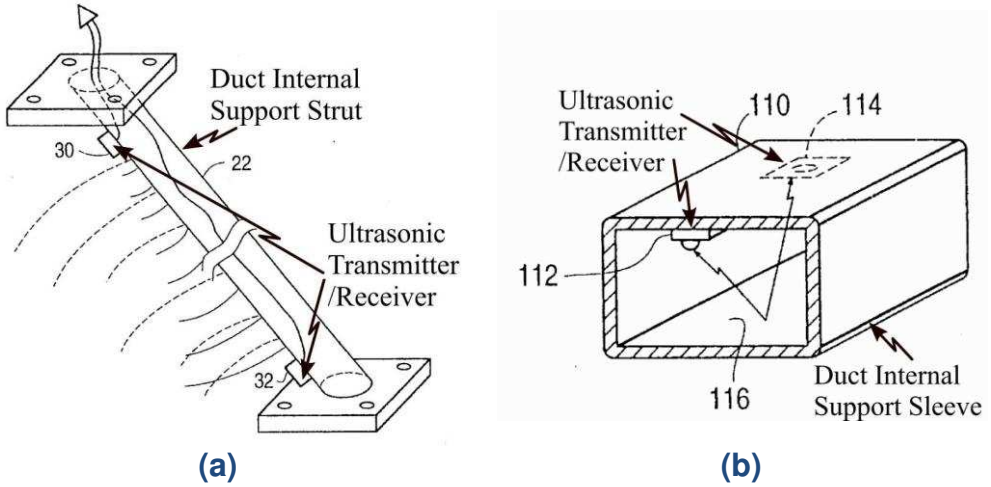

Figure 2.2. Ultrasound air velocity detect or for HVAC ducts patent by Strass *et al*; (a) Strut, (b) Sleeve.
(Source: Strass *et al*, [15] (sheets. 1-2))

According to the company's website neptronic.com [16] this device which they call the "Vector 3" is not yet commercialised but is designed for fume or laboratory hood applications which require precise control.

In 2002 a similar more developed device to the Bragg and Lynnworth's one port ultrasonic flow sensor was described by Rabalais and Sims [17] (p. 16) but was said to be only available on a case-by-case basis as they were still classed as experimental devices.

Also in 2002, Oleg Khrakovsky performed a measurement of atmospheric pressure airflow rate using a pair of clamp-on ultrasonic transducers fitted on a 250 mm plastic pipe which was described by Conrad and Lynnworth [18] (p. 60) but this configuration was reported as insufficient for a steel pipe installation because of the much higher acoustic impedance mismatch between steel and air.

The measurement of low airflow velocities in natural ventilation systems has created an interest in developing an acoustic airflow velocity measurement device. This is because of the linear response to flow velocity change these devices have, so their sensitivity does not degrade with the low airflow velocity as opposed to what happens with pressure differential airflow measurement devices.

In a study by Olmos [19] an ultrasonic airflow measurement device for measuring airflow and temperature within solar chimneys was developed. This incorporated a contra propagating pulse phase method with time of flight tracking similar to a method developed by the same author [20] in a previous study for an ultrasonic tank level meter. A procedure is suggested to calibrate the device on initial setup, which involves the closure of the solar chimney inlet so that the phase tracking can be zeroed. A particular zero crossing point from consecutive signal waveforms is tracked within a 24 µs moving window to calculate the offset from the initial calibration times.

In another study by Van Buggenhout *et al.* [21] on natural ventilation air flow measurement a device was created which could use between 1 and 16 transducer pairs fitted in a circular duct is shown in Figure 2.3 to measure the turbulent airflow to an accuracy of 9% for all 16 pairs and 24% for a single pair.

Figure 2.3. Acoustical ventilation rate sensor for naturally ventilated buildings by Buggenhout *et al*.
(Source: Buggenhout *et al*., [22] (p. 195))

The method used a 40 kHz carrier signal pulse train modulated by 180 Hz sinusoidal signal to improve the determination of the time of flight. It also reports that the accuracy of alternative airflow measurement methods in this situation ranged between 10% to 40% with the tracer gas method the being the most accurate but not suitable for long-term use.

A dual path ultrasonic gas flowmeter is shown in Figure 2.4 which used a simultaneous contra-propagating transit time technique utilizing the TDC-GP2 double threshold detection timing chip (Acam Corporation, Stutensee, Germany)

[23] for measuring the time of flight has been developed and tested by [24], [25] Chen *et al.*

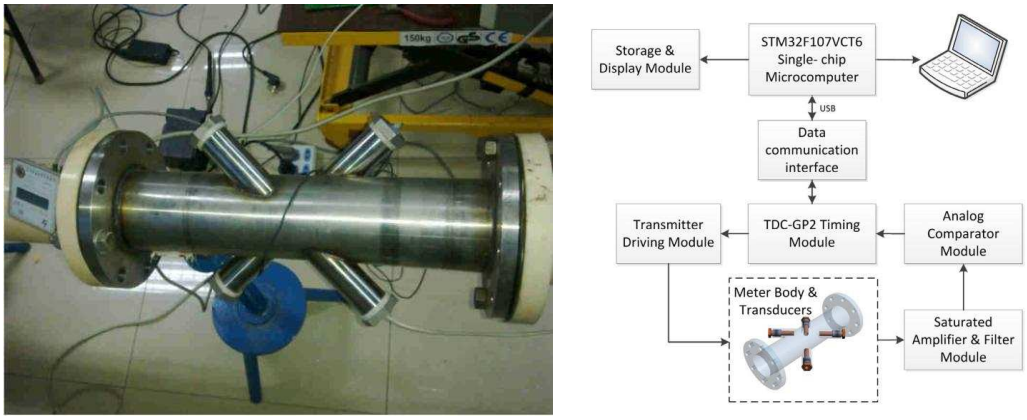

(a) (b)

Figure 2.4. Dual path ultrasonic gas flowmeter using TDC chip: (a) Body (Source: Chen *et al.*, [26] (p. 287)), (b) Schematic. (Source: Chen *et al.*, [27] (p. 286)),

This device is reported to have a relative error of ±3% with a repeatability of better than 1.6%. The time to digital converter (TDC) chip uses a double threshold technique to pinpoint the start of the received waveform and avoid problems with signal noise, which is low-cost, but its accuracy could be severely affected by fluctuations in the received signal voltage amplitude [28] (pp. 330-331), [29] (p. 2) and the variation in the DC offset in consecutive waveforms.

2.2 Ultrasonic Flowmeter Simulation

According to Reyes [30] there are generally four types of simulation method used to assess Ultrasonic flow meter design overall performance. They are the mathematical model, wave propagation equation, ray-trace method and the Helmhotz integral - ray-trace method. The following subsections describe these methods in further detail.

2.2.1 Mathematical model

The simplest mathematical model to predict the ultrasonic flowmeter acoustic transit times uses mean fluid or gas flow velocity and mean in-duct air temperature to predict the speed of sound. The flowmeter used for the following examples is shown in Figure 2.5a and b.

Figure 2.5b shows the magnitude of flow velocities, simulated by ANSYS Fluent CFD software package, across the duct cross section at 160 duct diameters from the 250 mm diameter inlet with a mean flow velocity of 1 m/s. The Figure 2.5b also shows the measurement zone of this device which is equivalent to the width of the transducer along the diameter of the duct. Due to this limited coverage and

positioning of this measurement zone the mean flow velocity in this example could be over estimated by about 7%.

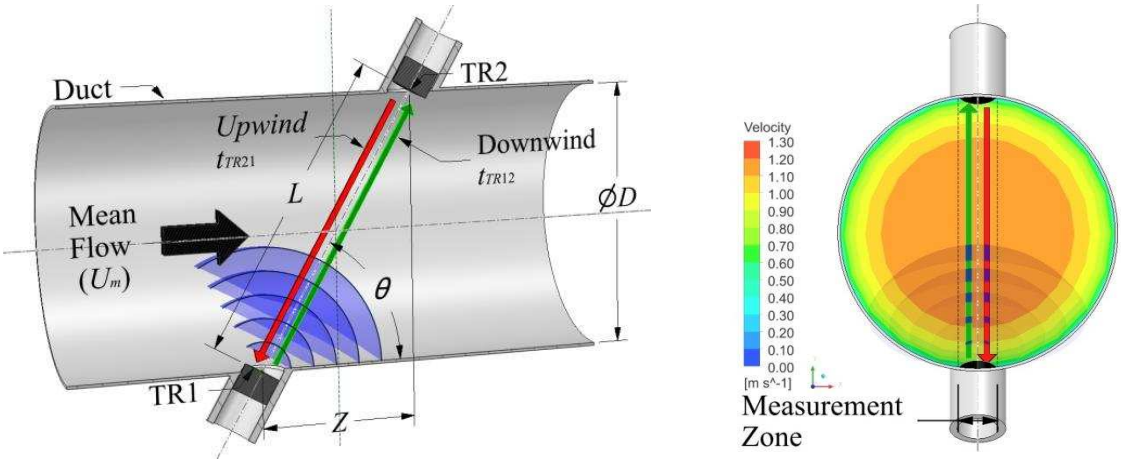

(a) **(b)**

Figure 2.5. Single "Z" shaped path acoustic transit time flow meter in a circular duct;
(a) Cross-section view along axial path, (b) Cross-section view perpendicular to axial path showing the CFD simulated flow velocity distribution at 160 duct diameters from the 1 m/s mean flow velocity inlet of 250 mm diameter.

The approximate speed of sound c, in still dry air of temperature t in degrees Celsius is given by the following Equation (2.1) [31] but more accurate and complex equation models are available as well [32] (p. 2):

$$c \approx 331.45 \sqrt{1 + \frac{t}{273}} \text{ m/s} \tag{2.1}$$

The single path acoustic transit time flow meter geometric parameter values are given by Equation (2.2), which utilises Pythagoras' theorem and the Equation (2.3):

$$L = \sqrt{D^2 + Z^2} \tag{2.2}$$

Where

D diameter of duct (m);
Z axial separation distance of transducers (m);
L acoustic path length (m).

$$\theta = \tan^{-1}\frac{D}{Z} \tag{2.3}$$

Where

θ is the acute angle between the acoustic path and the axial centreline of the duct.

Hence the transit time can be predicted by the following Equation (2.4):

$$t_{TR} = \frac{L}{c \pm U_m \cos\theta} \tag{2.4}$$

Where

U_m is the mean airflow velocity along the acoustic path (m/s).

The mean airflow velocity U_{TTM} across the acoustic path can be calculated using Equation (2.5) [33] without the need to know the speed of sound:

$$U_{TTM} = \frac{L}{2\cos\theta}\left(\frac{1}{t_{TR12}} - \frac{1}{t_{TR21}}\right) \tag{2.5}$$

Where

t_{TR12} downwind transit time along the acoustic path;

t_{TR21} upwind transit time along the acoustic path.

This model is implemented in LabVIEW as described in Section 6.1 but does not provide very accurate results when compared to an actual flowmeter located where the flow profile is fully developed or is distorted by bends or other disturbances up wind of the device.

Mathematical models have been developed to predict the fully developed flow profile in a cylindrical vessel using the Reynolds number calculated from the kinematic viscosity of the fluid or gas to be simulated. The Equations (2.6)-(2.10), which are an excerpt from a paper written by Krause [34] can be used to model a laminar or turbulent flow profile. The results obtained using this model are shown in Figure 2.6 for various flows with different Reynolds numbers.

$$u = \bar{u}(\beta u_{lam} + (1-\beta)u_{turb}) \tag{2.6}$$

$$u_{lam} = 2\left(1 - \frac{r^2}{R^2}\right) \tag{2.7}$$

$$u_{turb} = 1 + \frac{2.652 + 1.768\ln(1 - r/R)}{3.48 - 1.74\ln(41.7/\mathrm{Re}^{0.9})} \tag{2.8}$$

$$\beta = \frac{1}{1 + (\mathrm{Re}/\mathrm{Re}_0)^4} \tag{2.9}$$

$$\mathrm{Re} = \frac{2R}{\nu}\bar{u} \tag{2.10}$$

The model above was originally proposed by Willatzen [35]. The variable terms used in the model are explained below:

Where

u is the calculated airflow velocity at radial distance r;

$\bar{u}$ is the mean airflow velocity along the profile path;

ν is the kinematic viscosity;

R is the radius of the duct or pipe;

r is the radial distance coordinate point of the duct or pipe that the flow profile will be calculated for;

u_{lam} is the result calculated for a completely laminar flow profile;

u_{turb} is the result calculated for a strongly turbulent flow profile;

Re_0 is the Reynolds number of the region for laminar to turbulent flow, which is set at a value of 2000;

β is the ratio of laminar to strongly turbulent flow that the resultant flow profile is to be constructed from, so that the transition from laminar to turbulent flow is smoothed.

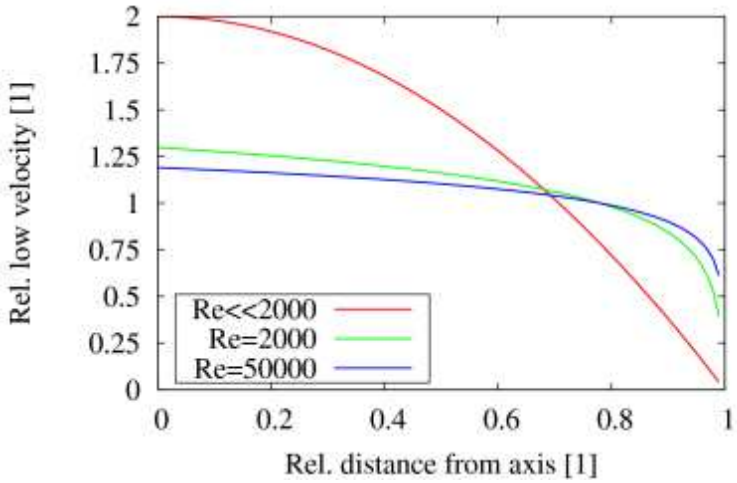

Figure 2.6. Combined laminar and turbulence flow profile model proposed by Willatzen for flow at various Reynolds numbers. (Source: Krause [36])

The Figure 2.7 below shows three examples of results produced by the model illustrated in Figure 2.6. Figure 2.7a shows that the flow profile becomes more laminar with the reduction in duct diameter, which also reduces the Reynolds number. Figure 2.7b shows that there is relatively small change in the flow profile with the change in flow velocity for a duct which is 1 m diameter and that the three normalised profiles converge at a radius which is about 0.4 m. Figure 2.7c shows the percentage error between the profile path mean flow velocity and the duct total mean flow velocity for different diameter ducts. This shows that the predicted error is between 6 and 18% and the larger the diameter of the duct or faster the flow velocity the smaller the percentage error is.

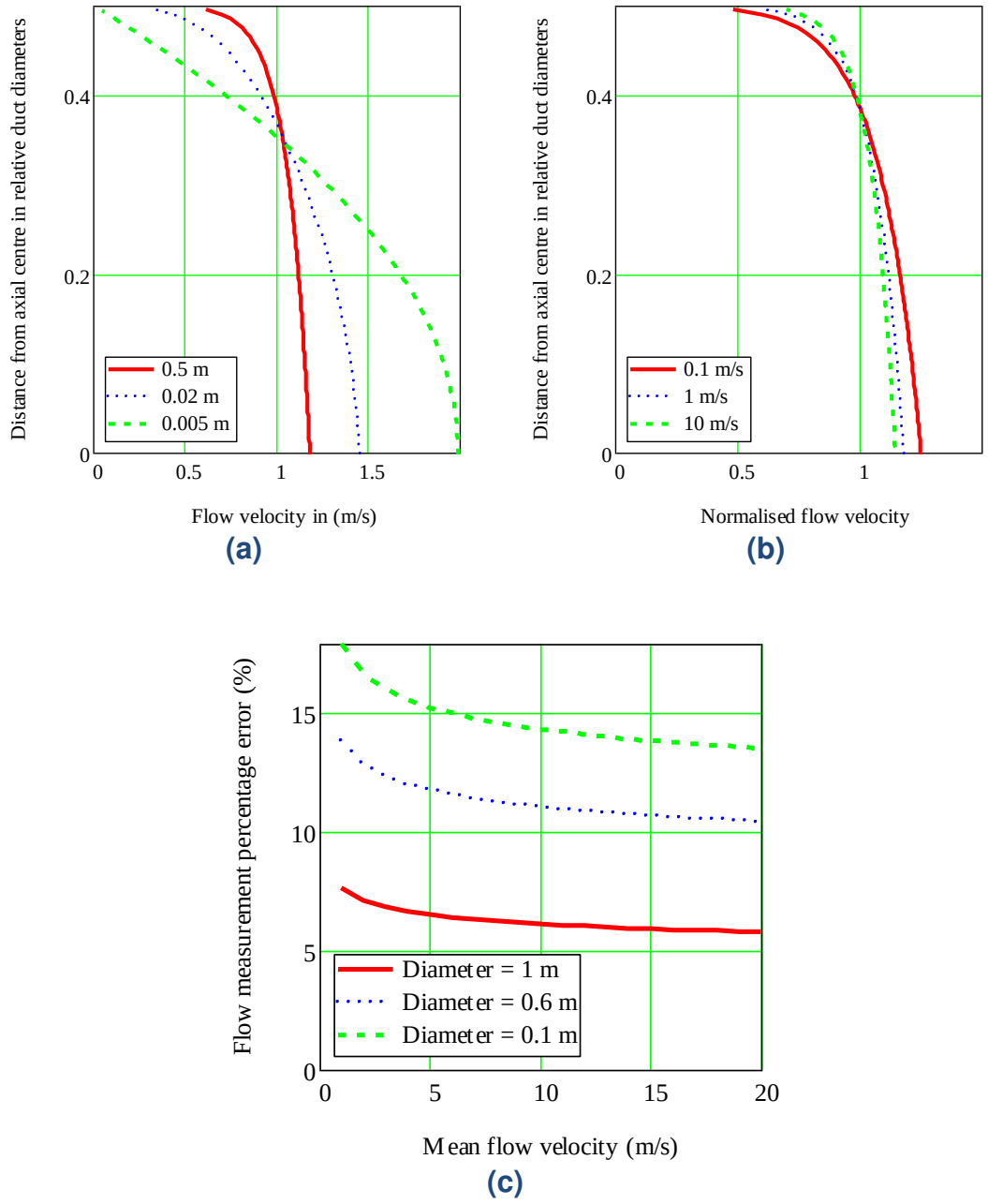

Figure 2.7. Willatzen mathematical laminar and turbulence flow profile model example results.

a) Equal duct total mean flow velocity of 1 m/s with varying duct radii.
b) 1 m duct diameter with a selection of flow velocity.
c) Profile path mean to total mean flow velocity percentage error.

The model shows that the percentage error is fairly consistent with change in flow velocity and there is a normalised radial distance where the profile normalised flow velocity has less variability with changes in flow velocity or duct diameter. There are some serious limitations to this model described by Equations (2.6)-(2.10) which is that they only model the fully developed flow profile. The flow profile in most practical applications, will deviate considerably from this model. The profile will depend on the actual distance, the device is fitted from a disturbance. To reach fully developed flow, it can take from 30 to 160 equivalent duct diameters in

length from the intake or disturbance [37] which is further explored in Section 6.3. This model only describes a round duct/pipe. There is another model for rectangular duct/pipe laminar flow profiles which is described by Muramatsu *et al.* [38].

2.2.2 Wave propagation equation

This method solves differential equations for pressure, density and fluid velocity to predict the three-dimensional velocity flow fields and the acoustic pressure signals transmitted through the fluid and also the pipe body. This technique is computationally expensive and very few examples using this method solely to simulate an ultrasonic flowmeter have been found in the literature.

A method using finite difference time domain (FDTD) is described by Muramatsu *et al.* [38] to simulate the 3-D ultrasonic sound propagation of a flowmeter in a numerically modelled rectangular duct flow field containing air. The model was reported to take 45 minutes [38] (Fig. 5) to simulate on a Fujitsu Primequest 580 high-performance server with 32 CPUs.

Another method is described by *Luca et al.* [39] which uses the discontinuous Galerkin (DG) method which is a hybrid method combining features of both finite element and finite volume methods. A two-dimensional simulation of a clamp on flowmeter was simulated using this method. To accelerate the speed of the simulation, it was implemented on a graphical processing unit (GPU). The authors are also working towards producing a three-dimensional version of the simulation.

2.2.3 Ray-trace method and the Helmhotz integral ray-trace method

In acoustic ray tracing sound is represented by an array of three-dimensional coordinates which represent points or particles of sound energy along the acoustic wave front, which then travel from the transmitter's surface through the flow field at approximately the speed of sound of the medium. The coordinate is updated with the original velocity vector for the sound particle trajectory and the velocity field until the particle of sound hits the receiver. At the receiver the number of particles for that time of arrival are collated and used to construct the receiver signal waveform. The flowchart [40] (p. 80) below in Figure 2.8, which is an excerpt of a thesis by Francis J. Weber shows the steps involved in a computer program which uses Ray tracing to simulate an ultrasonic flowmeter of the type shown in Figure 2.5.

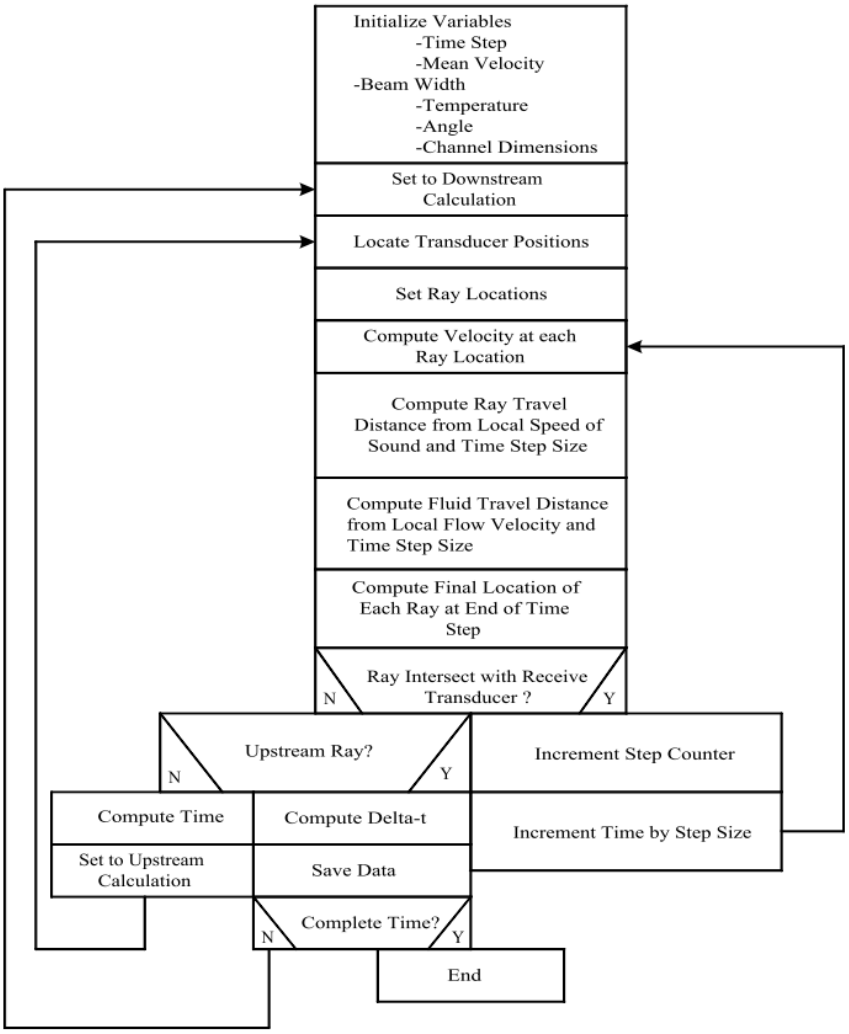

Figure 2.8. Flowchart of a modified raytrace method computer program by Weber *et al.*
(Source: Weber *et al.* [41](p.80))

Further information on the acoustic ray tracing method can be obtained from a paper by *Looss et al.* [42] and also in more detail by Weber [40] (p. 34).

The Helmhotz integral ray-trace method (HIRM) is said to include wave effects omitted by the standard ray tracing method, though its complexity to be implemented is greater [30] (p. 4). The main wave effect that standard ray tracing cannot model is diffraction. So HIRM uses the principle developed by Huygens that light and sound can be modelled by an array of spherical wave sources. The path of the acoustic ray to any target point can then be calculated solving the Helmhotz integral to determine the initial wave trajectory for each of the wave point sources [43]. This method has been combined with finite element method (FEM) to reduce the computational expense of a completely FEM solution for the reasons explained in Section 6.2.2. The Figure 2.9 below which is an excerpt from an article by Bezděk *et al.* [44] shows that in this hybrid method most of the moving fluid is simulated using HIRM except for a narrow region close to the vessel wall.

The piezoelectric transducer and the acoustic signal through the pipe wall is also simulated using FEM.

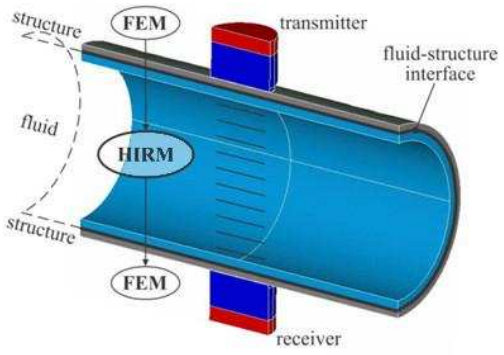

Figure 2.9. FEM-HIRM hybrid simulation method used by Bezděk et al. (Source: Bezděk et al. [45] (p. 771))

This method of simulation is especially useful for non-invasive clamp on type transducer flowmeters. The complex acoustic wave patterns caused by diffraction, absorption and reflections due to acoustic impedance mismatches can be simulated using less memory than required for a full FEM solution.

2.3 Summary of Chapter 2

A summary of the developments in the field of acoustic flow rate measurement devices suitable for HVAC purposes has been presented. The designs by Bragg and Lynnworth and Strauss *et al.* show that single sided devices with a reflective acoustic path have been considered in the past, but as yet have not been fully commercialised. A research study by Olmos and another study by Van Buggenhout *et al.* both show promising results for low velocity ultrasonic airflow measurement devices. The TDC-GP2 double threshold detection timing chip has been demonstrated by Chen *et al.* to produce accurate airflow measurements of ± 3% using a dual non-reflective path airflow meter.

Also an overview of the current research and methods for simulating ultrasonic airflow flowmeters has been presented. Four types of simulation model are presented. They are a deterministic numerical model, wave propagation equation method, ray-trace method and the Helmhotz integral ray-trace method. The deterministic numerical model is simple to implement, but results are the least accurate of all the models described in this chapter, but still useful for producing approximate results for design configuration purposes. The wave propagation equation model using FDTD is very difficult to implement, time consuming and requires large computing resource but does simulate wave phenomena such as refraction. Similarly the Helmhotz integral ray-trace method is very difficult to

implement, but the computing time is much reduced. The ray tracing method has much reduced computational overheads compared to the wave propagation equation method, but does not simulate all wave phenomena.

Chapter 3.

HVAC Energy Throughput Measurement Method Theory and Sensor Technologies

In this chapter:

The first subsection describes the method for calculating energy throughput of a HVAC system. The second Section 3.2 gives an overview of the types of sensors that are available to measure temperature, humidity and the airflow rate. Also, Section 3.2.3.4 gives a general overview of acoustic flow measurement devices.

3.1 Measurement of HVAC Energy Throughput Methods

Two methods for calculating the energy throughput of a HVAC system are described in the following subsections. The first method disregards the effect of water vapour content on enthalpy level to simplify the calculation. The second method is more lengthy and requires the measurement of humidity in conjunction with temperature and mass flow used in the first method. This method should be used when there is a change in water vapour content of the air or greater accuracy is required.

3.1.1 Energy throughput calculations (heat only, constant water vapour level)

This section explains how to calculate energy throughput of a simple ventilation heating system where it is assumed that there is no change in the air water vapour content. As shown in Figure 3.1 the airflow rate and temperature is monitored before and after the heater coil. The HVAC symbols for Figure 3.1 are reproduced from ASHRAE Standard 134-2005 (RA 2014) -- Graphic Symbols for Heating, Ventilating, Air-Conditioning, and Refrigerating Systems (ANSI Approved) [46]. The majority of the equations used in the following two sections are from the ASHRAE Handbook of Fundamentals, chapter 1 [47] described by the table called "SITUATION 3." where dry bulb temperature t, relative humidity ϕ and pressure p is given.

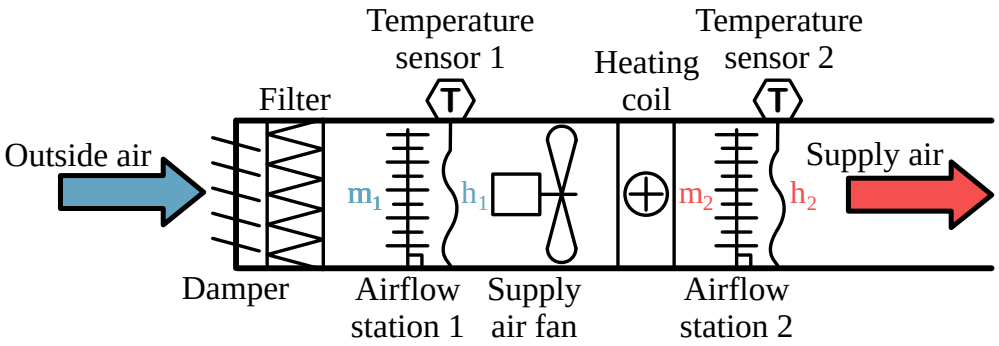

Figure 3.1. Ventilation heating system with airflow monitoring scenario.

Equations for energy throughput where there is no change in water vapour content are as follows;

3.1.1.1 *Air density calculations*

Absolute temperature T in Kelvins (K) can be calculated from degrees Celsius (°C) by the following relationship [47] (p. 1.2):

$$T = t + 273.15 \tag{3.1}$$

The barometric pressure of atmospheric air can be calculated by the following equation [47] (p. 1.1):

$$p = 101.325(1 - 2.25577 \times 10^{-5} Z)^{5.2559} \tag{3.2}$$

Where

p barometric pressure (kPa);

Z altitude (m).

The density of air can be calculated by using the ideal gas law:

$$\rho = \frac{p}{RT} \tag{3.3}$$

Where

ρ density of dry air (kg/m^3);

p pressure (kPa);

T absolute temperature (K);

R gas constant for dry air is 287.042 (J/kg K) obtained from [47] (p. 1.1).

3.1.1.2 *Mass flow rate calculations*

Calculate the duct cross sectional area for a circular duct using the following Equation (3.4) or for a rectangular duct multiply height by width:

$$A = \left(\frac{\pi}{4}\right) \times D^2 \tag{3.4}$$

Where

A duct cross sectional area (m^2);

D diameter of duct (m).

Calculate mass flow rate using the following equation:

$$m = U_m \, A \, \rho \tag{3.5}$$

Where

m mass flow rate in (kg /s);

U_m measured duct mean airflow velocity (m/s);

A duct cross sectional area (m^2);

ρ density of dry air (kg/m^3).

3.1.1.3 *Energy throughput calculations given mass flow and dry Bulb temperature*

Equation (3.6) [47] (p. 1.9) is used to calculate the amount of enthalpy or energy per kilogram of dry air relative to the air at 0℃. No water is being taken away or added so the specific humidity ratio $\gamma = M_w/(M_w + M_{da})$ will not change in this scenario so the rise due to evaporation or condensation of water is zero. The enthalpy change due to sensible heat rise or cooling of the water vapour can be ignored in most cases because it is very small, being no more than +1.5% of the total enthalpy change in the worst-case scenario. However, if a more accurate result is required, then the calculations in Section 3.1.2 should be used which take into account the energy needed or released to heat or cool the water vapour content in the duct air.

$$h_{da} \cong 1.006t \tag{3.6}$$

Where

h_{da} specific enthalpy of the air (kJ/kg);

t temperature in Celsius (°C).

Calculate rate of energy throughput in kilowatts using the following Equation (3.7) [10]:

$$Q = m_2 h_2 - m_1 h_1 \tag{3.7}$$

Where

Q rate of energy throughput (kJ/s) or (kW);

m_1 mass flow rate before heat exchanger (kg /s);

m_2 mass flow rate after heat exchanger (kg /s);

h_1 enthalpy of air before heat exchanger (kJ/kg);

h_2 enthalpy of air after heat exchanger (kJ/kg).

3.1.1.4 *HVAC faults which could be detected by monitoring of airflow, temperature and power consumption.*

The following Figure 3.2 shows some examples of common faults which could be detected by the monitoring of airflow and temperature before and after a air handling unit. The energy throughput levels could be calculated and compared against a known baseline or the energy input could be measured by measuring electrical power consumed and the energy supplied to the heater coils using a heat meter. A drop in efficiency could be used to indicate a problem in this heating system.

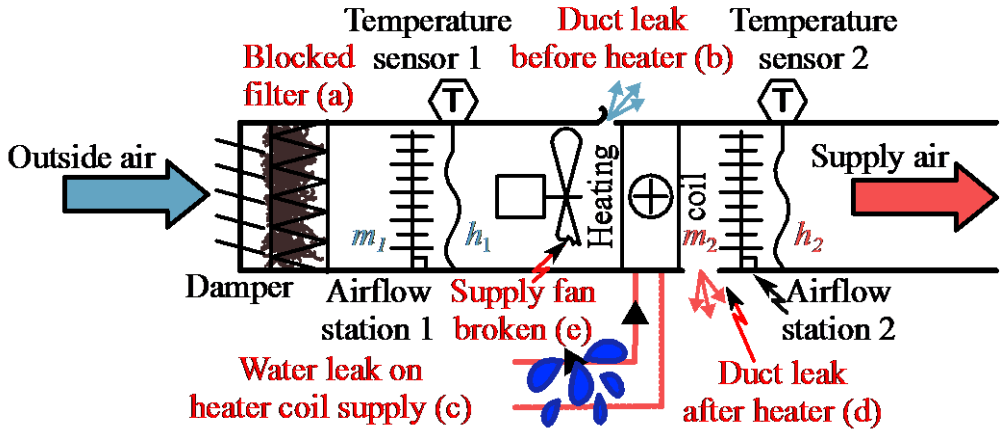

Figure 3.2. Ventilation heating system showing a selection of faults.

List of heating system fault scenarios as shown in Figure 3.2;

a) Blocked air filter causing reduction in m_1, m_2 mass flow rates, reducing supply fan efficiency and causing a reduction in the maximum heating rate.
b) Duct leak before heating coil causing reduction in m_2 mass flow rate.
c) Water leak on heating coil supply causing a reduced h_2 enthalpy level and increased boiler energy usage.
d) Duct leak after heater causing reduction in m_2 mass flow rate but h_2 enthalpy level the same or slightly reduced.
e) Broken supply air fan causing reduction in m_1, m_2 mass flow rates, reducing supply fan efficiency and causing a reduction in the maximum heating rate similar to condition (a).

3.1.2 Energy throughput calculations (taking into account water vapour content)

Equations for energy throughput where there is change in water vapour content (Cooling>Dew point)/Dehumidification or Humidification are as follows;

3.1.2.1 Humidity ratio calculations

Calculate the water vapour saturation pressure over liquid water for temperature range 0 to 200 ℃ using the following Equation (3.8) [47] (p. 1.2) absolute :

$$\ln p_{ws} \cong \frac{C_8}{T} + C_9 + C_{10}T + C_{11}T^2 + C_{12}T^3 + C_{13}\ln T \tag{3.8}$$

Where

p_{ws} $= e^{\ln p_{ws}} =$ saturation pressure (Pa);
T absolute temperature (K);
C_8 $=-5.8002206 \times 10^3$;
C_9 $= 1.3914993$;
C_{10} $=-4.8640239 \times 10^{-2}$;
C_{11} $= 4.1764768 \times 10^{-5}$;
C_{12} $=-1.4452093 \times 10^{-8}$;
C_{13} $= 6.5459673$.

Calculate the actual partial pressure of water vapour from a percentage relative humidity reading using the following Equation (3.9) [47] (p. 1.8):

$$p_w = \phi p_{ws} \tag{3.9}$$

Where

p_w partial of water vapour pressure (Pa);
ϕ relative humidity (ratio)$= \%RH/100$;
$\%RH$ relative humidity (percentage).

Calculate the humidity ratio using the following Equation (3.10) [47] (p. 1.8):

$$W = 0.621945\frac{p_w}{p - p_w} \tag{3.10}$$

Where

W humidity ratio;
p_w partial of water vapour pressure (Pa) $= \phi p_{ws}$;
p barometric pressure (kPa).

3.1.2.2 Energy throughput calculations given mass flow, dry bulb temperature and humidity ratio

Calculate the amount of enthalpy per kilogram of dry air relative to the air at 0℃ using the following Equation (3.11) [47] (p. 1.9):

$$h \cong 1.006t + W(2501 + 1.86t) \tag{3.11}$$

Where

h specific enthalpy of moist air (kJ/kg)
t temperature in Celsius (°C)

Calculate rate of energy throughput in kilowatts using Equation (3.7).

3.1.2.3 HVAC faults which could be detected by monitoring of airflow, temperature, humidity and power consumption.

The following section explains how to calculate energy throughput of a ventilation heating and cooling system where there could be a change in the air water vapour content by humidification or dehumidification. As shown in Figure 3.3 the airflow rate and temperature is monitored before and after the humidifier and heating/cooling coils. As before, in Section 3.1.1.4, the energy throughput levels could be calculated and compared against a known baseline or the energy input could be measured by measuring electrical power consumed and the energy supplied to the heater/cooling coils using heat meters. A drop in efficiency could be used to indicate a problem in this heating/cooling system.

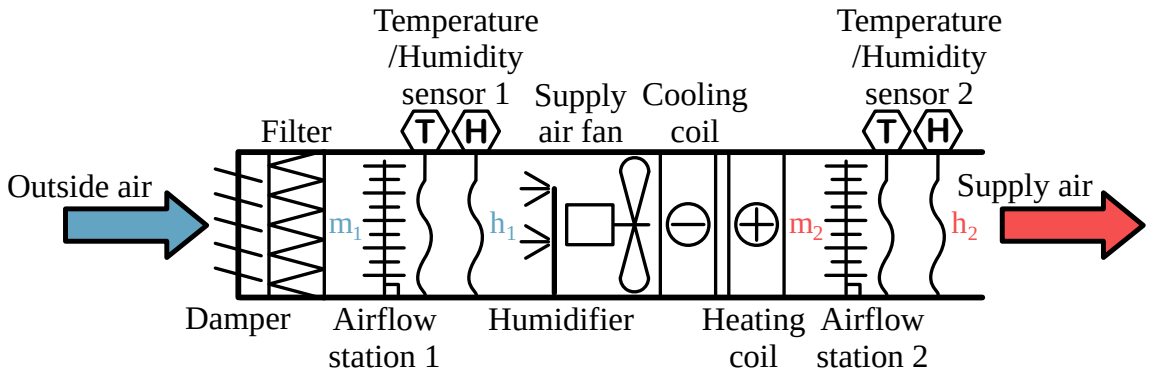

Figure 3.3. Ventilation humidification, heating and cooling system with airflow monitoring scenario.

List of humidification, heating and cooling fault scenarios, which could possibly occur in the above system shown in Figure 3.3:

a) A humidifier running in a hot climate even though not required or duct leakage producing excessive indoor humidity levels, which if it is mitigated by reducing thermostat setting by 1.1° C, which is described by Domanski *et al.* [48] (p.83) would increase the annual energy usage by 20%.
b) The heating and cooling coils are both running at the same time.
c) The cooling coil chillers refrigerant is undercharged. A system that is undercharged by 30% will typically increase energy usage by 20% in simulation scenarios [48] (p. 73).
d) The cooling coil chillers refrigerant is overcharged. A system that is overcharged by 30% will typically increase energy usage by 10-16% in simulation scenarios [48] (p. 73).

3.2 Brief Overview of Current Ventilation Sensors Technologies

The following subsections describe, what are the types of sensors available to measure temperature, humidity and airflow rate, which provide the input data needed by Equations (3.1-3.11).

3.2.1 Temperature sensors

It is important to consider the accuracy and stability of the temperature measurement technology used, as a small variation in the temperature can significantly affect the energy throughput calculation results. A summary of a selection of temperature sensors and their typical accuracies, costs and measurement ranges is shown in Table 3.1 below.

Table 3.1. Comparison of air temperature sensor probes.

Sensor type	Accuracy °C	Temp range °C	Part no.[1]	Cost[1]
Thermocouple	K,J ±1.5, T ±0.5	-25 to 1100	M12JSS-M3-U-200-G	£32
Resistor Temperature Devices (RTD)	±0.3 °C	-259 to 1000	RTD-805	£64
Thermistor	±0.2 °C	-50 to 150	OL-705	£49

[1]Data collected from http://www.omega.co.uk/ by author (accessed on 25 May 2016).

3.2.1.1 Thermocouple

Thermocouples use the principle known as the Seebeck effect [49]. They are made with two pieces of wire, which are of different metals and joined in two places by twisting, soldering or welding the ends of the wire together. If there is a difference in temperature between the two junctions there will be a small voltage produced. One of the junctions needs to have its temperature stabilised or precisely measured using a device such as a resistor temperature device (RTD) or thermistor so that the thermocouple probe differential temperature can be referenced. Accuracy of a thermocouple is highly dependent on its cold junction temperature measurement and the choice of dissimilar wire metals used. Typically the accuracy of a K and J type probe would be ±1.5 ℃ and a T type probe would be ±0.5 ℃. Generally thermocouples are more suited to applications, where a large temperature range is required to be measured, for example -25 ℃ to 1100 ℃.

3.2.1.2 Resistor Temperature Devices(RTD)

Platinum RTD's are the most stable long-term temperature measurement devices because they are resistant to corrosion. Their accuracy is better than ±0.3 ℃ for a

standard DIN/IEC 60751 Class A device measuring in the temperature range between 0° and 70 °C.

3.2.1.3 *Thermistor*

A thermistor is a resistive device made of metal oxides, which is sensitive to temperature changes. Their resistance is high, which is usually about 2K Ohms at 25° C so that the connecting cable resistance causes minimal temperature reading error. The resistance of these devices is not linear over a temperature range so parameters called Steinhart-Hart coefficients need to be calculated by calibrating the thermistor at a number of different temperatures. Once this is done their accuracy can be ±0.2 °C or better. The measurement range which is typically between -50 °C to +150 °C is much smaller then RTD's and thermocouples. If these devices are used constantly at a temperature below -25 °C and above 75 °C, which is outside the typical HVAC measurement range, their resistance may start to decrease. However this can be corrected by a recalibration.

3.2.2 Humidity sensors

3.2.2.1 *Dew point*

A chilled mirror hygrometer measures the dew point to about ±0.2 °C accuracy which equates to a minimum accuracy ±1.25 %RH at 20 °C. It uses a temperature controlled surface to measure the point at which water vapour is condensed from the air, which is called the dew point. This type of meter is large, expensive and the condensing surface requires periodic cleaning to retain its accuracy.

3.2.2.2 *Relative humidity*

Historically a wet and dry bulb thermometer has been used to measure relative humidity. This measures the difference in temperature drop caused by evaporation, of a constantly wet thermometer bulb to a dry thermometer bulb. This method has the disadvantage that the wet bulb requires periodic wetting. Commonly available electronic relative humidity sensors use a capacitive sensor, which has a permeable dielectric material that is open to the environment and as it absorbs more or less water vapour, the value of its capacitance is modified. The accuracy of the sensor could be affected by contaminants contacting with the dielectric material so an air filter should be fitted to the sensor to avoid this risk. The most accurate devices like the HYT-221 or SHT25 contain memory which is used to retain calibration data to adjust the output so it is correct to a minimum of usually ±2 %RH with a temperature measuring accuracy of ±0.2 °C as shown in

Table 3.2. Alternatively much lower cost devices are available such as the AM2303 which has a claimed accuracy of typically ±2 %RH(Max ±5 %RH) and ±0.5 ℃ for temperature or the DHT11 which has a claimed accuracy of ±5 %RH and ±2 ℃ for temperature.

Table 3.2. Comparison of capacitive type humidity sensors.

Model No.	Accuracy %RH	Accuracy °C	Cost
HYT-221	±1.8	±0.2	<£39[1]
SHT25	±1.8	±0.2	<£8[1]
AM2303	Typ ±2(Max ±5)	±0.5	<£6[2]
DHT11	±5	±2	<£1[2]

[1]Data collected from http://www.farnell.com by author (accessed on 26 August 2015).
[2]Data collected from http://www.ebay.co.uk by author (accessed on 26 August 2015).

3.2.3 Air flow sensors

The following section explains methods for the measurement of in-duct airflows but further information can be obtained from BS EN 16211:2015 [50] for measurement methods for circular and rectangular ducts using Pitot static (Prandtl), hot wire, mechanical anemometer, fix flow measurement devices and tracer gas. Also ASHRAE Fundamentals Handbook [47] (pp. 36.14-36.21) has extensive information on a greater range of devices and methods for measuring airflow, along with their advantages and disadvantages.

3.2.3.1 Pressure differential methods

The most commonly used means of measuring ventilation flow rate incorporate a pressure differential measurement technique. The easiest and therefore lowest cost method is the orifice plate flowmeter as shown in Figure 3.4. Their volumetric mass flow rate measurement accuracy is said to be in the range from 1% to 5% [47] (p. 36.21). However this technique is not popular because of the large discharge coefficient between 0.6 and 0.85, which creates uncertainty in the measurement due to varying turbulence levels. The discharge coefficient [47] (p. 3.10) is a factor used to compensate for small losses due to viscous effects with boundaries and the jet contractions which reduce the effective flow area by a factor of up to 0.6, which the Bernoulli equations do not take into account.

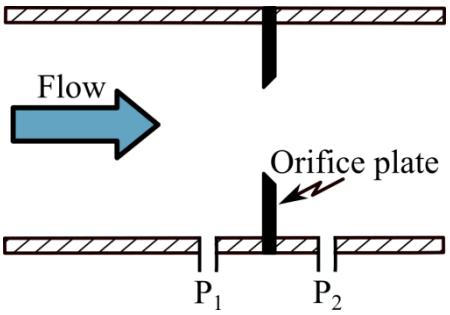

Figure 3.4. Orifice plate flowmeter.

The orifice plate restricts the flow of the air, creating a point where an accumulation of fibrous dust could cause a blockage. This restriction of flow creates a large pressure drop so requiring increased energy to move the air through the ventilation duct. A high amount of turbulence is created at the plate, which generates increased noise levels.

The Venturi tube as shown in Figure 3.5 has an improved discharge coefficient, compared to the typical orifice plate flowmeter. The flow profile shape does not affect the measurement very much compared to other types of flowmeter. Their volumetric or mass flow rate measurement accuracy is said to be between 0.5% and 2% [47] (p. 36.21).

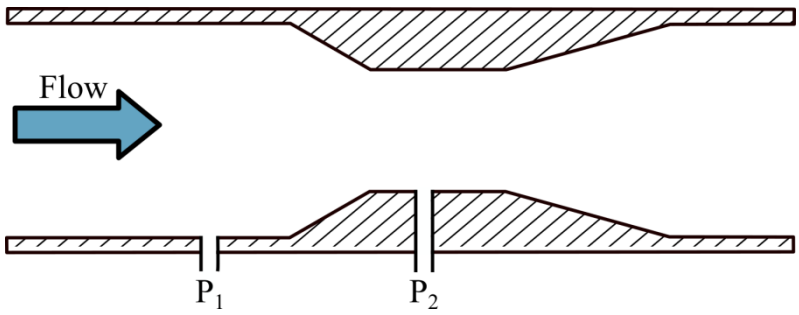

Figure 3.5. Short form Venturi tube flowmeter.

The discharge coefficient values are typically 0.984 for a cast tube, 0.985 for a welded tube and 0.995 for a machined tube. The discharge coefficient is used to compensate for the difference in the actual flow rate compared to the theoretical flow rate [51] (p. 15/7), which is caused by the surface friction of the Venturi. Generally a Venturi is expensive to manufacture and requires a large amount of space to accommodate fitting. A typical accuracy for a pressure meter for measuring airflow velocity is about ±1 Pascal, which as shown in Figure 3.6 using a Venturi with a ratio of diameters of about 0.6 the accuracy is affected significantly below 2 m/s with mean flow velocity reading percentage error of greater than 5% at 1.82 m/s.

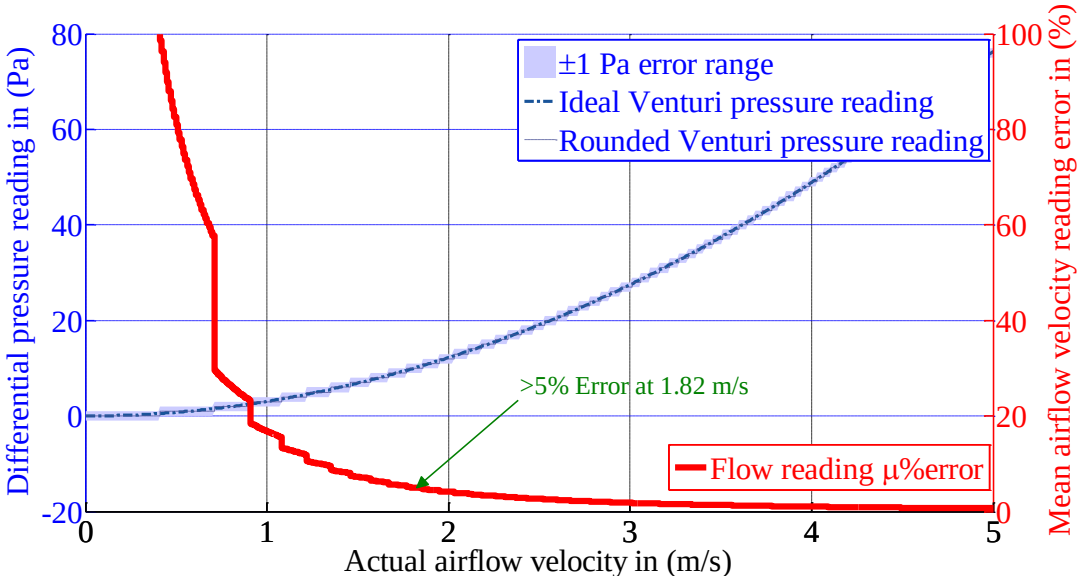

Figure 3.6. Venturi tube differential pressure reading %error with a ±1Pa accuracy manometer device.

The Pitot tube as shown in Figure 3.7 is commonly used to measure duct flow velocity because the probe can be easily inserted into the duct via a small drill hole.

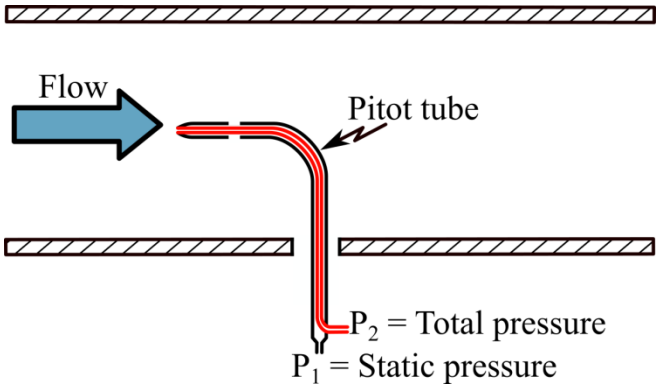

Figure 3.7. Pitot tube.

It can only measure a specific airflow velocity at a single point, so to measure the average flow velocity across the duct a series of measurements need to be taken in a pattern as shown in Figure 3.8 a,b [47] (p. 36.18) or as in BS EN 16211:2015 [50] (section 8.2), which compensates for flow profile differences across the duct caused by duct wall friction.

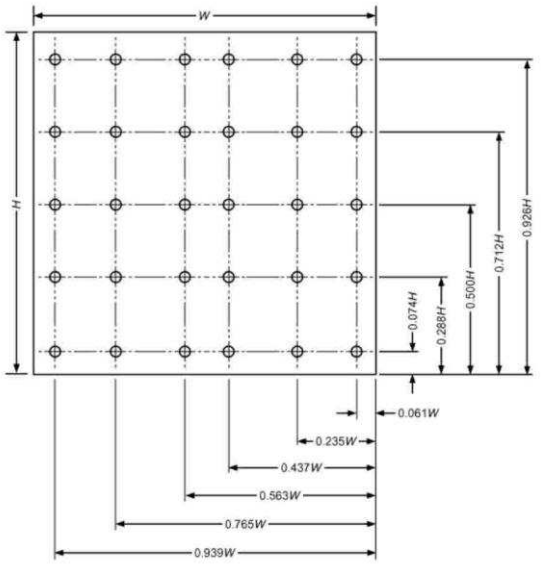

Duct Dimensions	No. of Points for Traverse Lines	Position Relative to Inner Wall
460 mm < *H*, *W* < 750 mm	5	0.074, 0.288, 0.500, 0.712, 0.926
750 mm ≤ *H*, *W* ≤ 900 mm	6	0.061, 0.235, 0.437, 0.563, 0.765, 0.939
H, *W* > 900 mm	7	0.053, 0.203, 0.366, 0.500, 0.634, 0.797, 0.947

Log-Tchebycheff Rule for Rectangular Ducts

Note: Example duct has 5 × 6 (*H* × *W*) measurement pattern, as for rectangular duct of 600 × 750 mm.

(a)

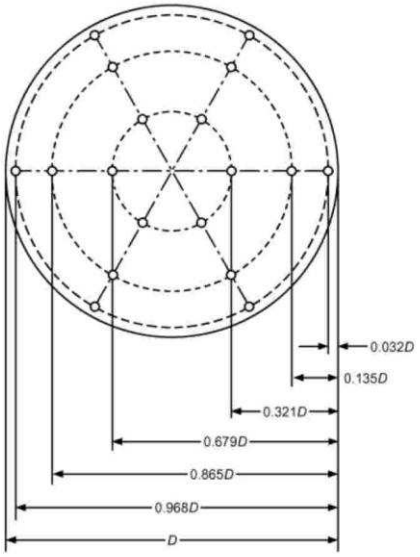

No. of Measuring Points per Diameter	Position Relative to Inner Wall
6	0.032, 0.135, 0.321, 0.679, 0.865, 0.968
8	0.021, 0.117, 0.184, 0.345, 0.655, 0.816, 0.883, 0.979
10	0.019, 0.077, 0.153, 0.217, 0.361, 0.639, 0.783, 0.847, 0.923, 0.981

Log-Linear Rule for Circular Ducts

(b)

Figure 3.8. ASHRAE duct traverse flow measurement rules; (a) Square duct traverse, (b) Circular duct traverse. (Source: ASHRAE, [47] (p. 36.18))

Equation (3.12) describes the Pitot tube differential pressure in Pascals generated by an incompressible flow. It can be seen in equation (3.13) that there is a square law relationship between the pressure differential ΔP and the airflow velocity v which means at low airflow velocities the pressure differential is very small.

$$\Delta P = \frac{1}{2}\rho v^2 \tag{3.12}$$

$$\text{if air density is } \rho = 1.2\ \text{kg}/m^3 \therefore\ \Delta P = 0.6v^2 \tag{3.13}$$

Non-standard atmospheric pressure conditions require a more elaborate equation than Equation (3.12) to calculate the airflow velocity [52], [53].

Using the typical ±1 Pascal resolution pressure meter. The Pitot tube results shown in Figure 3.9 are more affected by low flow velocity than the Venturi using the same pressure meter. Below a flow velocity of 2 m/s the reading percentage error could be greater than 20% [50] (section 7.4).

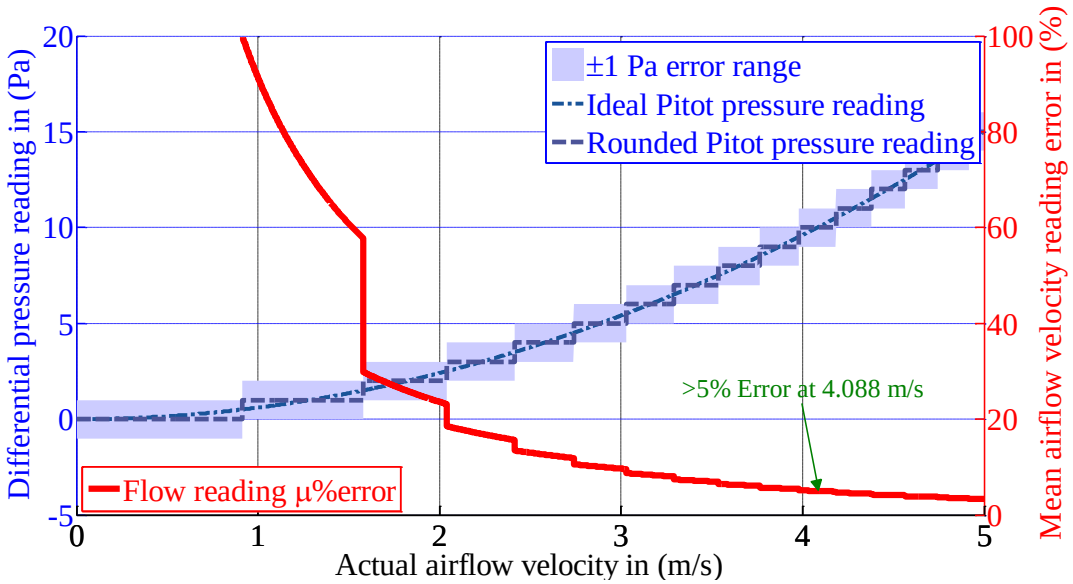

Figure 3.9. Pitot tube differential pressure reading %error with a ±1Pa accuracy manometer device.

To cover lower flow velocities a device with a limited lower pressure reading range and better resolution would have to be used but these more sensitive devices are very expensive. The accuracy of the duct traverse methods varies from 2 to 10% according to the ASHRAE Fundamentals Handbook [47] (p. 36.21). A traverse can be done at most points in the duct system where access allows it. This method is very time-consuming and requires a minimum of 25 measurement points per traverse. Pitot tubes are required to be aligned parallel to the duct direction within 15° [52], [53], which can be difficult to judge as the probe is usually hidden; for up to 50° of misalignment, this problem can be corrected by using a Kiel probe instead of a Pitot tube, but this probe requires a much larger access hole which is similar in size to that required by a typical hotwire type airflow measurement probe. Accurate differential pressure gauges suitable for measuring low flow velocities are expensive and need to be zeroed at the start of each measurement traverse run.

Velocity pressure arrays operate similar to an array of Pitot tubes, but connected in parallel to a single differential pressure gauge. An array of pressure monitoring ports is placed into the flow to sample the total pressure and a similar array monitors the pressure in the reverse direction. The velocity of the airflow can be calculated using the Pitot tube Equation (3.12). As shown in Figure 3.10, various velocity pressure array monitoring probes exist. They can be in the shape of a single straight multi-point probe, crossed or in a grid formation such as in the Wilson flow grid.

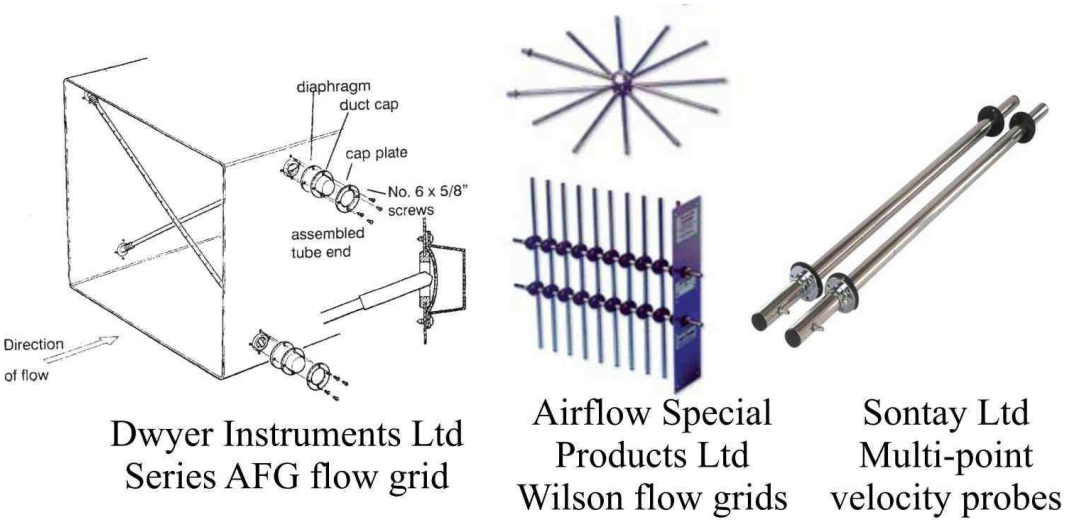

Figure 3.10. A selection of velocity pressure arrays

The Wilson flow grid measures the average airflow over the entire ventilation duct with little restriction on airflow but is difficult to fit into an existing ventilation system and then remove if required elsewhere. The main benefit of velocity pressure arrays is that they can measure the mean flow velocity with varying duct flow profiles. The ports on the array may become blocked by dust so periodic checks and cleaning are necessary for this type of flowmeter. The mean of the pressure difference, used to calculate the mean velocity measurement may not be the same as the mean of individual velocity measurements if it had been done using multiple Pitot tube devices because the pressure to velocity conversion is not linear but the error is negligible if the majority of readings are within ±25% of the mean pressure value [53].

3.2.3.2 Propeller type

Propeller type or vane anemometers as shown in Figure 3.11 use a horizontal pivoted shaft with vanes radiating outwards.

Figure 3.11. Mini vane anemometers.

The shaft is then connected to either a generator or pulse counter, which gives indication of the number of revolutions in a period of time. They are relatively low-cost compared to other types of anemometer, but do suffer from mechanical wear

and can be easily damaged so require periodic maintenance for cleaning, lubricating and calibration. They do not take into account the flow profile, unless the anemometer covers the whole of the duct area, so similar to the Pitot tube, a traverse of the duct needs to be done to calculate the mean flow. The propeller or cup type anemometers do have a tendency to overestimate flow velocity in turbulent flow because the propeller will accelerate faster then it decelerates [54] (ch. 5.4).

3.2.3.3 *Thermal*

The amount of convective heat transfer created by the airflow is used to calculate the airflow speed. Hotwire sensors as shown in Figure 3.12 can be constant voltage, constant current or constant temperature.

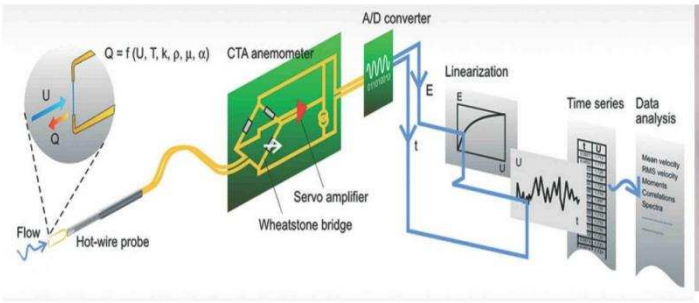

Typical contant temperature
hot wire device configuration
Source: Dantec Dynamics Inc

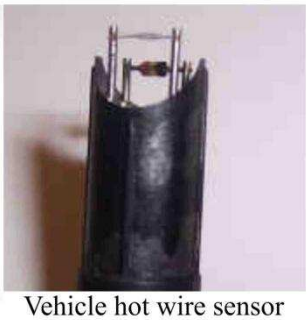

Vehicle hot wire sensor
hot wire at top
Air temperature thermistor
behind and slightly below
Source: http://www.g33.co.uk

Figure 3.12. Hot wire anemometers

A constant current sensor will use the voltage dropped across a wire to calculate the airflow required to drop the temperature of the wire from the ambient. The constant temperature sensor will use the amount of current required to maintain its temperature as an indication of the airflow velocity. Hotwire devices are good at measuring the full range of velocities in difficult turbulent air at the precise spot required. Unlike pressure differential flow measurement techniques hotwire devices are more sensitive the lower the flow velocity [55] (p.376), [50] (section 7.3-7.4) but the drawback is that contaminants can alter readings so periodic cleaning and re-calibration is required. There are hotwire devices in car mass airflow sensors that use a periodic heating cycle to burn off contaminants from sensor wires, but in air HVAC system this could be a potential fire hazard. Also hotwire devices can be sensitive to rapid airflow, temperature changes causing errors in flow speed measurements and even with temperature compensation [56],

[57] this can be a problem for short periods of time until temperature compensation becomes effective.

3.2.3.4 *Acoustic flow measurement devices*

According to Lynnworth and Liu [58] acoustic flow measurement devices have been around for at least 60 years. There are many types based on methods such as sing-around, phase difference, Doppler, cross correlation, vortex shedding, acoustic resonance and time of flight which can also incorporate a contra-propagating technique to eliminate zero flow calibration drift which was first described in a 1956 patent by Swengel [59] for a device to measure fluid velocity. This device used piezoelectric crystals connected to rods to transmit an acoustic signal upstream and then downstream to calculate the flow velocity using the phase difference between the two signals. Swengel's continuous transmit signal device is shown in Figure 3.13a and the pulsed version is shown in Figure 3.13b.

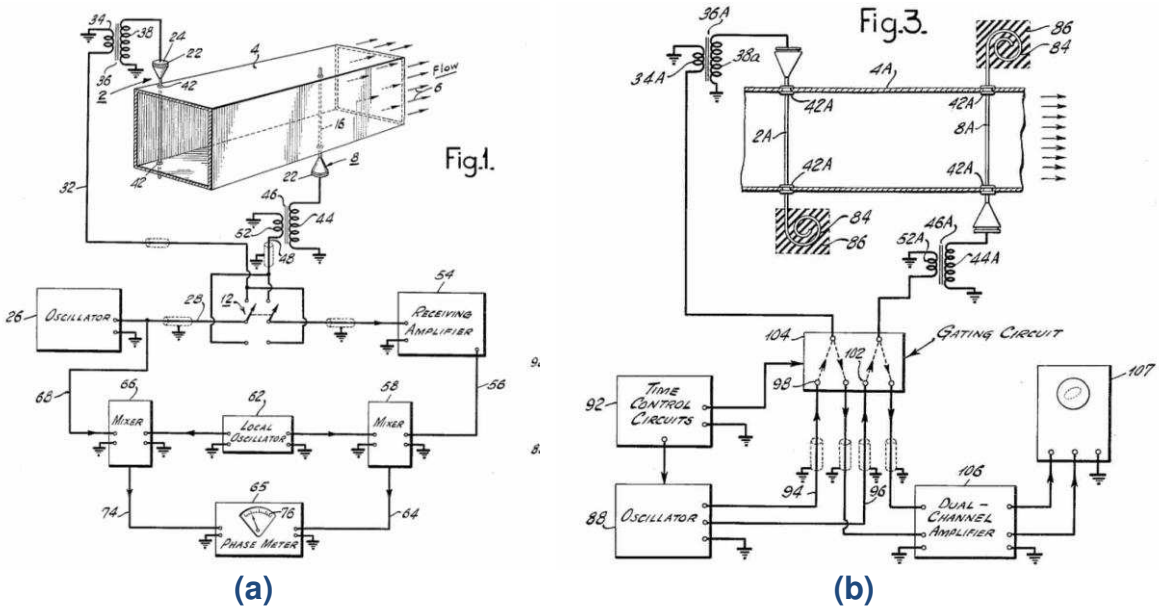

Figure 3.13. Ultrasonic contra propagating fluid velocity measuring system by R. C. Swengel; (a) Continuous, (b) Pulsed. (Source: Swengel [60], [61])

Sonic transducer technology

Open structure type ultrasonic sensors

The open structure ultrasonic transducer shown in Figure 3.14 is low-cost and available in transmitter/receiver pairs but is capable of doing both roles if necessary. They have much higher sensitivity then other types of ultrasonic transducers, because the piezoelectric ceramic is open to the air. This makes these types of sensor unsuitable for the outdoor environment. They may be

suitable for use in a ventilation system but may be affected long-term by condensation and dust build up.

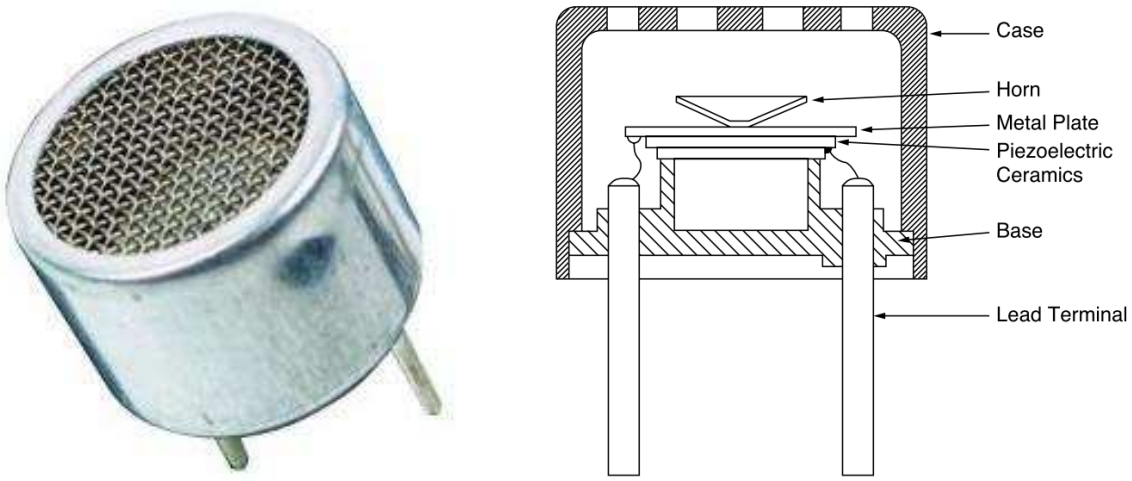

(a) (b)

Figure 3.14. Ultrasonic transducer Air/Open type;
(a) Body - source Maplins Electronics Ltd,
(b) Cross-section - source Murata Manufacturing Co, Ltd.

Enclosed structure type ultrasonic sensors

Enclosed ultrasonic sensors as shown in Figure 3.15 are sealed to protect against water and dirt ingress but are around four times the cost of the open type. The drawback of this is that the receiver electrical output is greatly reduced and ringing of the transducer is increased. Also the drive voltages from the transmitter need to be increased to operate at the same sound pressure level as the open type.

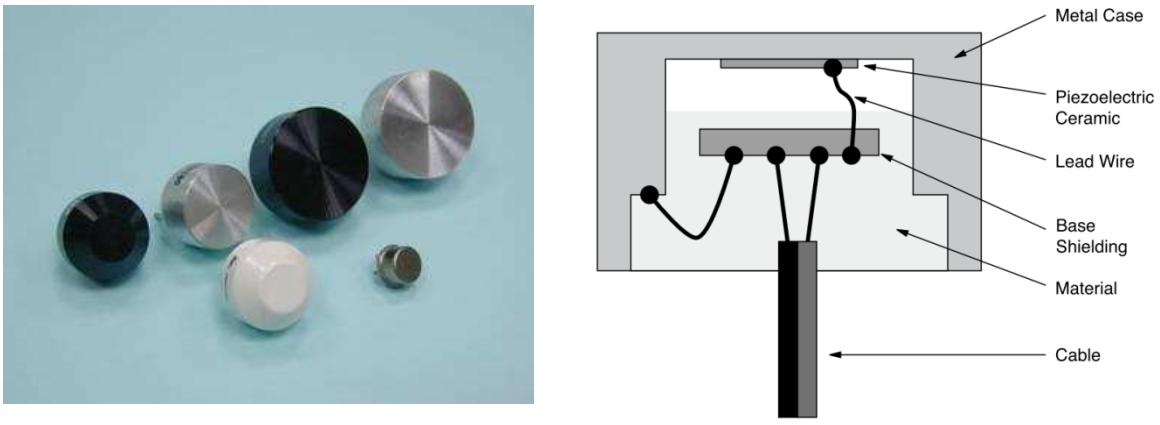

(a) (b)

Figure 3.15. Ultrasonic transducer enclosed type;
(a) Bodies - source Pro-Wave Electronic Corp,
(b) Cross-section - source Murata Manufacturing Co, Ltd.

As frequencies increase above 70 kHz the transducer requires acoustic impedance matching as shown in Figure 3.16 between the piezoelectric and air. This is because horizontal flexing of the piezoelectric material is no longer able to produce usable vibration so the vertical flexing is used.

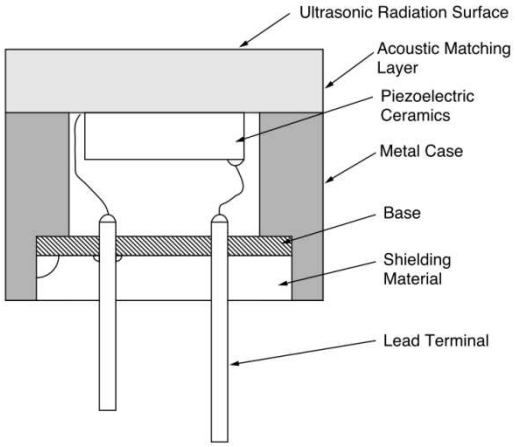

Figure 3.16. High frequency ultrasonic transducer enclosed type; (a) Cross-section - source Murata Manufacturing Co, Ltd.

Enclosed type high frequency ultrasonic transducers do not look externally different to the lower frequency type transducers, but generally these devices are slightly more expensive than the 40 kHz enclosed type transducers. The benefit of using a higher frequency is that better accuracy of measurement can be obtained.

Overall comparison of piezoelectric transducers

Table 3.3 shows a comparison of piezoelectric transducers with open or enclosed structure, above and below 70 kHz resonance frequency.

Table 3.3. Comparison of piezoelectric transducers.

Transducer type	Sensitivity(dB)	Sound pressure (dB)	Drive Vp-p Max	Water-proof	Cost[1]	Other notes
Open structure <70Khz	Min –63 to -70	120	30	No	>£2	Fairly low-cost with high sensitivity but not waterproof.
Open structure >70Khz	Min –63 to -73	120	50	No	>£60	High cost and not waterproof
Enclosed structure <70Khz	Min -70 to -87	103-106	100-160	Yes	>£10	Moderate cost and waterproof but high drive voltage required.
Enclosed structure >70Khz	Min -47 to -74	110-120	120	Yes	>£100	Waterproof with high resolution, high cost and high drive voltage required.

[1]Data collected from http://uk.farnell.com by author (accessed on 3 August 2015).

The open structure transducers are generally of much lower cost compared to enclosed type transducers but they are not waterproof or dustproof, this probably makes them unsuitable for HVAC applications but this would require further environmental testing of the transducers as some problems such as condensation might be mitigated by placing the sensor with the open side facing downwards so that water and dust does not collect on it and build up. The enclosed types of transducers appear to be much more robust but their sensitivity and sound pressure level is reduced and they require a much higher drive voltages to produce the same level of sound pressure output as the open type transducers.

High frequency enclosed type transducers, would produce a system with a higher measurement sensitivity but with increased component cost. Other types of transducer technology are available such as capacitive micro-machined ultrasonic transducer (CMUT) [62], [63] but have not as yet become a off the shelf component. They do offer the potential that transducers of various shapes and beam patterns could be developed, which could cover a wider distance than the circular ultrasonic transducers. A benefit of using a wider transducer is that a greater area of the duct can be covered so increasing airflow measurement accuracy.

Sing around

The sing around method uses the received signal to instigate the next transmission which the repetition frequency of the transmissions minus the zero flow repetition frequency is proportional to the flow velocity. This method can also use contra propagating to avoid problems with zero flow calibration and inaccuracies caused by flow medium temperature changes. Transmit repetition interval jitter [58] can be a problem with this technique.

Phase difference

The phase difference method can be done using a pulsed [19], [64] or continuous [33], [65], [66] transmit signal. The anemometer designed by Han *et al.* [33], [65], [66] which is shown in Figure 3.17a and b utilises the method of continuous phase difference measurement which requires a temperature sensor to correct for the variation in the speed of sound. As the speed of sound increases with temperature, there is a reduction in the number of wavelengths needed to fill the space between the transmitter and receiver. So for an increase in the air temperature with in a constant flow, the phase difference is reduced. The benefit of this method is that a very high measurement update rate, which is equal to the transmitter frequency can be achieved. This design is lower cost to implement than the contra propagating method, but would be prone to errors at low airflow velocities which could cause air temperature variation across the acoustic measurement path's. The flow velocity error rate on this anemometer was demonstrated to be within 2%.

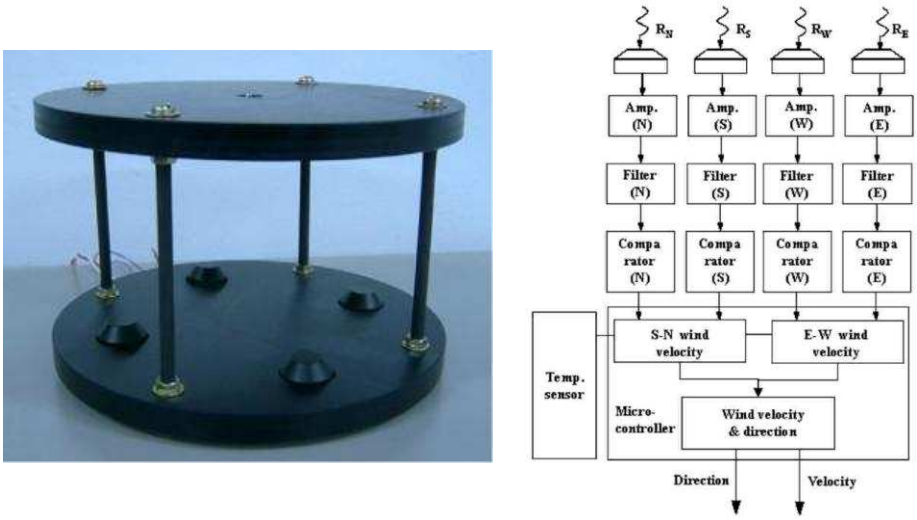

(a) (b)

Figure 3.17. Ultrasonic 2D anemometer utilizing phase differents method; (a) Body, (b) Receiver schematic (Source: Han *et al* [67], [68])

Doppler

The acoustic Doppler method is not suitable for measuring duct airflow velocity as large particles are required to be travelling in the flow for the acoustic signal to bounce off and create the frequency shift relative to the velocity of the particles.

Cross-correlation

The cross correlation flowmeter uses two pairs of opposing transmitter/receiver transducers placed typically on the outside of the pipe a distance apart so that small changes in the acoustic transit time caused by such things as temperature and flow velocity can be correlated to similar changes at the pair of transducers downstream. Figure 3.18 shows a schematic diagram and typical transit time signal waveforms provided by Bentley [55] (p.344) to describe the basic operation of a ultrasonic cross correlation flowmeter.

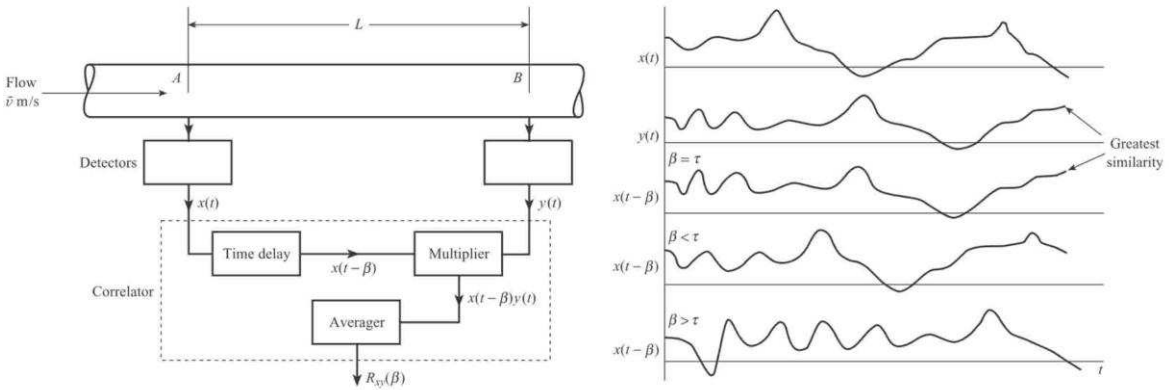

Figure 3.18. Ultrasonic cross correlation flowmeter schematic diagram and typical signal (Source: Bentley [69] (p. 345))

Clamp on cross correlation flowmeters are often used to measure natural gas pipeline flow rates but are not yet suitable for measuring steel ventilation duct flow rates as the acoustic impedance difference is much greater between steel and air compared to steel and pressurised natural gas [70]. The increased acoustic impedance difference between steel and air means that very little signal can be transmitted through the duct wall and virtually all is reflected straight back. If a plastic pipe/duct is selected it should make it possible to measure airflow at atmospheric pressures because of the lower acoustic impedance of plastic compared to steel. It has been reported by Rabalais and Sims that Oleg Khrakovsky [17], using a transit time method, that it was possible to measure airflow in a plastic pipe using clamp on acoustic transducers. This method and the clamp on cross correlation method could be suitable for measuring airflow in a domestic ventilation system where plastic ducting is more commonly used without the requirement to cut access holes in the ducting for installation. The severely attenuated acoustic signals could make these flowmeters prone to errors and require intensive signal processing which increases the cost of the device. There is also a minimum flow rate that can be measured using the cross correlation method, so when measuring near zero flow conditions the output measurement value would be random or indeterminate.

Vortex shedding

The vortex shedding flowmeter as shown in Figure 3.19 uses the principle known as "Bénard-von Kármán vortex street" [55] (p.333), [71] (p. 395) which also can be seen when a flag ripples in the wind on a flagpole.

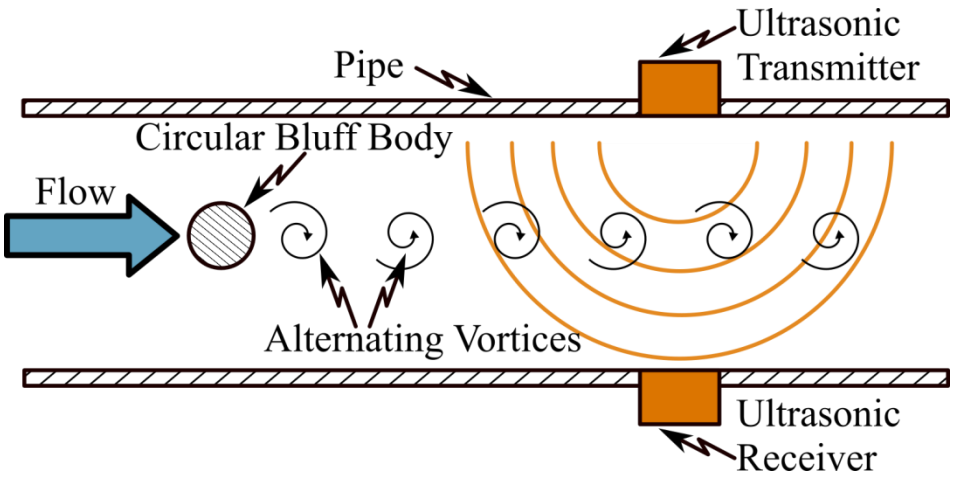

Figure 3.19. Vortex shedding ultrasonic flowmeter diagram.

The period of the ripples, which consist of alternating clockwise and anticlockwise vortices is proportional to the flow velocity. The ultrasonic time of flight or phase difference is constantly monitored as this changes due to the vortices direction of

spin. The fundamental frequency of this signal is used to calculate flow velocity but a number problems can occur. If the fluid/gas is very turbulent this can create spurious extra oscillations in the measurement signal and if flow velocity is very low then no discernible vortices will be created [72] (p.100). This type of flowmeter like most types of flowmeter obstruct the flow which could lead to blockages. These obstructions also create an increase in the pressure drop of the system and therefore reduce the total efficiency.

Acoustic resonance

An acoustic resonance anemometer is presented in a patent produced for FT technologies Ltd (Teddington, UK) [73]. This 1997 patent describes an acoustic anemometer which produces standing waves from transducers energised at Eigen frequencies to measure airflow speed and direction. The acoustic signal is generated between two parallel plates and then received by a separate receiver as shown in Figure 3.20.

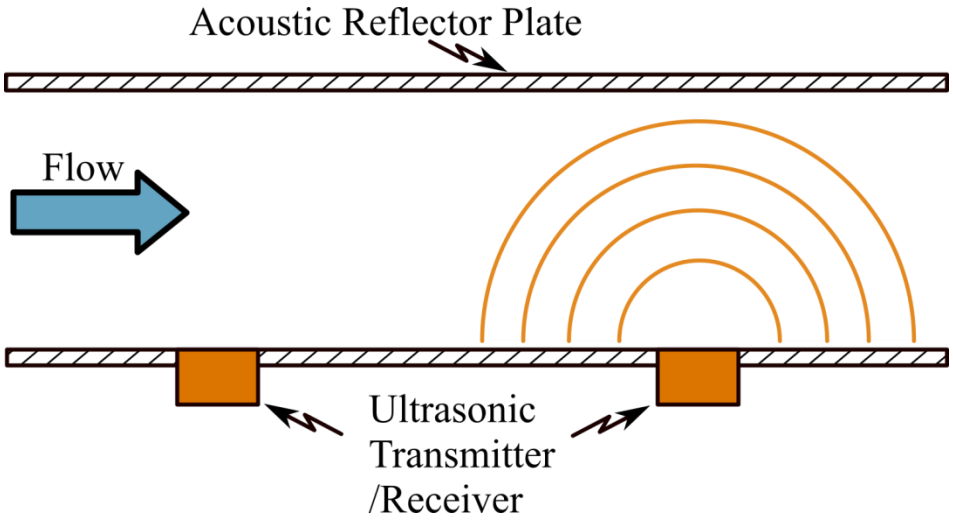

Figure 3.20. Acoustic resonance anemometer diagram.

The maximum signal amplitude is obtained when the acoustic path length is multiples of the acoustic signal wavelength which is varied until this is reached. The speed and direction of airflow can be calculated by measuring the resonant frequencies in at least four directions. The benefit of this system, which is not yet utilised for measuring duct flow is that the signal has a high signal-to-noise ratio so could cope with highly turbulent conditions.

Time of flight

The direct time of flight method is usually done by contra propagating acoustic pulses and using digital signal processing techniques to calculate the pulse arrival time by correlating the transmit signal with the received signal. The transit time

acoustic flow meter in Figure 2.5 works on the principle that sound waves will propagate faster in the direction of the flow than against it. The measured inverse transit time difference varies proportionally with the change in flow velocity. The main advantage of the transit time method is that the effect of the temperature on the speed of sound of the medium to be measured is cancelled out. Figure 2.5 shows a typical acoustic transit time gas flow meter arrangement [74]. Acoustic transducers TR1&2 are placed on opposite sides of the duct and separated horizontally so that the upwind and downwind acoustic signals are affected differently by the airflow. As the horizontal distance between the transducers is increased, the flow induced proportional time difference is also increased and therefore improves the sensitivity of the device. To reduce errors caused by noise and fluctuating signal levels the absolute transit time is usually measured by using the cross-correlation [28], [75–78] digital signal processing (DSP) method [79] which compares the digital representation of the transmit and received waveforms to calculate the delay between them. Ultrasonic flow sensors are commonly used to measure pipeline liquid flow in industrial applications but not so common for gas flow [80]. There are commercially available systems for use in monitoring industrial processes such as exhaust gases [74], [81], mine ventilation [82], [83], tunnel, ventilation [84], and automotive test bed intakes [85], [86], but the historically high cost has restricted their applications in HVAC systems.

3.1 Summary of Chapter 3

This chapter describes how to calculate the enthalpy level of the air in the ventilation duct, with and without taking into consideration the amount of water vapour in the air. Using the second method which accounts for the enthalpy change of the water vapour in the air, in scenarios where there is no actual change in water vapour mass compared to the dry air mass can improve the accuracy of enthalpy by up to 1.5%.

The minimum configuration for measuring enthalpy change where there is no change in the water vapour content of the air or where an accuracy of better than 1.5% is not required is to use a temperature sensor before and after the heat exchanger.

In the situation where there is a change in water vapour content of the air or higher accuracy is required then a temperature and humidity sensor should be used before and after the heat exchanger or humidifier/dehumidifier to measure

enthalpy change but often capacitive type humidity sensors incorporate a highly accurate temperature sensor as well.

How to calculate the energy throughput is then described using the enthalpy levels at two different parts of a HVAC ventilation system together with the relevant mass flow rates.

A overview of sensor technology and the authors opinion on their suitability for measuring the following HVAC ventilation system parameters temperature, humidity and airflow rate is given.

The most suitable device for measuring temperature is the thermistor because the accuracy is better than ± 0.2 ℃ over the temperature range 0 to 70℃. They do have a limited temperature range but can accommodate the range of temperatures expected in a HVAC system.

In HVAC applications the capacitive type humidity sensor is the best suited device for measuring the relative humidity, to calculate the water vapour content of the air. Their relative humidity accuracy can be better than ±2 % and they also have the benefit that the same device can measure temperature to ±0.2 ℃ as well.

The orifice plate flowmeter causes a large pressure drop in the ventilation duct system so increasing energy usage. Venturis are one of the most accurate devices for measuring HVAC mass air flow rate but are expensive and usually long, which could cause installation problems. They also require frequent zeroing, calibration and maintenance. Pitot tubes have accuracy problems measuring flow velocities below 2 m/s and can only measure the flow velocity at a single spot. Velocity pressure arrays such as a Wilson flow grid can measure the air velocity across the duct but suffer from similar problems to other pressure differential devices that is the pressure sensors are expensive and require frequent zeroing, calibration and maintenance.

Hotwire anemometers are a better option for measuring low velocity airflow at a single spot but are prone to inaccuracies caused by contamination of the wire with dirt and sudden air temperature changes.

Propeller type anemometers are low-cost but prone to physical damage and mechanical wear so require periodic maintenance for cleaning, lubrication and calibration.

Acoustic flow measurement devices have been around for at least 60 years and are quite commonly used for measuring fluid flow velocity. There are many

methods such as sing around, phase difference, Doppler, cross correlation, vortex shedding, acoustic resonance and time of flight. Acoustic ultrasonic transducers are produced in an open or enclosed type structure. The open type transducers are generally lower cost and more sensitive than the enclosed type. The enclosed type are more durable in environments which contain contaminants such as water and dirt.

The following chapter gives an overview of the development system which was designed and constructed by the author to test various configurations for a low-cost acoustic airflow measurement device with the capability to measure energy throughput. Enclosed type ultrasonic transducers, were chosen because of their robustness. Open type ultrasonic transducers could still be a lower cost solution but would require further testing.

Chapter 4.INSTRUMENT DESIGN AND CONSTRUCTION

In this chapter:

4.1 Development System Overview

An ultrasonic duct airflow development system was constructed by the author which had the flexibility to test various measurement techniques. This system was used for measuring airflow using the ultrasonic transducers in two different configurations.

The first configuration used three transducers with the middle transducer producing a continuous acoustic signal. The upwind and downwind receivers were used to measure the phase difference so that the actual time of flight could be estimated for calculating airflow velocity. This system successfully operated and had a high update rate equal to the frequency of the transducer and did not require a demultiplexer circuit but had two major drawbacks that the zero flow rate measurement would drift by a few tenths of a metre per second due to temperature differences between the transmitter and receiver's. In situations where there was some movement of airflow, this drift wasn't a significant problem as the temperature gradient of the air across the transducers would be less variable. The other drawback was that this configuration required three transducers, which would be more costly to produce than the second configuration shown in Figure 4.1 which only needs two transducers.

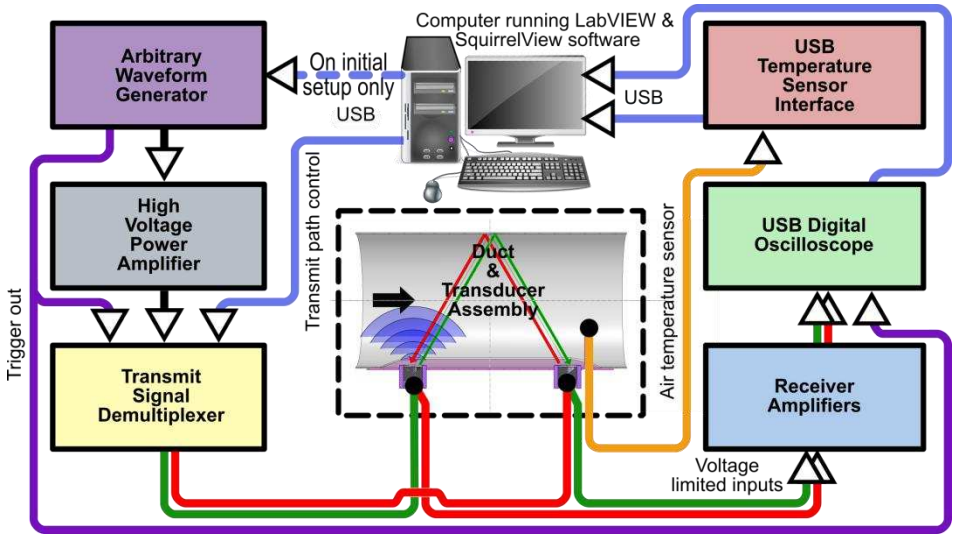

Figure 4.1. Schematic of the ultrasonic duct airflow measuring device development system.

The second configuration used contra-propagation to mitigate the zero flow drift problem. This had the benefit that the same parcel of air was being used to calculate the airflow velocity with only a minor difference due to the time lag between upwind and downwind measurement cycles. Various techniques such as the phase difference with temperature corrections and time of flight using cross correlation were tested using this configuration. A computer running LabVIEW® 10 (National Instruments, Austin, TX, USA) was used to control and read data from the various subsystems via universal serial bus (USB). These subsystems were the arbitrary waveform generator (AWG), transmit signal demultiplexer, digital oscilloscope and temperature sensors interface.

A Tektronix AFG3021C 25 MHz single channel computer AWG was used so that any type of transmit drive signal could be produced and manipulated quickly by the extensively modified LabVIEW instrument driver software. The output of the AWG was fed into a PA95 (Apex Microtechnology, Tucson, AZ, USA) high voltage power amplifier capable of driving the ultrasonic transducer to its maximum voltage of approximately 100 Volts peak to peak. This was then switched through two LH1500AT (Vishay Intertechnology, Malvern, PA, USA) solid-state relays (SSR) within the high voltage demultiplexer specifically designed for the task by the author which could switch a single input between at least two outputs. The demultiplexer was also controlled by the computer through a PicoLog® 1012 (Pico Technology, St Neots, UK) USB data acquisition device. The transmit signals were then connected, depending on the demultiplexer state, to one of two 400EP14D (Pro-Wave Electronic Corp., New Taipei City, Taiwan) 40 kHz enclosed type piezoelectric transducers which would transmit an ultrasonic signal through the duct to a receiving transducer. The received signal would be then amplified after

passing through a diode voltage limiter input circuit to a multistage operational amplifier to boost the signal voltage by greater than 1000 times. This was then digitized by a USB oscilloscope, which is shown in Figure 4.2, for processing by the computer running the LabVIEW® control and signal processing software.

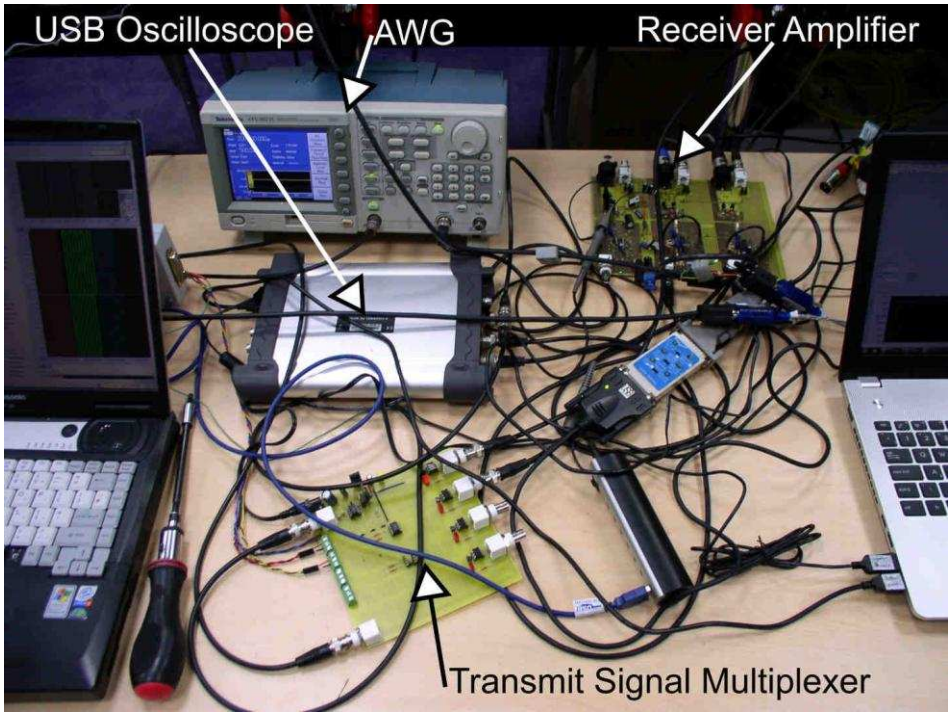

Figure 4.2. Photograph of development system hardware excluding the temperature sensor interface, high voltage power amplifier and transducer assembly.

A Grant type U thermistor probe was used to measured the in duct air temperature and was monitored via a Squirrel® SQ2020 Series Data Logger (Grant Instruments, Shepreth, UK).

4.2 HVAC Ultrasonic Duct Airflow Measurement Instrument Description

4.2.1 Transducer configuration

A single reflective path ultrasonic flow meter design was chosen as the preferred solution. The transducers are mounted on the same side so that they can be constructed as a single assembly which is fitted to the duct wall. This should reduce the overall cost as it simplifies installation and reduces the number of cable assemblies required. A benefit of this design is that one of the major critical dimensions, the axial separation distance of the transducers can be permanently fixed in one assembly. Another is that the effect of airflow swirl can be mitigated by the use of the reflective path.

The single reflective "V" shaped differential transit time flow meter path geometric parameter values are given by Equations (4.1) and (4.2). Equations (4.1) utilises Pythagoras theorem to calculate the acoustic path length between the transducers. The same distance would be achieved with a non-reflective path flowmeter that had a diameter of twice that of the reflective type of flowmeter.

$$L = \sqrt{2D^2 + Z^2} \tag{4.1}$$

$$\theta = \tan^{-1}\frac{2D}{Z} \tag{4.2}$$

Figure 4.3 shows a representation of an ultrasonic flow meter design with a reflective “V” shaped path with the transducers mounted perpendicular to the duct wall.

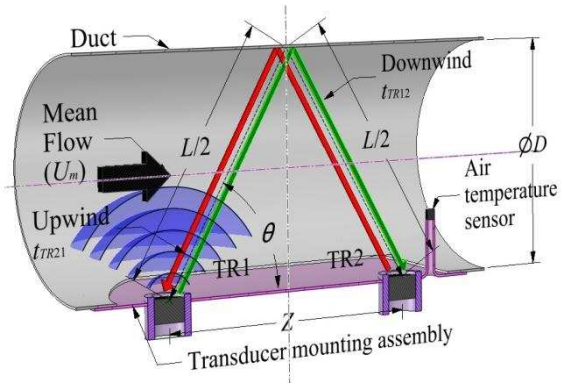

Figure 4.3. A reflective "V" shape single path acoustic differential transit time flow meter in a cylindrical duct.

To explore the sensitivity of airflow measurements on duct size and instrument spacing, in the following table the effects on airflow velocity measurement of unintentional deviation of up to ±10 mm for the transducers axial separation distance Z and the duct diameter D or duct height H are shown. The flow meter scenario used for results in Table 4.1 is a duct with a diameter or height of 100 mm and a transducer axial separation of 200 mm with a mean airflow of 10 m/s.

Table 4.1. Deviation of *Z* or *D,H* on airflow velocity measurement.

	Deviation in (mm)	**-10**	**-5**	**0**	**5**	**10**
Z	Airflow results (m/s)	11.050	10.512	10.000	9.512	9.050
	Deviation from 10 m/s as (%)	10.497	5.125	0.000	-4.875	-9.502
D,H	Airflow results (m/s)	9.987	9.997	10.000	9.997	9.988
	Deviation from 10 m/s as (%)	-0.131	-0.032	0.000	-0.030	-0.119

The transducer pair axial separation width Z is fixed at manufacture as a large error could be cause by the alteration of this separation distance as shown in Table 4.1 where a 5% deviation in separation can cause >10% error in flow measurement. A deviation in diameter or height of the duct of 5% only causes a

very small error of <0.05%. This has the benefit that the vertical height of the duct could be affected by a number of factors such as duct mounting arrangements, pressure and bending stresses and the airflow measurement would not change significantly. There is also a possibility that this configuration could be used as a transferable portable device on a number of ducts with different diameters. If, in practice, the circular duct deforms to a slightly elliptical shape, this only causes a small change in the cross-sectional area of the duct so not affecting volumetric flow rate significantly.

If an ultrasonic transducer with a wide beam width is selected they can be both mounted level to the printed circuit board so reducing the need for an angled mounting assembly. A reduction in the signal strength is the cost of this mounting arrangement but this is small when using a transducer such as the 400EP14D, see Appendix A for datasheet, which has a −6 dB beam width of 135°, as shown in Figure 4.4 which only amounts to an extra 2 dB of attenuation for the complete path for both the experimental configurations. This also allows a wide range of duct diameters to be accommodated as the duct increases the shortest path direction will move closer to the centre of the transducer beam so reducing the transducer attenuation. The reflective path does not attenuate the signal significantly because 99.99% of the signal energy is reflected because of the high acoustic impedance difference between air and steel [55] (pp. 439-443).

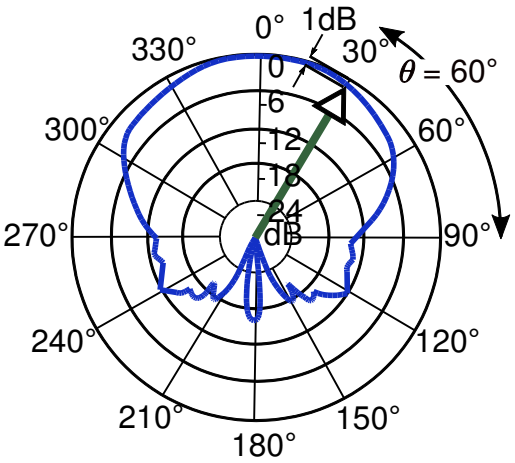

Figure 4.4. 400EP14D enclosed type piezoelectric transducer polar diagram superimposed with the typical acoustic path direction attenuation.

To reduce errors caused by noise and fluctuating signal levels the absolute transit time is usually measured by using the cross-correlation [76] digital signal processing (DSP) method [79] which compares the digital representation of the transmit and received waveforms to calculate the delay between them.

In this study a phase shift or differential transit time method similar to that described by Han *et al.* [33] and De Cicco *et al.* [87] is used to reduce the cost of implementation for this application. In the differential transit time method the estimated transit time is found by using a two stage calculation. In the first stage, the zero flow transit time is calculated with Equation (4.3). In this equation the acoustic path length in Equation (4.1) is divided by the speed of sound in Equation (2.1), which is derived from the airflow temperature.

$$t_{U0} = \frac{L}{c} \tag{4.3}$$

In the second stage, half the actual measured differential transit time is added or subtracted from the zero flow transit time depending on the airflow direction, which is represented in the Equation (4.4) below.

$$t_{TR} = t_{U0} \pm \frac{\Delta t_{TR}}{2} \tag{4.4}$$

The airflow velocity can then be calculated by using the inverse transit time difference calculate.

The selection of the transducers axial separation distance Z needs to be a compromise between sensitivity and the maximum allowable phase difference. The phase difference is the offset in degrees or time between two waveforms having the same frequency. The maximum allowable symmetric phase difference is ±180°, which equates to ± 12.5 µs time delay for a transducer frequency of 40 kHz, if a phase difference beyond this range is encountered the velocity reading will wraparound and for example a positive reading will then become negative. To avoid this, a margin of about 50% above the maximum typical air velocity was used as the maximum measurable air velocity. Hence the device should typically operate within a phase shift value of ±120° for a symmetrical plus and minus velocity range. The positive airflow velocity range can be increased at the expense of reducing the negative airflow velocity range if negative air velocities are unlikely to be created. The following Equation (4.5) is used to calculate the typical maximum differential transit time allowable for the ±120° maximum phase shift range specified.

$$\Delta t_{max} = \frac{1}{(360/120) f_0} \tag{4.5}$$

The maximum transducer axial separation distance Z_{max} for the specified maximum differential transit time Δt_{max} and maximum typical air velocity U_{upper} can be calculated using Equation (4.6) below which is derived from equations described by Lie *et al.* [88]. The transducer separation Z distance can be shortened to extend the air velocity measurement range but the measurement accuracy could be degraded by timing resolution being too large or by noise on the receive signal.

The maximum horizontal transducer separation distance for the specified maximum differential transit time and maximum typical air velocity can be calculated using Equation (4.6) below which is derived from equations described by Lie *et al.* [88]. The transducer separation distance can be shortened to extend the air velocity measurement range but the measurement sensitivity will be reduced.

$$U_{DTTM} \approx \frac{c^2 \Delta t}{2Z} \;\therefore\; Z_{max} \approx \frac{c^2\,\Delta t_{max}}{2U_{upper}} \tag{4.6}$$

4.2.2 Ultrasonic transducer transmitter subsystem

The output voltage signal of the AWG was amplified about 100 times by a unit, as shown in Figure 4.5, containing an APEX PA95 very high power operational amplifier device. The enclosure and PCB that the PA95 was mounted on had been constructed by Dr. Wichian Ooppakaew for his Ph.D. [89].

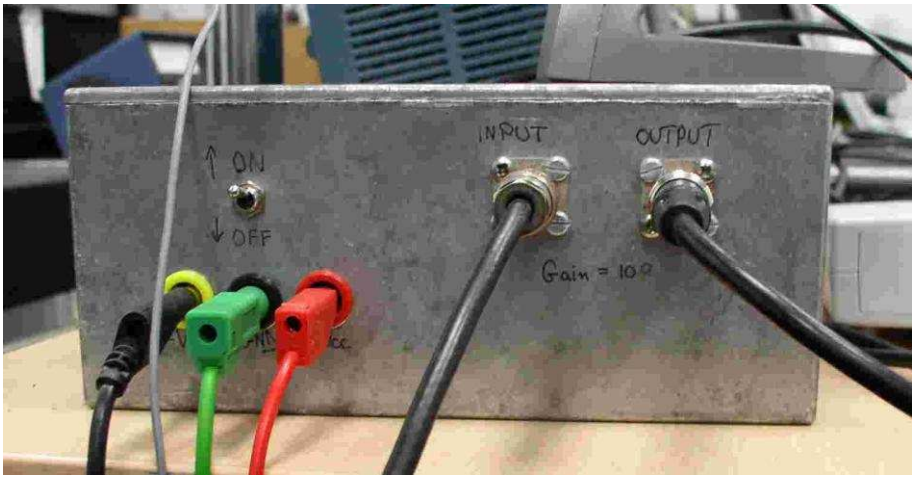

Figure 4.5. Picture of W. Ooppakaew PA95 High Voltage Amplifier unit.

It had been manufactured to datasheet recommendations with some modifications by the author to adjust the voltage gain from 10 to 100 as shown in Appendix C in Figure C.1. As shown in Figure 4.6 below this was then fed through a SSR device with the capacity to handle very high voltages and also have a much higher switching life compared to electromechanical relays.

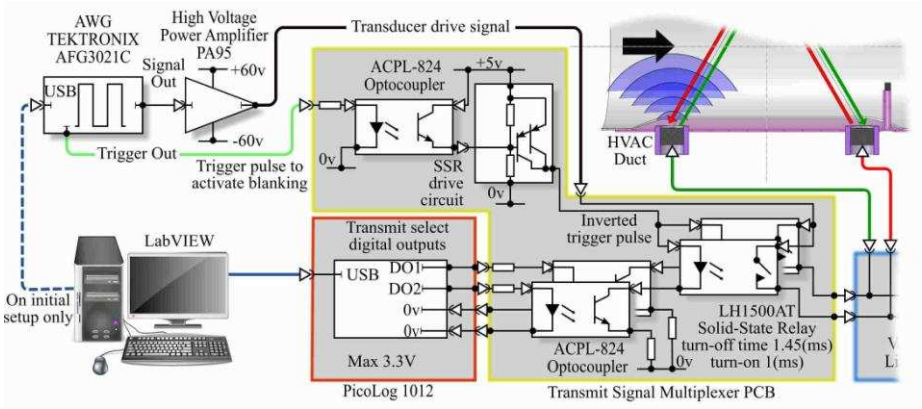

Figure 4.6. Overview schematic of the ultrasonic transducer transmitter subsystem.

The 10 pF output off capacitance value of the LH1500AT SSR was an important consideration in the selection of this device. As capacitance increases It reduces the cut-off frequency of the high pass filter this capacitance forms [90]. If it was too high the high frequency noise from the high power amplifier would pass through the device even in the off state which would increase the noise level into the receiver amplifiers. The LabVIEW software connected to a PicoLog 1012, which has only two digital output channels, was used to control the SSR devices via ACPL-824 optocoupler when required. The SSR device chosen had a turnoff delay of about 1.5 ms which was used as the switch off delay from the falling edge of the inverted AWG trigger out. Hence, as soon as the transmitter pulses were generated the SSR would start switching off but by the time it had actually turned off the pulses had passed through the device and the system was now ready for reception of the reflected ultrasonic pulses. Figure 4.7 shows the high voltage signal demultiplexer, which was designed and constructed by the author.

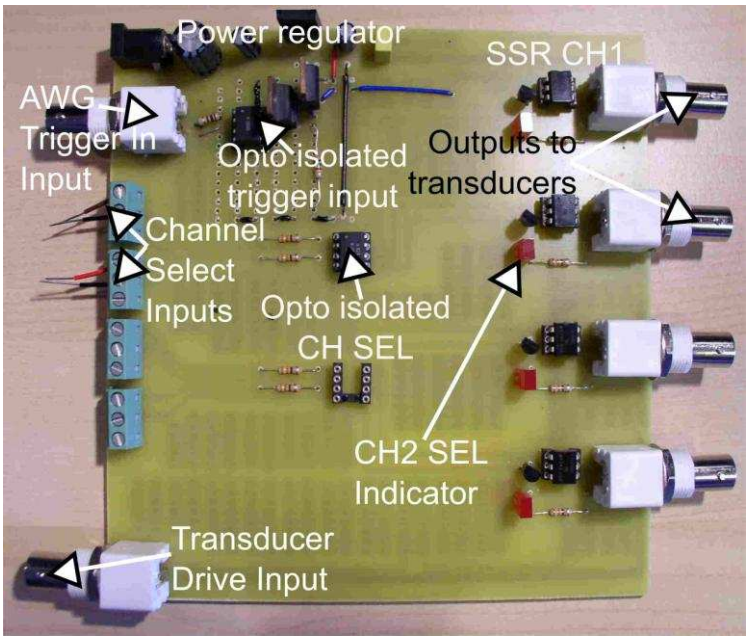

Figure 4.7. Photo of High Voltage Demultiplexer.

See Figure C.2 in Appendix C for the schematic used for the transmit signal demultiplexer PCB fabrication.

Shown in Figure 4.8, as the red waveform is a typical 40 kHz ultrasonic transducer receiver response to an opposing transmitter, using the apparatus shown in Figure 4.18 and driven by two pulses at a pulse rate of 40 kHz.

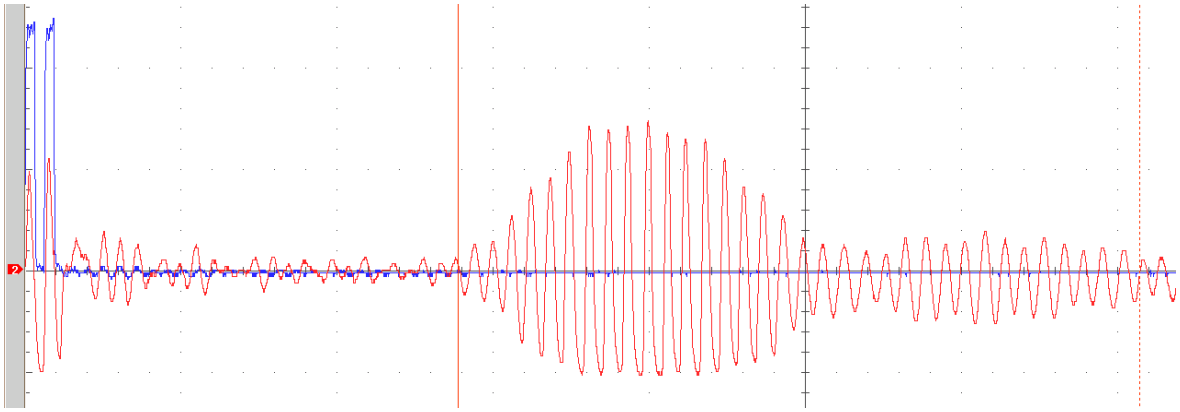

Figure 4.8. Typical high Q factor ultrasonic transducer receive response signal to multi-pulse stimulation.

There is significant ringing as the transducer has very little damping. This has the benefit that a cyclic transmitter signal can produce a larger response at the receiver transducer than a single cycle but this can make it difficult to detect the start of the received signal waveform and reduces the maximum update rate as more blanking time is required to allow the signal to fade, so as to not cause excessive noise on the next receive period. Techniques such as using a DSP correlation function are usually used to find the start of the receiver signal but this requires significant computational power to calculate the time delay between a typical transmit waveform signal and the actual received signal. Other techniques were investigated to help minimise the complexity of the software and hardware. This involved investigating a pulse compensation technique, which uses the linear time invariant (LTI) signal processing technique described by Ooppakaew and Danaher [91] to model the response of the transducer by using a stepped input. The stepped response received signal shown in Figure 4.9 is iteratively processed by Matlab code, supplied by the authors principal supervisor at the time Prof S. Danaher, which finds the system response transfer function for the transducer.

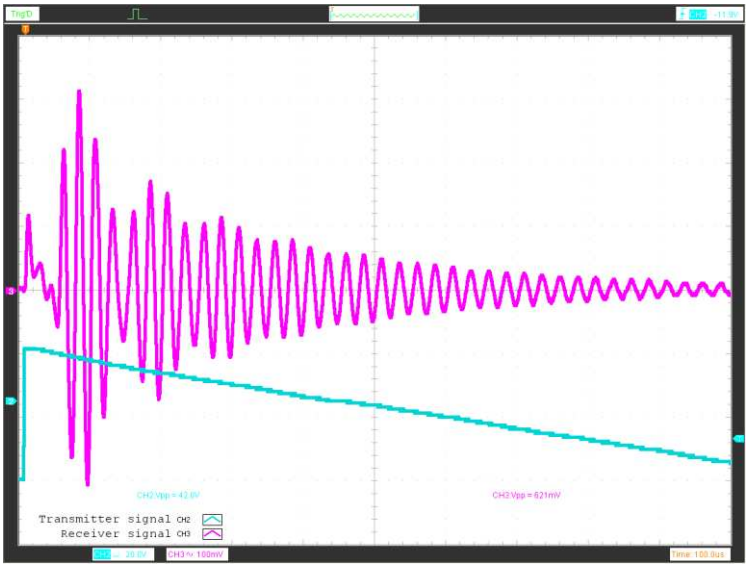

Figure 4.9. Stepped input response of 400EP14D transducer.

After this transfer function has been calculated an arbitrary selected output signal can be fed into the function and the input waveform required will be generated. The results in Figure 4.10 show that the method does work but received signal level is very small when compared to signal noise. The output could also be improved by using a higher input signal level or using a more responsive and sensitive open type transducer.

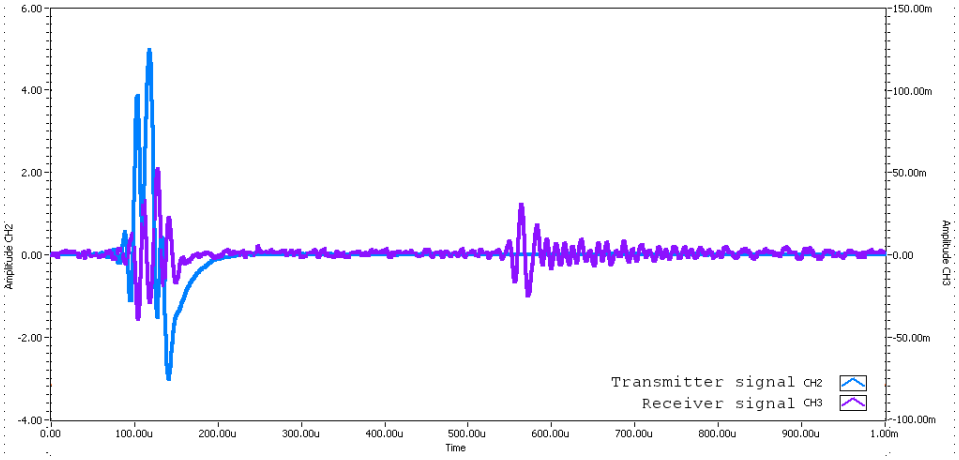

Figure 4.10. Using LTI technique to produce a short receive signal.

Similar results, shown in Figure 4.11, to the LTI technique results were obtained by using consecutive sine wave cycles that are 180° phase shifted to each other.

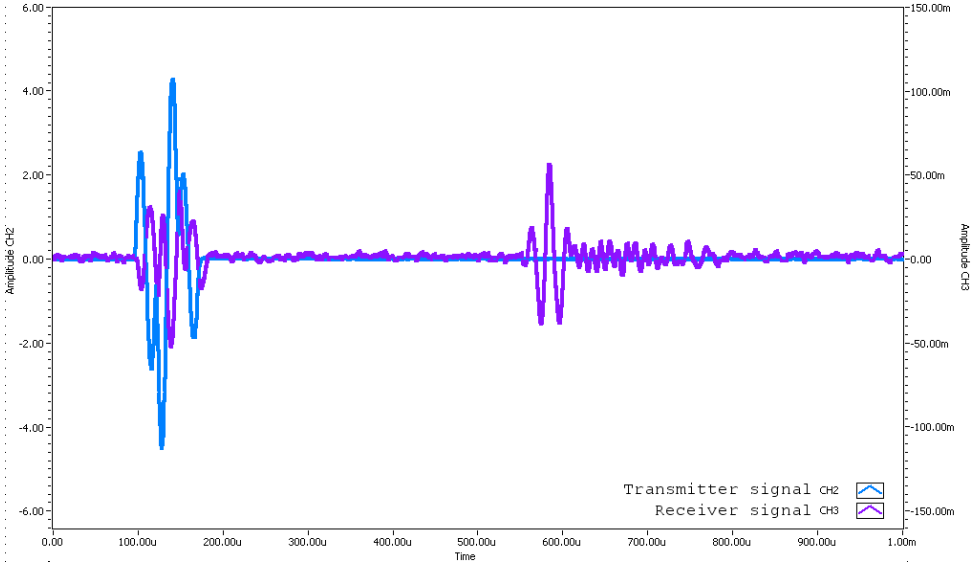

Figure 4.11. Using anti-phase sine wave cycles.

The second cycle is slightly larger than the first cycle to induce the transducer to go into anti-phase oscillations similar to the self interference type method [92], [93]. The following cycles are added to reduce ringing from the transducer. This produces a receiver signal, which could be easily detected by a voltage comparator circuit with the mean of the rising and falling edge of the pulse time measurements taken as the time of flight.

This method was used to alleviate problems with the receive transducer ringing. The ringing can be induced by the direct transmission of sound through the duct wall as well as through the normal air acoustic path. The transmit signal used a series of square waves at the transducer operating frequency of 40 kHz, that was generated by a LabVIEW VI created by the author to control a Tektronix AFG3021C arbitrary waveform generator. A section of the VI front panel is shown in Figure 4.12.

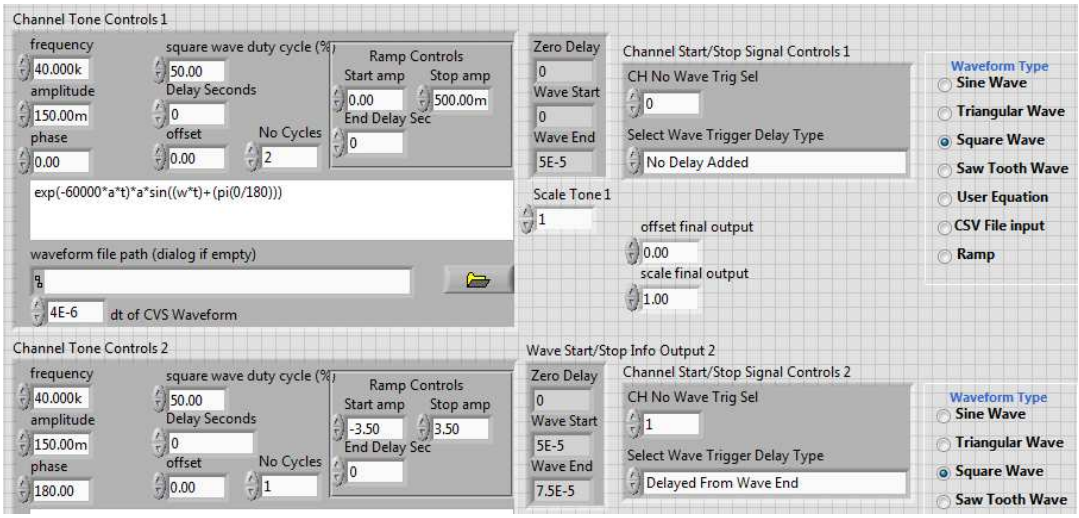

Figure 4.12. Labview AWG pulse generator VI.

The VI can generate various waveforms such as sine, triangular, sawtooth, ramp and from a waveform equation. A CSV file containing waveform data point voltage values can also be used with the sample period time setup in the VI. Each waveform can contain any number of cycles which can be programmed to start at various trigger points such as the end or start of a waveform with a delay time if required. The actual transmitter signal used in the experiments was done by transmitting a square wave pulse with a 180° phase shift relative to a pair transmitted previously with no delay between them, as shown in Figure 4.13.

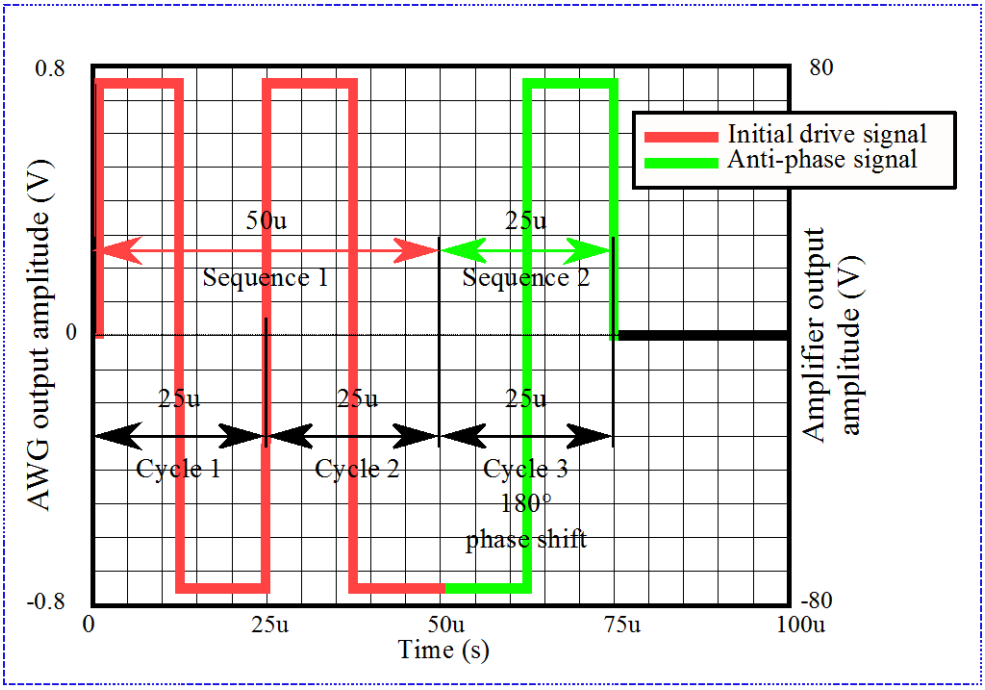

Figure 4.13. Transducer transmit drive waveform.

Table 4.2 shows the parameters required to be selected in the AWG, LabVIEW pulse generator driver software for waveform shape generation. A high peak to peak voltage of 150 volts is used to drive the ultrasonic transducer to reduce the signal-to-noise ratio of the received waveform.

Table 4.2. AWG waveform sequence parameters

Sequence No.	Frequency (Hz)	Relative phase (Deg)	No. of waveform cycles	Waveform shape	AWG amplitude output in Volts peak to peak	Amplifier amplitude output in Volts peak to peak	Delay type
1	40K	0	2	Square	1.5	150	No delay added
2	40K	180	1	Square	1.5	150	Delayed from wave end (Seq. No.1)

The following Table 4.3 shows the AWG configuration parameters, which are also selected in the AWG, LabVIEW pulse generator driver software for waveform

shape generation. The burst mode internal trigger rate of 10 Hz is much lower than the theoretical maximum pulse repetition frequency due to the waveform processing and display processing time required by the computer.

Table 4.3. AWG waveform general settings

Setting name	Value	Notes
AWG waveform memory type	Internal	Data uploaded from LabVIEW to AWG internal memory
Number of waveform points	63000	128K maximum for AFG3021C
Burst mode	Enabled	Repeat waveform at rate below
Burst mode internal trigger rate (Hz)	0.1 to 10	Initial rate low to check de-multiplexing operation is correct
Burst count	1	One waveform per internal trigger event
Waveform points frequency (MHz)	12.6	For information - not directly user selectable
Waveform DC offset (V)	0	No offset

This waveform could be generated using a "H bridge" type circuit [94] typically used for DC motor direction control. The ultrasonic transducer would be connected where the motor should be normally connected, as shown in Figure 4.14.

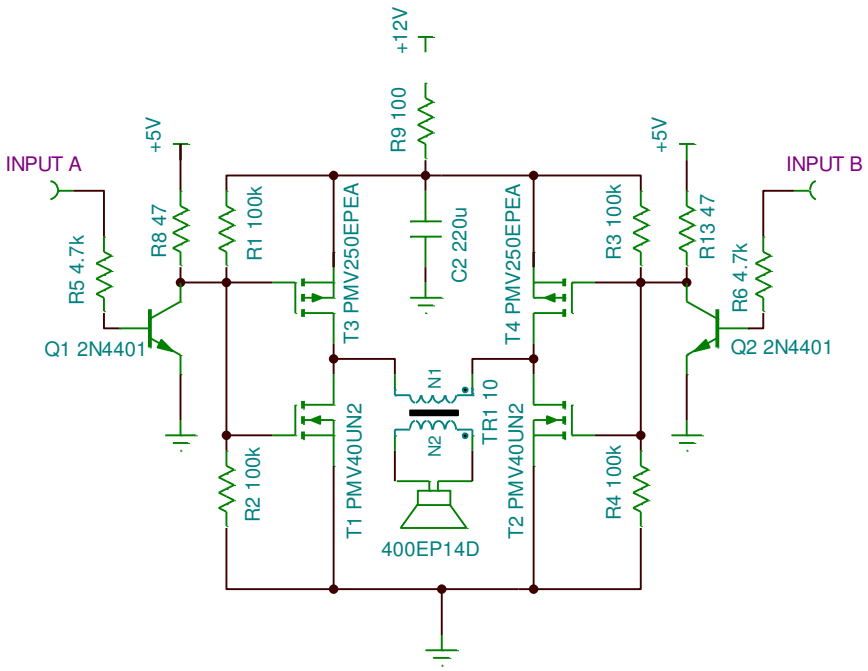

Figure 4.14. H Bridge ultrasonic transducer transmitter circuit.

This "H Bridge" ultrasonic transducer transmitter circuit has been adapted to generate a transducer drive with higher voltages by using a transformer such as the Pro-Wave K000001 transducer matching transformer with a turn ratio of 1:10. Using the transformer also has the benefit that the impedance of the transducer which is 1000 ohms for the Pro-Wave 400EP14D can be matched to a low impedance source of 10 ohms. Input "A" should be taken high by the microcontroller when a positive pulse is required and input "B" should be taken high when a negative pulse is required.

The ringing was reduced to some extent which enabled a higher measurement rate to be used but this was still not enough for the 100 mm wide square duct because of the short time of flight. It was found that by pressing lightly on the top surface of the transducers with the point of a finger the ringing could be suppressed. It was then found that the finger could be replaced with a piece of reusable mounting putty similar to Blu Tack®, which was moulded in a dish like shape as shown in Figure 4.15.

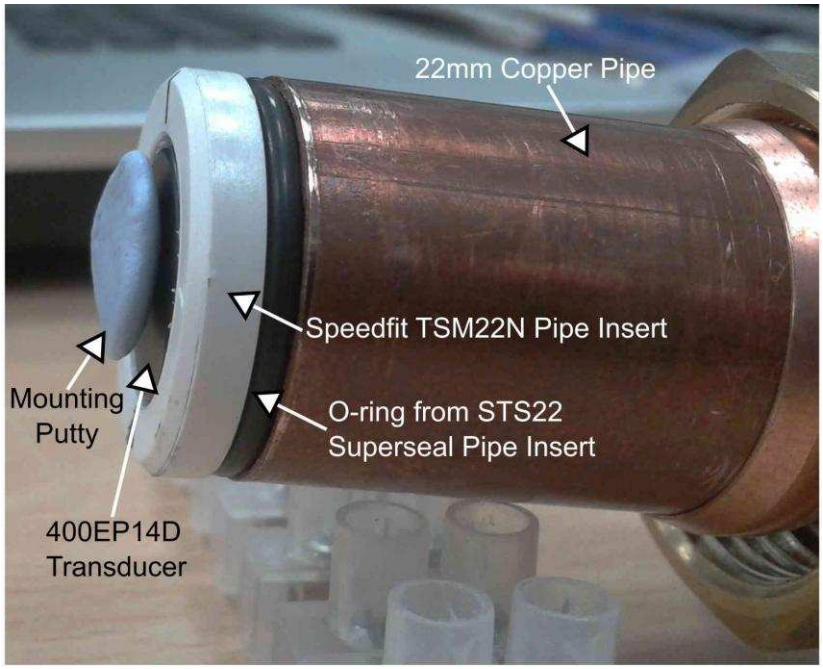

Figure 4.15. Photograph of the 400EP14D transducer mounting arrangement and putty used to damp ringing in 100 mm square duct tests.

This seemed to work best when the contact point was as small as possible without the putty being able to fall off. As this was not a solution that could be used permanently a "W" acoustic path was used later after the results in the thesis for the square duct had been taken. The acoustic signal was reflected off the adjacent duct wall twice giving more time for the ringing to dwindle. When the "W" acoustic path was used the parameter D was doubled to take this into account. An active transducer damping circuit as described by Miller *et al.* [95] was also a possible solution for this problem but has not been tested in this study.

The transducer was mounted as shown in Figure 4.16, into a John Guest® 22 mm TSM22N Speedfit® pipe insert using the same putty as mentioned before to fill the gap between the transducer and the inside of the pipe insert.

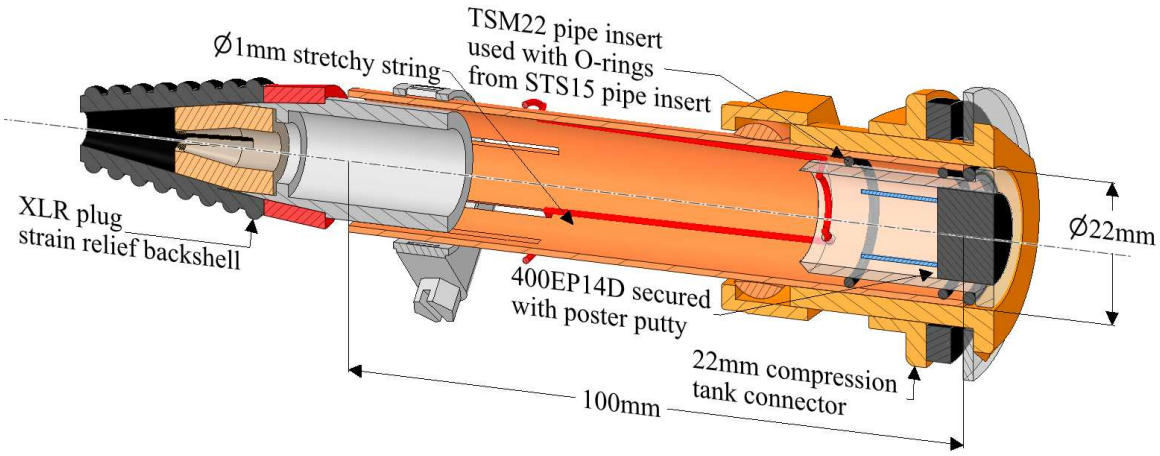

Figure 4.16. Ultrasonic transducer mounting system for acoustic/vibration isolation.

Three rubber O-rings were used to provide vibration isolation between the pipe insert and the 22 mm copper pipe. The O-rings were taken from John Guest® 22 mm STS22 Speedfit® superseal pipe inserts which each have two O-rings which one is slightly smaller than the other. At least two of the smaller O-rings were used per transducer mounting. The pipe insert was forced against one of the larger O-rings by the use of elastic beading wire connected to the other end of the copper pipe. The back shell of a XLR type electrical connector, which was secured by a hose clamp was used to provide cable strain relief to protect the delicate connections of the 400EP14D ultrasonic transducer. The transducer assembly was then attached to the duct with a 22 mm compression flanged tank connector. The tank connector had modifications, one of which was to allow the 22 mm pipe to travel all the way through the connector, which was done on a lathe. The second modification was to chamfer the edges of the connector flange as shown in Figure 4.17, so that it would create less turbulence and airflow resistance inside the duct.

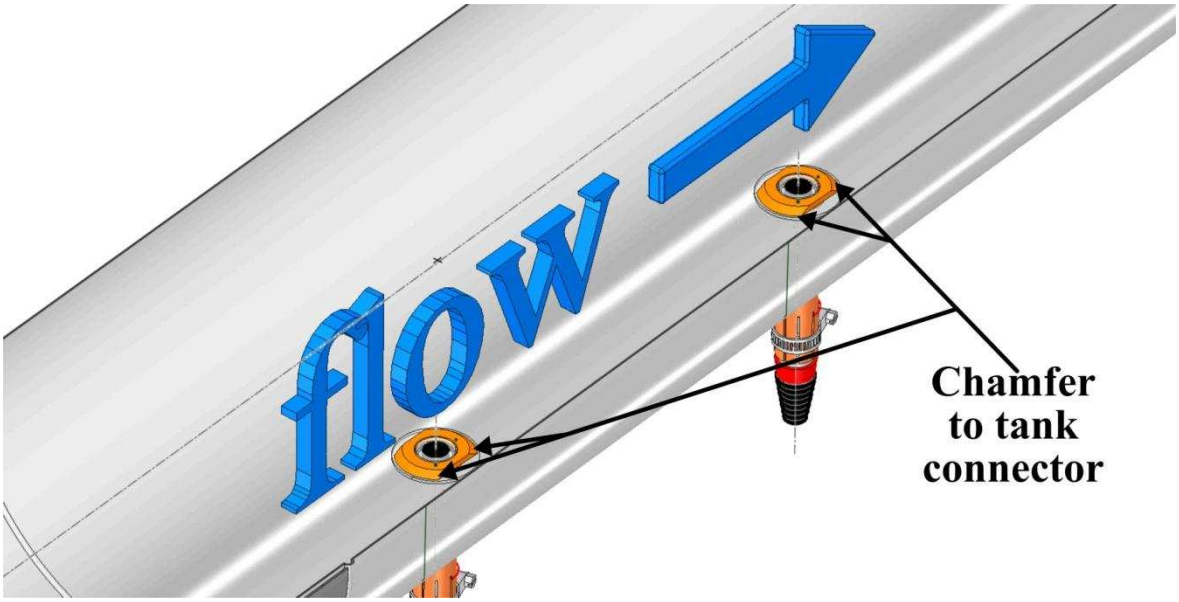

Figure 4.17. A pair of Ultrasonic transducer assemblies fitted to a cross-section of a circular duct.

Two opposite sides of the chamfered flange was removed using a milling machine so that it would fit flush in a circular duct and not distort the duct when the tank connector nut was tightened.

4.2.3 Ultrasonic transducer receiver subsystem

Due to the electrically noisy environments in which the ultrasonic flowmeter could be possibly used which could be caused by, for instance HVAC fan motors, fluorescent lighting and cables carrying high current it would be important to have the a high pass filter to remove the 50/60 Hz mains pickup. On initial experiments using a Brüel & Kjaer (Nærum, Denmark) four channel Microphone Conditioning Amplifier, It was found that the majority of the signal was a 50 Hz sine wave signal, due also to the relatively small ultrasonic transducer receiver input signal achieved. The microphone conditioning amplifier did have the built-in capability of high and low pass filters, but the maximum configurable high pass filter cut-off frequency was too low at 20 Hz, to have enough effect on the interfering 50 Hz signal. As shown in Figure 4.18, a high pass filter was required to attenuate the 50 Hz signal at the output of the microphone amplifier to produce a signal, which was steady enough to be analysed.

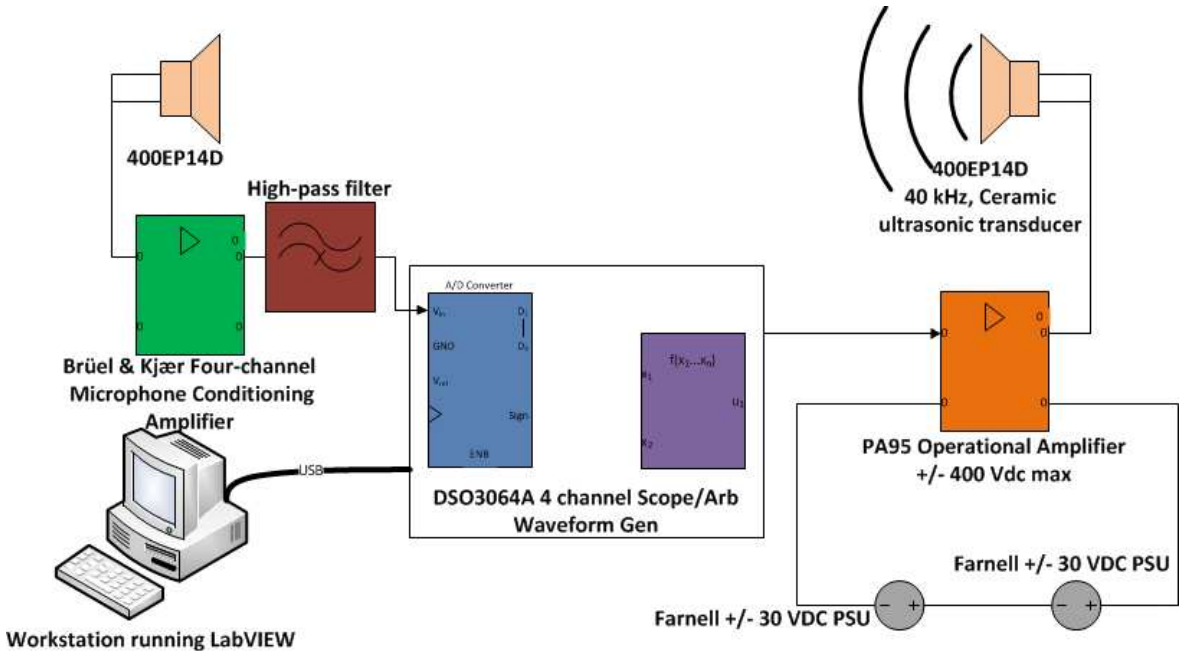

Figure 4.18. Ultrasonic anemometer single path test setup.

It was decided to design an amplifier that was tailored for the specific task of amplifying the 40 kHz ultrasonic receiver signal so that actually required cut-off frequencies and gain levels could be specifically set. As shown in Figure 4.19 the first stage of the receiver circuit consists of a load resistor which the energy from the mainly capacitive ultrasonic transducer is dissipated in, so creating a potential difference.

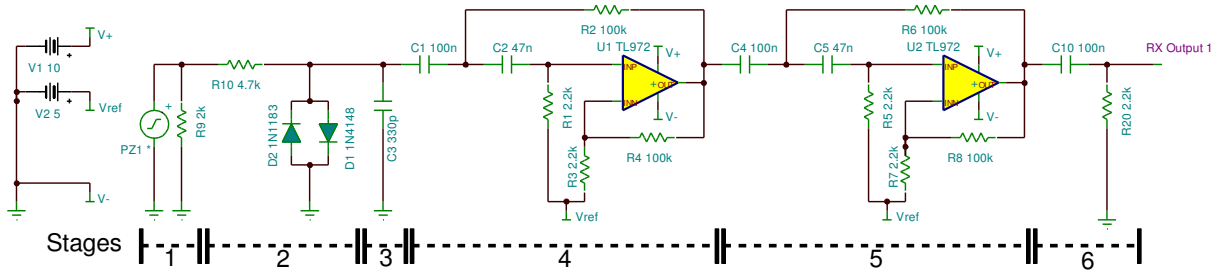

Figure 4.19. Ultrasonic transducer single channel receiver amplifier circuit diagram.

The second stage consists of a current limiting resistor and two signal diodes connected in opposite directions from 0 V to the receiver signal to limit the maximum input voltage to no more than 0.6 V. The current limiting resistor also forms part of the stage 3 resistor capacitor low-pass filter. The low-pass filter as shown in Figure 4.20 has a cut-off frequency of 100 kHz to remove high frequency noise.

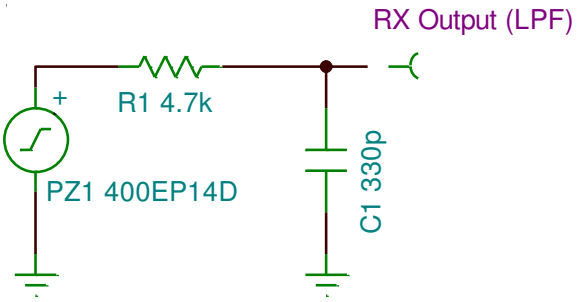

Figure 4.20. Stage 2-3 Low-pass filter schematic

Equation (4.7) was used to calculate the resistance value R_1 required to obtain the desired cut-off frequency. The capacitor value of 330 pF was selected first and then the appropriate resistance value was found. If the value of resistance had been too low for example <2k or too high >10k then the capacitor value could of been changed to bring the resistance into an acceptable range which would not take power away from the ultrasonic transducer and would provide sufficient current for the active filter circuits to minimise signal noise.

$$fc = \frac{1}{2\pi R_1 C_2} \therefore R_1 = \frac{1}{2\pi fc \times C_2} \quad (4.7)$$

Where

fc Cut-off frequency (Hz)

R_1 Resistor value (Ω)

C_1 Capacitor value (F)

A Bode plot of this low-pass filter circuit is shown in Figure 4.21, which was generated using TINA-TI version 9, which is a free spice-based analogue simulation program which can be downloaded from the Texas Instruments website.

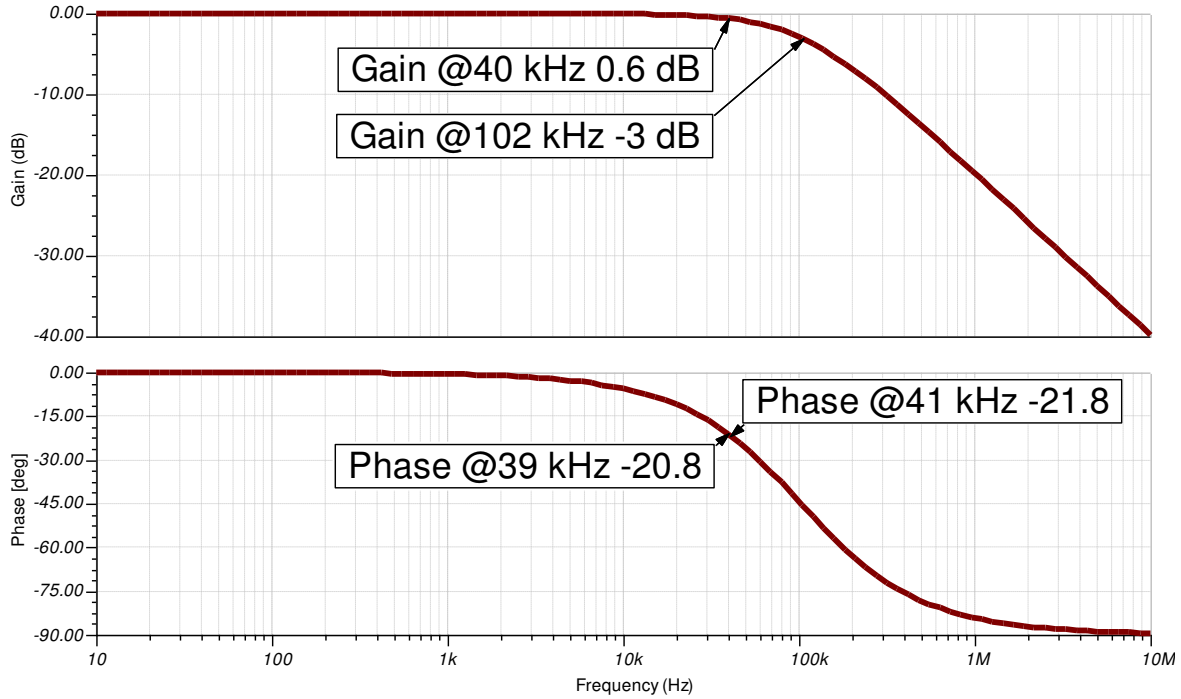

Figure 4.21. Stage 2-3 Low-pass filter, gain and phase response Bode plot using TINA-TI V9

In the following two stages the signal is amplified by a second-order Sallen-Key high pass filter designed as shown in Figure 4.22 with the aid of a software program called FilterPro™ from Texas Instruments Incorporated (Dallas, TX, USA).

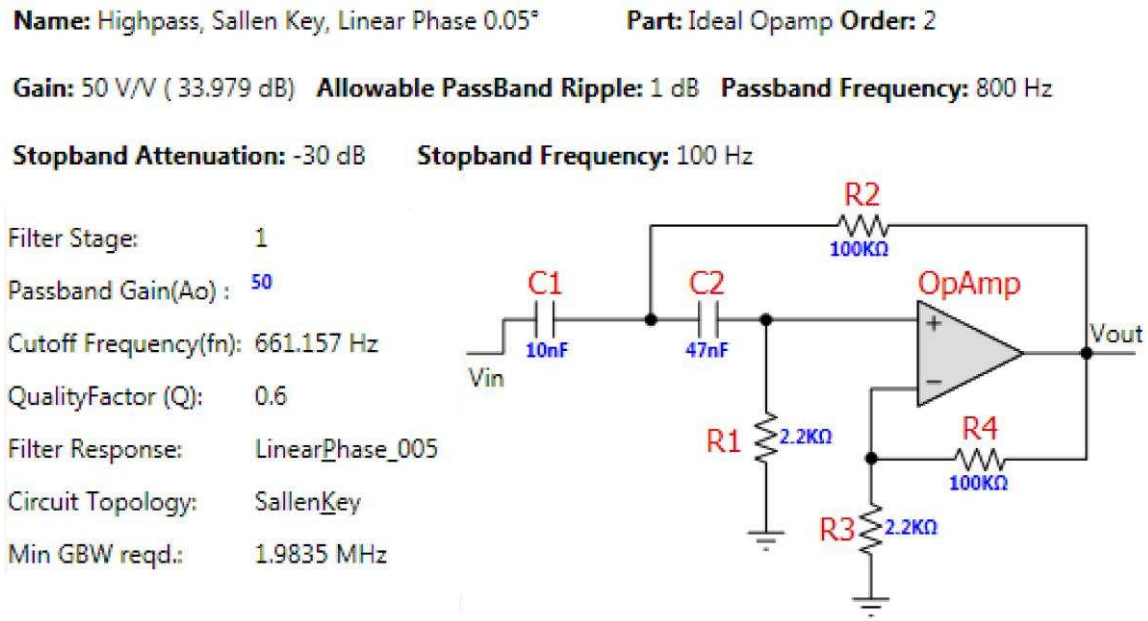

Figure 4.22. High-pass Sallen-Key filter designed using FilterPro™.

The high-pass Sallen-Key filter topology was chosen in preference to the high-pass multiple feedback topology as is suggested by Leach [96] (p. 24) that multiple feedback high pass filters are not stable circuits because at high frequencies the input node becomes shorted to virtual ground because of the feedback capacitors.

FilterPro has the ability to design low-pass, high-pass and band-pass filters using multiple feedback or Sallen-Key topologies. The frequency response results of the active filter circuit are instantly displayed when values are changed in the software user interface. Resistor and capacitor values can be adjusted so that preferred values can be used which can help to lower the cost of the design. The cost can be reduced because usually the more common the value is the better the price will be and the use of identical values in different parts of the circuit, reduce time to set up the PCB assembly pick and place machines. Other benefits of using identical values are that a higher volume of components can be purchased at a lower price and also pick and place machines with fewer feeder slots can be used.

The individual Sallen-Key high-pass filter stages were designed to have a stop band set at 100 Hz and to be a minimum of −30 dB below the pass band set at 800 Hz to give a flatter phase or group delay response through the transducer 40 kHz operating frequency bandwidth range of ± 1 kHz. If the pass band was placed closer to the transducer frequency the phase response would be steeper at the transducer frequency unless a higher order filter design was used which would require more components. The main function of this active filter is to suppress 50/60 Hz noise while amplifying the transducer receive signal by a voltage gain of 50.

The following equations describe how to calculate the resistor and capacitor values required for the Sallen-Key high pass filter with voltage gain, topology as shown in Figure 4.22. The inverting input negative feedback resistor R_4 can be specified to be, equal to or less than 100 kΩ if low noise is the priority, or higher if power consumption is more important. The following Equation (4.8) [96] (p. 23) can be used to calculate the value of R_3 required for the specified amplifier voltage gain.

$$K = 1 + \frac{R_4}{R_3} \therefore R_3 = \frac{R_4}{K - 1} \tag{4.8}$$

Where

K Asymptotic high frequency gain (1)

The resonant frequency in radians per second of the filter can be calculated using the following Equation (4.9) [96] (p. 23) if the resistor and capacitor values are already known.

$$\omega_0 = \frac{1}{\sqrt{R_1 R_2 C_1 C_2}} \tag{4.9}$$

Where

ω_0 Resonant frequency (Hz)

The Q factor of this second-order filter circuit can be calculated using Equation(4.10) [96] (p. 23) and is used to specify the characteristics of the pass band amplitude and phase shift response. A Q factor equal to $1/\sqrt{2}$ gives the flattest pass band frequency response of a Butterworth filter and a Q factor equal to $1/\sqrt{3}$ gives the flattest pass band, group delay of a Bessel filter.

$$Q = \frac{\sqrt{R_1 R_2 C_1 C_2}}{R_2(C_1 + C_2) + (1 - K)R_1 C_2} \tag{4.10}$$

Where

Q Quality factor (1)

The following Equation (4.11) [96] (p. 24) is used to calculate the -3 dB cut-off frequency in radians per second.

$$\omega_3 = \omega_0 \left[\left(1 - \frac{1}{2Q^2}\right) \sqrt{\left(1 - \frac{1}{2Q^2}\right)^2 + 1} \right]^{-1/2} \tag{4.11}$$

Where

ω_3 -3 dB lower cut $-$ off frequency (Radians per second)

To calculate the value required for capacitor C_2 use this Equation (4.12) with a few simplifications as follows; Let $\mathrm{R_1} = \mathrm{R_3}$ and $\mathrm{R_2} = \mathrm{R_4}$ then let $C_1 = 100$ nF. This equation is derived from Equations (4.9) and (4.11), by transposing the Equations (4.11) to equal ω_0 so that they could be combined. The capacitor value of C_1 may need altering depending on the cut-off frequency required.

$$C_2 = \frac{1}{C_1 R_1 R_2 \, \omega_3 \left[\sqrt{\left(\frac{0.5}{Q^2} - 1\right)^2 + 1} - \frac{0.5}{Q^2} + 1 \right]} \tag{4.12}$$

The eventual circuit shown in Figure 4.23, has different component values to the actual calculated values because this makes the components less costly and easier to source.

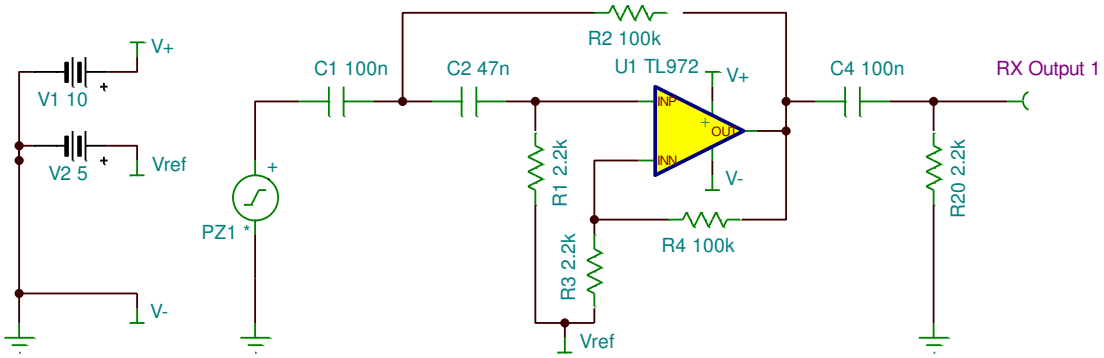

Figure 4.23. Stage 4 or 5 high-pass filter schematic

As shown in Figure 4.24 the difference in component values does alter the cut-off frequency from 800 Hz to 1800 Hz but this difference is not critical, as it is far away from the 40 kHz operating frequency of the amplifier. The main objective of this amplifier is to boost the transducer received signal while suppressing 50/60 Hz mains hum Interference.

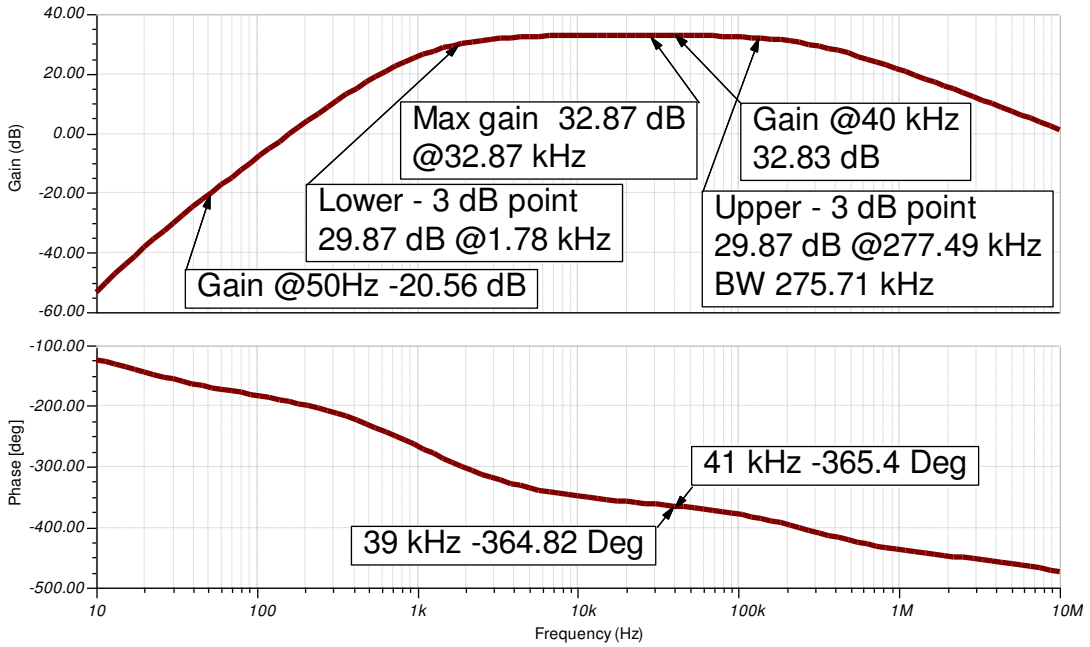

Figure 4.24. Stage 4 or 5 high-pass filter, gain and phase response Bode plot

The overall lower cut-off frequency was 2.3 kHz as shown in Figure 4.25 and the upper was 60.8 kHz with an overall designed voltage gain of 1400 at 40 kHz (in practice a value of 1000 was achieved).

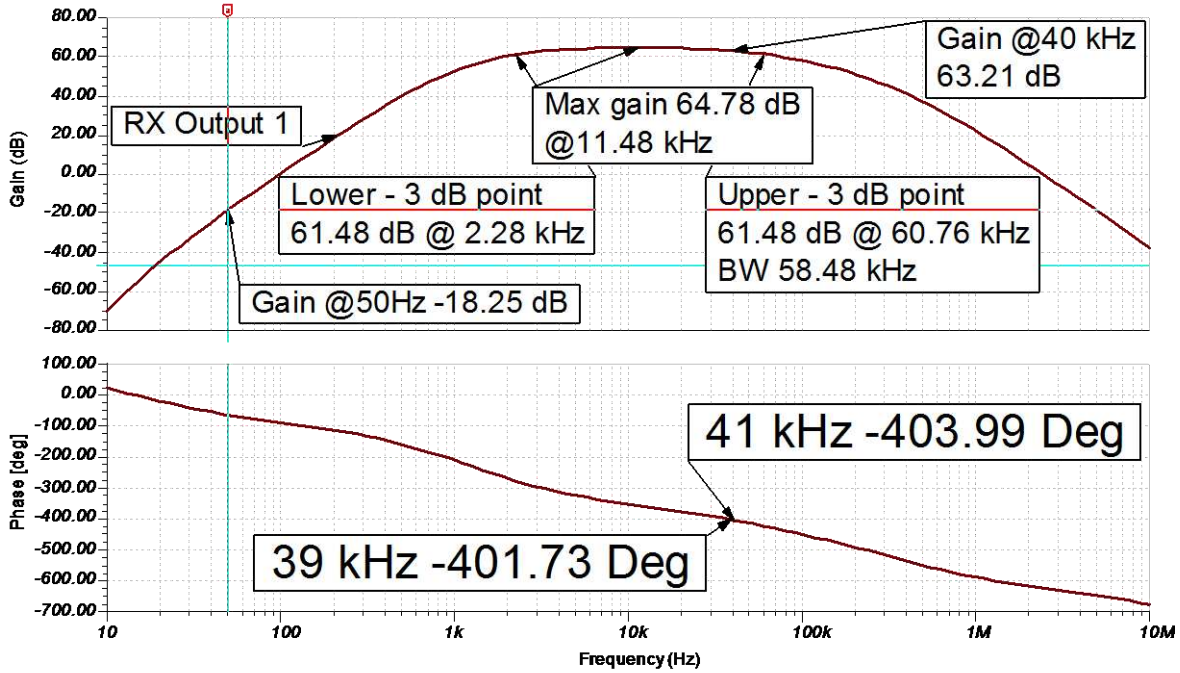

Figure 4.25. Overall receiver amplifier gain and phase response Bode plot using TINA-TI V9.

The amount of calculated phase change due to the receiver amplifier circuit is only 2.26° for the bandwidth of the 400EP14D ultrasonic transducer which is important if the amplifier is used to measure phase difference between two receiver channels. The above Bode plot and the schematic diagram shown in Figure 4.19 of the receiver amplifier was also generated using TINA-TI version 9. The One of the benefits of using this software was that the rail-to-rail very-low-noise operational amplifier TL972 had a TINA-TI Spice model available.

So that the receiver amplifier could be powered from a single rail power supply or battery, a voltage regulator [97] (p. 6) was used to bias one of the operational amplifier inputs as shown in Figure C.3 in Appendix C. This had the benefit that power supply noise could be better rejected, compared to methods that use a resistor divider or a Zener diode, which is especially beneficial for this application where low noise is required due to the small signal input voltage.

The output of the final operational amplifier stage was then connected in series to a capacitor to remove the DC component. It was found that if the output of this stage was not loaded by a resistor to 0 V the amplifier would start to oscillate when triggered by an external electrical noise event. The actual dual channel 40 kHz ultrasonic receiver amplifier constructed by the author is shown in Figure 4.26 below.

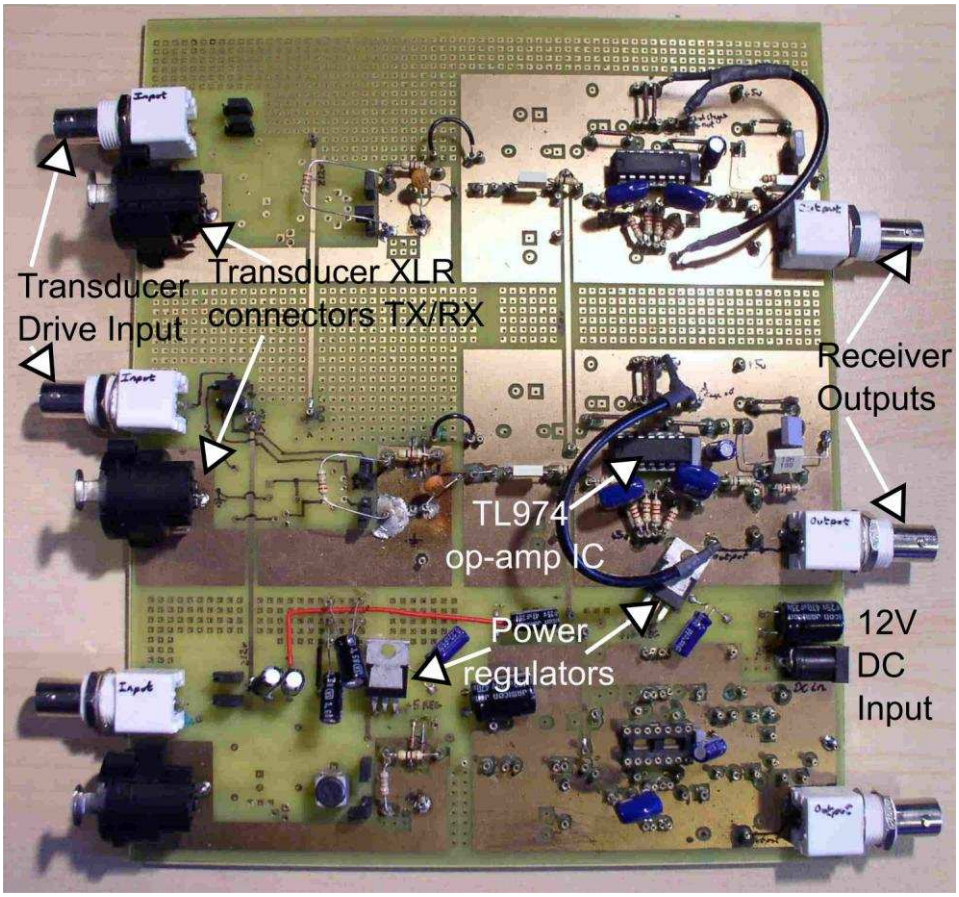

Figure 4.26. Photo of dual channel 40 kHz ultrasonic receiver amplifier.

As shown in Figure 4.27, the output of the receiver amplifiers were connected to a USB digital oscilloscope which was synchronized by the trigger out signal from the AWG to start sampling the incoming receive signal at a rate of 5 MHz. This data was then transferred to the computer to be processed by the LabVIEW software to provide airflow measurements.

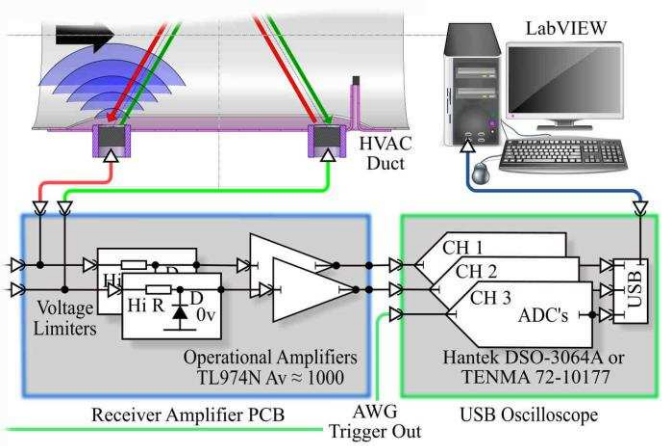

Figure 4.27. Overview schematic of the ultrasonic transducer receiver subsystem.

4.2.4 Signal detection method

To determine the time of flight time difference between the two receive signal.

The zero crossing time and crossing direction could have been used but there was a problem with the receiver waveform having a fluctuating DC offset which could cause jitter of the zero crossing point time, thus causing errors. To alleviate this problem, the positive and negative zero crossing points time of detection were recorded from the expected zero flow time of arrival which was calculated by Equation (4.3) plus a one cycle delay which gave the waveform shown in Figure 4.28 . The signal would be processed by the LabVIEW software which would start looking for the first positive transition. After this event had occurred, it would look for the following negative transition and repeat until two cycles had been detected. The next step was to calculate the positive and negative half cycle midpoints from the zero crossing event times which in turn would be used to calculate a whole cycle midpoint as shown in Figure 4.29 and by using Equation (4.13).

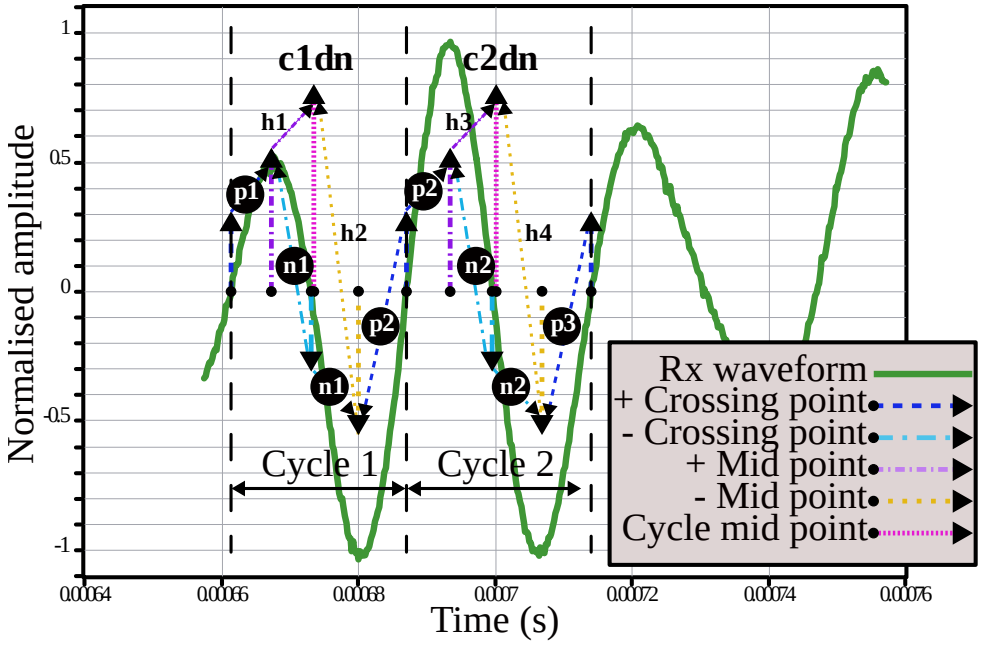

Figure 4.28. Determination of receiver downwind path waveform cycle's midpoints from zero crossing points.

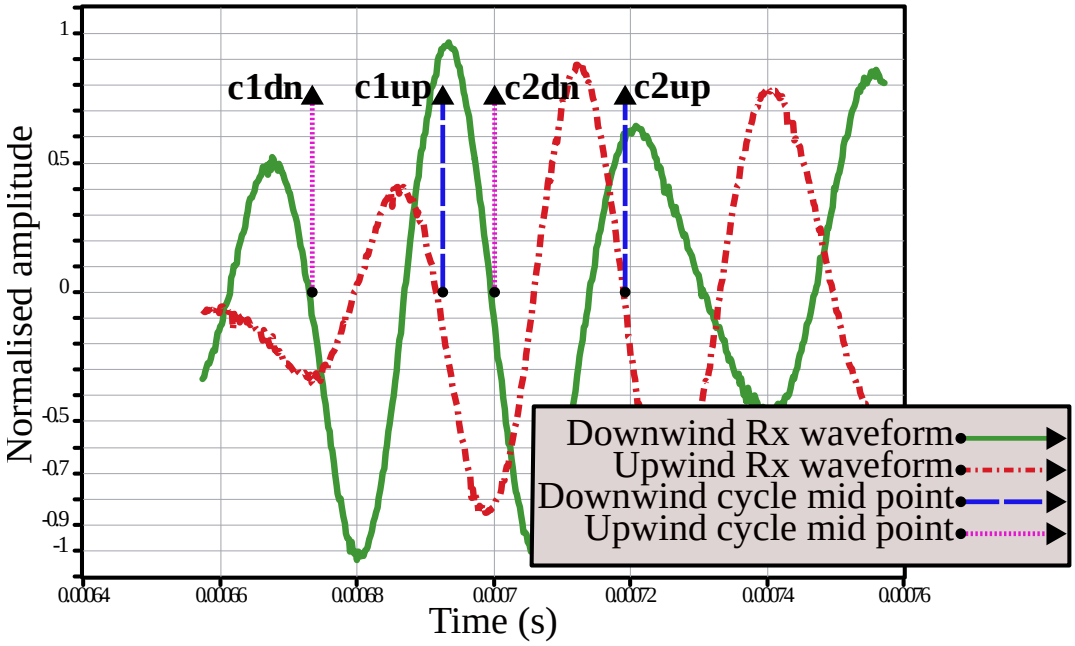

Figure 4.29. Illustration of cycle midpoints for upwind and downwind receiver waveforms.

$$t_{c1dn} = \frac{t_{n1}}{2} + \frac{t_{p1}}{4} + \frac{t_{p2}}{4} \tag{4.13}$$

The time difference is calculated using Equation (4.14), by subtracting the first downwind cycle midpoint from the first upwind cycle midpoint and then the same for the second cycle midpoint from which the mean of these two results can be calculated.

$$\Delta t_{TR} = \frac{(t_{c1dn} - t_{c1up}) + (t_{c2dn} - t_{c2up})}{2} \tag{4.14}$$

The mean airflow speed across the centre of the duct can then be calculated by using the Equations (2.1, 4.1-4.4, 2.4-2.5) in that order.

4.2.5 Duct air temperature subsystem

The air temperature was measured with a Grant type U thermistor part number FF-U-VS-0 which was placed at about half the radius into the duct to avoid the slight temperature change that occurs near the duct wall because of the internal and external duct air temperature difference. The thermistor accuracy was reported to be ± 0.2 ℃ for the temperature range 0 ℃ to 70 ℃. The Grant 2020 datalogger which the thermistor was connected to as shown in Figure 4.30 was configured to send temperature information to a computer running the Grant SquirrelView Plus software. On another computer running LabVIEW the messages from the datalogger containing the temperature information which was formatted in a sequence of 32-bit single-precision, floating-point numbers starting from the

eighth byte were able to be read. This was done as the University owned a number of these data loggers and one was available. To use National Instruments (NI) hardware would have incurred extra expense but would've been much easier to interface to. The thermistor was chosen because of its higher accuracy in the ambient air temperature range compared to thermocouple devices.

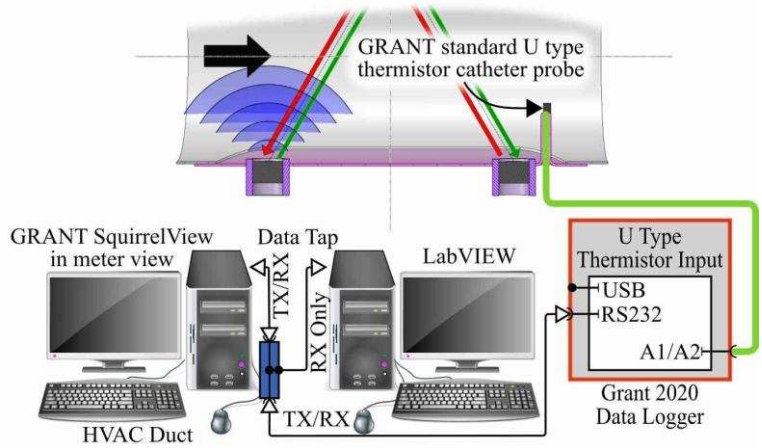

Figure 4.30. Overview schematic of the air temperature subsystem.

4.2.6 Instrument capacitive type relative humidity sensor network

Relative humidity and temperature was measured by the DHT11 (Aosong Electronics Co, Guangzhou, China) capacitive type relative humidity sensors and DS18S20 1-Wire temperature sensor (Maxim Integrated, San Jose, USA). The DHT11 relative humidity measurement accuracy is reported to be ± 5% and the DS18S20 is ± 0.5 ℃. The sensors were placed at three locations in the HVAC airflow test rig. The locations were at the inlet and the outlet of the HVAC unit and just after the ultrasonic airflow meter. Each humidity sensor was connected to a Microchip (Chandler, AZ, USA) PIC 12f683 as shown in Figure 4.31, so that they could be remotely monitored.

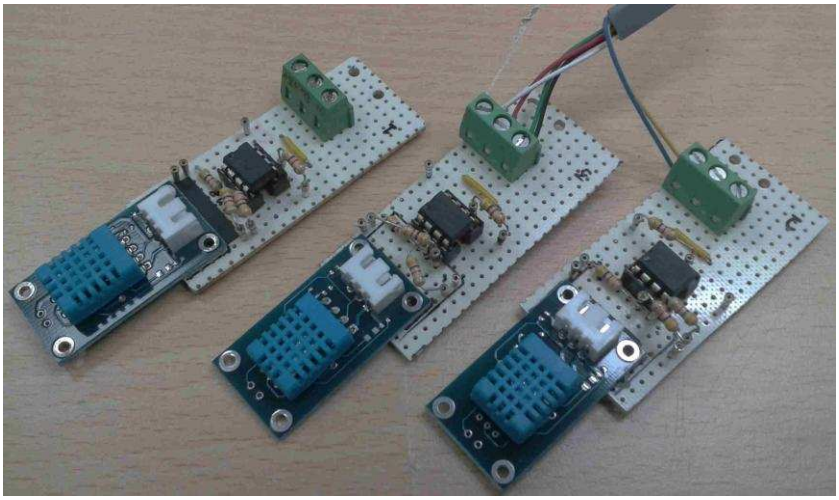

Figure 4.31. DHT11 humidity sensor circuit boards.

The PIC was loaded with code which emulates a 1-wire device. This code was developed by Eric Ward and supplied to the author by Prof Sean Danaher. Sean and Eric are both members of the Navitron renewable energy and sustainability forum hosted at https://www.navitron.org.uk . The code is supplied on the thesis DVD data disk. Each PIC was given a individual address code by setting links on the circuit board. The circuit board was then insulated using self amalgamating tape. This circuit board was then connected to the 1-wire bus using standard BS 6312 431A British Telecom (BT) connectors as shown in Figure 4.32 .

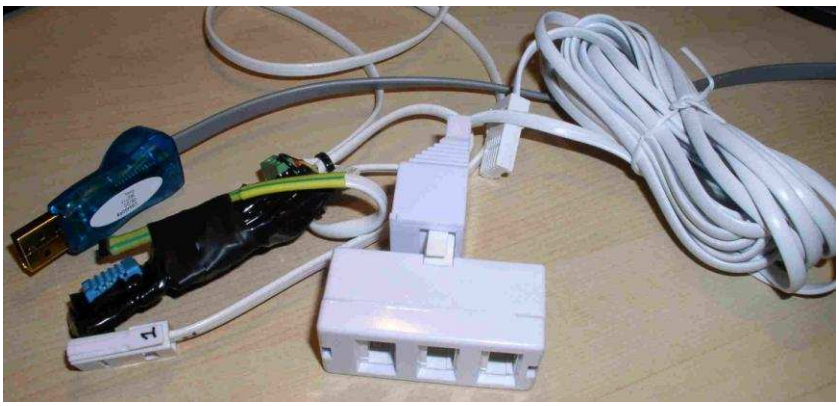

Figure 4.32. Humidity and temperature sensor network.

The BT connector was used because the multi-way parallel connectors which are BT telephone sockets splitters are low-cost and commonly available. The 1-wire bus cable was then connected to a DS9490R 1-Wire to USB adapter. LabVIEW was then used to read in the data from the sensors.

4.3 Laboratory HVAC Unit and Venturi Overview

The aim of the experiment was to test the ultrasonic duct airflow measurement device against a Venturi flowmeter over a range of airflow speeds and temperatures. An existing air conditioning laboratory unit and a Venturi air bench were used to provide an adjustable duct airflow rate and temperature in the range 16 to 44° C at a measured rate for comparison to the acoustic flowmeter device under test as shown in Figure 5.1.

4.3.1 Laboratory HVAC unit

4.3.1.1 Description of a HVAC laboratory unit

The air conditioning laboratory unit was a model A660 as shown in Figure 4.33, produced by P.A.Hilton Ltd. (Stockbridge, UK).

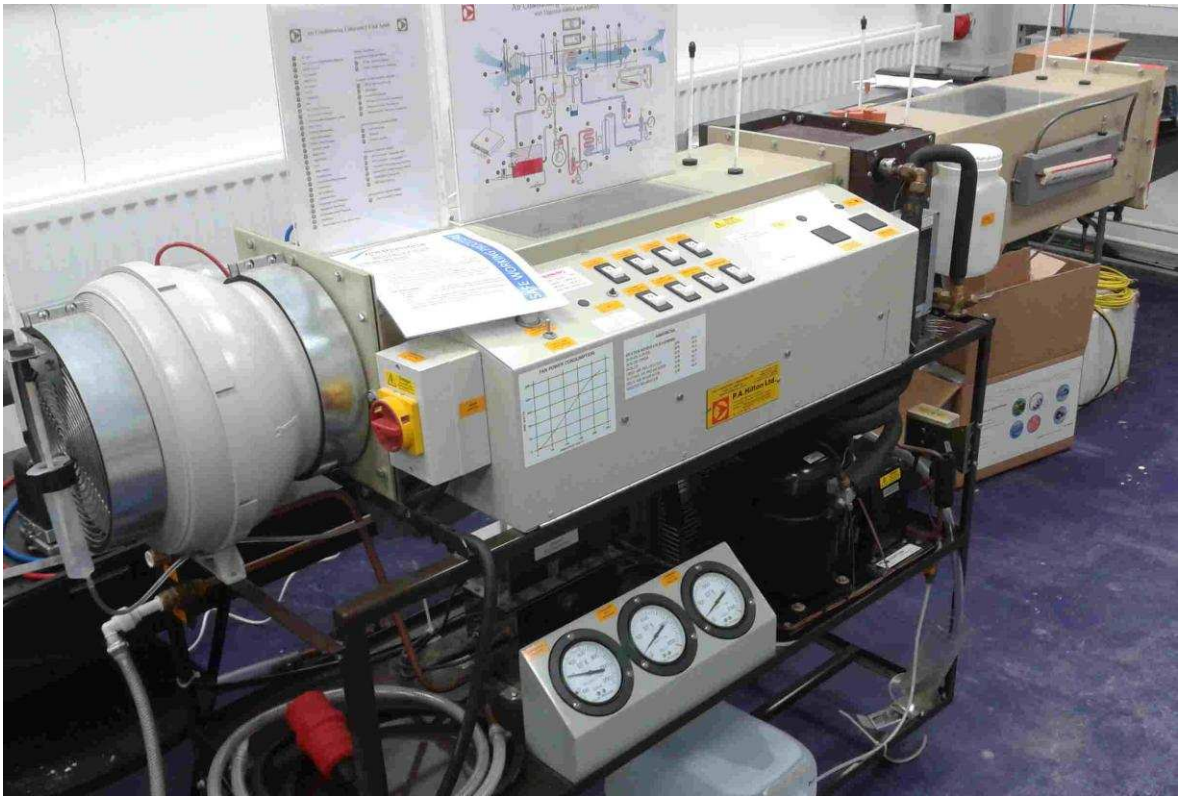

Figure 4.33. Air conditioning laboratory unit.

It consisted of a 230 V AC 210 W inlet fan to supply air to a duct containing four separate 1 kW heaters and a single cooling heat exchanger with about 2 kW capacity as shown in Figure 4.34.

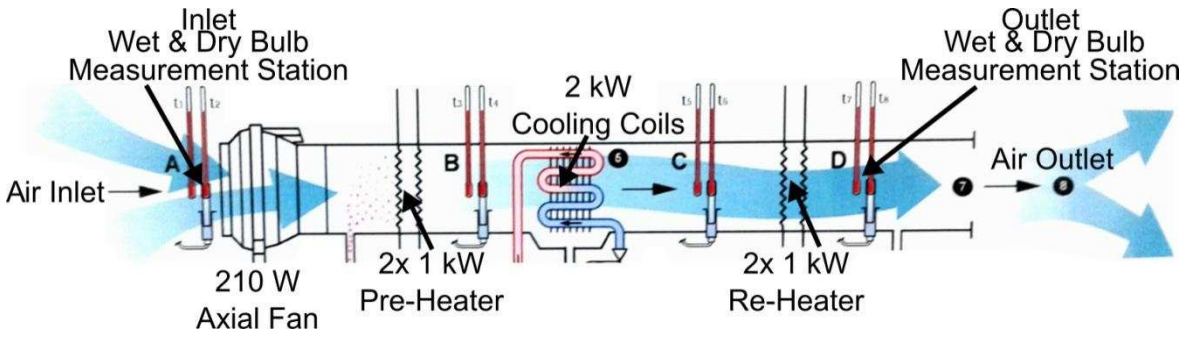

Figure 4.34. Air conditioning laboratory unit simplified schematic diagram adapted from diagram mounted on unit.

The full schematic which is mounted above the air conditioning laboratory unit is shown in Appendix D. Four measurement stations containing wet and dry bulb thermometers were in the unit but only the first station at the inlet and the last one at the outlet were used to measure the change in the enthalpy. During testing it was found that there were inaccuracies in the wet and dry bulb temperatures which was later found to be caused by the radiant heat from the heaters and inlet fan. This error was corrected by using a 2 mm thick insulated foam, normally used as underlay for laminate flooring. This was then clad on the outside with aluminium foil tape, to reflect the radiant heat away from the bulb of the thermometer as

shown in Figure 4.35. This shows the dry bulb air inlet temperature thermometer being shielded from the radiant heat of the fan and its motor.

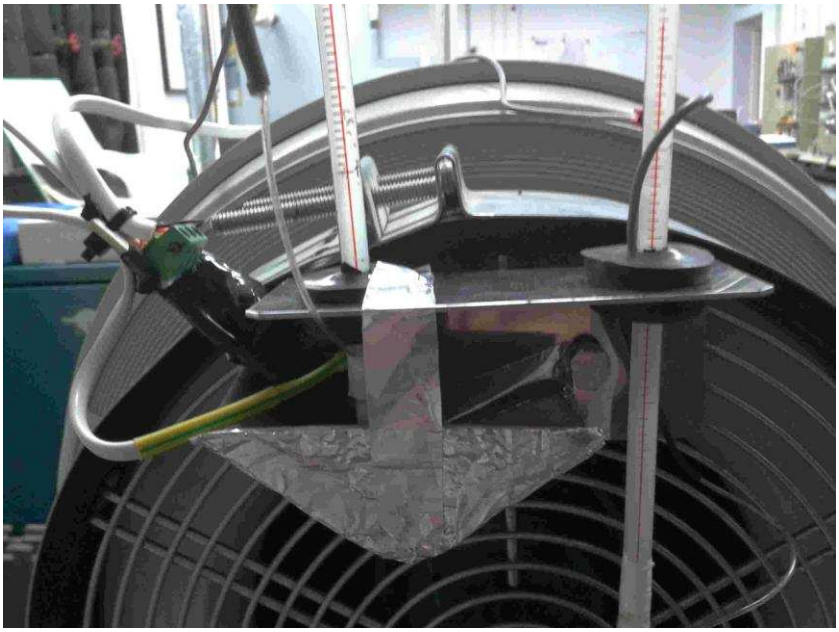

Figure 4.35. Air inlet, dry bulb thermometer and its radiant heat shield.

The unit also incorporated steam humidification capacity of up to 5 kW, but this was not used by experiments described in this thesis. The airflow rate was adjustable to at least 0.14 m^3 per second via a rotary knob which could adjust the fan supply voltage from 115V AC to about 225V AC.

4.3.2 Venturi airflow measurement system

A Venturi was used to measure the airflow rate accurately, as it is one of the most accurate differential pressure measurement instruments.

4.3.2.1 Description of the Venturi airflow measurement system

The Venturi used in the experiments, which is shown in Figure 4.36, was a short-form Venturi [98] made by Airflow Developments Ltd (High Wycombe, UK).

Figure 4.36. Short-form Venturi used in experiments.

The Venturi main dimensions were 139.82 mm (5½") for the pipe diameter and 89 mm (3½") for the throat diameter with a overall length of 762 mm (30"). Further dimensions of the Venturi are shown 4.37.

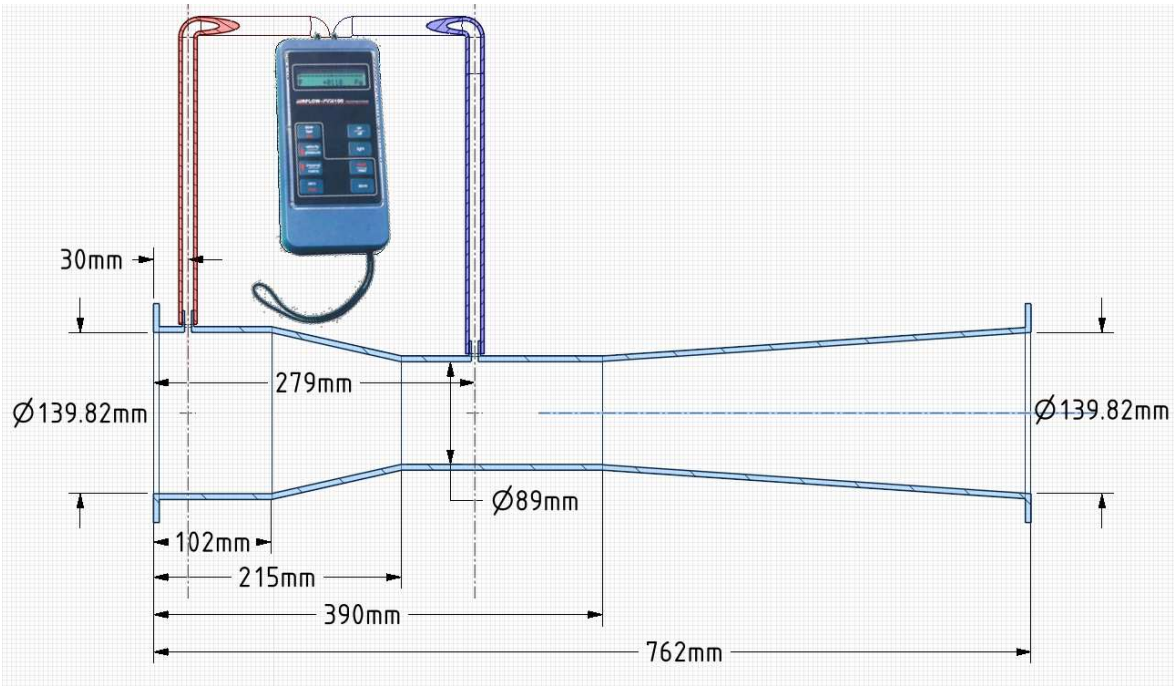

Figure 4.37. Short-form Venturi dimensions.

A 698 mm (27½") section of round duct/pipe which is equivalent to 5 hydraulic diameters was connected before the Venturi, which contained two 50 mm long, honeycomb flow straighteners to reduce the flow swirl.

4.3.2.2 *Venturi airflow equations*

The following Equation (4.15) is adapted from the ASHRAE handbook [47] (p. 36.19) with the addition of a discharge coefficient correction value [98]:

$$w = \rho V_1 A_1 = \rho V_2 A_2 = C_d A_2 \sqrt{\frac{2\rho(p_1 - p_2)}{1 - \beta^4}} \tag{4.15}$$

Where

w mass flow rate in (kg /s);
ρ density of dry air (kg/m^3);
V_1 velocity of airflow stream in pipe (m /s);
V_2 velocity of airflow stream in throat (m /s);
A_1 pipe flow area (m^2);
A_2 throat flow area (m^2);
C_d discharge coefficient, typically,
$= 0.984$ for a casted tube or classic Venturi,
$= 0.985$ for a welded tube or short form Venturi,
$= 0.995$ for a Venturi with a machined entrance cone;

p_1 pipe pressure (kPa);

p_2 throat pressure (kPa);

β ratio of diameters $\frac{D_2}{D_1}$.

Where for a Venturi

D_1 pipe diameter;

D_2 throat diameter.

The density of the air was calculated using the ideal gas law Equation (3.3). The air temperature was calculated from the mean of the inlet and outlet air temperatures which were measured by thermistors of the type described in section 4.2.5.

4.3.2.3 *LabVIEW software for Venturi airflow measurements*

The differential pressure across the Venturi was measured by a PVM100 micromanometer (Airflow Developments, High Wycombe, UK) which had an accuracy of ± 1% of the reading or ± 1 Pa, whichever was the greatest. This was connected to the computer running LabVIEW via a serial to USB adapter. A LabVIEW program was developed by the author to read in the RS232 (1200,N,8,1) serial measurement data from the PVM100 and calculate the airflow mass flow rate, volume rate and airflow velocity with corrections for air density variation. To compensate for the assumed Venturi inside surface roughness a discharge coefficient of 0.9877 was used.

4.4 Duct Dry Bulb and Wet Bulb Temperature Measurement Subsystem

To measure the enthalpy levels before and after the air conditioning laboratory unit and calculate the air density through the Venturi a number of thermistor temperature sensors were placed at the locations listed below in Table 4.4 and then connected to the grant data logger as described in section 4.2.5.

4.4.1 Locations of wet and dry bulb measurement stations

The location descriptions for the placement of the Grant type U thermistors, part number FF-U-VS-0, temperature sensors used for measuring wet and dry bulb temperatures are listed below in Table 4.4.

Table 4.4. List of Wet and dry bulb measurement station locations

Location	Ch No.	Descr.	Type
HVAC lab unit	1	Inlet	Dry bulb
	2	Inlet	Wet bulb
	6	Outlet	Dry bulb
	4	Outlet	Wet bulb
Venturi	7	Inlet	Dry bulb
	5	Outlet	Dry bulb
Ultrasonic flowmeter	8	Outlet	Dry bulb

Figure 4.38 shows the wet and dry bulb measurement station locations illustrated on a drawing of ultrasonic flowmeter testing rig.

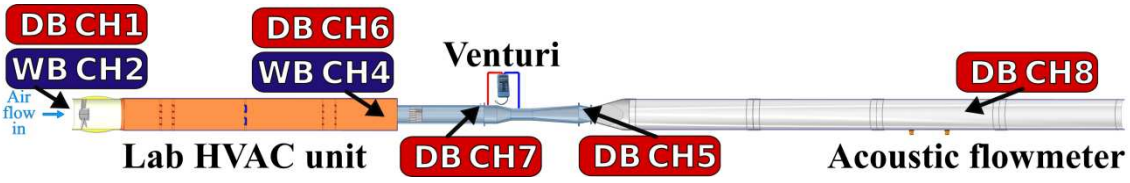

Figure 4.38. Diagram Wet and dry bulb measurement station locations.

The location, measurement type and channel number is used to interpret the measurement data contained in Excel files contained on the Thesis DVD Data Disk.

4.5 Overview of the complete ultrasonic flowmeter testing rig

The air conditioning laboratory unit and Venturi was connected to a round or square duct containing the ultrasonic flowmeter under test, as shown in Figure 4.39, for various tests.

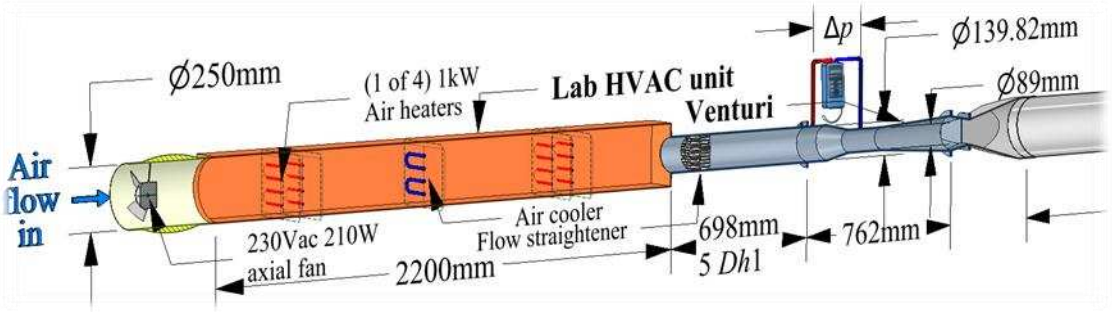

(a)

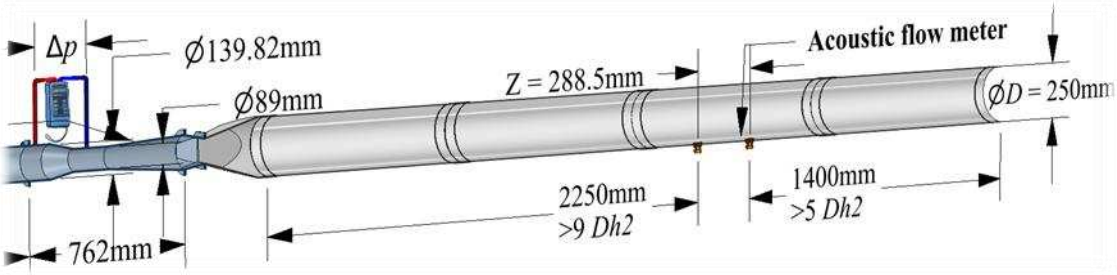

(b)

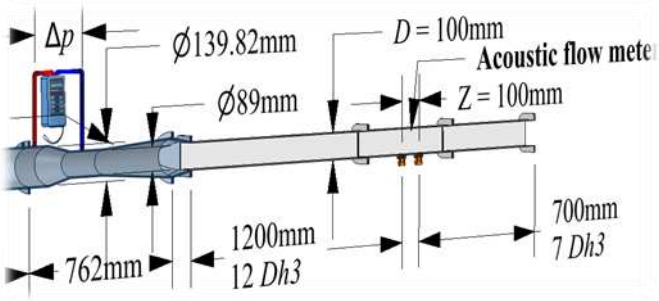

(c)

Figure 4.39. (a) Front section of the ultrasonic flowmeter testing rig; (b) End section of the round duct flowmeter testing rig; (c) End section of the square duct flowmeter testing rig.

The test duct lengths before and after the ultrasonic acoustic airflow meter were constructed following recommendations described in the American Society of Heating, Refrigerating and Air Conditioning Engineers (ASHRAE) fundamentals [47] (p. 36.18) for measuring flow in ducts. This requires measurements to be done at least the equivalent of 7.5 hydraulic diameters in length after, and 2 hydraulic diameters before, a disturbance. See Section 6.3 on Flowmeter Application Case Studies for a more detailed explanation of this recommendation. The Venturi has only five hydraulic diameters before a disturbance but two 50 mm honeycomb flow straighteners are used to mitigate the need for the extra duct length required.

4.6 Summary of Chapter 4

An overview of the ultrasonic duct airflow development system, which was used to develop the duct airflow measurement instrument is described at the beginning of the chapter. The design for the ultrasonic duct airflow measurement instrument which uses two transducers in a contra-propagating mode was selected due mainly to the measurement drift observed which was caused by duct air temperature differences during zero flow conditions. An air temperature measurement sensor was included in the design for two main reasons which were to correct errors caused by the speed of sound change and calculate the enthalpy level. Temperature corrections were used because it simplifies the signal processing of the acoustic signal, which only requires a phase difference measurement using specially selected zero crossing points. The temperature measurement capability was already needed for measuring the enthalpy level which could be preferably obtained from a thermistor or a good quality capacitive humidity sensor, which generally have very accurate temperature measurement capabilities in the ambient temperature range.

A single reflective path ultrasonic flow meter design was chosen as the preferred solution. The most significant benefit of this design is that one of the major critical dimensions, the axial separation distance of the transducers can be permanently fixed in one assembly. Another benefit is that the effect of airflow swirl can be mitigated by the use of the reflective path. The transducers are mounted tangentially to the duct surface to simplify mounting arrangement.

In this study a phase shift or differential transit time method is used to reduce the cost of implementation. In the differential transit time method the estimated transit time is found by using a two stage calculation. In the first stage, the zero flow transit time is calculated from the air temperature, which is used to calculate the speed of sound from which the time required for the sound to travel the acoustic path length between the transducers is calculated. At the second stage of the calculation, half the actual measured differential transit time, which is measured using the phase difference, is added or subtracted from the zero flow transit time depending on the airflow direction. These two transit times are then fed into the well-known inverse transit time difference (ITTD) [99] formula presented in Equation (2.5) to calculate the airflow velocity rate.

An AWG controlled via LabVIEW was used to produced the bipolar transmit signal which consisted of two square waves followed by a square wave which is 180° phase shifted relative to the pair transmitted previously. The anti-phase signal is used to reduce transducer ringing, which reduces the noise level in the response signal. The output of the AWG was fed into a high voltage power amplifier capable of driving the ultrasonic transducer to its maximum voltage of approximately 100 Volts peak to peak. This was then switched through two solid-state relays (SSR) within the high voltage demultiplexer specifically designed for the task by the author which could switch a single input between at least two outputs. The demultiplexer was also controlled by the computer through a PicoLog® 1012 USB data acquisition device. The transmit signals were then connected, depending on the demultiplexer state, to one of two 40 kHz enclosed type piezoelectric transducers which would transmit an ultrasonic signal through the duct to a receiving transducer. The received signal is then amplified after passing through a multistage operational amplifier designed and built by the author to boost the signal voltage by more than 1000 times. This was then digitized by a USB oscilloscope, which is shown in Figure 4.2, for processing by the computer running the LabVIEW® control and signal processing software. The amplifier also incorporates the characteristics of a band pass filter, which reduces the high and

low frequency noise. The main noise problem was 50/60 Hz mains pickup, which was reduced by using a high pass filter and processing the zero crossing points to find the receive cycle waveform cycle midpoints. The up and downstream receive signal waveform full cycle midpoints were then used to calculate the time difference due to airflow velocity.

Eight Grant type U thermistor probes were used to measured temperatures, which were monitored via a Squirrel® SQ2020 Series Data Logger via LabVIEW. Six of the sensors were used to calculate energy throughput by measuring dry and wet bulb temperatures before and after the air conditioning laboratory unit. The other two were used for calculating the air density in the Venturi.

A relative humidity and temperature sensor network was developed using DHT11 capacitive type relative humidity sensors and 1-Wire DS18S20 temperature sensors. This sensor network was developed to eventually replace the grant data logger and also be upgradable with better accuracy humidity sensors, such as the HYT-221 or SHT25, which can measure temperature very accurately as well.

This experimental setup was done to test the ultrasonic duct airflow measurement device against a Venturi flowmeter over a range of airflow speeds and temperatures.

Chapter 5.

TESTING

In this chapter:

5.1 Experimental Setup

The aim of the experiment was to test the ultrasonic duct airflow measurement device as shown in Figure 5.1 against a Venturi flowmeter over a range of airflow speeds and temperatures.

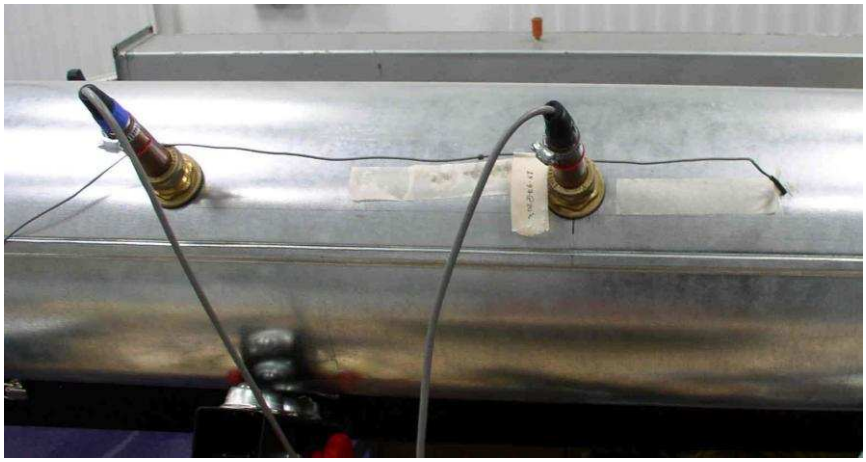

(a)

(b)

Figure 5.1.(a) Photograph of 250 mm diameter round duct acoustic flowmeter, (b) Photograph of 100 mm wide square duct acoustic flowmeter.

The air conditioning laboratory unit with a Venturi meter as shown in Figure 4.39a was used to provide an adjustable duct airflow rate and temperature in the range

16 to 44 ℃ for comparison with the acoustic flowmeter device under test. Tests were carried out on a 250 mm diameter cylindrical duct (Figure 5.1a and Figure 4.39b) then on a 100 mm wide square duct (Figure 5.1b and Figure 4.39c) to cover the majority of duct installation types and flow velocities. The negative airflow velocity range was adjusted to a minimum to increase the positive velocity range so that the device would operate at maximum sensitivity for positive flow velocities.

In the first test, a series of airflow rates was produced by varying the inlet fan voltage in steps of 10 V between 120 to 210 V AC. At each voltage step, the Venturi flow rate was recorded against the acoustic flowmeter airflow rate. This test was to check the linearity and the maximum percentage root mean square (RMS) error of the ultrasonic flowmeter compared to the Venturi with varying flow rates. Table 5.1 lists the operating values of the reference Venturi airflow measurement system for the comparison period time of approximately 1 min.

Table 5.1. (a) Operating values for airflow reference system with 250 mm diameter circular duct attached and, (b), with 100 mm wide square duct attached.

Inlet Fan (V)	Mean Venturi Air Temp (°C)	Mean Venturi Δ Pressure Readings (Pa)	Standard Deviation of Venturi Pressure Readings (Pa)	Calculated Venturi Mean Mass Flow Rate (kg/s)	Calculated Venturi Inlet Flow Velocity (m/s)	Calculated Duct Mean Airflow Velocity (m/s)
120	20.9	128	0.35	0.1170	6.44	2.04
130	20.9	156	0.63	0.1294	7.12	2.26
140	20.8	182	0.50	0.1397	7.68	2.44
150	20.7	209	0.42	0.1496	8.23	2.61
160	20.6	231	0.43	0.1572	8.65	2.74
170	20.6	250	0.78	0.1634	8.99	2.85
180	20.6	262	0.68	0.1675	9.22	2.92
190	20.5	275	0.40	0.1716	9.44	2.99
200	20.3	286	0.72	0.1748	9.61	3.04
210	20.2	294	1.04	0.1773	9.75	3.09

(a)

Table 5.1. *Cont.*

Inlet Fan (V)	Mean Venturi Air Temp (°C)	Mean Venturi Δ Pressure Readings (Pa)	Standard Deviation of Venturi Pressure Readings (Pa)	Calculated Venturi Mean Mass Flow Rate (kg/s)	Calculated Venturi Inlet Flow Velocity (m/s)	Calculated Duct Mean Airflow Velocity (m/s)
120	23.1	83	0.43	0.0941	5.21	7.99
130	23.2	102	0.29	0.1042	5.77	8.85
140	23.2	122	0.45	0.1140	6.31	9.68
150	23.2	141	0.45	0.1223	6.77	10.39
160	23.1	154	0.00	0.1280	7.08	10.87
170	23.2	166	0.21	0.1328	7.35	11.28
180	23.2	175	0.21	0.1364	7.55	11.58
190	23.2	183	0.00	0.1395	7.72	11.85
200	23.3	189	0.29	0.1417	7.84	12.04
210	23.2	195	0.49	0.1439	7.96	12.22

(b)

The second test consisted of setting the fan voltage to the maximum step voltage of 210 V AC and measuring the flow rates with different levels of cooling and heating on the air conditioning laboratory unit. This test was to check the maximum percentage RMS error of the ultrasonic flowmeter with a selection of air temperatures between 16 and 44 ℃ because, as shown in Equation (2.1), the speed of sound changes with temperature which may lead to errors if temperature corrections for the speed of sound were functioning incorrectly.

5.2 Results and Discussion of Ultrasonic Airflow Measurement *vs.* Venturi

Figure 5.2 shows the reference airflow velocity measured by the Venturi against the ultrasonic airflow measurement device under test in a circular and square duct. In the 250 mm diameter circular duct, the range of airflow velocities produced was limited by the output of the inlet fan to between 2 m/s and 3.25 m/s so, in the second set of tests, the smaller size of the duct resulted in a higher range of flow velocities of between 8 m/s and 12.25 m/s. The RMS percentage error reduces as the airflow velocity increases due possibly to the flattening flow profile, due to increased turbulence which can be predicted by the Reynolds number as calculated in Equation (2.10). So as the Reynolds number increases the error due to flow profile is reduced, which would also happen when the diameter of duct is increased.

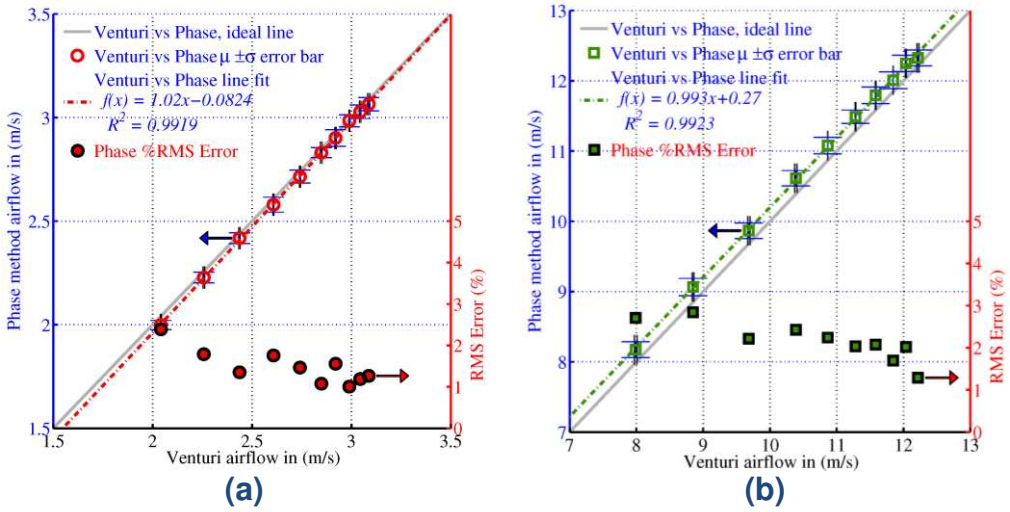

Figure 5.2. *Cont.*

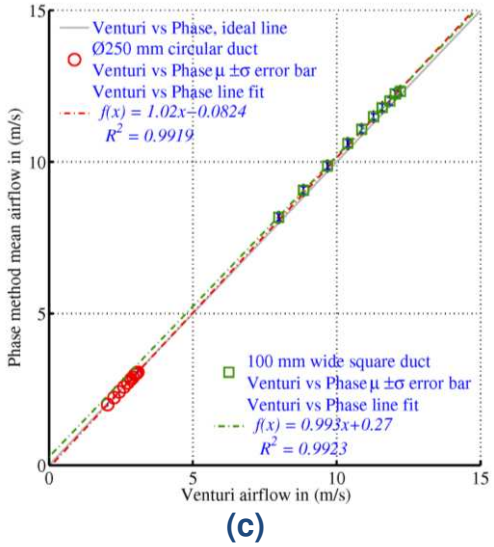

Figure 5.2. (a) 250 mm diameter circular duct ultrasonic airflow measurement vs. Venturi; (b) 100 mm wide square duct ultrasonic airflow measurement vs. Venturi; (c) Combined results of circular and square duct airflow measurements *vs.* Venturi.

In both configurations the RMS percentage error was less than 3% with a linear response as shown by the high R^2 values for the straight line fit across the range of air velocities tested. These findings are similar to the results obtained by Olmos [19] and van Buggenhout et al. [21].

5.3 Results and Discussion of Airflow Measurements with Varying Air Temperature

Figure 5.3 shows the Venturi velocity against the ultrasonic airflow measurement device under test in a circular and square duct with a range of air temperatures.

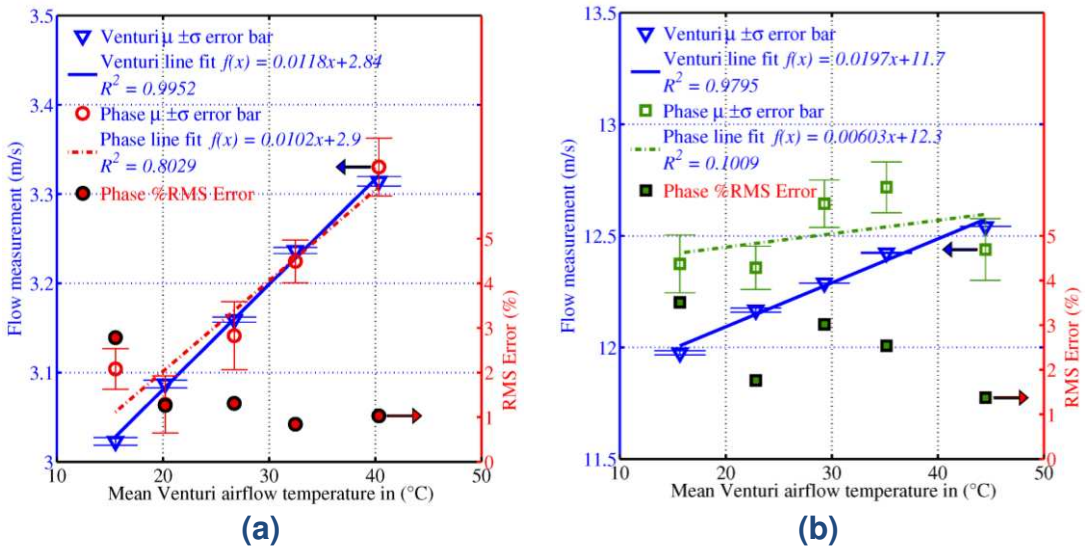

Figure 5.3. (a) 250 mm diameter circular duct ultrasonic airflow measurement vs. Venturi with varying air temperature; (b) 100 mm wide square duct ultrasonic airflow measurement vs. Venturi with varying air temperature.

The maximum fan output rate was set on the air conditioning unit and not altered during the tests. There was a small increase in the measured flow rates as the temperature increased due to the expansion of the air in the duct after being heated. In both the circular and square duct scenarios the RMS percentage error was less than 3.5% with no compensation implemented for the error caused by the flow profile shape [42], [100–103]. The low value of R^2 for the results shown in Figure 5.3b could be due to the overlap of transmitter ringing with the received signal or the signal processing algorithm not being robust enough to cope with this situation in a small duct. One possible solution to alleviate this would be a "W" shaped acoustic path to double the time of flight.

5.4 Results and Discussion of Ultrasonic Airflow Energy Throughput Measurement *vs.* Venturi

Figure 5.4 below shows the difference in energy throughput measurements on the Venturi, compared to the ultrasonic flowmeter.

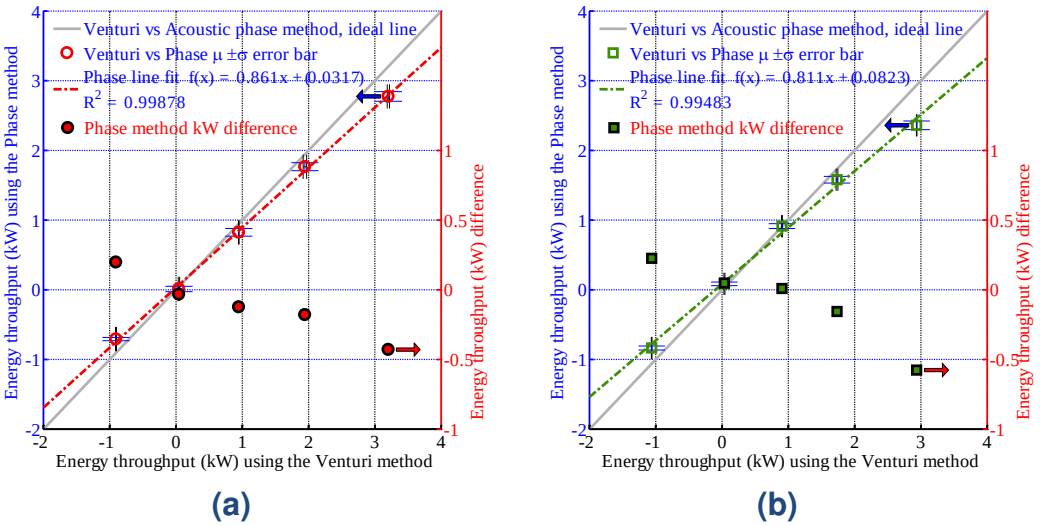

Figure 5.4. (a) 250 mm diameter circular duct ultrasonic airflow energy throughput measurement vs. Venturi; (b) 100 mm wide square duct ultrasonic airflow throughput measurement measurement vs. Venturi.

There is a significant difference between the Venturi and the ultrasonic flowmeter energy throughput measurement which is mostly due to the cooling or heating of the in-duct air, via the surface of the duct wall between the flowmeters. As there needs to be a minimum separation distance between the flowmeters for the flow profile to settle, The duct should be insulated from the outside ambient air temperature so that a more accurate comparison of the flowmeters energy throughput can be achieved. Also the ultrasonic flowmeter could be placed directly before the Venturi as it does not affect the flow profile.

5.5 Summary of Chapter 5

This chapter describes the testing, which was carried out on the ultrasonic flowmeter fitted to a 250 mm diameter round duct or a 100 mm wide square duct in comparison to a Venturi flowmeter. The results were obtained from 30 runs of varying airflow, temperature and duct type. Overall, the airflow measurement accuracy was better than 3.5% RMS, compared to the Venturi flow rates. Preliminary results for energy throughput were presented, but there is significant difference due to heat loss through the duct wall. This could be remedied in future experiments by placing the ultrasonic flowmeter before the Venturi and minimising the distance between them. Also the outer walls of the flowmeters and any ducting between them should be well insulated.

Chapter 6.

INSTRUMENT SIMULATION AND APPLICATION CASE STUDIES

In this chapter:

This chapter explores the measurement error performance of the ultrasonic flowmeter in various common installation scenarios with non-ideal flow profiles caused by bends in the duct before the flowmeter. Typically ultrasonic flowmeters that measure across the centre of a straight cylindrical pipe or duct have a measurement error of up to 33% for laminar flow and up to 7% for turbulent flow [101]. Solutions to mitigate this error have been analysed using simulation and results are presented. Simulation has the benefit that scenarios can be more quickly tested and it reduces the cost of the experimental apparatus and time required.

6.1 LabVIEW 2D Mathematical Model

To calculate the expected results and accuracy for the dimensional parameters. A mathematical model was developed in LabVIEW with user configurable inputs as shown in Figure B.2 in Appendix B. This calculator is useful for evaluating the following:

1) Expected time of arrival for acoustic signal.
2) Ultrasonic receiver voltage gain required.
3) Signal phase difference in degrees or seconds.
4) Assessing airflow meter plus and minus velocity range limits due to ± 180° signal phase measurement range limitations of the design.
5) Selecting transducer axial separation distance for maximum flowmeter sensitivity.

This simulation model was unable to predict measurement errors due to the flow profile shape along the acoustic path, so more complex solutions which utilised CFD software were investigated.

6.2 Computational fluid dynamics

6.2.1 Airflow simulation

Duct longitudinal flow velocities are not uniform across the duct because the flow is affected by friction created between the air and the duct wall. To collect experimental data for different scenarios where the flow meter could be installed would be very time-consuming and difficult to do because of the different types and sizes of duct fittings required. This is especially true for the larger fittings, which require a huge amount of space and a powerful fan for moving the air at the required velocity. So for these reasons, CFD simulation software has been used to obtain the three-dimensional flow velocity data required for the flowmeter application case studies of various installation scenarios. There are many commercial CFD simulation software packages available such as COMSOL and ANSYS Fluent/CFX [104–108] which are well-suited to performing HVAC duct flow simulation tasks. The flow in HVAC ducts is mainly turbulent with a Reynolds number >4000 *Re.* Except for when there is a situation of very low flow velocity within a duct of small diameter, such as an airflow of <0.75 m/s with a duct diameter of less than 0.1 m. A k-epsilon turbulence model was used to compute the three-dimensional airflow for the in-duct flowmeter scenarios as this model has good convergence rate and relatively low memory requirements [109]. There are other models such as k-omega or the shear stress transport (SST) which is a hybrid model using both k-epsilon and k-omega to produce more accurate results, but due to time constraints It was not possible to evaluate the scenarios with these models. A suggestion for future work would be to evaluate these other models and produce time-dependent data so that the flow meter could be simulated over a period of time.

6.2.2 Acoustic simulation

A short investigation into finite element analysis (FEA) software was carried out to simulate the acoustic and flow simulation. It was found that after trialling a FEA package called COMSOL Multiphysics that simulations of an ultrasonic In-duct flowmeter would take a long time to process and consume large amounts of memory. This is because it is recommended by the software developers that at

least 12 degrees of freedom (DOF) are required per wavelength in one dimension. At the ultrasonic frequency of 40 kHz, the wavelength is very small, 8.5 mm. For example to simulate a three-dimensional space of a 250 mm diameter round duct, which was 600 mm long then $12^3 = 1728\,DOF$ are required per three-dimensional wavelength sized block of space as a minimum. So for the area required 80,000,000 DOF would be needed. In actual tests using a high-end laptop with a i7-3610QM Intel processor an acoustic time dependant simulation with a 1,000,000 DOF consumed about 16 GB of memory and took over 12 hours to solve for a time series of about 2 milliseconds. Figure 6.1 shows the result of the pressure wave generated by a Gaussian shaped acoustic pulse positioned at the bottom front corner.

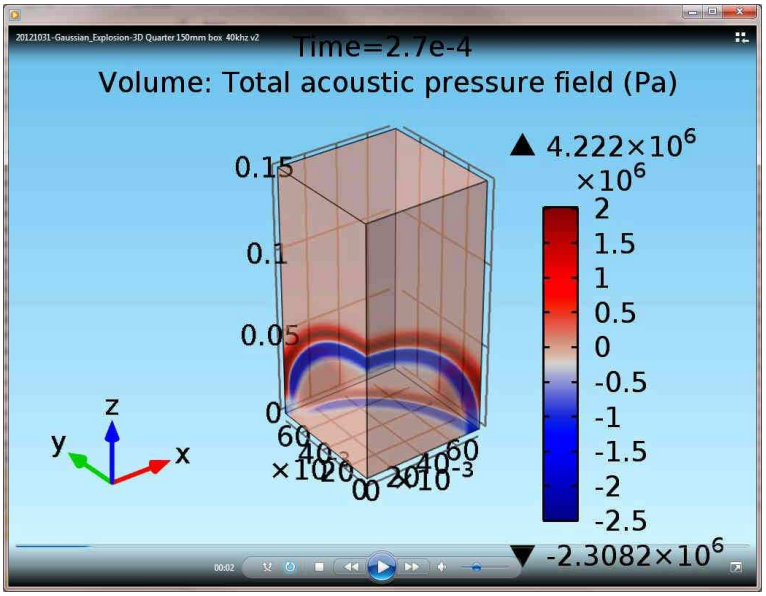

Figure 6.1. Screenshot of a 3-D acoustic pulse simulation done using COMSOL multi-physics in a quarter section of a cube of air.

After a period of two weeks, It was still unknown how the acoustic physics would be coupled to the fluid flow physics in the COMSOL simulation software. It was decided that this method was probably going to be unworkable unless there was some availability of a supercomputer to calculate the results quickly enough.

It was then decided to develop an in-house solution using the ray tracing method described in Section 2.2.3, combined with the required CFD airflow velocity data. This would provide faster solution times, but would be slightly compromised because certain wave phenomena would not be simulated. The actual simulation code developed is described in Section 6.4 with results of simulations presented in Section 6.6.

6.3 Flowmeter Application Case Studies

When an in-duct airflow meter installation or airflow measurement probe traverse is carried out it is recommended by ASHRAE [47] (p. 36.18) that this is done with a separation of at least 3 and 7.5 hydraulic diameters in length before and after a disturbance. The airflow disturbance could be typically caused by a fan, bend, T-junction or exhaust vent. Figure 6.2 shows an example of this, a cross-section of a round duct system with bends before and after the airflow meter, with the suggested minimum duct lengths annotated.

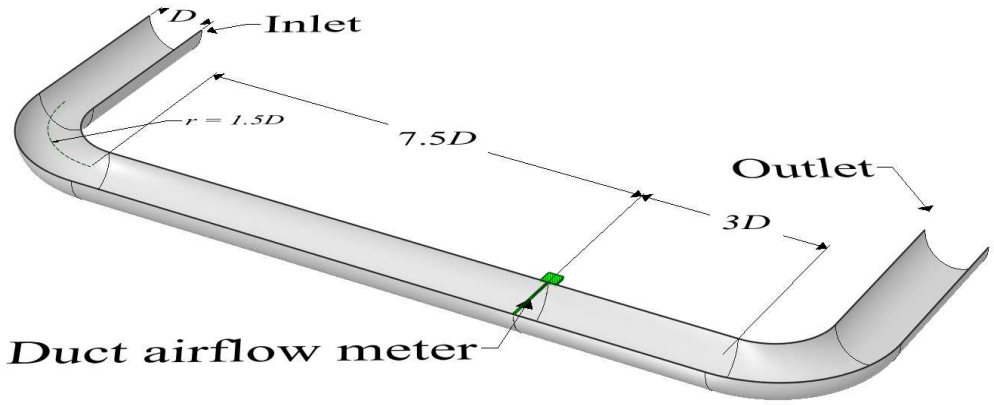

Figure 6.2. ASHRAE minimum recommended duct lengths before and after airflow measurement point

The hydraulic diameter, symbol Dh, of a duct is equivalent to four times the internal cross-sectional area divided by the perimeter length of the duct internal walls [47] (p. 21.7); so for round or square ducts the hydraulic diameter is equivalent to the diameter or width of the duct.

In buildings it can be difficult to find long straight sections of at least 7.5 hydraulic diameters in length, to meet the preconditions stipulated by standards or manufacturers, therefore airflow measurement devices are often placed in suboptimal locations which can cause measurement errors due to flow profile disturbances.

To assess the effect of flow profile variation on measurement of the mean flow velocity across the duct, a series of scenarios using square or round ducts with and without airflow disturbances before the measurement point were simulated using CFD software. The error percentage between the duct total mean flow velocity and two straight paths parallel to each other as shown in Figure 6.3 were compared. One of these measurement paths was the centreline path of the duct and the other was parallel to it halfway between the centreline and the duct wall.

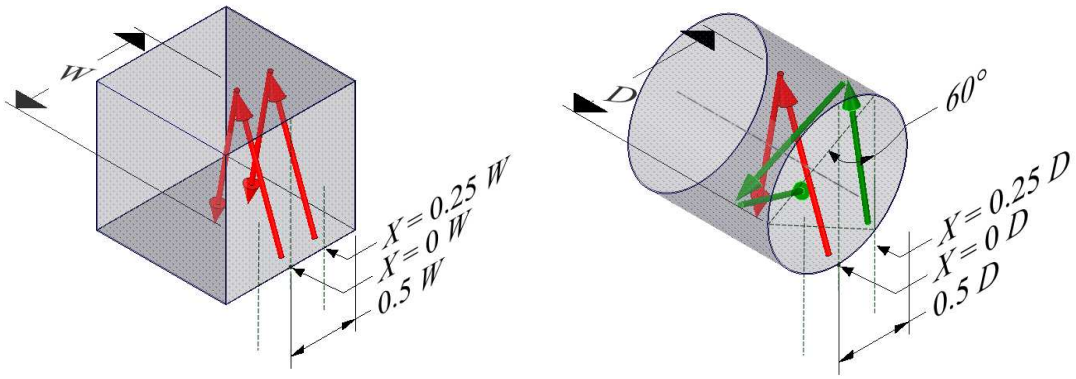

(a) (b)

Figure 6.3. CFD simulation mean flow across the duct selected paths for, (a) Square duct (b) Round duct scenarios.

Similar analysis to this was carried out by Zhao *et al.* [107] on a dual path ultrasonic flowmeter mounted in a square pipe which was used to measure water volumetric flow rate. The flowmeter was then mounted to a larger circular pipe via a transition close to the meter body. The results of the simulations and experiments concluded that the optimum sound path position was 0.65 times the half side length of the square pipe cross-section or as in the geometric reference style used in this document $\mathrm{x} = 0.325\ \mathrm{W}$ from the centre of the pipe or duct. As shown in the Figure 6.4 below 0.65 times the half cycle length of the square pipe cross-section is equivalent to $0.52(\mathrm{D}/2)$ on the circular pipe or $\mathrm{x} = 0.26\ \mathrm{W}$.

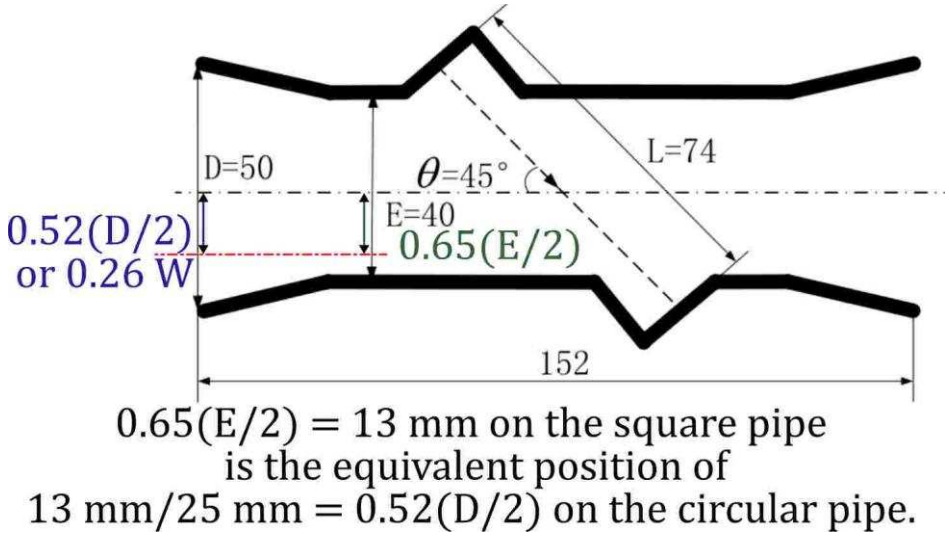

Figure 6.4. Longitudinal cross-section of a dual path square shaped ultrasonic flowmeter by Zhao *et al.*

6.3.1 Straight duct lengths

The square and round straight duct CFD simulation scenarios are shown as follows in Figure 6.5 (not shown to scale);

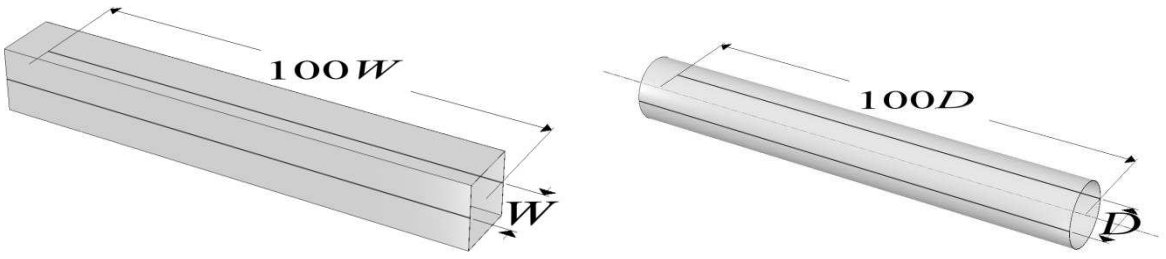

(a) (b)

Figure 6.5. Straight duct 100 *W* or *Dh* long CFD simulation scenario for (a) Square duct (b) Round duct.

At the inlet of the CFD simulation the airflow velocity in the duct longitudinal direction is uniform but as it flows along the duct, it becomes more distorted because of the air friction with the duct wall as shown in Figure 6.6 by the blue flow profile line bending as it approaches the duct wall at x or y = ± 0.05 m. The Z axis, which is the longitudinal dimension of the duct is condensed so that comparison of the profiles can be made more easily. The blue profile lines have arbitrary units but do represent the relative change in the flow profile along the duct.

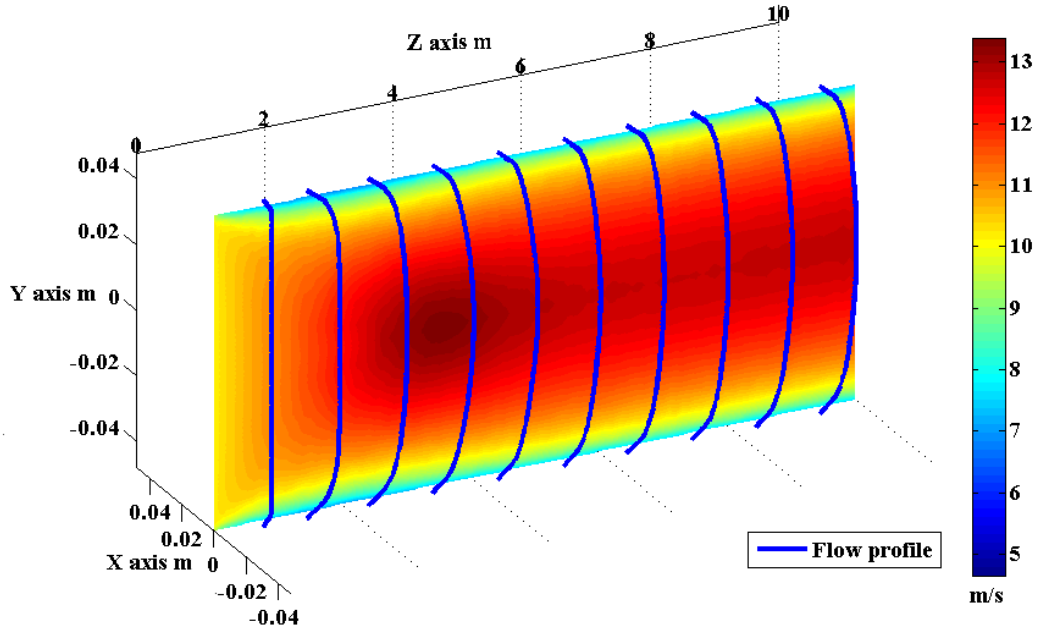

Figure 6.6. Square straight duct 100 *W* CFD results along z plane for x = 0.

This flow profile is bowler hat shape and is flatter across the middle of the duct than the more pointed parabolic shape of a laminar flow profile, due to the high level of turbulence. In a square or round duct of the same dimensions and airflow velocities at 20℃ the Reynolds number [47] (p. 21.6), varies from 16,600 at (0.1 D, 2.5 m/s) to 415,000 at (0.5 D, 12.5 m/s). The larger the duct effective hydraulic diameter or mean flow velocity is, the larger the Reynolds number will be. The error offset of the centreline mean flow is reduced as the Reynolds number increases due to the flattening of the flow profile [110] (p. 90). The size of random

errors may increase as the turbulence increases but errors due to air temperature may decrease with increased mixing of the air.

Figure 6.7 shows the error percentage compared to the mean flow for two flow measurement lines from bottom to top of the duct at x = 0 W and x = 0.25 W from the centre of the duct for all the following combinations of duct sizes, (0.1,0.3,0.5) m, and flow velocities, (2.5,5.7.5,10,12.5) m/s. The flow profile is symmetrical about the centreline of the duct so for x = -0.25 W the results are very similar.

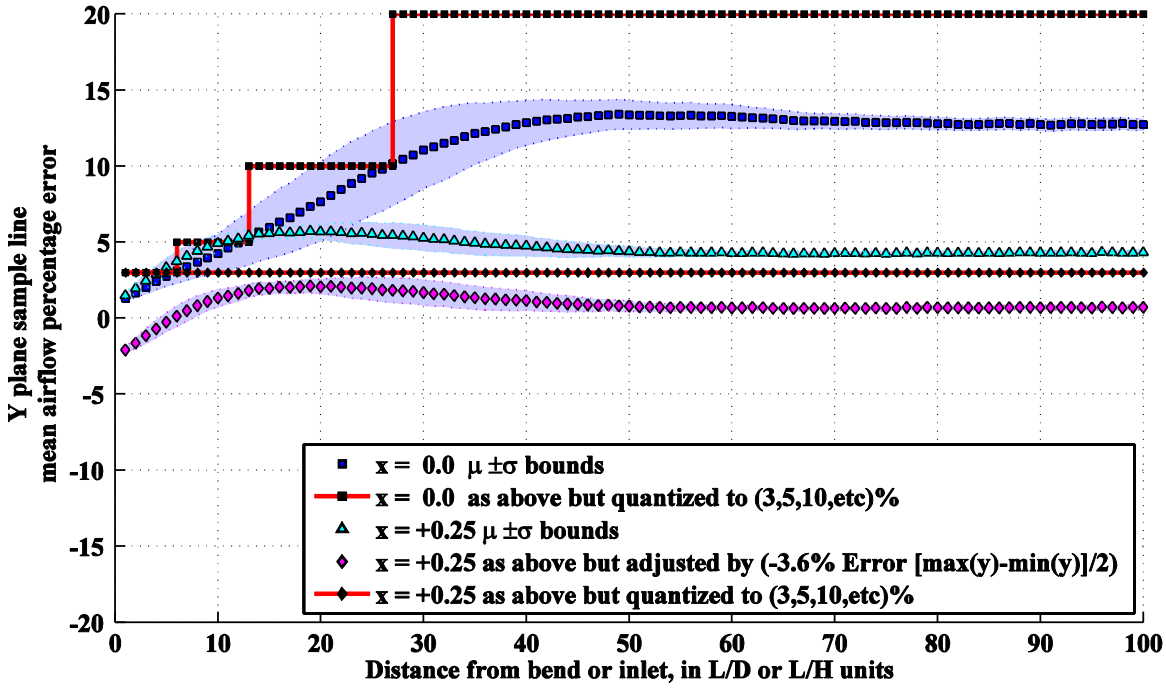

Figure 6.7. Square duct CFD analysis mean total flow vs X = 0, 0.25 path flow percentage error.

The x = 0 measurement plane shows that there is a steady increase in the measurement error from 0% to 13%, at about 50 hydraulic duct diameters in length from the inlet. Where the error percentage plot line, levels out this is described as the fully developed flow profile and observations of duct flow suggest this happens somewhere between 30 and 160 [37], [111] hydraulic duct diameters in length from the inlet. The shaded blue areas illustrate the ± 1 sigma variance of the result. This area represents where 68% of the actual results obtained for that simulation scenario would fall within. The results have been quantized for easier interpretation. The levels chosen represent the typical error thresholds used in HVAC airflow measurement station standards [112], [113] that the measurement would be within. The distance <20 duct lengths and >8, although less than 8 would be an advantage is in the region where the error percentage varies the most, which is not ideal. So a solution is to use a different measurement plane location as shown in Figure 6.3a, which is midway between the wall and the centre of the

duct [114], [104] (p.34). The results show at that this position the variation in the measurement is much less. The fourth line of Figure 6.7 with the diamond shaped markers has an offset calibration adjustment of -3.6% which was calculated by taking, the mean of minimum and maximum measurement values and subtracting this from the measured values. This produces a result which is under the 3% error threshold.

The following Figure 6.8 shows the CFD results for a round duct of 100 hydraulic duct diameters in length, for the same range of duct diameters and airflow velocities as the previous square duct. The error range for the centreline mean flow measurement which is 7% is much reduced compared to the square duct which was 13%. This is thought to be caused by the relatively shorter perimeter of the round duct which also has no acute corners to restrict flow.

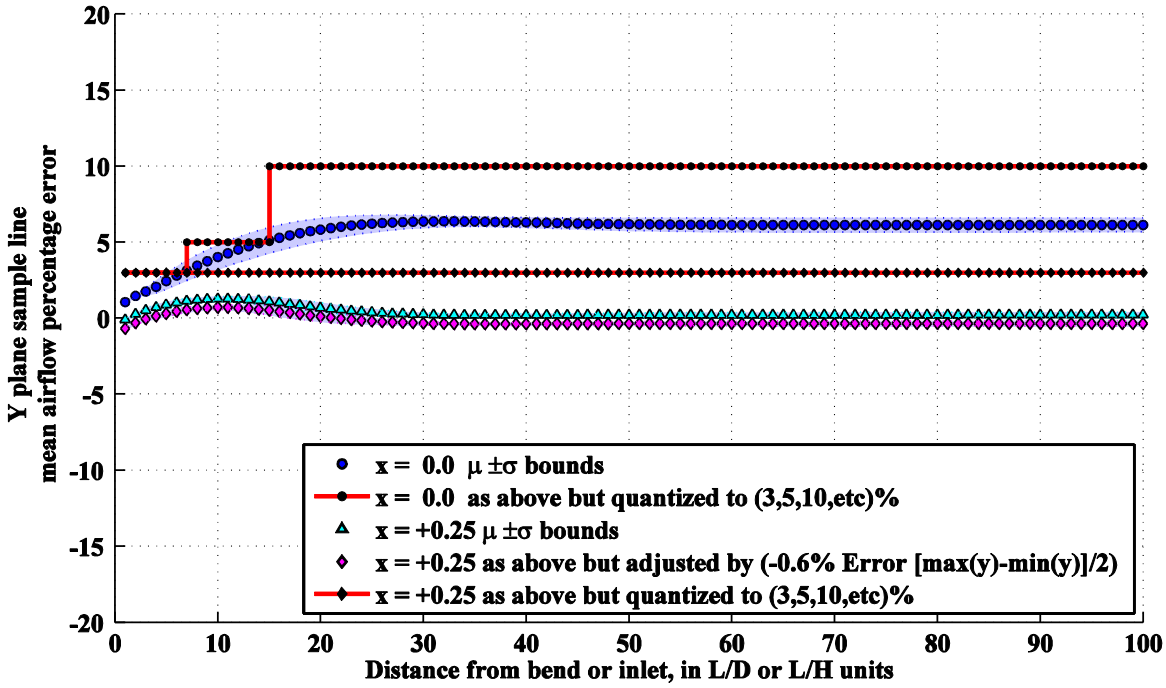

Figure 6.8. Round duct CFD analysis mean total flow vs X = 0,0.25 path flow percentage error.

Similar to the square duct a chordal measurement path has also been simulated, which is positioned at 0.25 duct diameters from the centre of the duct. In reality, this path as shown in Figure 6.3b, [104] (p. 36), [115], would require two more paths to form the shape of an equilateral triangle in the XY plane but also stretched longitudinally along the duct to enable a single sided reflective path configuration to be maintained. This centric sound path has a much reduced error of <2% and possibly could be further reduced by using the difference between this flow measurement and the centreline measurement value to produce corrections.

6.3.2 After a bend/elbow

Scenarios have been simulated using CFD software to determine the three-dimensional flow velocities after a disturbance for a range of flow velocities and duct diameters or widths.

The scenarios tested are as follows:

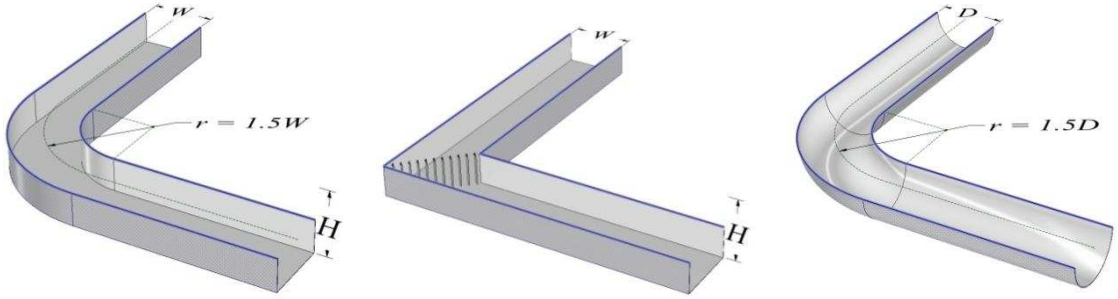

(a) **(b)** **(c)**

Figure 6.9. Duct flow measurement after a bend scenarios; cross sections of ducts.

a) Square duct 90° elbow, smooth radius, without turning vanes, r/W = 1.5.
b) Square duct 90° elbow, mitred, double thickness turning vanes.
c) Round duct 90° elbow, r/D = 1.5.

These scenarios are a subset of the ones used in the European standard EN 14277:2006 [113] for rating the measurement accuracy and sensitivity of fixed airflow rate measurement devices to flow disturbance. This standard is used to classify the minimum distance from a disturbance that the maximum error of below ± 5% and ± 10% can be obtained. The AMCA standard [112], which is also used for rating ventilation fixed airflow measurement devices, states that devices with a measurement cross-sectional area of less than 0.1858 m² shall not deviate by more than ± 3% or by ± 2% if larger. So a reference boundary error threshold of ± 3% has also been annotated on the simulation results.

6.3.2.1 Square duct 90° smooth elbow

The flow magnitude data for a single CFD duct bend simulation which has a duct width of 0.5 m and a mean flow velocity of 12.5 m/s is shown in Figure 6.10.

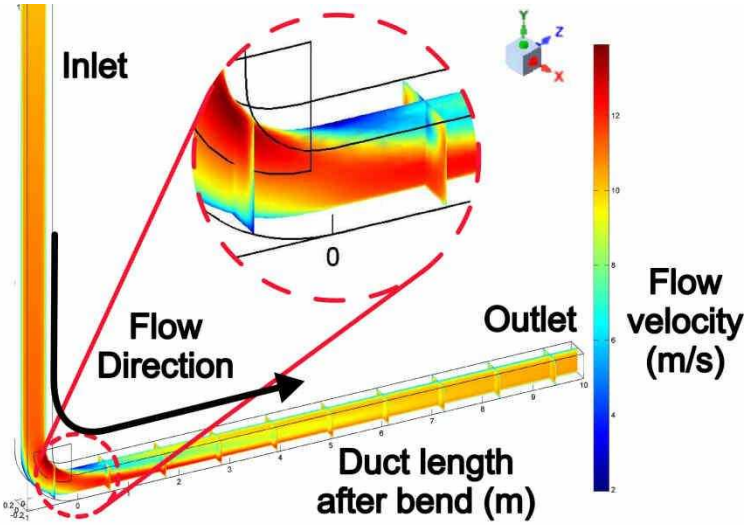

Figure 6.10. CFD flow velocity simulation of a square duct with 90° smooth elbow.

The high-speed flow in the centre of the duct migrates to near the outside wall of the duct after the bend because of the centripetal force due to the change in direction of the air. A secondary flow [116] is created, as more of the flow moves to the outside, it pushes the flow already there, up the sides of the duct. So the peak flow across the y plane moves from the centre of the duct towards the side of the duct.

Further CFD simulations were done on permutations of duct sizes, (0.1,0.3,0.5) m, and flow velocities, (2.5,5.7.5,10,12.5) m/s, as shown in Figure 6.11b. This figure shows the 1 Sigma deviation level across the duct as compared to the mean flow across the whole of the duct cross sectional area.

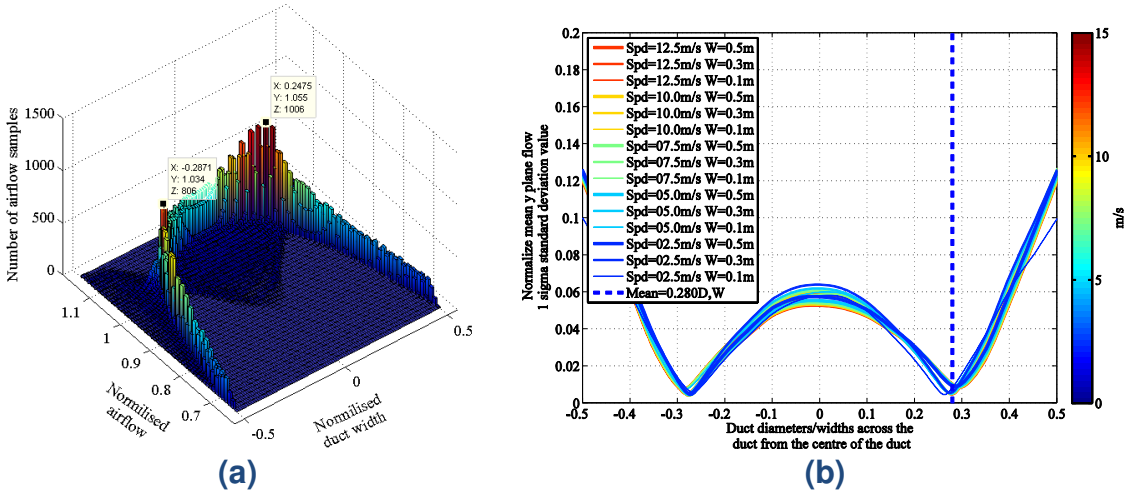

(a) (b)

Figure 6.11. Square duct with round bend upwind, normalised mean and standard deviation of airflow in y plane along z.

a) Histogram of normalised airflow and duct with sample results.

b) Standard deviation of normalised airflow sample results.

The histogram in Figure 6.11a shows the normalised mean airflow velocity for normalised lateral duct width position at each longitudinal duct width position from 1 to 100. The normalised mean airflow velocity is the measured airflow along a path divided by the total duct mean airflow. Normalised duct width is the distance from the duct centreline divided by the actual duct width. The above histogram shows that there is a strong convergence of sample points between ± 0.2 and ± 0.3 duct widths from the centreline of the duct. As shown above in Figure 6.11b there is a point at about ±0.28 duct widths from the centre of the duct where the flow variation at different distances from the bend is much smaller. For example in the worst-case scenario simulated, a duct of 0.3 m width with a flow velocity of 2.5 m/s, the normalised airflow standard deviation in the centre of the duct would be 0.06, compared to 0.01 at the 0.28 duct widths position which would equate to a 80% reduction in error on a calibrated system when placed at this position, compared to measurements taken at the centre of the duct.

The analysed CFD results in Figure 6.12 for the square duct with smooth 90° elbow show a large deviation of up to -14% for the centreline mean results closer than 8 duct lengths to the end of the bend.

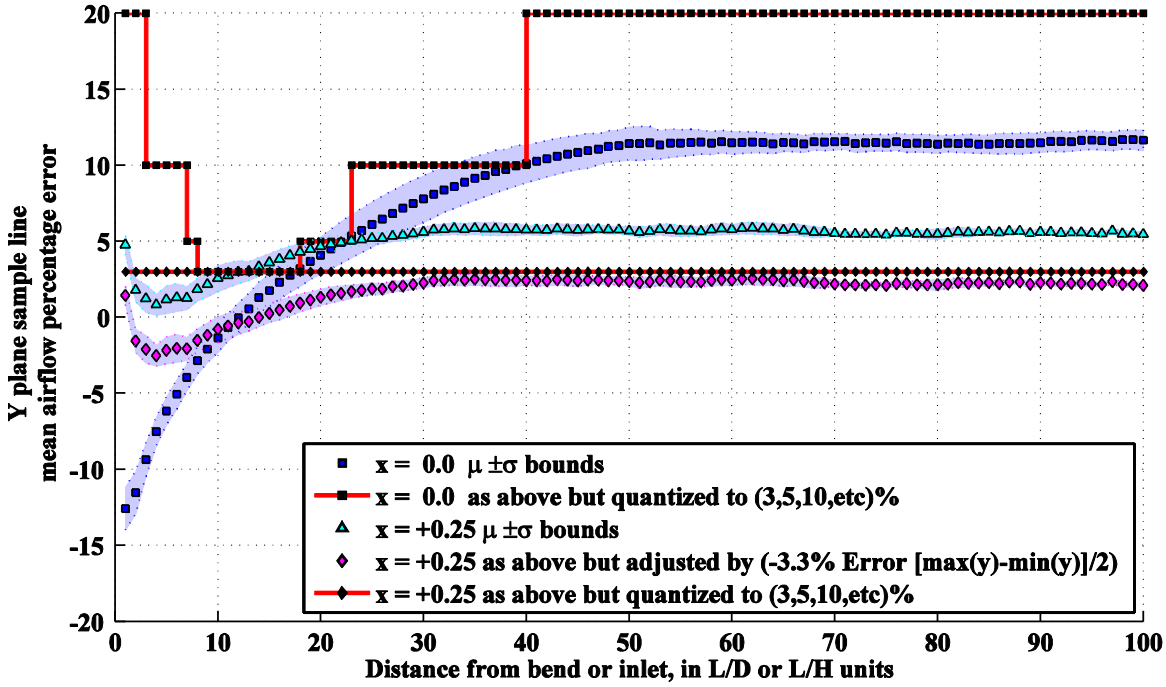

Figure 6.12. Square duct with 90° smooth elbow, CFD analysis, mean total flow vs X = 0, 0.25 path flow percentage error.

The results for duct lengths value >8 followed a similar curve as the straight square duct results shown in Figure 6.7 and reach developed flow at about the same distance even though the flow profile is distorted after the bend, compared to the inlet flat profile of the straight square duct CFD simulation. The $+0.25D$ off

centre line results are below the 3% error boundary for the whole of the range analysed.

6.3.2.2 *Square duct 90° elbow with turning vanes*

The flow magnitude data for a single CFD duct bend simulation which has a duct width of 0.5 m and a mean flow velocity of 12.5 m/s is shown in Figure 6.13.

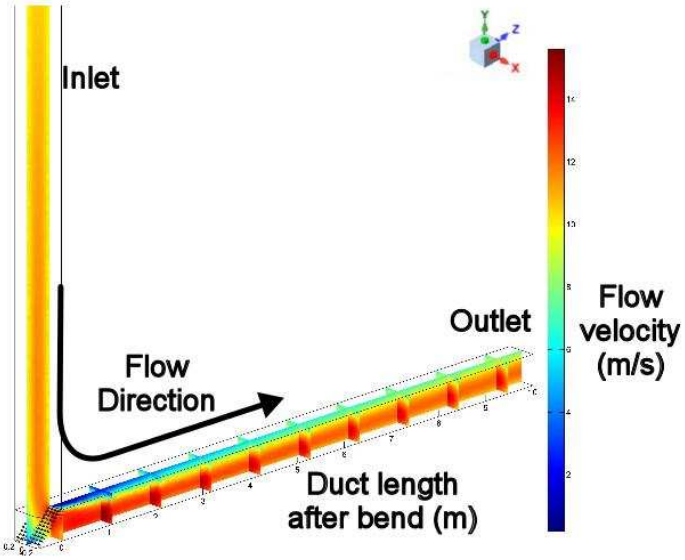

Figure 6.13. CFD flow velocity simulation of a square duct with 90° mitred bend with double thickness turning vanes.

Similar to the square duct with 90° smooth elbow the high-speed flow in the centre of the duct migrates to near the outside wall of the duct after the bend. Further CFD simulations were done on permutations of duct sizes, (0.1,0.3,0.5) m, and flow velocities, (2.5, 5) m/s, as shown in Figure 6.14b. The reduced flow velocity range is due to CFD solutions not converging possibly because of the extra meshing required for the turning vanes, making this scenario more difficult to solve.

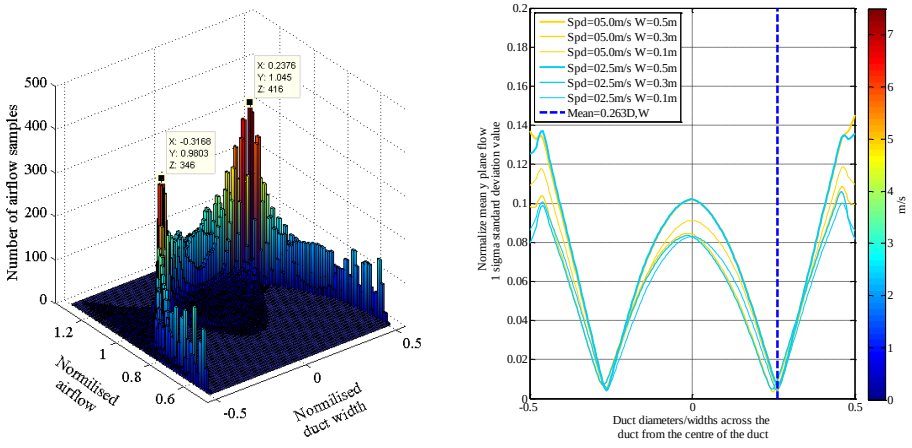

(a) (b)

Figure 6.14. Square duct with 90° mitred bend with double thickness turning vanes, normalised mean and standard deviation of airflow in y plane along z.

a) Histogram of normalised airflow sample results.

b) Standard deviation of airflow sample results.

As shown above there is a point which is about 0.263 duct widths from the centre of the duct where the flow variation at different distances from the bend is much smaller. For example in the worst-case scenario simulated, a duct of 0.5 m width with a flow velocity of 2.5 m/s, the standard deviation in the centre of the duct would be 0.1, compared to 0.01 at the 0.263 duct widths position which would equate to a 90% reduction in error on the calibrated systems when placed at a range of positions along the duct.

The analysed CFD results in Figure 6.15 for the square duct with turning vanes show a large deviation of up to -20% for the centreline mean results closer than 15 duct lengths to the end of the bend. These results of are only below the 3% error rate for between 15 and 23 duct lengths after the bend.

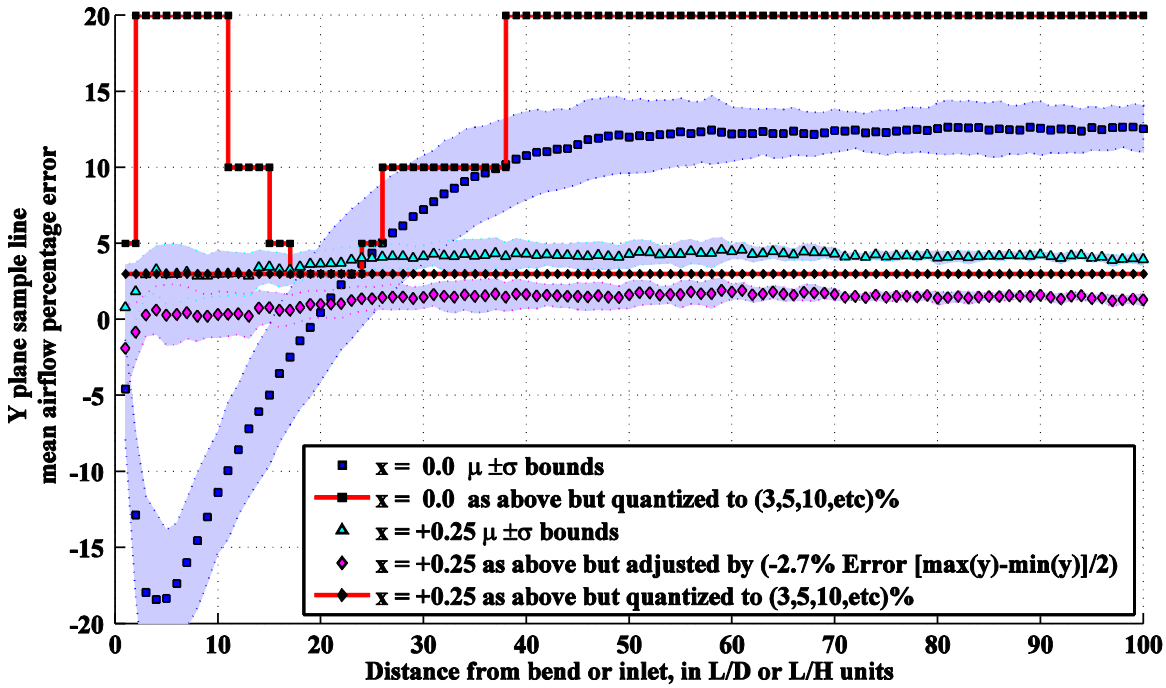

Figure 6.15. Square duct with 90° mitred bend and turning vanes, CFD analysis, mean total flow vs X = 0,0.25 path flow percentage error.

6.3.2.3 Round duct 90° elbow

The flow magnitude data for a single CFD duct bend simulation which has a duct width of 0.5 m and a mean flow velocity of 12.5 m/s is shown in Figure 6.13.

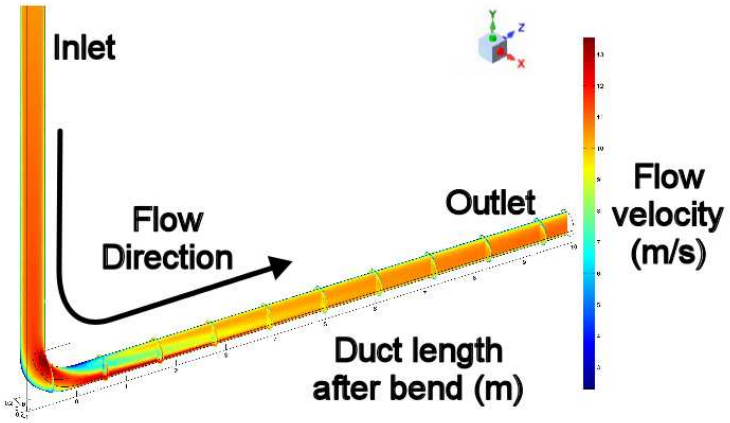

Figure 6.16 CFD flow velocity simulation of a round duct bend

Similar to the previous bend scenarios, the flow after the bend is diverted from the centre of the duct to the sides. As shown below in Figure 6.17b there is a point at about 0.21 duct widths laterally from the centre of the duct where the flow variation at different distances from the bend is much smaller.

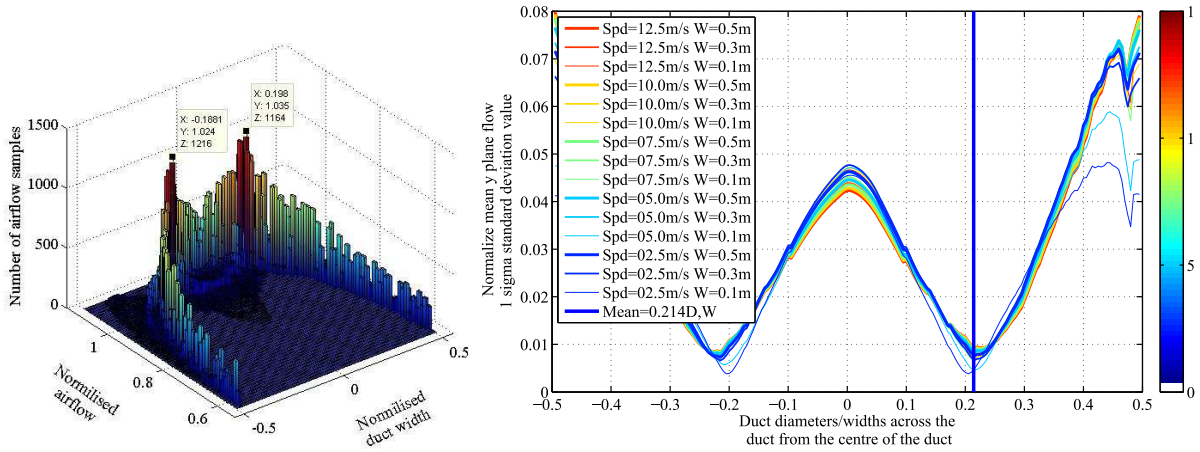

(a) (b)

Figure 6.17. Round duct with bend, normalised mean and standard deviation of airflow in y plane along z.

a) Histogram of normalised airflow sample results.
b) Standard deviation of airflow sample results.

For example in the worst-case scenario simulated, a duct of 0.3 m width with a flow velocity of 2.5 m/s, the standard deviation in the centre of the duct would be 0.045, compared to 0.01 at the 0.21 duct widths position which would equate to a 75% reduction in error on the calibrated systems when placed at a range of positions along the duct. As shown in Figure 6.18 there is a large deviation of up to -17% for the centreline results closer than 8 duct lengths are to the bend.

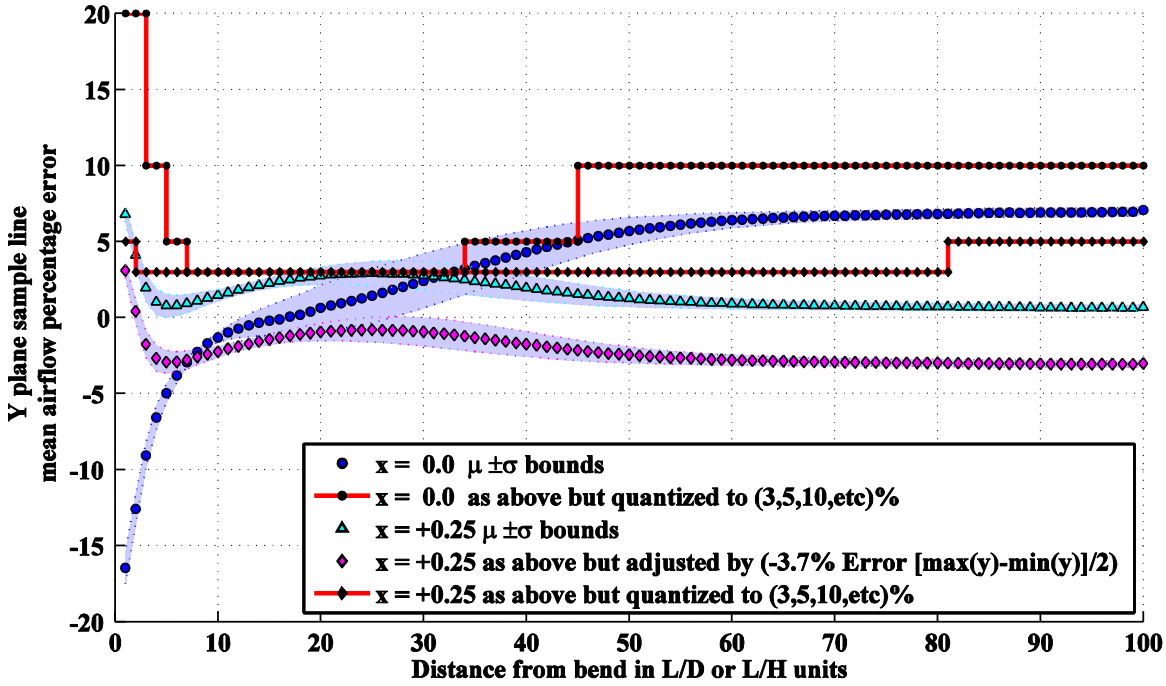

Figure 6.18. Round duct with bend, CFD analysis, mean total flow vs X = 0,0.25 path flow percentage error

The centreline results do stabilise eventually but this takes about 70 duct lengths to happen, which is a much longer distance then the straight round duct CFD simulation results in Figure 6.8 which was about 30 duct lengths. Although the round duct centreline results are better than both of the square duct centreline scenario results, the 0.25 D offset position results are not as good as the corresponding square duct results. The 0.25 D offset position calibrated results at <3 or > 81 duct lengths are in the 5% error region.

6.3.3 Conclusion for CFD results

Table 6.1 below shows a summary of the percentage error results against the duct total mean flow.

Table 6.1. Summary of results for CFD duct scenarios.

Description of duct scenario	x = 0		x = +0.25	
	@ 100 L/D,L/H	max error 1-100 L/D,L/H	@ 100 L/D,L/H	max error 1-100 L/D,L/H
Round straight	+7%	7%	<2%	<2%
Round 90° elbow	+7%	-17%	4%	-4%
Square straight	+13%	14%	<1%	+3%
Square 90° elbow, smooth radius	+12%	-14%	<3%	-3%
Square 90° elbow, turning vanes	+15%	-20%	<3%	-3%

The fully developed centreline path mean flow to duct total mean flow error is better for the round duct at 7% then the square duct at 13%. The 0.25 duct diameter/width offset position calibrated results for the square and round straight

length of the duct are within the 3% error region and so are both the calibrated results for the square duct bend scenarios. The round duct bend 0.25 *D* offset calibrated results are slightly above the 3% region just after the bend for three duct lengths and then again after 81 duct lengths. So for centreline results the round duct is better. The square duct is better for measurement of disturbed flow profiles using the ± 0.25 duct widths centreline offset position.

6.4 MATLAB 3D Ultrasonic In-Duct Flowmeter Monte Carlo Ray/Particle Tracing Simulation.

As using finite element analysis (FEA) software like COMSOL to do the acoustic simulation would have taken a long time to process and required a computer system with a larger amount of memory than was available. It was decided that this method was probably unworkable. So acoustic ray tracing was investigated and a solution was developed which used Matlab to produce a Monte Carlo type simulation of a random distribution of particles which are released from the central transducer at the calculated speed of sound and are reflected by the duct boundary when a collision is detected as shown in Figure 6.19.

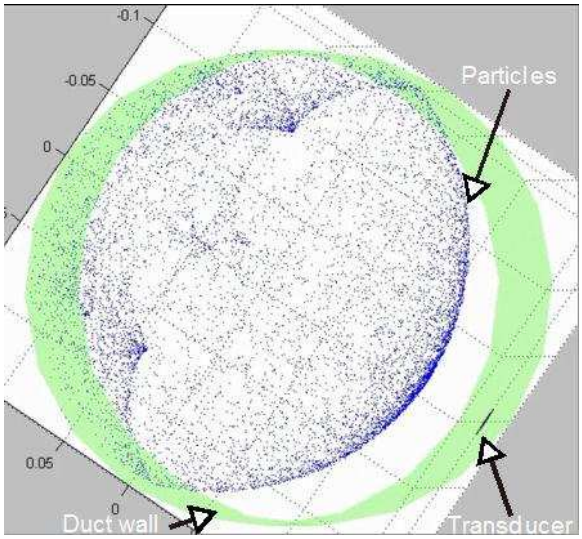

Figure 6.19. 3D ultrasonic in-duct flowmeter Monte Carlo ray/particle tracing simulation using Matlab.

This model was adapted by the author from Matlab code, which was originally developed by Prof Sean Danaher and used for generating what would be the expected receive signal waveform in acoustic ultra-high energy neutrino telescopes [117]. The number of particles detected at each receiver for each timeslot is recorded in a histogram, which is then multiplied by the transducer transmit waveform using the Matlab digital filter function to produce a representation of the receiver signal for each transducer. A more detailed description of this code, which is listed in Appendix E, is given in Section 6.5.

6.5 Flowmeter Monte Carlo Ray/Particle Tracing Simulation Software Program Description.

The Matlab code, which is listed in Appendix E.2, uses a modified version of the acoustic ray tracing method to simulate the effects of duct airflow profile variation on the measurement accuracy of a single reflective acoustic path flowmeter. The upwind and downwind path are both simulated simultaneously as shown in Figure 6.20 The upwind receiver face is green and the downwind is blue with the transmitter being black.

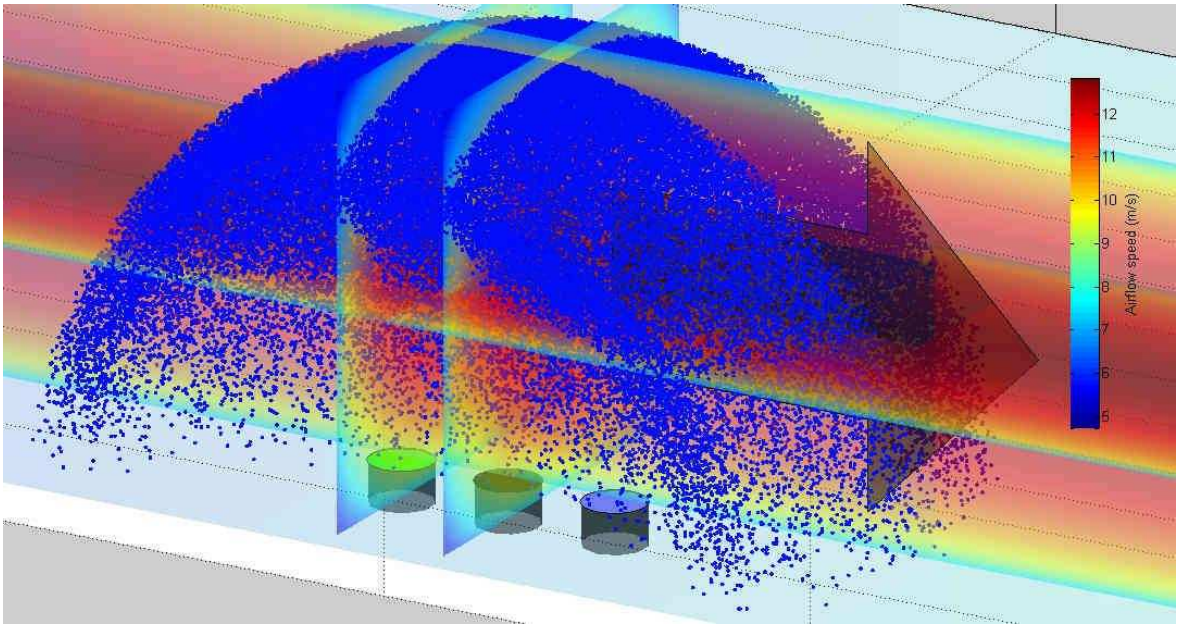

Figure 6.20. Visualisation of a ultrasonic in-duct flowmeter Monte Carlo ray/particle tracing simulation of a square duct.

Square and round profile ducts are supported in this code by allocating "squ" or "cir" to the "sim_type" constant. Figure 6.21 shows the Excel xlsx format for the three-dimensional flow velocity data.

J10

	A	B	C	D	E	F	G	H
8								
9	x	y	z	umps	vmps	wmps	Umean	Dwidth
10	-0.048	-0.048	0	-0.03298	-0.03298	9.113499	10	0.1
11	-0.046	-0.048	0	-0.02608	-0.02831	9.400289	10	0.1
12	-0.044	-0.048	0	-0.01865	-0.02355	9.64062	10	0.1
13	-0.042	-0.048	0	-0.01684	-0.02638	9.631682	10	0.1
14	-0.04	-0.048	0	-0.01736	-0.02821	9.615278	10	0.1

D=0.1m Um=10mps | D=0.3m Um=10mps | D=0.5m Um=10m

Figure 6.21 Import format of three-dimensional flow velocity data.

The data is required to start at location A10. The variables *x*, *y*, and *z* are the position coordinates in meters of the Cartesian flow velocity vector in m/s described by *umps*, *vmps* and *wmps*. The variable *z* is the longitudinal duct

position coordinate which starts at 0 to represent the inlet of duct under test. The variable *x* represents the vertical dimension and *y* is the horizontal dimension, which are both at zero in the middle of the cross-sectional face of the duct along the *z* dimension. The variable *Umean* is the mean velocity along the duct and *Dwidth* is the width or diameter of the duct. The program then converts the data from each sheet of the spreadsheet to a Matlab .mat file so that when the program is run again using the input filename, It can be more quickly loaded into the workspace.

The following are constants, which need to be entered by the user in the program code; `Z` which is the longitudinal distance between the transducers; `Tranducer_height_above_inner_duct` is the height above the duct wall of the transducer circular transmit face which needs to be greater than zero so that the particles are transmitted inside the duct. `Tranducer_radius` is the radius of the transducer. `TempC` is the air inlet temperature in degrees C used to calculate the speed of sound. `Hits_required` is the total number of hits on the receiver required before the simulation runs for the duct longitudinal location will cease. `Plus_minus_percent_toi` is the percentage deviation of the calculated time of arrival for the acoustic pulse, for which particles that are expected to arrive outside this time are not simulated so increasing the simulation speed. `theta_range` is the horizontal angle range in degrees centred on the transmitter longitudinal axis and this is also used to limit the number of particles. `Fsamp` is the simulation frequency of the minimum time step. `Min_duct_sim_step_num` is approximately the minimum number of steps the simulation is allowed to use to cross the duct and get back to the receiver. The number of simulation steps is always much higher than this number because the step size is randomised so that the flow velocity sample points are different on each run of the simulation.

The start positions of the particles which represent the acoustic signal wavefront are distributed evenly across the transducer face. The particles are emitted in a Lambertian distribution, but this can be modified in the code to make the beam width narrower. Some of these particles are then filtered out, depending on parameters set at the beginning of the code. As the particle travels by stepping through the medium on its initial trajectory, the three-dimensional flow data is interpolated and the positional change caused by the flow velocity is processed.

If the particle goes past a duct boundary then that particle is flagged for reflection to be carried out. The reflection process is very simple on the square duct. The

velocity vector, which is perpendicular to the boundary is simply reversed and the position is reflected about the boundary as well. The reflection process for the circular duct is more complicated. The whole simulation time step size is reduced to a minimum if any particle is detected within the distance that it could possibly go beyond the duct boundary on the next simulation step. The reflection is calculated using the normal vector of the duct wall.

The particle is then ready to be detected by the receiver transducer. This is done by checking the positional coordinates within the detector boundary. To improve timing accuracy the magnitude of the distance past the detector is use to calculate the time required to travel that distance so it can be deducted from the previous time of arrival. The particle time of rivals are then collated into a histogram, where each bin is the size of the reciprocal of simulation sample frequency.

The transducer receiver waveform is generated by using a digital filter function which uses the transmit waveform shape as a transfer function. The time delay between the two receiver signals can then be calculated using various techniques such as cross correlation and therefore calculate the simulated flowmeter velocity reading as shown in Figure 6.22.

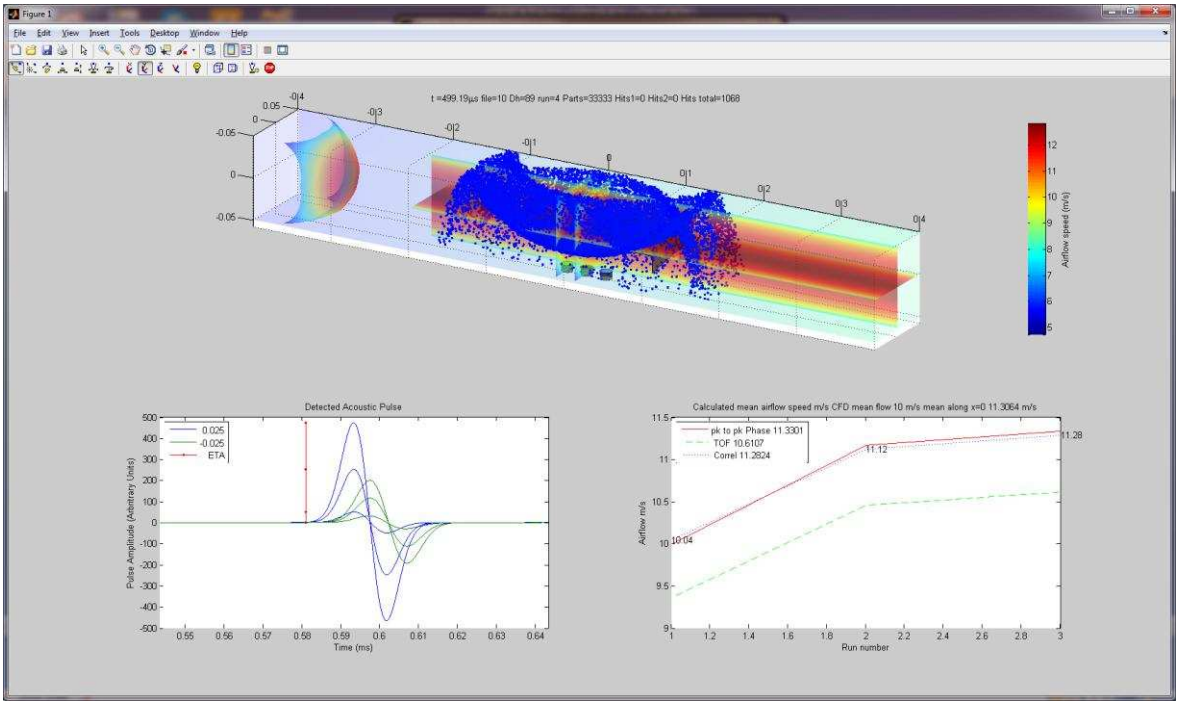

Figure 6.22 Ultrasonic in-duct flowmeter simulation showing flow velocity results.

The program, then outputs this data to an Excel spreadsheet for further post processing by another Matlab program to produce the graphs, as shown in Figure 6.23.

6.6 3D Ultrasonic In-Duct Flowmeter Monte Carlo Ray/Particle Tracing Simulation Results

The following section show the results of the Monte Carlo ray/particle simulation, compared to the CFD analysis as used in the previous Section 6.3. The error percentage shown is between the duct total mean flow velocity and the CFD centreline acoustic path mean flow value or the Monte Carlo particle simulation results for the same acoustic path. The distance from the duct bend for the simulation is selected by using the unique numbers of the Fibonacci sequence and 100 for the end of the range value. This was done because it would've taken much more time to simulate every duct width point along the longitudinal direction of the duct so a compromise is to use a sequence which is similar to the rate of change in the CFD mean centreline flow velocity values.

6.6.1 Straight duct lengths

6.6.1.1 Square duct

Figure 6.23 shows the square duct Monte Carlo particle simulation results represented by the dark blue square markers is similar to the CFD centreline mean velocity flow results represented by the light blue triangles. This shows that the simulation in this case is performing well and producing consistent results which have strong correlation with the CFD results.

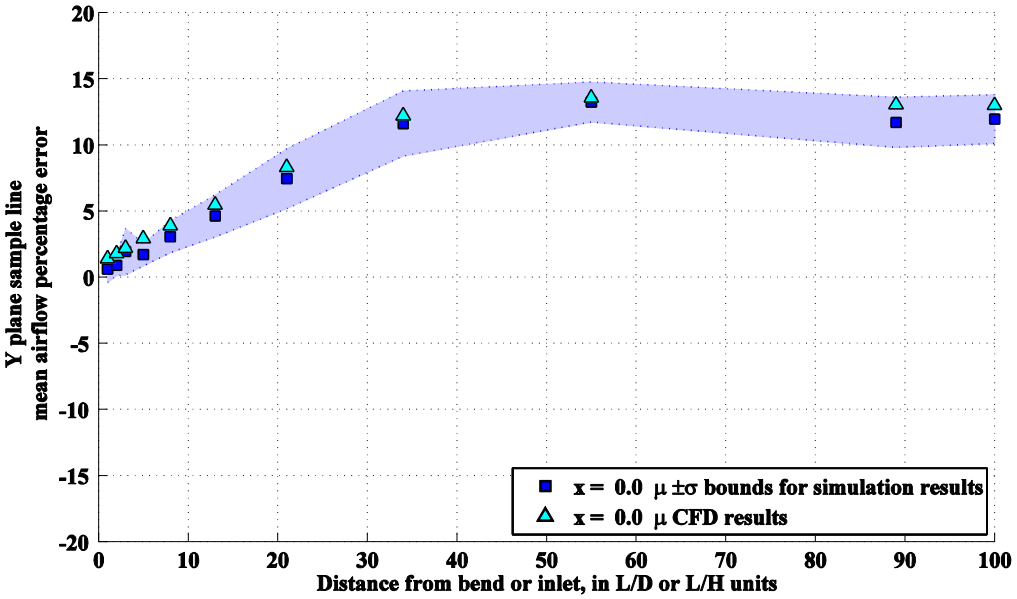

Figure 6.23. Square duct Monte Carlo particle simulation vs CFD analysis mean total flow at X = 0 path flow percentage error.

6.6.1.2 *Round duct*

Figure 6.24 also shows there is a strong correlation between Monte Carlo particle simulation and the CFD results for the straight round duct test scenario.

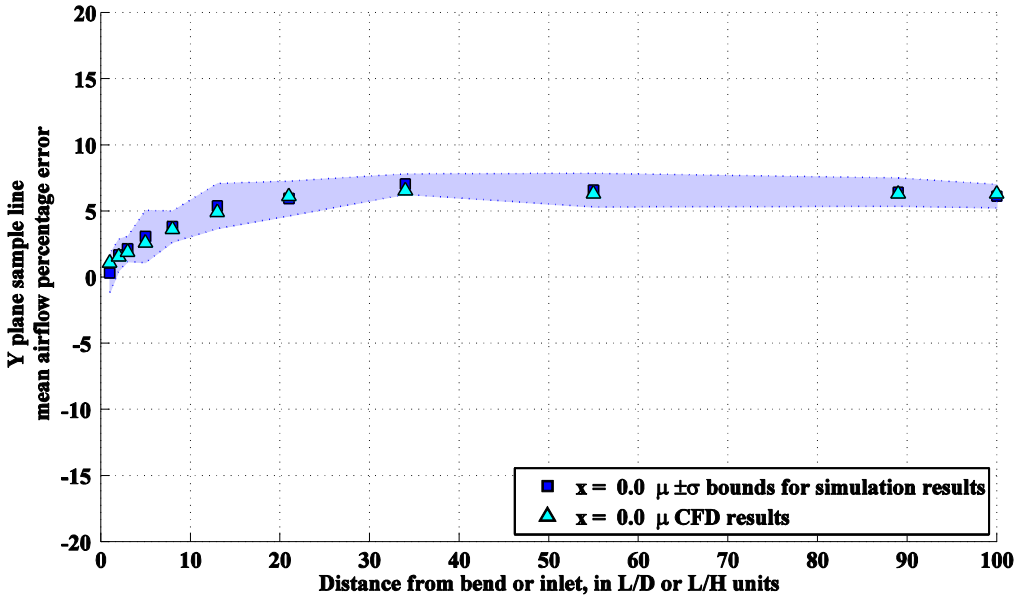

Figure 6.24. Round duct Monte Carlo particle simulation vs CFD analysis mean total flow at X = 0 path flow percentage error.

6.6.2 After a bend/elbow

6.6.2.1 *Square duct 90° smooth elbow*

Figure 6.25 also shows there is a strong correlation between Monte Carlo particle simulation and the CFD results for the square duct with 90° smooth elbow test scenario.

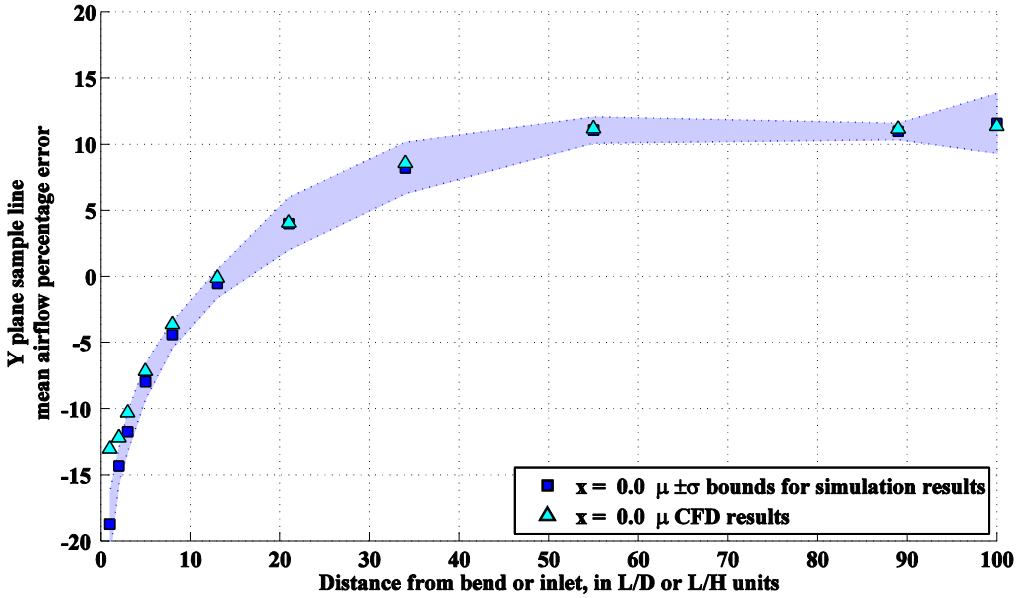

Figure 6.25. Square duct with 90° smooth elbow, Monte Carlo particle simulation vs CFD analysis mean total flow at X = 0 path flow percentage error.

6.6.2.2 *Square duct 90° mitred elbow with turning vanes*

Figure 6.26 also shows there is a strong correlation between the Monte Carlo particle simulation and the CFD results for the square duct with a 90° mitred elbow and turning vanes test scenario.

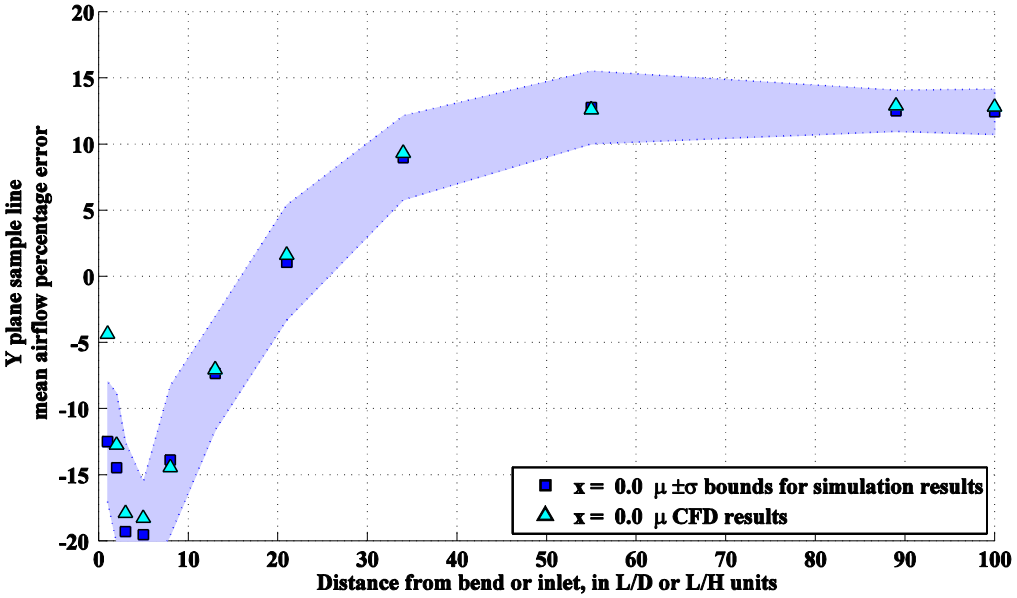

Figure 6.26. Square duct with 90° mitred bend and turning vanes, Monte Carlo particle simulation vs CFD analysis mean total flow at X = 0 path flow percentage error.

6.6.2.3 *Round duct 90° elbow*

Figure 6.27 also shows there is a strong correlation between the Monte Carlo particle simulation and the CFD results for the round duct with a 90° elbow test scenario.

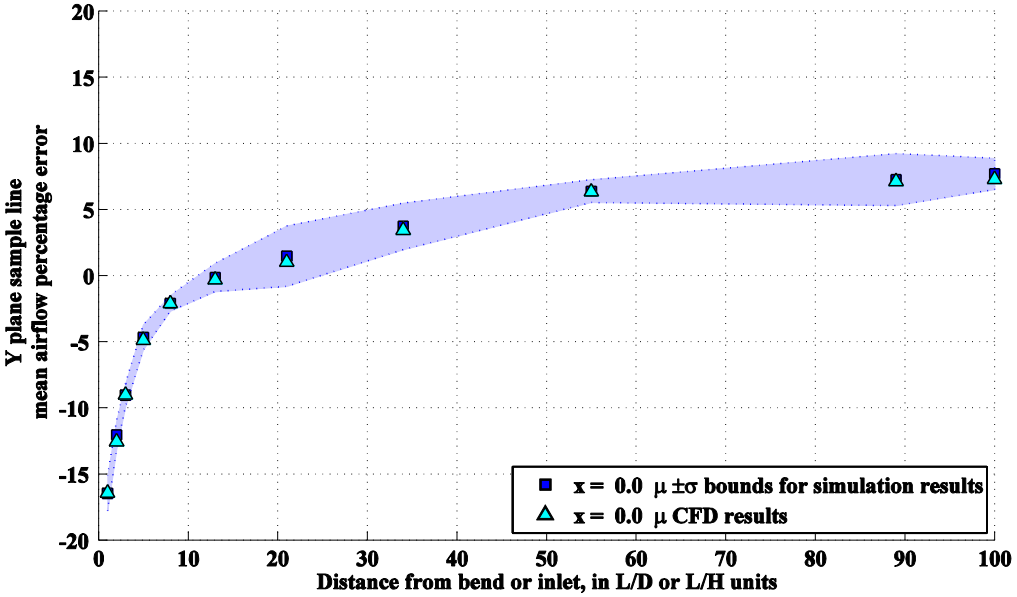

Figure 6.27. Round duct with bend, Monte Carlo particle simulation vs CFD analysis mean total flow at X = 0 path flow percentage error.

6.6.3 Conclusion for Monte Carlo particle simulation results

All of the five duct scenario results for the Monte Carlo particle simulations show that there is a strong correlation with the centreline CFD mean flow velocity analysis. This shows that the simulation in all cases studied, performed well and produced consistent results.

6.7 Summary of Chapter 6

This Chapter describes the results using CFD simulation software to model the flow for ducts of various sizes and airflow velocities with and without bends. The author has determined that if the airflow velocity is measured across the centre line of the duct then the error can be as high as 7% for the round duct and 13% for the square duct. A solution to reduce these errors is proposed by the author, which is to mount the ultrasonic transducers using a 0.25 duct diameter/width offset position. Analysis of the CFD data suggests that this error would be reduced to below 3%.

When a bend is introduced into the duct CFD simulation at a position before the measurement position and the sampling traverse path is aligned parallel to the inlet section axial path of the duct, then the airflow velocity error measured across this path can be as high as 17% for the round duct and 20% for the square duct but using the 0.25 duct diameter or width offset position, the amount of error can be reduced to as little as 4%. This means that the ultrasonic flowmeter could be placed greater than 1 hydraulic diameter after the bend and still achieve reasonable results according to the simulations.

A Matlab Monte Carlo particle simulation program that simulates acoustic flowmeter in round and square ducts is described and results show that there is a strong correlation with the centreline CFD mean flow velocity analysis which shows that the simulation in all cases studied is performing well and producing consistent results.

Chapter 7.

CONCLUSIONS

In this chapter:

7.1 Research aims

The research topic, which was to investigate and develop a practical low-cost device for measuring HVAC air flow rate and energy throughput was chosen for the following reasons, which are also set out in Chapter 1.

At the beginning of this study, long-term energy costs were increasing, for example UK industrial fuel prices had increased by 118% [1] (p. 37) in the 10 year period from 2004. Recently the price of crude oil which all fuel prices are generally driven by [1] (p. 37) has dropped rapidly from $109 in 2014 to under $32 and then back up again to just under $50 by June 2016. So far this has yet to affect domestic dual fuel bills by anywhere near the percentage drop of the crude oil fuel price with most bills only reducing by about 5% [118] . The impact on rising cost of fossil fuels and the global community awareness of the environmental effects of increasing levels of greenhouse gases have incentivised innovation in the renewable energy generation and conservation sector. Domestic and industrial property owners are now more likely to consider fitting energy-saving options and renewable energy generation systems as it becomes more viable because of the shorter payback times, which can be due to the following factors; rising cost of energy, lowering cost of implementation and the introduction of government incentive schemes. The UK government has a scheme called the renewable heat incentive which supports air-to-water heat pumps but does not support air-to-air heat pumps because they have not found a adequate way of metering the usable heat [6] (pp. 40-41). They also acknowledge that it is important to have the right strategy for supporting air-to-air source heat pumps because of the large number already installed for cooling (air conditioning) purposes. Tran *et al.* [3] also report

that there was no reliable method of measuring the seasonal performance of an air- to-air heat pump as they found it was difficult to measure airflow rate and the air enthalpy over a long period of time.

Buildings with ever higher levels of insulation and air tightness are being specified which is requiring the installation of ventilation systems to provide the minimum number of air changes and also reduce energy usage by recovering the heat or cooling energy from the air before it is expelled. In the future this will necessitate the need for monitoring of the operating performance of these systems so that air quality or building energy efficiency [7], [8] is not detrimentally affected. The World Health Organisation (WHO) has stated that "globally, 4.3 million deaths were attributed to household air pollution (HAP) in 2012" of which 99,000 are in Europe [11]. The main medical conditions which are affected by indoor air pollution are stroke, ischaemic heart disease, chronic obstructive pulmonary disease (COPD), lower respiratory disease and lung cancer. Chemicals such as formaldehyde, which can be omitted by furniture and other materials can irritate the lungs. Also particulates and nitrogen oxide from heating and cooking appliances can damage the lungs or heart and increase a person's sensitivity to allergens already in the home. It is suggested by the Royal College of Physicians (RCP) in their 2016 report called "Every breath we take: the lifelong impact of air pollution" that possible solutions to this problem is maintenance of good ventilation and reducing pollution sources which could be done by introducing emission standards/limits [12] (p.26).

The aim of this research was to develop a sensor system that was practical and low-cost which could measure the amount of energy transferred through a ventilation duct by measuring the airflow velocity, temperature and humidity of the air travelling through the duct.

7.2 Achievements

Designed and tested an in-duct ultrasonic airflow measurement device in a round and square duct which when compared to a Venturi flowmeter had an accuracy better than 3.5% RMS, which the results of are presented in Chapter 5. An account of this study for just the airflow measurement is published [13] in Sensors, which is an open access journal which is ranked 10th out of the 56 journal titles listed by the Thomson Reuters Corporation in the instruments and instrumentation science category.

Conducted a review into the current research and technology suitable for the measurement HVAC airflow rates.

Assembled and configured all apparatus required to measure the airflow rate for calculating the accuracy of the ultrasonic airflow meter under test. This was done using a short form Venturi and an electronic differential pressure meter from which the data was then processed by a LabVIEW program developed by the author to measure the airflow rate and energy throughput.

Developed and created a real-time temperature monitoring system using LabVIEW to measure enthalpy and calculate air density using an existing datalogger which was at the time non-compatible with LabVIEW. Constructed a sensor network to monitor DHT11 capacitive humidity sensors and DS18S20 temperature sensors in real-time.

Conducted CFD simulations on various sizes of square and round ducts before and after a 90° bend in the duct to analyse the affect the flow profile would have on the ultrasonic flowmeter designed by the author in this study.

Developed a MATLAB 3D acoustic in-duct flowmeter Monte Carlo ray/particle tracing simulation program which can simulate acoustic flowmeters in a square or round duct and the effects of a three-dimensional flow profile on the transducers received acoustic signal.

7.3 Conclusion

The proof of concept in-duct ultrasonic flowmeter developed by the author has a very good accuracy of better than 3.5% RMS over the range of flow velocities tested. The range of airflow velocities used in the test was limited by the output of the inlet fan to between 2 m/s and 3.25 m/s for the 250 mm diameter circular duct and 8 m/s to 12.25 m/s for the smaller 100 mm wide square duct. If further testing is conducted in the future, a fan with the capability of supplying a steady flow velocity of at least 10 m/s in the circular duct would be recommended. The lower range of airflow velocities were not tested at this time, because as shown in Figure 3.6, a drop in flow velocity severely affects the accuracy of the reference airflow measuring device which was the Venturi tube with a ±1 Pascal accuracy manometer. A manometer with an accuracy of ± 0.1 Pascal or better would be preferred for measuring lower airflow velocities but could not be obtained by the author, due to the cost of the device and the budget available.

The CFD simulations show that approximately the equivalent length of 50 duct widths for the straight square duct and 30 duct diameters for the straight round duct from the inlet are required to achieve a fully developed flow profile. This is more than the suggested minimum 7.5 hydraulic diameters recommended as the measurement distance from a disturbance, which is fully described in Section 6.3. Analysis of the CFD data suggest that if the airflow velocity is measured where the duct flow profile is fully developed then the measurement error of the mean flow velocity across the centre line of the duct, compared to the total mean flow can be as high as 7% for the round duct and 13% for the square duct. The CFD simulation data suggest that the 3.5% RMS error achieved during testing was due to the ultrasonic flow meter being only being 9 to 12 duct widths or diameters from the outlet of the Venturi. This meant that the flow profile could not have been fully developed, therefore if the flowmeter had been installed further away from the Venturi the error should have been greater as the flow profile becomes more developed due to the duct wall friction. A device which measures the mean centreline flow velocity could be still useful in applications such as measuring the airflow rate of an air intake for a internal combustion engine or at the inlet for a HVAC system as the flow profile will be flatter near the inlet.

For other situations the CFD simulation data suggest that the ultrasonic flowmeter should be offset from the centreline of the duct by ± 0.25 duct diameters or widths. This could reduced the error for the flowmeter to below 4% for any duct scenario described in this thesis, which even includes locations as close as a single duct diameter or width after a bend. A square or rectangular duct is ideal for this configuration as the opposite duct wall reflects the acoustic signal better than the circular duct. Greater accuracy could be obtained by installing another ultrasonic flowmeter on the same side of the duct wall at the other 0.25 duct width position for situations where the flow profile is not symmetrical.

Testing of the energy throughput measurement capability of the device was not carried out to the full satisfaction of the author, due to time constraints. The author suggest that if testing was to be redone then the heat loss between the reference airflow measurement device and the ultrasonic airflow measurement device should be minimised by insulating the outside of the duct and minimising the distance between the devices. Also the ultrasonic flowmeter could be placed directly before the Venturi as the ultrasonic flowmeter would not significantly effect the flow profile.

7.4 Original contribution to knowledge

Designed and tested a ventilation duct airflow measurement device for round or square ducting using an ultrasonic differential transit time method with the following features. The transducers are mounted together on the same side of the round or square duct so that the critical distance between the transducers cannot be altered so reducing errors caused by incorrect installation and also making the installation simpler.

Square wave pulses are used which are less costly to produce than a sinusoidal burst waveform because a DAC device is not required in the circuit. An anti-phase transmit pulse technique is used to reduce transducer ringing, which reduces minimum duct diameter distance and allows increased sensor update rate.

Receiver signal processing complexity is reduced by using a selection of zero crossing points at a time window determined from the duct airflow temperature which produces reliable results.

Developed a MATLAB 3D acoustic in-duct flowmeter Monte Carlo ray/particle tracing simulation program which can simulate acoustic flowmeters in a square or round duct and the effects of a three-dimensional flow profile on the transducers received acoustic signal.

Using the CFD data of square or round duct airflow after a bend. Analysed the mean flow across the centre line at various distances from the bend to calculate the percentage error compared to the total mean flow of the duct.

Provided and analysed a solution to the large centreline flow measurement errors in square and round ducts of up to 20% after a bend by offsetting the measurement from the centreline by 0.25 duct widths or diameters, which reduces the error to <4% for all duct scenarios analysed.

7.5 Future work

In the future the design could be further improved by the following:

Integrating into the system, a capacitive humidity sensor with an accuracy better than the ±5 %RH accuracy of the DHT11.

Extensive testing on a wider variety of duct sizes and duct shapes, such as rectangular with a greater range of airflow velocities, temperatures and water vapour content amounts.

Experimental testing of the device when fitted in close proximity to disturbances such as bends in different types of duct shape and with turning vanes, where appropriate, and corroborate the computer modelling.

Experimental testing of the 0.25 duct widths or diameters offset solution proposed for improving errors caused by the developing flow profile and flow disturbances such as bends at various distances from the disturbance or inlet.

Extending the airflow measurement range by improving the phase measurement of the received signals to beyond ± 180°.

Add calibration corrections required for inaccuracies caused by duct airflow profile.

Add corrections for humidity change which slightly affect the speed of sound.

Appendix A. 400EP14D Ultrasonic Transducer Datasheet.

Air Ultrasonic Ceramic Transducers — 400EP14D

Asymmetric Beam Patterns

Specification

400EP14D	Transceiver
Center Frequency	40.0±1.0KHz
Bandwidth (-6dB FOM)	1.0KHz
Transmitting Sound Pressure Level at resonant frequency;0dB re 0.0002μbar per 10Vrms at 30cm	103dB min. (Transducer alone)
Receiving Sensitivity at resonant frequency 0dB = 1 volt/μbar	-78dB min. (Transducer alone)
Nominal Impedance (Ohm)	1000
Ringing (ms)	1.2 max.
Capacitance at 1KHz ±20%	1600 pF
Temperature Compensated Type	3200 pF
Max. Driving Voltage (cont.)	20Vrms
20 bursts, 25ms repetition rate	100Vpp
Total Beam Angle -6dB Wide	135° typ.
Total Beam Angle -6dB Narrow	85° typ.
Operation Temperature	-30 to 70°C
Storage Temperature	-40 to 80°C

All specification taken typical at 25°C
Both lead pins and lead wires output are available

Models available:

1	400EP14D	Black Painted Housing
2	400EP14DC	Temperature compensated (TC)
3	400EP14DCR	T.C. + Rubber Sleeve

Dimensions: dimensions are in mm

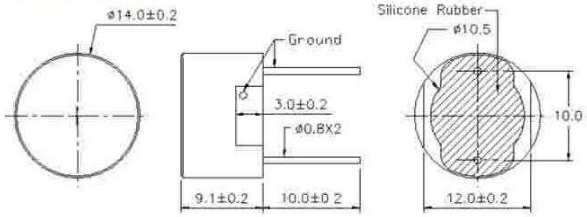

Impedance/Phase Angle vs. Frequency

Tested under 1Vrms Oscillation Level

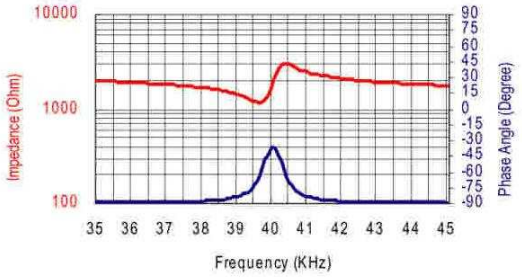

Sensitivity/Sound Pressure Level

Tested under 10Vrms @30cm

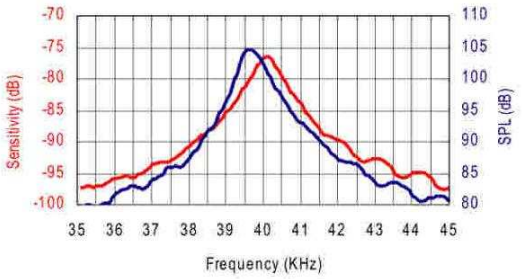

Beam Angle: Tested at 40.0Khz frequency

Wide Angle _____ Narrow Angle _____

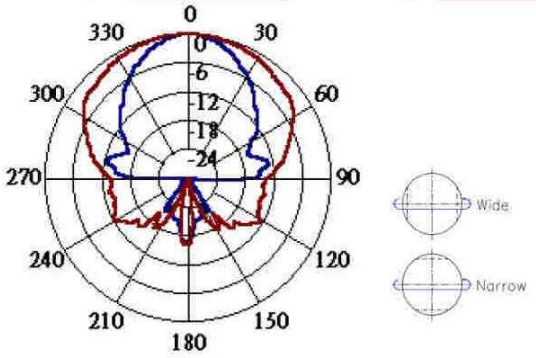

S. Square Enterprise Company Limited
Pro-Wave Electronics Corporation

Http://www.pro-wave.com.tw ; E-mail: sales@pro-wave.com.tw ; Tel: 886-2-22465101 ; Fax: 886-2-22465105

Appendix B. Determining Ultrasonic Receiver Signal Voltage Output.

The following example as shown in Figure B.1 uses the same 250 mm diameter duct and 400EP14D transducers used in testing which had a horizontal separation distance of 288.5 mm.

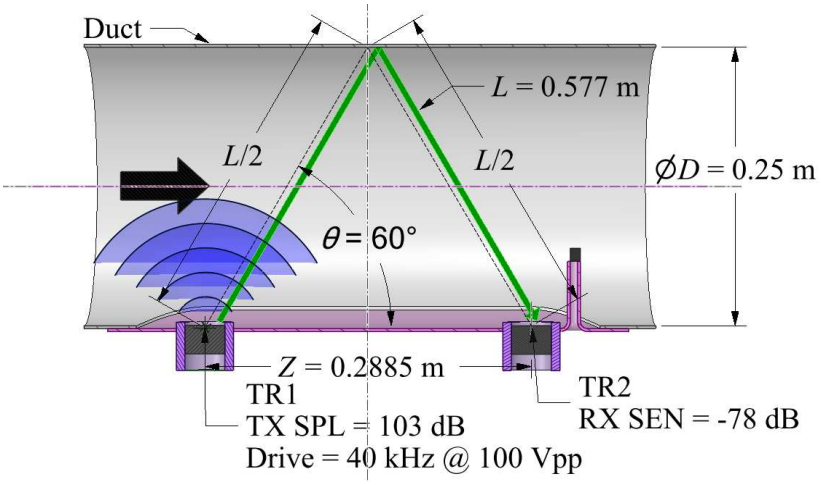

Figure B.1 Ultrasonic receiver signal voltage calculation scenario diagram.

Data sheet parameters in Appendix A for the 400EP14D (Pro-Wave Electronic Corp, Taiwan) 40 kHz enclosed type piezoelectric transducers show that;

Transmitting sound pressure level (SPL) at 40 kHz is a minimum of 103 dB, where 0 dB is equal to 0.0002 µbar at 30cm when driven with a 10 Vrms signal.

Receiver sensitivity at 40 kHz is a minimum of -78 dB, where 0 dB is equal to 1 Vrms per 1 µbar of sound pressure.

Relative SPL [119], [120] due to geometric divergence at acoustic path length L, where L has been calculated to be 0.577 m using Equation (4.1).

$$Atten_{div} = 20\log\left(\frac{30}{100L}\right) = -5.6850\ \text{dB} \tag{B.1}$$

Calculate the continuous RMS voltage equivalent for a transmitter signal pulse peak to peak voltage of 100 V.

$$TX_{rms} = 0.707\left(\frac{100\ V_{pp}}{2}\right) = 35.35\ \text{Vrms} \tag{B.2}$$

SPL gain for actual transmitter drive voltage compared to the reference 10 Vrms signal.

$$SPL_{gain} = 20\log\left(\frac{TX_{rms}}{10}\right) = 10.9678\ \text{dB} \tag{B.3}$$

Attenuation due to atmospheric conditions like temperature, pressure and humidity is small due to the 40 kHz ultrasonic frequency used and the short distance [119].

$$Atten_{atm} = 0.1886\ \text{dB/m} \times L = \ 0.1089\ \text{dB} \tag{B.4}$$

The SPL at the receiver is the addition of the reference SPL for the transmitter transducer plus additional gain because of increased drive voltage plus attenuation for spatial divergences and atmospheric absorption.

$$SPL_L = \text{SPL} + SPL_{gain} + Atten_{div} - Atten_{atm} = \ 106.3760\ \text{dB} \tag{B.5}$$

Convert SPL to µbar.

$$SPL_{L\mu bar} = 10^{\frac{SPL_L}{20}} = 41.6704\ \mu\text{bar} \tag{B.6}$$

Convert receiver sensitivity to µbar per volt.

$$RX_{Vrms/\mu bar} = 10^{\frac{RX_{sen_L}}{20}} = 125.8925\ \mu\text{Vrms} \tag{B.7}$$

Calculating receiver voltage output.

$$RX_{Vrms} = SPL_{L\mu bar} \times RX_{Vrms/\mu bar} = 5.2560\ \text{mVrms} \tag{B.8}$$

This voltage was very small and therefore required amplifying to make it usable for signal processing purposes. To perform repeated calculations of the receiver voltage and timing parameters a LabVIEW application shown in Figure B.2 was developed and is included on the disk provided on the inside back cover of this thesis.

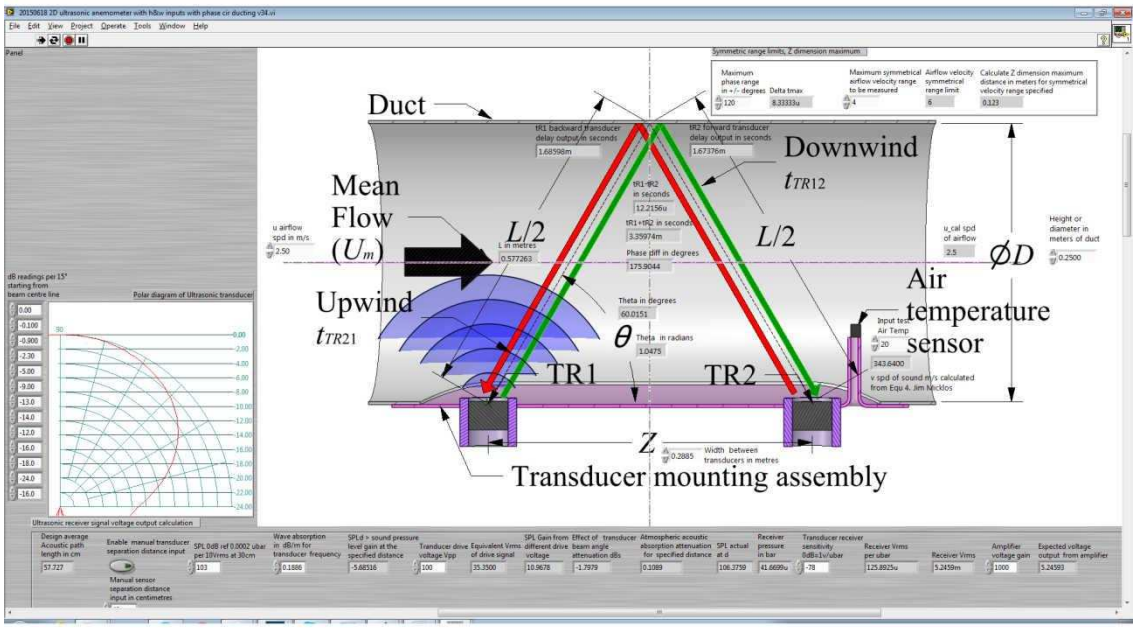

Figure B.2 LabVIEW ultrasonic flowmeter calculator.

Appendix C. Schematic and PCB Designs.

C.1. PA95 high voltage amplifier schematic

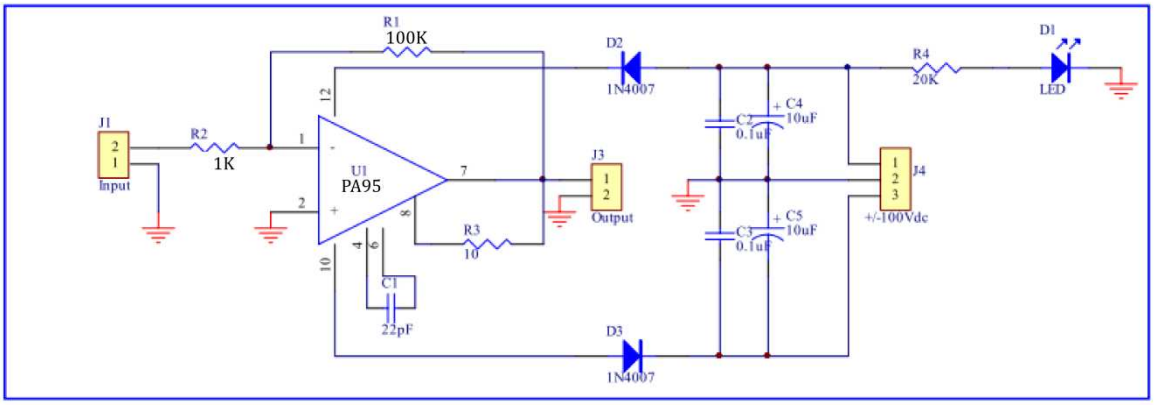

Figure C.1 PA95 high voltage amplifier schematic, adapted by the author. (Source: Ooppakaew, [121] (p. 127))

C.2. Transmit demultiplexer subsystem

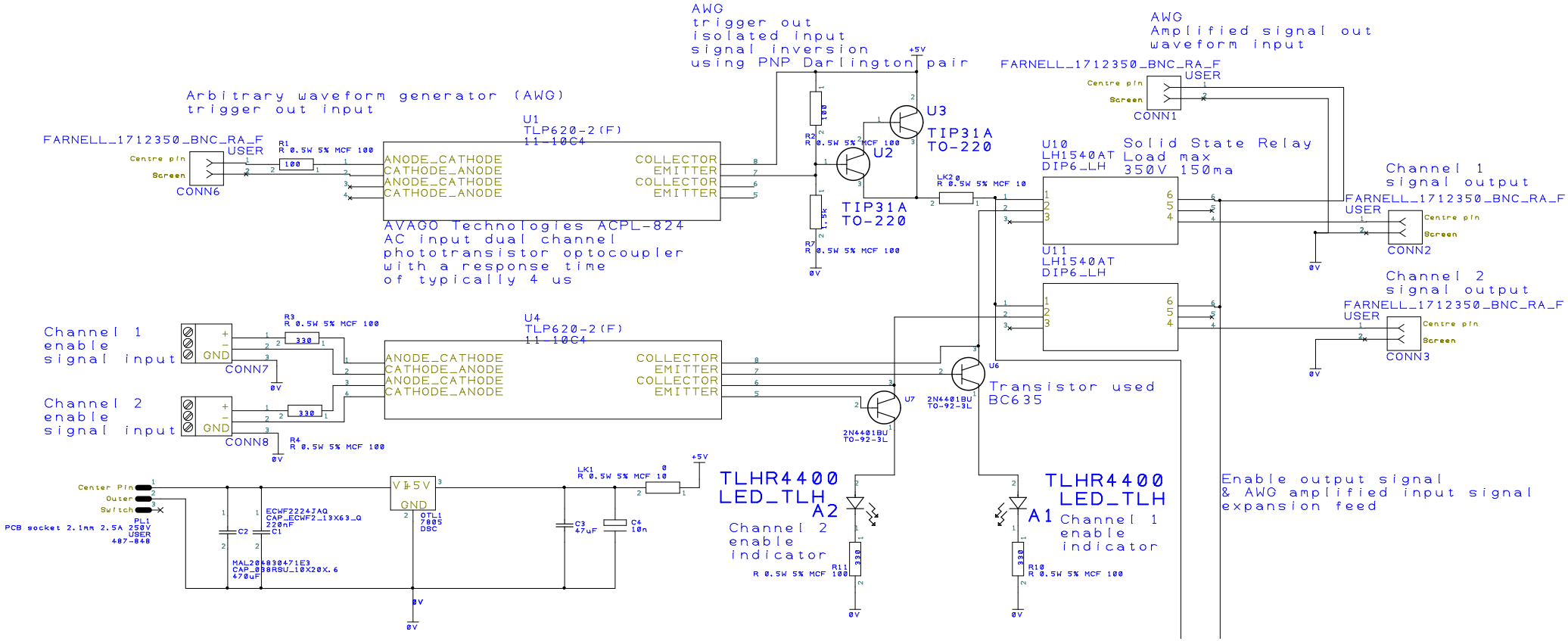

Figure C.2 Transmit signal demultiplexer, PCB schematic.

C.3. Ultrasonic transducer receiver subsystem

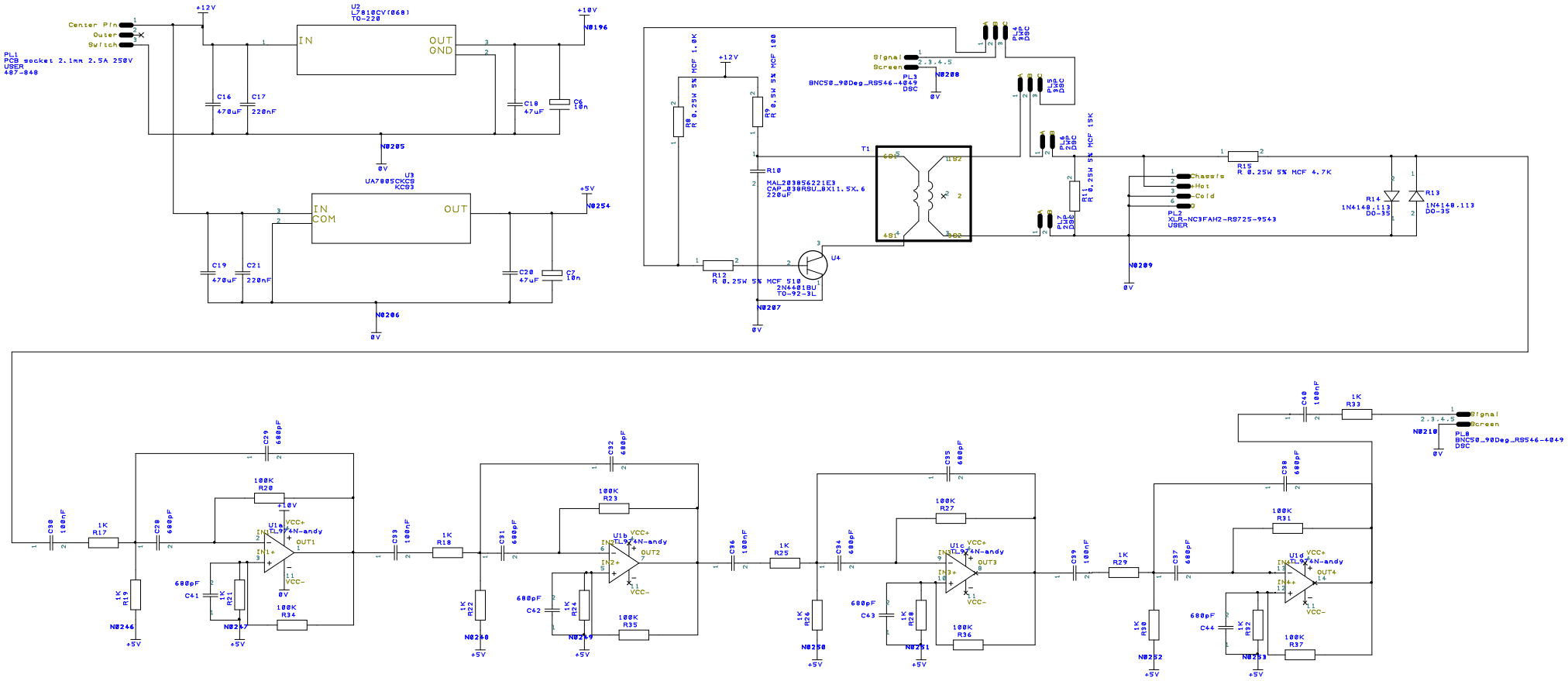

Figure C.3 Ultrasonic transducer receiver subsystem, PCB schematic.

The above schematic was designed for prototyping to support various amplifier and filter topologies so for actual component values fitted see Figure 4.19.

Appendix D. Air conditioning laboratory unit schematic.

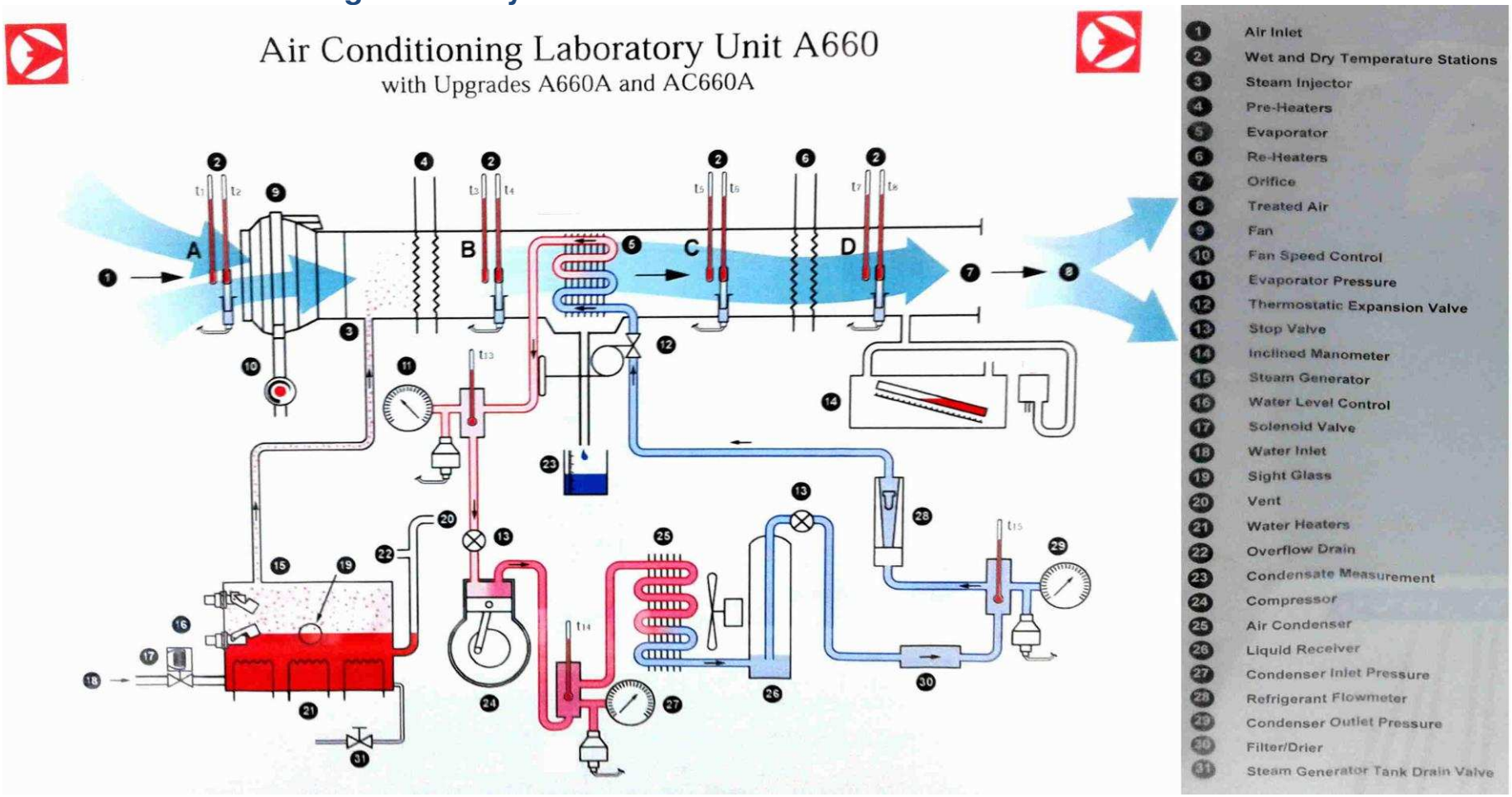

Figure D.1 Air conditioning laboratory unit schematic.

Appendix E. Flowmeter Monte Carlo Ray/Particle Tracing Simulation Software Matlab Code Listing.

E.1. Table of contents

E.2. Matlab program code listing

Initialise Matlab workspace variables

```
clear all
close all
Results_hist = [];
figtab = [];
Results_files = [];
Results_Dh = [];
Results_n = [];
Results_nrun = [];
Results_DuctAirflowRate = [];
Results_Duct_airflow_rate_predicted_error_rng_val_mps  = [];
Results_predicted_error_rng_val_mps_error_percent  = [];
Results_DuctWidth = [];
Results_DuctType = [];
Results_Z = [];
Results_Duct_log_T_all_points_3D_mean_w = [];
Results_PhaseDiff = [];
Results_u_cal_pk_phase = [];
Results_u_cal_TOF = [];
Results_u_cal_correlation = [];
Results_u_cal_correlation_error_percent = [];
Results_Duct_all_points_3D_w_across_x_y0_z0_mean = [];
Results_Duct_all_points_3D_w_x0_across_y_z0_mean = [];
Results_Duct_0dot5_width_w = [];
Results_Duct_dist_mean_flow = [];
Results_fsamp = [];
Results_Loop_count_avg = [];
Loop_count_array = [];
h_figure_table = figure(2); %create figure for table of results
set(gcf,'Name','Table of results')
```

Declare constants

```
sim_type = 'squ'; %Square>'squ' duct/pipe and circular>'cir' duct/pipe
if sim_type == 'squ' %3D flow data filename without xlsx extension
FILENAME_STR = strcat('20150510-squ_duct_v4Dh100')
end
if sim_type == 'cir'
FILENAME_STR = strcat('20150520-cir_duct_with_90deg_bend_v5')
end
test_const_flow = 0; %If 1 set import CFD flow data to a constant flow value
Duct_airflow_rate_test = 0; %Constant flow value
zero = 0;
% Create Fibonacci sequence for hydraulic diameters similation points
%i.e. Dh = [ 1 2 3 5 8 ]
N=100;
fib = [1 2 3];
idx = 2;
while fib(idx) <= N
     idx=idx+1;
     fib(idx)=fib(idx-2)+fib(idx-1)
end
fib(idx) = N;
display(fib)
```

Import CFD data from EXCEL spreadsheet .xlsx or MATLAB .mat file

```
Excel = actxserver('excel.application');
% Cleanup EXCEL application for COM server.
cleanUp = onCleanup(@()xlsCleanup(Excel, [FILENAME_STR,'.xlsx']));
%if 3-D flow data Matlab .mat does not exist, open Excel file to create it
if exist([FILENAME_STR,'.mat'], 'file')~= 2
Workbook = invoke(Excel.Workbooks, 'open', [FILENAME_STR,'.xlsx'])% Open Excel file
Sheets = Excel.Worksheets;%get EXCEL application ref to worksheets
NumSheets = get(Sheets, 'Count');%find out how many worksheets there are
Workbook.Close %close EXCEL COM server connection
Excel.Quit
Excel.delete
Data = [];
for Sheet = 1:NumSheets %Import all the sheets
[DataInput, ~, ~] = xlsread([FILENAME_STR,'.xlsx'],Sheet);
Data = cat(3,Data ,DataInput);
fprintf('Copying Excel sheet %u to workspace. \n',Sheet)
end
save([FILENAME_STR,'.mat'],'Data'); %save data as Matlab data file for speed
end % as a Excel file is very slow to load
load([FILENAME_STR,'.mat']); %load flow velocity data
NumSheets = size(Data,3)%Number of sheets in Data
```

>Create main figure

```
scrsz = get(0,'ScreenSize');
figure1 = figure('Position',[scrsz(3)*0.05 scrsz(4)*0.05  scrsz(3)*0.9 scrsz(4)*0.85 ]);
```

0 Main program loop : processing each airflow data file

```
for sheet = NumSheets:-1:1 %
for Dh = fib %close all;
```

```
clearvars -except sheet zero sim_type bin_step_size_max scrsz...
    figure1 FILENAME_STR Data h_figure_table fib...
    Results_files...
    Dh...
    Results_Dh...
    Results_n...
    Results_nrun...
    Results_Loop_count_avg...
    Results_DuctAirflowRate...
    Results_Duct_airflow_rate_predicted_error_rng_val_mps...
    Results_predicted_error_rng_val_mps_error_percent...
    Results_DuctWidth...
    Results_DuctType...
    Results_Z...
    Results_Duct_log_T_all_points_3D_mean_w...
    Results_PhaseDiff...
    Results_u_cal_pk_phase...
    Results_u_cal_TOF...
    Results_u_cal_correlation...
    Results_u_cal_correlation_error_percent...
    Results_Duct_all_points_3D_w_across_x_y0_z0_mean...
    Results_Duct_all_points_3D_w_x0_across_y_z0_mean...
    Results_Duct_0dot5_width_w...
    Results_Duct_dist_mean_flow...
    Results_fsamp...
    Results_Table...
    figtab...
    test_const_flow...
    Duct_airflow_rate_test...
    Loop_count_array;
clf(figure1,'reset')
%Predefine arrays for run step results
Mean_Phase_Hist = [];
Phase_Filtered_Hist = [];
u_cal_correlation = [];
u_cal_TOF = [];
u_cal_pk_phase = [];
```

>Input parameters for acoustic transducers and position in duct:

```
Z = 0.025; %Distance between tranducers in metres
u=[ Z  -Z ]; %Detector Z axis positions in metres
Tranducer_height_above_inner_duct = 0.001; %Height of tranducer above duct wall
%Acoustic transducer parametersAre you are
Tranducer_radius = 0.007; %Transducer radius in metres
Tranducer_depth = 0.0091; %Transducer depth in metres
Tran_f0 = 40000; %Tranducer centre frequency 40khz
%Acoustic Medium parameters
TempC = 20; %Duct Air temperature in degrees C
```

>Input parameters for simulation:

```
Num_particles = 10000 ; %start number of points for first run
Hits_required = 100; %number hits on detectors required to complete a simulation
Loop_count_dis_ratio = 1000; %Display only every so many loop counts
Plus_minus_percent_toi = 33; % Plus and minus percentage of  toi(time of interest)
%Speed up simulation by limiting the azimuth angle about 0° so reducing
%particles which come into contact with the sides of the duct
theta_range = 30 % range of theta in degrees 10 Degs = +/-5 Degs about 0 and 180 Degs
Azimuth on duct z plane
Fsamp = 100e6;  %Sampling rate of simulation
Min_duct_sim_step_num = 100; % minimum number of simulation steps across the square duct
and back
```

>Calculated Simulation parameters

```
Tranducer_radius_sq = 0.007^2;
Spdofsoundperstep = (331.5+0.607*TempC)/Fsamp; %Speed of sound per sim step
Simstart = clock; %Store Simulation start time for calculating runtime
Theta=1:180;
```

```
TX_polar_dist = sin(Theta*pi/180);%Lambertian Distribution
x3D_temp = Data(:,1,sheet);
z3D_temp = Data(:,3,sheet);
Duct_length_z3D = max(z3D_temp)-min(z3D_temp);
z3D_temp_unique = (unique(z3D_temp)); % calculate mesh z dim' step size
z3D_temp_step_size = z3D_temp_unique(2)-z3D_temp_unique(1);
Duct_airflow_rate = max(Data(:,7,sheet)); % read mean sim CFD airflow from data file col 7
```

>Calculate x dimension duct width in metres

```
%by finding Min and Max values and adding twice the difference  between the first two
adjacent Xgrid points to this value
duct_width_x3D = max(x3D_temp)-min(x3D_temp)+2*diff(x3D_temp(1:2));
duct_length = duct_width_x3D*8; %duct length in metres (z dim)
```

>Calculate circular duct parameters

```
if sim_type == 'cir' %Calculate circular duct parameters
    cylr = (duct_width_x3D/2); %Cylinder radius m
    cylr2 = cylr^2;  %Cylinder radius squared for collision detection parameter
end %Calculate circular duct parameters
```

>Calculated parameters for duct:

```
L = sqrt((2*(duct_width_x3D-Tranducer_height_above_inner_duct))^2+Z^2); %single reflective
acoustic path length
Spd_of_sound=(331.5+0.607*TempC); %Speed of sound at Air temperature in C
t_U0 = L/Spd_of_sound; % 0 m/s transit time in seconds
%Calculate expected transit time different
theta_LZ=atan2d(duct_width_x3D*2,Z);
if test_const_flow > 0 %Do if the const flow test switch set
    Duct_airflow_rate = Duct_airflow_rate_test;
end %flow test switch set
t_TR12_predicted = L/(Spd_of_sound+Duct_airflow_rate*cosd(theta_LZ));
t_TR21_predicted = L/(Spd_of_sound-Duct_airflow_rate*cosd(theta_LZ));
Delta_t_TR_predicted = t_TR21_predicted - t_TR12_predicted;
Duct_airflow_rate_predicted = (L/(2*cosd(theta_LZ)))*(1/t_TR12_predicted -...
    1/t_TR21_predicted);
min_t_step = 1/Fsamp; %minimum time step calculation
Duct_airflow_rate_predicted_min = (L/(2*cosd(theta_LZ)))*(1/(t_TR12_predicted+min_t_step) -
...
    1/(t_TR21_predicted-min_t_step));
Duct_airflow_rate_predicted_max = (L/(2*cosd(theta_LZ)))*(1/(t_TR12_predicted-min_t_step) -
...
    1/(t_TR21_predicted+min_t_step));
Duct_airflow_rate_predicted_error_rng_val_mps =((Duct_airflow_rate_predicted-
Duct_airflow_rate_predicted_min)+...
    (Duct_airflow_rate_predicted_max-Duct_airflow_rate_predicted))/2;
```

>Allocate imported duct airflow velocity array to column variable names

```
z3D_temp_up = Data(:,3,sheet)-((round(u(1)/z3D_temp_step_size))*z3D_temp_step_size)-
(Dh*duct_width_x3D);
z3D_temp_up = (round(z3D_temp_up*10000))/10000; %replace values near to zero with zero
%shift z index by Dh distanced required for upwind
z3D_temp_dn = Data(:,3,sheet)-(Dh*duct_width_x3D);
z3D_temp_dn = (round(z3D_temp_dn*10000))/10000;
zi_up = find(z3D_temp_up <= 0 & z3D_temp_up >= -(duct_length/4));
z3D_up = z3D_temp_up(zi_up);
zi_dn = find(z3D_temp_dn > 0 & z3D_temp_dn <= (duct_length/2));
z3D_dn = z3D_temp_dn(zi_dn);
z3D = vertcat(z3D_up, z3D_dn);
x3D = vertcat(Data(zi_up,1,sheet), Data(zi_dn,1,sheet));
y3D = vertcat(Data(zi_up,2,sheet), Data(zi_dn,2,sheet));
u3D = vertcat(Data(zi_up,4,sheet), Data(zi_dn,4,sheet));
v3D = vertcat(Data(zi_up,5,sheet), Data(zi_dn,5,sheet));
w3D = vertcat(Data(zi_up,6,sheet), Data(zi_dn,6,sheet));
u3D(isnan(u3D)) = 0;
v3D(isnan(v3D)) = 0;
w3D(isnan(w3D)) = 0;
if test_const_flow > 0 %Do if the const flow test switch set
    u3D = (u3D.*0);  %u is the velocity field x component
    v3D = (v3D.*0);  %v is the velocity field y component
    w3D = (w3D.*0)+Duct_airflow_rate_test; %w is the velocity field z component
end %end flow test
```

>Calculate airflow velocity Mesh Grid size xyz

```
x_size = length(unique(x3D));
y_size = length(unique(y3D));
z_size = length(unique(z3D));
```

>Convert x,y,z spatial data to Matlab N-D Grid format

```
%x rows should increment
%y columns should increment
x_ndgrid = reshape(x3D,x_size,y_size,z_size);
y_ndgrid = reshape(y3D,x_size,y_size,z_size);
z_ndgrid = reshape(z3D,x_size,y_size,z_size);
u_ndgrid = reshape(u3D,x_size,y_size,z_size);
v_ndgrid = reshape(v3D,x_size,y_size,z_size);
w_ndgrid = reshape(w3D,x_size,y_size,z_size);
```

>Transform N-D Grid to Mesh Grid

```
%x columns should increment
%y rows should increment
x_meshgrid = permute(x_ndgrid,[2 1 3]);
y_meshgrid = permute(y_ndgrid,[2 1 3]);
z_meshgrid = permute(z_ndgrid,[2 1 3]);
u_meshgrid = permute(u_ndgrid,[2 1 3]);
v_meshgrid = permute(v_ndgrid,[2 1 3]);
w_meshgrid = permute(w_ndgrid,[2 1 3]);
```

>Define interpolation function on N-D Gridded airflow Data set uvw.

```
Inter_ndgrid_u = griddedInterpolant(x_ndgrid,y_ndgrid,z_ndgrid,u_ndgrid,'cubic','linear');
Inter_ndgrid_v = griddedInterpolant(x_ndgrid,y_ndgrid,z_ndgrid,v_ndgrid,'cubic','linear');
Inter_ndgrid_w = griddedInterpolant(x_ndgrid,y_ndgrid,z_ndgrid,w_ndgrid,'cubic','linear');
```

>Calculate Simulation runtime and reception time of interest

```
flight_time_zero_flow = ((L)/(331.5+0.607*TempC)); % TOF of measurement
timeofinterest = ((L)/(331.5+0.607*TempC))+(1/Tran_f0)/2; % time of interest of measurement
simruntime = timeofinterest+4*(1/Tran_f0); %Simulation runtime in seconds
No_of_sample_Bins = floor(simruntime*Fsamp)+1; %No of receiver sample bins required
pulse=zeros(No_of_sample_Bins,length(u)); % Array for the  detectors
%Calculate flight time number of time steps and divide by a number
%which is the minimum number of simulation loops allowed.
bin_max_div = floor(timeofinterest*Fsamp/Min_duct_sim_step_num);
```

>Circular duct traverse parameters

```
if sim_type == 'cir'
```

```
    log_T_6_points_y = ([0.032 0.135 0.321 0.679 0.865 0.968]-0.5).*duct_width_x3D; % Log-
Tchebycheff circular duct
    log_T_6_points_x = zeros(1,length(log_T_6_points_y));
    log_T_6_points_z = ones(1,length(log_T_6_points_y)).*duct_width_x3D*Dh;
    log_T_6_points_xyz_port1 = [log_T_6_points_x;log_T_6_points_y;log_T_6_points_z];
    log_T_6_points_xyz_port2 = rotz(120)*log_T_6_points_xyz_port1;
    log_T_6_points_xyz_port3 = rotz(240)*log_T_6_points_xyz_port1;
    log_T_6_points_xyz_port_123 = [log_T_6_points_xyz_port1 log_T_6_points_xyz_port2
log_T_6_points_xyz_port3];
    Duct_log_T_all_points_3D_w = Inter_ndgrid_w(log_T_6_points_xyz_port_123(1,:)
,log_T_6_points_xyz_port_123(2,:),log_T_6_points_xyz_port_123(3,:));
    Duct_log_T_all_points_3D_mean_w = mean(Duct_log_T_all_points_3D_w(:));
```

>Test to display Log-T circular duct traverse Airflow monitoring points

```
    figure(3)
    % Create wall profile view of the circular duct
    [Xcir,Ycir,Zcir] = cylinder((duct_width_x3D/2),360)
    plot3(Ycir(1,:),Xcir(1,:),Zcir(1,:))
    view(2)
    axis equal
    grid on
    hold on

scatter3(log_T_6_points_xyz_port_123(1,:),log_T_6_points_xyz_port_123(2,:),log_T_6_points_x
yz_port_123(3,:));
```

```
        for bin_num = 1:size(log_T_6_points_xyz_port_123(1,:),2)

text(log_T_6_points_xyz_port_123(1,bin_num),log_T_6_points_xyz_port_123(2,bin_num),0,num2st
r(Duct_log_T_all_points_3D_w(bin_num)))
        end
    hold off
    display(['Log-T circular duct traverse airflow measurement '...
    num2str(Duct_log_T_all_points_3D_mean_w) ' m/s at '...
    num2str(Dh) ' Dh'])

end %Circular duct traverse parameters
```

>Rectangular duct traverse parameters

```
if sim_type == 'squ'

    log_T_5_points = [0.074 0.288 0.500 0.712 0.926]; % Log-Tchebycheff Rectangular ducts
    [log_T_5_points_x, log_T_5_points_y] = ndgrid(log_T_5_points,log_T_5_points);
    log_T_5_points_dim_y = (duct_width_x3D*log_T_5_points_y)-duct_width_x3D/2;
    log_T_5_points_dim_x = (duct_width_x3D*log_T_5_points_x)-duct_width_x3D/2;
    Duct_log_T_all_points_3D_w = Inter_ndgrid_w(log_T_5_points_dim_x
,log_T_5_points_dim_y,repmat(zero,size(log_T_5_points_dim_x)));
    Duct_log_T_all_points_3D_mean_w = mean(Duct_log_T_all_points_3D_w(:));
```

>Test to display Log-Tchebycheff Rectangular duct traverse Airflow monitoring points

```
    figure(3)
    % Create wall profile view of the square duct
    x=[1 1 -1 -1 1];
    y=[1 -1 -1 1 1];
    z = [0 0 0 0 0];
    y = y*duct_width_x3D/2; % Scale duct width to actual
    x = x*duct_width_x3D/2;
    plot3(x,y,z,'LineWidth',3)
    hold on
    view(2)
    axis equal
    grid on

scatter3(log_T_5_points_dim_x(:),log_T_5_points_dim_y(:),ones(size(log_T_5_points_dim_x(:))
).*duct_width_x3D*Dh);
    for bin_num = 1:size(log_T_5_points_dim_x(:),1)
        text(log_T_5_points_dim_x(bin_num),log_T_5_points_dim_y(bin_num),...
            duct_width_x3D*Dh,...
            num2str(Duct_log_T_all_points_3D_w(bin_num)))
    end
    hold off
    display(['Log-T Rectangular duct traverse airflow measurement '...
        num2str(Duct_log_T_all_points_3D_mean_w) ' m/s at '...
        num2str(Dh) ' Dh'])

end %Rectangular duct traverse parameters
```

>Calculate the airflow velocity mean across x=0 axis

```
Duct_all_points_3D_w =
Inter_ndgrid_w(x_ndgrid(:,:,1),y_ndgrid(:,:,1),z_ndgrid(:,:,fix(z_size/2)));
Duct_all_points_3D_mean_w = mean(Duct_all_points_3D_w(:));
Duct_all_points_3D_w_across_y_plane =
Inter_ndgrid_w(x_ndgrid(fix(x_size/2)+1,:,fix(z_size/2))...
    ,y_ndgrid(fix(x_size/2)+1,:,fix(z_size/2)),z_ndgrid(fix(x_size/2)+1,:,fix(z_size/2)));
Duct_all_points_3D_mean_w_across_y_plane = mean(Duct_all_points_3D_w_across_y_plane(:));
increment_xy_plane_index = 0.001;
xy_plane_index = -duct_width_x3D/2:increment_xy_plane_index:duct_width_x3D/2;
[X1,X2,X3] = ndgrid(xy_plane_index, xy_plane_index,0:(Duct_length_z3D/10):Duct_length_z3D);
Duct_all_points_3D_w_across_x_y0_z0 = ...
    Inter_ndgrid_w(xy_plane_index,...
    repmat(zero,size(xy_plane_index)),...
    repmat(zero,size(xy_plane_index)));
Duct_all_points_3D_w_across_x_y0_z0_mean = mean(Duct_all_points_3D_w_across_x_y0_z0);
Duct_all_points_3D_w_x0_across_y0_z0 = ...
    Inter_ndgrid_w(repmat(zero,size(xy_plane_index)),...
    xy_plane_index,...
    repmat(zero,size(xy_plane_index)));
Duct_all_points_3D_w_x0_across_y_z0_mean = mean(Duct_all_points_3D_w_x0_across_y0_z0);
Duct_all_points_3D_w_across_y_plane_v2 = Inter_ndgrid_w(X1,X2,X3);
Duct_all_points_3D_mean_w_across_y_plane_v2 =
mean(mean(Duct_all_points_3D_w_across_y_plane_v2,2));
Duct_all_points_3D_mean_w_across_y_plane_v3 =
Duct_all_points_3D_mean_w_across_y_plane_v2(:);
y_profile_grid = -duct_width_x3D/2:duct_width_x3D/200:duct_width_x3D/2;
```

```
x_profile_grid = zeros(size(y_profile_grid));
z_profile_grid = zeros(size(y_profile_grid));
Duct_all_points_2wall_3D_w_across_y_plane =
Inter_ndgrid_w(x_profile_grid,y_profile_grid,z_profile_grid );
% plot(y_profile_grid,Duct_all_points_2wall_3D_w_across_y_plane);
Duct_all_points_2wall_3D_mean_w_across_y_plane =
mean(Duct_all_points_2wall_3D_w_across_y_plane(:));
ind_first =
find(Duct_all_points_2wall_3D_w_across_y_plane>Duct_log_T_all_points_3D_mean_w,1);
ind_last =
find(Duct_all_points_2wall_3D_w_across_y_plane>Duct_log_T_all_points_3D_mean_w,1,'last');
Duct_dist_mean_flow_first = y_profile_grid(ind_first);
Duct_dist_mean_flow_last = y_profile_grid(ind_last);
Duct_dist_mean_flow = (duct_width_x3D/2-
mean([abs(Duct_dist_mean_flow_first),abs(Duct_dist_mean_flow_last)]))/duct_width_x3D;
Duct_0dot5_width_w = Inter_ndgrid_w(duct_width_x3D/4 ,0,0);
```

>Select main figure

```
figure(figure1)
```

>Create Duct visualisation

```
if 1 == 1 %Used to create nested code sections only
```

```
    top_plot = subplot(2,2,1:2); % plot on vertical left side of figure
    set(top_plot,'CameraUpVector',[0 1 0] );
    hold on;
    colormap('jet');
```

>>Display 2D airflow profile with w vector velocity represented by height and colour

```
    h_flow_profile_cutplane_2D_height_vis=surf(x_ndgrid(:,:,1),y_ndgrid(:,:,1),...
        (Duct_all_points_3D_w./max(Duct_all_points_3D_w(:)))/10-
(duct_length/2),'faceAlpha',0.5);
    set(h_flow_profile_cutplane_2D_height_vis,'Facecolor','interp');
    grid('on')
    freezeColors; %Lock colors of plot, enabling multiple colormaps per figure
    %download at http://www.mathworks.com/matlabcentral/fileexchange/
    %7943-freezecolors---unfreezecolors/content/freezeColors/freezeColors.m
    if sim_type == 'squ'
```

>>Create mesh for external view of square duct

```
        x=[1 1 -1 -1 1];
        x=[x;x];
        y=[1 -1 -1 1 1];
        y=[y;y];
        z = [0 0 0 0 0; 1 1 1 1 1];
        y = y*duct_width_x3D/2; % Scale duct width to actual
        x = x*duct_width_x3D/2;
```

```
    end
    if sim_type == 'cir'
```

>>Create mesh for external view of circular duct

```
        [x,y,z] = cylinder(duct_width_x3D/2,40);
```

```
    end
```

>>Create duct mesh and scale to duct height/length

```
    Duct_Wall_Mesh = {x ;y ;z};
    Duct_Wall_Mesh{3} = (duct_length)*(Duct_Wall_Mesh{3}-0.5);
```

>>Display Duct walls

```
    h_Duct_wall = surf(Duct_Wall_Mesh{:},'faceAlpha',0.1);
    shading('interp');
```

```
    colormap('winter');
    cameratoolbar('NoReset')
    cameratoolbar('SetMode','orbit')
    cameratoolbar('SetCoordSys','y')
    freezeColors;
```

>>Add round transducer at u distance from z = 0

```
    patch((sin((0:360)*pi/180)*Tranducer_radius),zeros(1,361)-(duct_width_x3D/2-
Tranducer_height_above_inner_duct),0-cos((0:360)*pi/180)*Tranducer_radius,[1 0 0]);
    patch((sin((0:360)*pi/180)*Tranducer_radius),zeros(1,361)-(duct_width_x3D/2-
Tranducer_height_above_inner_duct),u(1)-cos((0:360)*pi/180)*Tranducer_radius,[0.5 0.5 1]);
    patch((sin((0:360)*pi/180)*Tranducer_radius),zeros(1,361)-(duct_width_x3D/2-
Tranducer_height_above_inner_duct),u(2)-cos((0:360)*pi/180)*Tranducer_radius,[0 1 0]);
    [xt,zt,yt] = cylinder(Tranducer_radius,10);
    Tranducer_Mesh = {xt;yt;zt};
    Tranducer_Mesh{2} = (Tranducer_depth)*(Tranducer_Mesh{2})-
(duct_width_x3D/2+Tranducer_depth-Tranducer_height_above_inner_duct);
```

>>Display Duct walls

```
    h_tranducer_middle = surf(Tranducer_Mesh{:},'FaceColor',[0 0
0],'faceAlpha',0.5,'EdgeColor','none');
    h_tranducer_up =
surf(Tranducer_Mesh{1},Tranducer_Mesh{2},Tranducer_Mesh{3}+u(1),'FaceColor',[0 0
0],'faceAlpha',0.5,'EdgeColor','none');
    h_tranducer_dn =
surf(Tranducer_Mesh{1},Tranducer_Mesh{2},Tranducer_Mesh{3}+u(2),'FaceColor',[0 0
0],'faceAlpha',0.5,'EdgeColor','none');
    %shading(h_tranducer,'interp');
```

>>Add Airflow direction arrow

```
    scale = 50 ;
    ydata = [   -1 1   1   2   0    -2  -1  -1  -1  ]./scale;
    zdata =( [   0   0  3   3   5    3   3     0 0]./scale)+u(1);
    xdata = (zeros(size(ydata))./scale)-0.001;
    patch(xdata,ydata,zdata,'k','faceAlpha',0.5)
```

>>Display slices of flow w vector data

```
    colormap('jet');
    h_flow_slices = slice(x_meshgrid, y_meshgrid,z_meshgrid,w_meshgrid,0,0.0,[u(1)/2
u(2)/2]);
    set(h_flow_slices,'FaceColor','interp',...
        'EdgeColor','none',...
        'DiffuseStrength',.8,'faceAlpha',0.5)
```

>>Duct plot annotation if required

```
xlabel('X axis m','HorizontalAlignment','center');% Create xlabel ylabel('Y axis
m','HorizontalAlignment','center');% Create ylabel zlabel('Z axis m','Rotation',1);% Create
zlabel
```

>>Duct plot rotate and zoom

```
    cameratoolbar('NoReset')
    freezeColors;
    axis vis3d;
    axis('equal');axis tight;
    camorbit(300,0,'camera');
    camorbit(0,20,'camera');
    camzoom(2);
    camroll(0);
    h_particle_hits_pass_point_array = [ ];%init particle past detector graphic ref array
    h_particle_hits_array  = [ ];%init particles hit on detector graphic ref array
    Hits_Total_all = 0;%init hits on all receivers count and all runs
    run = 0;%init simulation run count
    colorbar_airflow = colorbar()%add colorbar for flow velocity data
    ylabel(colorbar_airflow,'Airflow speed (m/s)')
    %colorbar function can cause problems with graphics card,comment out if problem occurs
    %http://uk.mathworks.com/matlabcentral/answers/53874-colorbar-error-how-to-fix-it

end
```

>O Sub-Program loop for analysing accumulative particle simulations on the same velocity dataset

```
while Hits_Total_all < Hits_required
```

```
    run = run+1;%increment run number
    Hits_Total = zeros(1,size(u,2));%init individual receiver hits per run count
    subplot(top_plot);%Select top plot window for duct visualisation
    bin_num = 0;%init receiver histogram index number
```

>>Delete particle hits after first run

```
    if run>1;%do only after first run
        delete(h_particle_hits_pass_point_array);%delete visualisation of particles past
detectors
        delete(h_particle_hits_array);%delete visualisation of particles hits on detectors
        h_particle_hits_pass_point_array = [ ];%re-init particle past detector graphic ref
array
        h_particle_hits_array  = [ ];%init particles hit on detector graphic ref array
    end
```

>>Declare particle structures

```
    P=struct('p',0,'v',0,'r',0);% Raytrace particles p=position v=vector r=reflection
    P.r.hit = false(length(u),Num_particles);
    P.r.hit_past = false(length(u),Num_particles);
    P.r.y.pos=false(1,Num_particles);
    P.r.y.neg=false(1,Num_particles);
    P.r.x.pos=false(1,Num_particles);
    P.r.x.neg=false(1,Num_particles);
    P.r.rs=zeros(1,Num_particles);
    P.r.r=zeros(1,Num_particles);
    P.p=[0; -(duct_width_x3D)/2; 0];
    P.p_hit=[0; -(duct_width_x3D)/2; 0];
    P.p=P.p(:,ones(Num_particles,1));
    P.p_hit=P.p_hit(:,ones(Num_particles,1));
    Hits_Total=zeros(1,size(u,2));
```

>>Declare particle emission distribution profiles

```
    phi=rand(Num_particles,1)*2*pi; %Generate particle initial trajectory azimuth angle 0
to 2pi radians (0 to 360 Degs)
    r=1e-6:1e-6:Tranducer_radius; %transducer face radius range values
    rho=pchip([0 cumsum(r+100*eps)/sum(r+100*eps)],[0 r],rand(Num_particles,1));%Throw MC
points rho
    [x_tx_face_pos,y_tx_face_pos] = pol2cart(phi,rho);%convert transducer face polar coord
to cartesian
        figure(4)
        set(gcf,'Name','Transducer emitter start points')
        h4 = plot(x_tx_face_pos,y_tx_face_pos,'.')
        axis('equal')%plot tx relative face position points
        xlabel('X or Duct Z axis','HorizontalAlignment','center');% Create xlabel
        ylabel('Y or Duct X axis','HorizontalAlignment','center');% Create ylabel
        figure(figure1)%return main figure
    P.p=[y_tx_face_pos -
(duct_width_x3D/2)*ones(Num_particles,1)+Tranducer_height_above_inner_duct
x_tx_face_pos]';
    phi=pchip([0 cumsum(TX_polar_dist+100*eps)/sum(TX_polar_dist+100*eps)],...
        [min(Theta)-(Theta(2)-Theta(1)) Theta],...
        rand(Num_particles,1));%Throw MC points for phi / elevation
    theta=(theta_range*rand(Num_particles,1))-theta_range/2; %MC points for theta / azimuth
    Part_Trajectory = {zeros(size(x_tx_face_pos));...
        zeros(size(x_tx_face_pos));...
        zeros(size(x_tx_face_pos))};% Initialise particle trajectory cell array
    [Part_Trajectory{:}] = sph2cart(theta*pi/180,(phi)*pi/180,1);
    Part_Trajectory = Part_Trajectory.';
        figure(5)
        set(gcf,'Name','Transducer emitter trajectories')
        h5 = plot3(Part_Trajectory{1},Part_Trajectory{2},Part_Trajectory{3},'.');
        axis('equal')%plot tx relative face position points
        % plot annotation if required
        xlabel('X or Duct Z axis','HorizontalAlignment','center');% Create xlabel
        ylabel('Y or Duct X axis','HorizontalAlignment','center');% Create ylabel
        zlabel('Z or Duct y axis','Rotation',1);% Create zlabel
        figure(figure1)%return main figure
    P.v=[Part_Trajectory{:,[ 2 3 1]}]';%convert generated coords to Duct coords, yzx to xyz
    % plot initial acoustic particle positions
    h_particles
=line(P.p(1,:),P.p(2,:),P.p(3,:),'lineStyle','none','marker','.','markerSize',2,'Color','g'
);
```

```
%h5=line(P.p(1,P.r.hit),P.p(2,P.r.hit),P.p(3,P.r.hit),'lineStyle','none','marker','.','mark
erSize',10,'Color','k');
```

>>Kill particles which are not going to reach receiver in time

```
    z_vel_req = (u(1)/timeofinterest); % Calculate actual Z Velocity required to reach the
receiver
    spdofsound = Spdofsoundperstep*Fsamp ; % Calculate the speed of sound per second
    z_vel_req_up = -(Duct_log_T_all_points_3D_mean_w+z_vel_req)*Spdofsoundperstep;
%/spdofsound;
    z_vel_req_dn = (-
Duct_log_T_all_points_3D_mean_w+z_vel_req)*Spdofsoundperstep;%/spdofsound;
    z_vel_req_up_fast = -
(Duct_all_points_3D_w_x0_across_y_z0_mean+(z_vel_req*(1+(Plus_minus_percent_toi/100))));
    z_vel_req_up_slow = -(Duct_all_points_3D_w_x0_across_y_z0_mean+(z_vel_req*(1-
(Plus_minus_percent_toi/100))));
    z_vel_req_dn_fast = (-
Duct_all_points_3D_w_x0_across_y_z0_mean+(z_vel_req*(1+(Plus_minus_percent_toi/100))));
    z_vel_req_dn_slow = (-Duct_all_points_3D_w_x0_across_y_z0_mean+(z_vel_req*(1-
(Plus_minus_percent_toi/100))));
    z_vel_req_up_fast = z_vel_req_up_fast/spdofsound;
    z_vel_req_up_slow = z_vel_req_up_slow/spdofsound;
    z_vel_req_dn_fast = z_vel_req_dn_fast/spdofsound;
    z_vel_req_dn_slow = z_vel_req_dn_slow/spdofsound;
    keep_slow_up=(P.v(3,:))<  z_vel_req_up_slow;% Drop points which are too slow upwind
    keep_fast_up=(P.v(3,:))>  z_vel_req_up_fast;% Drop points which are too fast upwind
    keep_slow_dn=(P.v(3,:))>  z_vel_req_dn_slow;% Drop points which are too slow upwind
    keep_fast_dn=(P.v(3,:))<  z_vel_req_dn_fast;% Drop points which are too fast upwind
    %create logical array of particle with z plane velocites which may hit detector
    keep = (keep_slow_up & keep_fast_up)|(keep_slow_dn & keep_fast_dn);
    %calculate number of particles kept
    sum_keep_slow = sum(keep);
    %delete particles data not required
    P.p=P.p(:,keep);  P.v=P.v(:,keep); P.r.hit=P.r.hit(:,keep);
    P.r.x.neg=P.r.x.neg(:,keep); P.r.x.pos=P.r.x.pos(:,keep);
    P.r.y.neg=P.r.y.neg(:,keep); P.r.y.pos=P.r.y.pos(:,keep);
    P.r.r=P.r.r(:,keep); P.r.rs=P.r.rs(:,keep);
    P.p_hit=P.p_hit(:,keep);
    P.r.hit_past =P.r.hit_past(:,keep);
%         figure(6)
%         set(gcf,'name','Particle z plane normalise velocity')
%         h6 = plot( P.v(3,:),'r*') %plot normalise z velocity vectors
%         figure(figure1)%return to main figure
    subplot(top_plot)%select duct visualisation plot
```

>>0 Particle simulation Loop

```
    Loop_count = 0; %Simulation loop count
    if sim_type == 'squ'
    Loop_count_dis_ratio = 1; %Display only every so many loop counts
    end
    if sim_type == 'cir'
    Loop_count_dis_ratio = 1; %Display only every so many loop counts
    end
    if sim_type == 'squ';
       bin_step_size = randi([1 bin_max_div]);
    end
    if sim_type == 'cir';
       bin_step_size = randi([1 bin_max_div]);
       %bin_step_size = bin_max_div*1;
    end
    while(bin_num<No_of_sample_Bins) %loop every microsecond
```

```
    Loop_count = Loop_count +1; %Simulation loop count
        if mod(Loop_count,Loop_count_dis_ratio) == 0 %plot every loop counts (Note plotting
expensive )

h_particles=line(P.p(1,:),P.p(2,:),P.p(3,:),'lineStyle','none','marker','.','markerSize',12
);

%h5=line(P.p(1,P.r.hit),P.p(2,P.r.hit),P.p(3,P.r.hit),'lineStyle','none','marker','.','mark
erSize',10,'Color','k');

%h1=line(P.p(1,:),P.p(2,:),P.p(3,:),'lineStyle','none','marker','.','markerSize',2,'Color',
'r'); %trace particles in red
            title(['t =' num2str(bin_num/(Fsamp/1e6)) '\mus'...
                ' file=' num2str(sheet)...
                ' Dh=' num2str(Dh)...
                ' run=' num2str(run)...
                ' Parts=' num2str(size(P.p,2))...
                ' Hits1=' num2str(Hits_Total(1))...
                ' Hits2=' num2str(Hits_Total(2))...
                ' Hits total=' num2str(Hits_Total_all)])
            drawnow;
        end %plot particles
        spdofsoundpersteps = Spdofsoundperstep*bin_step_size;
        P.p=P.p+P.v*spdofsoundpersteps;%move rays to new position
```

>>>Increment simulation time steps

```
        bin_num=bin_num+bin_step_size;
```

>>>Check if particle has gone outside of duct

>>>>Squared duct check

```
        if sim_type == 'squ';
        P.r.y.pos = (P.p(2,:)) > (duct_width_x3D/2); %Check for reflections in y direction
(hit top edge of duct)
        P.r.y.neg = (P.p(2,:)) < -(duct_width_x3D/2); %Check for reflections in y direction
(hit bottom edge of duct)
        end %Squared duct check
```

>>>>Cylindrical duct check

```
        if sim_type == 'cir';
        P.r.rs=sum(P.p(1:2,:).^2);
        P.r.y.neg = P.r.rs > cylr2; %Check for reflections (hit edge of cylinder)
        %cylr2_close_bounds = cylr2-(cylr2/(0.1*min_duct_sim_step_num));
        cylr2_close_bounds = (cylr-(Spdofsoundperstep*bin_max_div))^2;
        close_to_duct_wall = P.r.rs > cylr2_close_bounds;
        end %Cylindrical duct check
        if any(P.r.y.neg)
```

>>>Process particles hitting detectors

```
            %Count number of particles outside of duct before reflections;
            particles_outside_bottom_before  = sum(P.r.y.neg); %this is to check all have
been reflected correctly
            %uses Circular detector
            for j=1:length(u);
```

>>>>Process particle hits for each detector

```
                P.r.hit(j,:) = ~P.r.hit_past(j,:) & ((P.p(2,:) <= -
(duct_width_x3D/2)+Tranducer_height_above_inner_duct) & (((abs(P.p(3,:)-
u(j)).^2)+(abs(P.p(1,:))).^2)< Tranducer_radius_sq)); %Tranducer_radius
                if any(P.r.hit(j,:))
```

```
                    Hits_Total(j) = Hits_Total(j) + sum(P.r.hit(j,:)) %Calculate the
combined number of hits for both all detectors
                    %Draw particle hits passed the detector positions
                    h_particle_hits_pass_point
=line(P.p(1,P.r.hit(j,:)),P.p(2,P.r.hit(j,:)),P.p(3,P.r.hit(j,:)),'lineStyle','none','marke
r','.','markerSize',12,'Color','y');
                    h_particle_hits_pass_point_array = [h_particle_hits_pass_point_array
h_particle_hits_pass_point];
```

>>>>>Calculate distance from detector surface

```
                    Tranducer_dist_min= -
(duct_width_x3D/2)+Tranducer_height_above_inner_duct;%Calculate detector y axis position
inside duct
                    Dist_passed_tranducer_y = (P.p(2,P.r.hit(j,:))-Tranducer_dist_min);
%hits y axis positions minus the detector position
                    Dist_passed_tranducer_y_time =
Dist_passed_tranducer_y./P.v(2,P.r.hit(j,:));%Time=(Distance/Velocity)
                    Dist_passed_tranducer_x =
P.v(1,P.r.hit(j,:)).*Dist_passed_tranducer_y_time;%Distance=Velocity*Time x
                    Dist_passed_tranducer_z =
P.v(3,P.r.hit(j,:)).*Dist_passed_tranducer_y_time;%Distance=Velocity*Time z
                    Dist_passed_tranducer_mag =
sqrt(Dist_passed_tranducer_x.^2+Dist_passed_tranducer_y.^2+Dist_passed_tranducer_z.^2);
                    Dist_passed_tranducer_bin_Nos =
fix(Dist_passed_tranducer_mag/Spdofsoundperstep);
                    P.p_hit(2,P.r.hit(j,:))=P.p(2,P.r.hit(j,:))-Dist_passed_tranducer_y;
                    P.p_hit(1,P.r.hit(j,:))=P.p(1,P.r.hit(j,:))-Dist_passed_tranducer_x;
                    P.p_hit(3,P.r.hit(j,:))=P.p(3,P.r.hit(j,:));
                    for bin=1:length(Dist_passed_tranducer_bin_Nos)
```

>>>>>>Generate particle time series histogram for each detector

```
                        pulse((bin_num)-Dist_passed_tranducer_bin_Nos(bin)-1,j)=
pulse((bin_num)-Dist_passed_tranducer_bin_Nos(bin)-1,j)+1;
```

```
                    end
```

>>>>>Display detector particle hits

```
h_particle_hits=line(P.p_hit(1,P.r.hit(j,:)),P.p_hit(2,P.r.hit(j,:)),P.p_hit(3,P.r.hit(j,:)
),'lineStyle','none','marker','.','markerSize',10,'Color','r');
                    h_particle_hits_array = [h_particle_hits_array h_particle_hits];
                    P.r.hit_past(j,:)= P.r.hit_past(j,:) | P.r.hit(j,:);
```

```
                end %any(P.r.hit(j,:))

%h2=line(P.p(1,:),P.p(2,:),P.p(3,:),'lineStyle','none','marker','.','markerSize',2,'Color',
'r');
```

```
            end %j=1:length(u);
```

```
        end %any(P.r.y.neg)
```

>>>Process square duct reflections

```
 if sim_type == 'squ';
        if any(P.r.y.pos) % Reflect particle  position and  velocity if  above top of the
duct
            particles_outside_top_before = sum(P.r.y.pos); % Count number of particles to
be reflected
            P.v(2,P.r.y.pos) = -(P.v(2,P.r.y.pos)); %Reflect particle velocity vector
            P.p(2,P.r.y.pos) = (duct_width_x3D/2)-((P.p(2,P.r.y.pos))-(duct_width_x3D/2));
            P.r.y.pos = (P.p(2,:)) > (duct_width_x3D/2); %Check for reflections in y
direction (hit top edge of duct)
            particles_outside_top_after  = sum(P.r.y.pos); % Count number of particles
still  outside top of duct
        end
        if any(P.r.y.neg)
            particles_outside_bottom_before = sum(P.r.y.neg); % Count number of particles
to be reflected
            P.v(2,P.r.y.neg) = -(P.v(2,P.r.y.neg));
            P.p(2,P.r.y.neg) = (-duct_width_x3D/2)-((P.p(2,P.r.y.neg))+(duct_width_x3D/2));
            P.r.y.neg = (P.p(2,:)) < -(duct_width_x3D/2);
            particles_outside_bottom_after  = sum(P.r.y.neg);
        end

        P.r.x.pos = (P.p(1,:)) > (duct_width_x3D/2); %Check for reflections in x direction
(hit left edge of duct)
        P.r.x.neg = (P.p(1,:)) < -(duct_width_x3D/2); %Check for reflections in x direction
(hit right edge of duct
        if any(P.r.x.pos)
            particles_outside_right_before = sum(P.r.x.pos); % Count number of particles to
be reflected
            P.v(1,P.r.x.pos) = -(P.v(1,P.r.x.pos));
            P.p(1,P.r.x.pos) = (duct_width_x3D/2)-((P.p(1,P.r.x.pos))-(duct_width_x3D/2));
            P.r.x.pos = (P.p(1,:)) > (duct_width_x3D/2); %Check for reflections in x
direction (hit left edge of duct)
            particles_outside_right_after  = sum(P.r.x.pos);
        end
        if any(P.r.x.neg)
            particles_outside_left_before = sum(P.r.x.neg); % Count number of particles to
be reflected
            P.v(1,P.r.x.neg) = -(P.v(1,P.r.x.neg));
            P.p(1,P.r.x.neg) = (-duct_width_x3D/2)-((P.p(1,P.r.x.neg))+(duct_width_x3D/2));
            P.r.x.neg = (P.p(1,:)) < -(duct_width_x3D/2); %Check for reflections in x
direction (hit right edge of duct
            particles_outside_left_after  = sum(P.r.x.neg);
        end
 end
```

>>>Process circular duct reflections

```
 if sim_type == 'cir';
    if any(P.r.y.neg)
        fun = @(vectors,vectors_time) vectors.*vectors_time;
        Cir_vectors = P.v(1:2,P.r.y.neg); %Create matrix contain just x&y velocity vectors
        Cir_vectors_mag = sqrt(sum(Cir_vectors(1:2,:).^2)); %Calculate magitude of x&y
velocity vectors
        Cir_positional_overshoot = sqrt(sum(P.p(1:2,P.r.y.neg).^2))-cylr; %Calculate x&y
positional overshoot
        Cir_vectors_time = Cir_positional_overshoot./Cir_vectors_mag;
```

```
            Cir_position = P.p(1:2,P.r.y.neg)-(bsxfun(fun,Cir_vectors,Cir_vectors_time));
            vectors_mag_after = sqrt(sum(Cir_position(1:2).^2));
            s1=[-P.p(1:2,P.r.y.neg) ; zeros(1,sum(P.r.y.neg))]./cylr;%calculate unit normal to
surface
            P.v(:,P.r.y.neg)=P.v(:,P.r.y.neg)-2*s1*diag(sum(P.v(:,P.r.y.neg).*s1));%reflect
        end
    end
```

>>>Drop particles which go outside the cylinder ends

```
        keep=abs(P.p(3,:))< duct_length/2;%Keep particles where z is less than half duct
height
        P.p=P.p(:,keep);  P.v=P.v(:,keep);P.r.hit=P.r.hit(:,keep);
        P.r.x.neg=P.r.x.neg(:,keep); P.r.x.pos=P.r.x.pos(:,keep);
        P.r.y.neg=P.r.y.neg(:,keep); P.r.y.pos=P.r.y.pos(:,keep);
        P.r.r=P.r.r(:,keep); P.r.rs=P.r.rs(:,keep);
        P.p_hit=P.p_hit(:,keep);
        P.r.hit_past =P.r.hit_past(:,keep);
```

>>>Update particles with 3D air velocity data

```
        Simulation_time_step = (1/Fsamp)*bin_step_size;

P.p(1,:)=P.p(1,:)+(Inter_ndgrid_u(P.p(1,:),P.p(2,:),P.p(3,:))*Simulation_time_step);

P.p(2,:)=P.p(2,:)+(Inter_ndgrid_v(P.p(1,:),P.p(2,:),P.p(3,:))*Simulation_time_step);

P.p(3,:)=P.p(3,:)+(Inter_ndgrid_w(P.p(1,:),P.p(2,:),P.p(3,:))*Simulation_time_step);
```

>>>Increment simulation time steps

```
        if mod(Loop_count,Loop_count_dis_ratio) == 0
        delete(h_particles); %Delete visualisation of simulation particles
        end
        if sim_type == 'cir';
            if any(close_to_duct_wall)
                bin_step_size = 1
                Loop_count_dis_ratio = 500;
            else
            bin_step_size = randi([1 bin_max_div])
            Loop_count_dis_ratio = 10;
            end
        else
            bin_step_size = randi([1 bin_max_div])
            Loop_count_dis_ratio = 10;
        end

    end
```

>>O End of particle simulation Loop

```
 Hits_Total_all =  Hits_Total_all+sum(Hits_Total(:));
%delete(h_particle_hits_array);%Delete visualisation of particles past detector
Loop_count_array = [Loop_count_array Loop_count]; %Store sim step num count
```

Add 40khz bipolar pulse using filtering

```
bottom_left_plot = subplot(2,2,3);%Select figure 1 bottom left plot
pulse_samples_No = Fsamp/(Tran_f0/1.5); %Calculate number of samples required for the pulse
plus 50% more
pulse_samples_No_half = floor(pulse_samples_No/2); %Calculate +/- value of samples required
for the pulse
t = (-pulse_samples_No_half:pulse_samples_No_half)/Fsamp; %Calculate sample time series
tau = 4e-6;%Parameter for generating bipolar pulse
s = t.*exp(-t.^2/(2*tau^2));%Generate bipolar pulse for testing purposes
s = -s'./max(s); %Normalise (y rng becomes -1 to +1) bipolar pulse waveform levels
figure(6) %Create figure to display transmit waveform
set(gcf,'Name','Transmitter waveform')
subplot(2,1,[1,2])%Plot waveform with timescale of microseconds
plot(t*1e+6,s); grid on; xlabel('Time(\mus)'); ylabel('Norm amplitude');
figure(1) %Select main figure
subplot(bottom_left_plot)%Cross correlating particle time series histogram for each
detector
[c_pulse,lags_pulse] = xcorr(pulse(:,2),pulse(:,1));%-to find the delay between them
% figure(7) %Display cross correlation results if required
% plot(lags_pulse,c_pulse); grid on; xlabel('Lag'); ylabel('Cross-correlation');
% Find peak location to calculate time difference
[pks_lags_pos_pulse,locs_lags_pos_pulse]=findpeaks(c_pulse,'npeaks',1,'minpeakheight',max(c
```

```
_pulse/2));
lags_pos_pulse = locs_lags_pos_pulse*1/Fsamp;%Convert difference in number of time steps
into actual time difference
pulsebp=filter(s,1,pulse); %generate both receiver waveforms from transmit pulse waveform
and receiver histograms
plot_No = (length(pulsebp)-1);
h_pulsebp = plot((0:plot_No)*(Fsamp^-1*1e3),pulsebp),xlabel('Time (ms)'),ylabel('Pulse
Amplitude (Arbritrary Units)')
%Mark on plot the centre of the first waveform cycle at zero flow
h_line = line([(timeofinterest-(1/Tran_f0)/2)*10^3  (timeofinterest-(1/Tran_f0)/2)*10^3
],[0 max(pulsebp(:,1))],'Marker','.','LineStyle','-','Color','r')
set(gca,'xlim',[(timeofinterest-2*(1/Tran_f0))*1e3  (timeofinterest+2*(1/Tran_f0))*1e3
]),title('Detected Acoustic Pulse'), legend([h_pulsebp ;h_line],cellstr([num2str(u');'
ETA']),'Location','NorthWest')
hold on
[c,lags] = xcorr(pulsebp(:,2),pulsebp(:,1));%Cross correlating receiver waveforms for each
detector
%figure(8)
%plot(lags,c); grid on; xlabel('Lag'); ylabel('Cross-correlation');
[pks_lags_pos,locs_lags_pos] = findpeaks(c,'npeaks',1,'minpeakheight',max(c/2));
lags_pos = lags(locs_lags_pos)*1/Fsamp;
PhaseDiffpos_lags = (lags_pos/(25*10^-6))*360;
Duct_airflow_rate_correlation = (L/(2*cosd(theta_LZ)))*(1/(t_U0-lags_pos/2) -...
    1/(t_U0+lags_pos/2));
[pksUpos,locsUpos] =
findpeaks(pulsebp(:,1),'npeaks',1,'minpeakheight',max((pulsebp(:,1))/2));
[pksDpos,locsDpos] =
findpeaks(pulsebp(:,2),'npeaks',1,'minpeakheight',max((pulsebp(:,2))/2));
DiffPkpos = abs((locsUpos-locsDpos)/Fsamp);
[pksUneg,locsUneg] = findpeaks(-pulsebp(:,1),'npeaks',1,'minpeakheight',max((-
pulsebp(:,1))/2));
[pksDneg,locsDneg] = findpeaks(-pulsebp(:,2),'npeaks',1,'minpeakheight',max((-
pulsebp(:,2))/2));
DiffPkneg = abs((locsUneg-locsDneg)/Fsamp);
PhaseDiffpos(run) = (DiffPkpos/(25*10^-6))*360;
PhaseDiffneg(run) = (DiffPkneg/(25*10^-6))*360;
PhaseDiff(run) = mean([PhaseDiffpos(run) PhaseDiffneg(run)]);
if run>5 ks = run-5; else ks= 1; end
Mean_Phase = mean(PhaseDiff( ks:run));
Mean_Phase_Hist = [Mean_Phase_Hist Mean_Phase];
```

Calculate the speed of Airflow from phase angle in degree

```
%calculate approximate speed of sound from air temperature
%and length of a single wavelength
Spd_of_sound = 331.5+0.607*TempC;
Wave_length = Spd_of_sound/Tran_f0;
% Calculate anemometer equations input parameters
Duct_Sound_path_height_m = duct_width_x3D*2; %Duct height in metres
Duct_Sound_path_width_m = (u(1)-u(2));   %Effective longitudinal distance
% between transducers
% L=sqrt(Duct_Sound_path_height_m^2+((Duct_Sound_path_width_m/2)^2));
% L is the Sound path length in metres between transmitter and receiver
theta=atan2(Duct_Sound_path_height_m,Duct_Sound_path_width_m/2);
% Calculate wavelength per degree
wavelength_per_degree = Wave_length/360;
% Calculate actual sound path length difference in metres
% path_diff = wavelength_per_degree * Mean_Phase;
path_diff_now = wavelength_per_degree * PhaseDiff(run);
path_diff_lags = wavelength_per_degree * PhaseDiffpos_lags;
% Calculate time delays in seconds  for  ultrasonic paths  forward and
% backwards between transmit and  both receivers
tR1=(L+(path_diff_lags/2))/Spd_of_sound; %calculate delay for backwards path
tR2=(L-(path_diff_lags/2))/Spd_of_sound; %calculate delay for forwards path
tR1_tR2_diff = tR1-tR2;
tR1_now=(L+(path_diff_now/2))/Spd_of_sound; %calculate delay for backwards path
tR2_now=(L-(path_diff_now/2))/Spd_of_sound; %calculate delay for forwards path
tR1_tR2_diff_now = tR1_now-tR2_now;
% Calculate the flow velocity using the Contra propagating differential
% transit time method
u_cal_correlation(run)=(L/(2*cos(theta)))*(1/tR2-1/tR1);
u_cal_pk_phase(run)=(L/(2*cos(theta)))*(1/tR2_now-1/tR1_now);
u_cal_TOF_pos=(L/(2*cos(theta)))*(1/(locsUpos/Fsamp)-1/(locsDpos/Fsamp));
u_cal_TOF_neg=(L/(2*cos(theta)))*(1/(locsUneg/Fsamp)-1/(locsDneg/Fsamp));
u_cal_TOF(run)= mean([u_cal_TOF_pos,u_cal_TOF_neg]);
bottom_right_plot = subplot(2,2,4);
plot(u_cal_pk_phase(1:run),'r');
hold all
plot(u_cal_TOF(1:run),'--g');
plot(u_cal_correlation(1:run),':b');
xlabel('Run number');
ylabel('Airflow m/s');
title(['Calculated mean airflow speed m/s CFD mean flow ',...
    num2str(Duct_airflow_rate),' m/s mean along x=0 '...
    num2str(Duct_all_points_3D_w_x0_across_y_z0_mean),' m/s']);
legend(['pk to pk Phase ',num2str(u_cal_pk_phase(run))],[' TOF
',num2str(u_cal_TOF(run))],[' Correl
',num2str(u_cal_correlation(run))],'Location','NorthWest');
text(run,u_cal_correlation(run),[num2str(u_cal_correlation(run),'%4.2f' ),' ']);
subplot(top_plot);
Num_particles = round(Num_particles*(1/(size(P.p,2)/(Hits_required/3))));
```

```
end
%Collate the results of each run
Results_files = [Results_files; sheet];
Results_Dh = [Results_Dh; Dh];
Results_n = [Results_n; Num_particles];
Results_nrun = [Results_nrun; run];
Results_DuctAirflowRate = [Results_DuctAirflowRate; Duct_airflow_rate];
Results_Duct_airflow_rate_predicted_error_rng_val_mps =
[Results_Duct_airflow_rate_predicted_error_rng_val_mps;
Duct_airflow_rate_predicted_error_rng_val_mps];
Results_predicted_error_rng_val_mps_error_percent =
[Results_predicted_error_rng_val_mps_error_percent;...
    ((Duct_airflow_rate_predicted_error_rng_val_mps/Duct_airflow_rate))*100];
Results_DuctType = [Results_DuctType; sim_type];
Results_DuctWidth = [Results_DuctWidth; duct_width_x3D ];
Results_Z = [Results_Z; Z];
Results_Duct_log_T_all_points_3D_mean_w = [Results_Duct_log_T_all_points_3D_mean_w;
Duct_log_T_all_points_3D_mean_w];
Results_PhaseDiff = [Results_PhaseDiff; PhaseDiff(run)];
Results_u_cal_pk_phase = [Results_u_cal_pk_phase; u_cal_pk_phase(run)];
Results_u_cal_TOF = [Results_u_cal_TOF; u_cal_TOF(run)];
Results_u_cal_correlation = [Results_u_cal_correlation; u_cal_correlation(run)];
Results_u_cal_correlation_error_percent = [Results_u_cal_correlation_error_percent;...
    ((u_cal_correlation(run)/Duct_airflow_rate)-1)*100];
Results_Duct_all_points_3D_w_x0_across_y_z0_mean =
[Results_Duct_all_points_3D_w_x0_across_y_z0_mean;...
        Duct_all_points_3D_w_x0_across_y_z0_mean];
Results_Duct_all_points_3D_w_across_x_y0_z0_mean =
[Results_Duct_all_points_3D_w_across_x_y0_z0_mean;...
        Duct_all_points_3D_w_across_x_y0_z0_mean];
Results_Duct_0dot5_width_w = [Results_Duct_0dot5_width_w; Duct_0dot5_width_w];
Results_Duct_dist_mean_flow = [Results_Duct_dist_mean_flow; Duct_dist_mean_flow];
Results_fsamp = [Results_fsamp; Fsamp];
Results_Loop_count_avg = [Results_Loop_count_avg; mean(Loop_count_array) ];
%Store results in table if more than one has been completed
if (size(Results_files,1)) >1
Results_Table = table(...
    Results_files,...
    Results_Dh,...
    Results_n,...
    Results_nrun,...
    Results_Loop_count_avg,...
    Results_DuctAirflowRate,...
    Results_Duct_airflow_rate_predicted_error_rng_val_mps,...
    Results_predicted_error_rng_val_mps_error_percent,...
    Results_DuctWidth,...
    Results_DuctType,...
    Results_Z,...
    Results_Duct_log_T_all_points_3D_mean_w,...
    Results_PhaseDiff,...
    Results_u_cal_pk_phase,...
    Results_u_cal_TOF,...
    Results_u_cal_correlation,...
    Results_u_cal_correlation_error_percent,...
    Results_Duct_all_points_3D_w_x0_across_y_z0_mean,...
    Results_Duct_all_points_3D_w_across_x_y0_z0_mean,...
    Results_Duct_0dot5_width_w,...
    Results_Duct_dist_mean_flow,...
    Results_fsamp);
figure(h_figure_table);%Generate figure table of results
Results_Table_cell = table2cell(Results_Table);
t = uitable(h_figure_table,'Data',Results_Table_cell,'ColumnWidth','auto',...
'ColumnName',Results_Table.Properties.VariableNames);
%Get the Java scroll-pane container reference
jScrollPanel = findjobj(t);
%Modify the scroll-pane's scrollbar policies
%(note the equivalent alternative methods used below)
set(jScrollPanel,'VerticalScrollBarPolicy',22);  % or:
jScrollPane.VERTICAL_SCROLLBAR_AS_NEEDED
jScrollPanel.setHorizontalScrollBarPolicy(32);  % or:
jScrollPane.HORIZONTAL_SCROLLBAR_AS_NEEDED
%Write results two, separated spreadsheet file
writetable(Results_Table,[ FILENAME_STR,'_Results_v2.csv']);
%Set table width and height
table_extent = get(t,'Extent');
old_position = get(t,'Position');
table1_figure_oldposition = get(h_figure_table,'Position');
table1_figure_newposition = [scrsz(1)+50 scrsz(2)+50 scrsz(3)-100 scrsz(4)-100];
newposition = [table1_figure_newposition(1) table1_figure_newposition(2)
table1_figure_newposition(3)-100 table1_figure_newposition(4)-100];
set(t, 'Position', newposition);
set(h_figure_table, 'Position', table1_figure_newposition);
end %if result table size is >1
pause(3); %Pause simulation 3 seconds

end %for array of Dh values
end %for duct flow velocity scenarios, which is one per excel sheet
```

References

[1] "UK energy in brief 2015," [Online]. Available: https://www.gov.uk/government/statistics/uk-energy-in-brief-2015 [Accessed: 7 August 2015], 2015.

[2] "Fuel price indices for the domestic sector, 1996 to 2015 [Graph]. UK energy in brief 2015," Retrieved from: https://www.gov.uk/government/statistics/uk-energy-in-brief-2015 [Accessed: 29 April 2015], 2015.

[3] C. T. Tran, P. Rivière, D. Marchio, and C. Arzano-Daurelle, "Refrigerant-based measurement method of heat pump seasonal performances," *International Journal of Refrigeration*, vol. 35, no. 6, pp. 1583–1594, 2012.

[4] "RHI Evidence Report: Reversible Air to Air Heat Pumps 29th October 2011," [Online]. Available: https://www.gov.uk/government/uploads/system/uploads/attachment_data/file/371697/RHI_Evidence_Report_-_Reversible_Air_to_Air_Heat_Pumps.pdf [Accessed: 21 November 2014], 2014.

[5] A. Won, T. Ichikawa, S. Yoshida, and S. Sadohara, "Study on Running Performance of a Split-type Air Conditioning System Installed in the National University Campus in Japan," *JOURNAL OF ASIAN ARCHITECTURE AND BUILDING ENGINEERING*, vol. 8, no. 2, pp. 579–583, Nov. 2009.

[6] "Renewable Heat Incentive March 2011," [Online]. Available: https://www.gov.uk/government/uploads/system/uploads/attachment_data/file/48041/1387-renewable-heat-incentive.pdf [Accessed: 21 November 2014], 2011.

[7] J. Cui and S. Wang, "A model-based online fault detection and diagnosis strategy for centrifugal chiller systems," *Int. J. Therm. Sci.*, vol. 44, no. 10, p. 986, 2005.

[8] A. Dexter and J. Pakanen, "Fault detection and diagnosis methods in real buildings. International Energy Agency, Energy Conservation in Buildings and Community Systems, Annex 34: Computer-aided evaluation of HVAC system performance," [Online]. Available: http://www.ecbcs.org/annexes/annex34.htm [Accessed: 12 September 2014], 2001.

[9] Y. Yu, D. Woradechjumroen, and D. Yu, "A review of fault detection and diagnosis methodologies on air-handling units," *Energy Build.*, vol. 82, no. 0, p. 555, 2014.

[10] D. Yu, H. Li, and M. Yang, "A virtual supply airflow rate meter for rooftop air-conditioning units," *Build Environ*, vol. 46, no. 6, p. 1292, 2011.

[11] W. H. Organization and others, "Burden of disease from household air pollution for 2012," *World Health Organization*, 2014.

[12] S. Holgate, J. Grigg, R. Agius, J. R. Ashton, P. Cullinan, K. Exley, D. Fishwick, G. Fuller, N. Gokani, C. Griffiths, and others, "Every breath we take: The lifelong impact of air pollution, Report of a working party.," 2016.

[13] A. B. Raine, N. Aslam, C. P. Underwood, and S. Danaher, "Development of an ultrasonic airflow measurement device for ducted air," *Sensors (Switzerland)*, vol. 15, no. 5, pp. 10705–10722, 2015.

[14] M. I. Bragg and L. C. Lynnworth, “Internally-nonprotruding one-port ultrasonic flow sensors for air and some other gases,” in *Control, 1994. Control ’94. International Conference on*, 1994, vol. 2, pp. 1241–1247 vol.2.

[15] J. Strauss, H. Weinberg, and Z. Kopel, “Ultrasound air velocity detector for HVAC ducts and method therefor,” U.S. Patent 5 583 30110-Dec-1996.

[16] “Neptronic Patents.,” [Online]. Available: http://www.neptronic.com/NeptronicPatents.aspx [Accessed: 30 March 2016] (Archived by WebCite® at http://www.webcitation.org/6gOhIfzpE), 2013.

[17] R. A. Rabalais and L. Sims, “Ultrasonic Flow Measurement: Technology and Applications in Process and Multiple Vent Stream Situations,” [Online]. Available: https://www.idc-online.com/technical_references/pdfs/instrumentation/Ultrasonic_Flow_Measurement.pdf [Accessed: 15 September 2014] (Archived by WebCite® at http://www.webcitation.org/6icsohrV3), 2002.

[18] K. Conrad and L. Lynnworth, “Fundamentals of ultrasonic flow meters,” in *American School of Gas Measurement Technology*, 2002, vol. 1, pp. 53–54.

[19] P. Olmos, “Ultrasonic velocity meter to evaluate the behaviour of a solar chimney,” *Meas. Sci. Technol.*, vol. 15, no. 7, p. N49, 2004.

[20] P. Olmos, “Extending the accuracy of ultrasonic level meters,” *Meas. Sci. Technol.*, vol. 13, no. 4, pp. 598–600, 2002.

[21] S. Van Buggenhout, S. E. Ozcan, E. Vranken, W. Van Malcot, and D. Berckmans, “Acoustical ventilation rate sensor concept for naturally ventilated buildings,” in *ASHRAE TRANSACTIONS 2007 VOL 113, PT 2*, 2007, vol. 113, no. 2, pp. 192–199.

[22] S. Van Buggenhout, S. E. Ozcan, E. Vranken, W. Van Malcot, and D. Berckmans, “Photograph of sensor prototype with 32 acoustieal sensors [Photograph]. In: Acoustical ventilation rate sensor concept for naturally ventilated buildings,” in *ASHRAE TRANSACTIONS 2007 VOL 113, PT 2*, 2007, vol. 113, no. 2, pp. 192–199.

[23] “acam messelectronic gmbh: TDC-GP2,” [Online]. Available: http://www.acam.de/products/time-to-digital-converter/tdc-gp2/ [Accessed: 27 June 2014].

[24] Q. Chen, W. Li, and J. Wu, “Corrigendum to “Realization of a multipath ultrasonic gas flowmeter based on transit-time technique [Ultrasonics 54 (2014) 285–290],” *Ultrasonics*, vol. 54, no. 6, p. 1715 –, 2014.

[25] Q. Chen, W. Li, and J. Wu, “Realization of a multipath ultrasonic gas flowmeter based on transit-time technique,” *Ultrasonics*, vol. 54, no. 1, pp. 285–290, Jan. 2014.

[26] Q. Chen, W. Li, and J. Wu, “Two parallel-chord paths flowmeter body [Photograph]. In: Realization of a multipath ultrasonic gas flowmeter based on transit-time technique,” *Ultrasonics*, vol. 54, no. 1, p. 287, Jan. 2014.

[27] Q. Chen, W. Li, and J. Wu, “Schematic diagram of the ultrasonic flowmeter system [Diagram]. In: Realization of a multipath ultrasonic gas flowmeter based on transit-time technique,” *Ultrasonics*, vol. 54, no. 1, p. 286, Jan. 2014.

[28] M. Ashraf and H. Qayyum, “High Accuracy Time of Flight Measurement Using Digital Signal Processing Techniques for Subsea Applications,”

Journal of Signal and Information Processing, vol. Vol. 2, pp. 330–335, 2011.

[29] H. Hou, D. Zheng, and L. Nie, “Gas ultrasonic flow rate measurement through genetic-ant colony optimization based on the ultrasonic pulse received signal model,” *Measurement Science and Technology*, vol. 26, no. 4, p. 045005, 2015.

[30] J. Reyes, “Modeling and simulation of ultrasonic flow meters: State of art,” in *2010 IEEE ANDESCON Conference Proceedings, ANDESCON 2010*, 2010.

[31] D. A. Bohn, “Environmental Effects on the Speed of Sound,” *J. Audio Eng. Soc.*, vol. 36, no. 4, pp. 223–231, Apr. 1988.

[32] J. Reyes and A. Acevedo, “Simulation and experimental validation of a transit time in an ultrasonic gas flow meter using air,” in *ANDESCON, 2010 IEEE*, 2010, pp. 1–6.

[33] D. Han, S. Kim, and S. Park, “Two-dimensional ultrasonic anemometer using the directivity angle of an ultrasonic sensor,” *Microelectron. J.*, vol. 39, no. 10, pp. 1195–1199, 2008.

[34] J. Krause, “Ultrasonic Flow-meter and the Acoustic Waveguide in a Moving Medium,” in *COMSOL Users Conference 2007 Grenoble*, 2007.

[35] M. Willatzen, “Perturbation theory applied to sound propagation in flowing media confined by a cylindrical waveguide,” *Journal of the Acoustical Society of America*, vol. 109, no. 1, pp. 102–107, 2001.

[36] J. Krause, “Figure 4: Flow profile for three Reynolds-numbers as used in the turbulent model. [Graph]. In: Ultrasonic Flow-meter and the Acoustic Waveguide in a Moving Medium,” in *COMSOL Users Conference 2007 Grenoble*, 2007.

[37] K. Lien, J. Monty, M. Chong, and A. Ooi, “The entrance length for fully developed turbulent channel flow,” in *15th Australian Fluid Mechanics Conference*, 2004, vol. 15, pp. 356–363.

[38] K. Muramatsu, A. Kimoto, and S. Takahashi, “3D transient analysis of ultrasonic propagation in flow field using finite difference time domain method,” in *ICCAS-SICE, 2009*, 2009, pp. 3343–3346.

[39] A. Luca, R. Marchiano, and J.-C. Chassaing, “Numerical Simulation of Transit-Time Ultrasonic Flowmeters by a Direct Approach,” *IEEE transactions on ultrasonics, ferroelectrics, and frequency control*, vol. 63, no. 6, pp. 886–897, 2016.

[40] F. J. Weber Jr, “Ultrasonic beam propagation in turbulent flow,” WORCESTER POLYTECHNIC INSTITUTE, 2003.

[41] F. J. Weber Jr, “Figure 7-1 Flow Chart for Modified Ray Trace Method Computer Program [Flowchart]. In: Ultrasonic beam propagation in turbulent flow,” WORCESTER POLYTECHNIC INSTITUTE, 2003.

[42] B. Iooss, C. Lhuillier, and H. Jeanneau, “Numerical simulation of transit-time ultrasonic flowmeters: uncertainties due to flow profile and fluid turbulence,” *Ultrasonics*, vol. 40, no. 9, pp. 1009–1015, 2002.

[43] M. Bezděk, A. Rieder, H. Landes, R. Lerch, and W. Drahm, “A novel numerical method for simulating wave propagation in moving media,” in *Ultrasonics Symposium, 2004 IEEE*, 2004, vol. 2, pp. 934–937.

[44] M. Bezděk, A. Rieder, H. Landes, R. Lerch, and W. Drahm, “A novel boundary integral formulation for acoustic radiation in a nonuniform flow: Coupling to FEM and applications,” in *Proceedings - IEEE Ultrasonics Symposium*, 2005, vol. 2, pp. 771–774.

[45] M. Bezděk, A. Rieder, H. Landes, R. Lerch, and W. Drahm, “Fig. 1. The coupled FEM-HIRM simulation scheme. [Drawing]. In: A novel boundary integral formulation for acoustic radiation in a nonuniform flow: Coupling to FEM and applications,” in *Proceedings - IEEE Ultrasonics Symposium*, 2005, vol. 2, p. 771.

[46] *ASHRAE Standard 134-2005 (RA 2014) – Graphic Symbols for Heating, Ventilating, Air-Conditioning, and Refrigerating Systems (ANSI Approved)*. Atlanta, Ga: American Society of Heating, Refrigerating and Air Conditioning Engineers, 2014, p. 80.

[47] *ASHRAE handbook, 2009, Fundamentals*, S.I. edition. Atlanta, Ga: American Society of Heating, Refrigerating and Air Conditioning Engineers, 2009.

[48] P. A. Domanski, H. I. Henderson, and W. V. Payne, “Sensitivity Analysis of Installation Faults on Heat Pump Performance,” National Institute of Standards and Technology, Gaithersburg, MD 20899-8631, Technical Note 1848, Sep. 2014.

[49] “Seebeck effect,” in A Dictionary of Physics, Oxford Reference, 2009, [Online]. Available: http://www.oxfordreference.com [Accessed: 1 July 2016].

[50] *BS EN 16211:2015 Ventilation for buildings. Measurement of air flows on site. Methods. [Online] British Standards Online [Online]. Available: https://bsol.bsigroup.com/ [Accessed: 19 May 2016]*. British Standards Institution, 2015.

[51] S. Mannan, *Lees’ Loss prevention in the process industries: Hazard identification, assessment and control*. Butterworth-Heinemann, 2012, p. 15/7.

[52] “Airflow Type 4 Test Set Operation Instructions,” [Online]. Available: http://tsi.com/uploadedFiles/Product_Information/Literature/Manuals/Type_4_Test_Set_9004491-D-196.pdf [Accessed: 11 November 2014].

[53] “Airflow Type 5 Test Set Operating Instructions,” [Online]. Available: http://www.tsi.com/uploadedFiles/Product_Information/Literature/Manuals/Type_5_Test_Set_manual-99004492D02.pdf [Accessed: 11 November 2014].

[54] *Guide to meteorological instruments and methods of observation. Supplement*. Geneva: World Meteorological Organization, p. 124.

[55] J. P. Bentley, *Principles of measurement systems*, 4th ed. Harlow: Pearson/Prentice Hall, 2005.

[56] K. Noraznafulsima, “Temperature Compensation of a Thermal Flow Sensor by using Temperature Compensation Network,” 2009.

[57] R. Y. Que, R. Zhu, Q. Z. Wei, and Z. Cao, “Temperature compensation for thermal anemometers using temperature sensors independent of flow sensors,” *Measurement Science and Technology*, vol. 22, no. 8, p. 085404, 2011.

[58] L. C. Lynnworth and Y. Liu, “Ultrasonic flowmeters: Half-century progress report, 1955-2005,” *Ultrasonics*, vol. 44, no. 1, pp. E1371–E1378, 2006.

[59] R. C. Swengel, “Fluid velocity measuring system,” U.S. Patent 2 746 29122-May-1956.

[60] R. C. Swengel, “Fig. 1. is a block diagram. of a velocity measuring system embodying the invention. [Diagram]. In. Fluid velocity measuring system,” U.S. Patent 2 746 29122-May-1956.

[61] R. C. Swengel, “Fig. 3. is a block diagram of a modified measuring system. [Diagram]. In. Fluid velocity measuring system,” U.S. Patent 2 746 29122-May-1956.

[62] G. T. Bui, Y.-T. Jiang, and D.-C. Pang, “Two Capacitive Micro-Machined Ultrasonic Transducers for Wind Speed Measurement,” *Sensors*, vol. 16, no. 6, p. 814, 2016.

[63] M. Kupnik, E. Krasser, and M. Groschl, “3D-1 Absolute Transit Time Detection for Ultrasonic Gas Flowmeters Based on Time and Phase Domain Characteristics,” in *Ultrasonics Symposium, 2007. IEEE*, 2007, pp. 142–145.

[64] V. Pavlovi, B. Dimitrijevi, M. Stojcev, L. Golubovi, M. Živkovi, and L. Stamenkovi, “Realization of the ultrasonic liquid flowmeter based on the pulse-phase method,” *Ultrasonics*, vol. 35, no. 1, pp. 87–102, 1997.

[65] D. Han and S. Park, “A study on characteristics of continuous wave ultrasonic anemometer,” in *Sensors Applications Symposium (SAS), 2011 IEEE*, 2011, pp. 119–122.

[66] D. Han and S. Park, “Measurement range expansion of continuous wave ultrasonic anemometer,” *Measurement*, vol. 44, no. 10, pp. 1909–1914, 2011.

[67] D. Han, S. Kim, and S. Park, “Photograph of produced sensor module [Photograph]. In,” *Microelectron. J.*, vol. 39, no. 10, p. 1197, 2008.

[68] D. Han, S. Kim, and S. Park, “Block diagram of inner structure in receiving circuit [Diagram]. In,” *Microelectron. J.*, vol. 39, no. 10, p. 1197, 2008.

[69] J. P. Bentley, *Figure 12.21 Cross- correlation flowmeter – schematic diagrams and typical signals [Diagram]. In Principles of measurement systems*, 4th ed. Harlow: Pearson/Prentice Hall, 2005, p. 345.

[70] M. J. Scelzo, “A Clamp-On Ultrasonic Flowmeter for Gases,” [Online]. Available: https://www.gemeasurement.com/sites/gemc.dev/files/article-_a_clamp-on_ultrasonic_flowmeter_for_gases_1.6mb_pdf_english.pdf [Accessed: 24 October 2014] (Archived by WebCite® at http://www.webcitation.org/6iclzSpN2), 2001.

[71] M. Ding and U. S. O. of Naval Research., *Proceedings of the 5th Experimental Chaos Conference : June 28-July 1, 1999, Orlando, Florida*. Singapore ; River Edge, NJ: World Scientific, 2001.

[72] M. A. Crabtree, “Industrial flow measurement,” University of Huddersfield, Jun-2009.

[73] S. Kapartis, “Ultrasonic flow velocity sensor and method of measuring the velocity of a fluid flow, EP Patent App. EP19,970,302,423,” 1997.

[74] “Gas mass flow measurement from SICK,” [Online]. Available: https://www.sick.com/gb/en/product-portfolio/ultrasonic-gas-flow-measuring-

devices/mass-flow-measuring-devices/c/g288752 [Accessed: 29 June 2016] (Archived by WebCite® at http://www.webcitation.org/6iczQVBa2), 2016.

[75] G. Andria, F. Attivissimo, and N. Giaquinto, “Digital signal processing techniques for accurate ultrasonic sensor measurement,” *Measurement*, vol. 30, no. 2, pp. 105–114, 2001.

[76] S. Hirata, M. K. Kurosawa, and T. Katagiri, “Real-time ultrasonic distance measurements for autonomous mobile robots using cross correlation by single-bit signal processing,” in *Robotics and Automation, 2009. ICRA ’09. IEEE International Conference on*, 2009, pp. 3601–3606.

[77] A. Naba, M. F. Khoironi, and D. J. D. H. Santjojo, “Low cost but accurate ultrasonic distance measurement using combined method of threshold-correlation,” in *14th International Conference on QiR (Quality in Research), QiR 2015 - In conjunction with 4th Asian Symposium on Material Processing, ASMP 2015 and International Conference in Saving Energy in Refrigeration and Air Conditioning, ICSERA 2015*, 2015, pp. 23–25.

[78] M. Parrilla, J. J. Anaya, and C. Fritsch, “Digital signal processing techniques for high accuracy ultrasonic range measurements,” *Instrumentation and Measurement, IEEE Transactions on*, vol. 40, no. 4, pp. 759–763, Aug. 1991.

[79] F. Hofmann, “Fundamentals of Ultrasonic-flow measurement for industrial applications,” [Online]. Available: http://www.investigacion.frc.utn.edu.ar/sensores/Caudal/HB_ULTRASONIC_e_144.pdf [Accessed: 12 September 2014] (Archived by WebCite® at http://www.webcitation.org/6id3wrD7I), 2001.

[80] “GE’s Panametrics DigitalFlow™ GM868 general-purpose flow meter,” [Online]. Available: https://www.gemeasurement.com/flow-measurement/ultrasonic-gas/digitalflowtm-gm868-general-purpose-gas-ultrasonic-flow-meter [Accessed: 1 June 2016] (Archived by WebCite® at http://www.webcitation.org/6id4C0E4e), 2016.

[81] “GE’s Panametrics GF868 flare gas flow meter,” [Online]. Available: https://www.gemeasurement.com/flow-measurement/ultrasonic-gas/digitalflow-gf868-flare-gas-mass-ultrasonic-flow-meter [Accessed: 2 June 2016) (Archived by WebCite® at http://www.webcitation.org/6id4LgeYu), 2016.

[82] “Maestro AirScout Flowmeter system,” [Online]. Available: http://www.maestroventilation.com/products/airscout-flowmeter-air-flowmeter [Accessed: 2 June 2016], 2016.

[83] “FlowTRAX Ultrasonic Airflow Monitor,” [Online]. Available: http://accutroninstruments.com/flowtrax/ [Accessed: 2 June 2016] (Archived by WebCite® at http://www.webcitation.org/6id5BDGaq), 2016.

[84] “TunnelTech 301 Air Flow Monitor,” [Online]. Available: http://www.codel.co.uk/products/tunnel-sensors/flow-monitors/air-flow/ [Accessed: 6 June 2016] (Archived by WebCite® at http://www.webcitation.org/6id5K0wTl), 2016.

[85] M. Tauch, K. Witrisal, K. Kudlaty, S. Noehammer, and M. Wiesinger, “System identification method for Ultrasonic Intake Air Flow Meter for engine test bed applications,” in *Instrumentation and Measurement Technology Conference (I2MTC), 2012 IEEE International*, 2012, pp. 544–548.

[86] “AVL FLOWSONIX,” [Online]. Available: https://www.avl.com/-/avl-flowsonix-air [Accessed: 2 June 2016] (Archived by WebCite® at http://www.webcitation.org/6id5eO0gW), 2016.

[87] G. De Cicco, B. Morten, M. Prudenziati, A. Taroni, and C. Canali, “A 250 KHz Piezoelectric Transducer for Operation in Air: Application to Distance and Wind Velocity Measurements,” in *1982 Ultrasonics Symposium*, 1982, pp. 321–324.

[88] J. Lie, V. Tiponut, I. Bogdanov, S. Ionel, and C. D. Caleanu, “The Development of CPLD-based Ultrasonic Flowmeter,” in *Proceedings of the 11th Conference on Proceedings of the 11th WSEAS International Conference on Circuits - Volume 11*, 2007, pp. 190–193.

[89] W. Ooppakaew, “Advanced signal processing techniques for underwater acoustic transmission using steerable transducer arrays,” [Online]. Available: http://nrl.northumbria.ac.uk/11371/ [Accessed: 3 August 2015], 2012.

[90] “AVAGO; Low On-Resistance Solid State Relays; Application Note 1046,” [Online]. Available: http://www.avagotech.com/docs/5965-5978E [Accessed: 3 July 2014] (Archived by WebCite® at http://www.webcitation.org/6id69kZtt).

[91] W. Ooppakaew and S. Danaher, “Hydrophone calibration based on microcontrollers for acoustic detection of {UHE} neutrinos,” *Nuclear Instruments and Methods in Physics Research Section A: Accelerators, Spectrometers, Detectors and Associated Equipment*, vol. 662, Supplement 1, no. 0, pp. S249 – S253, 2012.

[92] C. H. Cai and P. P. L. Regtien, “Accurate Digital Time-Of-Flight Measurement Using Self-Interference,” *IEEE Trans. Instrum. Meas.*, vol. 42, no. 6, pp. 990–994, 1993.

[93] H. Ji-De, L. Chih-Kung, Y. Chau-Shioung, W. Wen-Jong, and L. Chih-Ting, “High-Precision Ultrasonic Ranging System Platform Based on Peak-Detected Self-Interference Technique,” *IEEE Trans. Instrum. Meas.*, vol. 60, no. 12, pp. 3775–3780, 2011.

[94] K. D. Wong, “A Sensitive DIY Ultrasonic Range Sensor,” [Online]. Available: http://www.kerrywong.com/2011/01/22/a-sensitive-diy-ultrasonic-range-sensor/ [Accessed: 4 August 2015] (Archived by WebCite® at http://www.webcitation.org/6id6Pxl5B), 2011.

[95] G. L. Miller, R. A. Boie, and M. Sibilia, “Active damping of ultrasonic transducers for robotic applications,” in *1984 IEEE International Conference on Robotics and Automation. Proceedings.*, 1984, vol. 1, pp. 379–384.

[96] W. Leach, “Dr. Leach’s Noise Potpourri,” [Online]. Available: http://users.ece.gatech.edu/mleach/ece4435/filtrpot.pdf [Accessed: 27 July 2015] (Archived by WebCite® at http://www.webcitation.org/6id6owkgw), 2003.

[97] C. Kitchin, “Biasing and Decoupling Op Amps in Single Supply Applications,” [Online]. Available: http://www.analog.com/media/en/technical-documentation/application-notes/AN-581.pdf [Accessed: 28 July 2014] (Archived by WebCite® at http://www.webcitation.org/6id76TALw), 2002.

[98] W. Howe, L. Dinapoli, and J. Arant, “2.29 Venturi Tubes, Flow Tubes, and Flow Nozzles,” *Instrument Engineers’ Handbook: Process measurement and analysis*, p. 374, 2003.

[99] A. A. Quaranta, G. C. Aprilesi, G. D. Cicco, and A. Taroni, “A microprocessor based, three axes, ultrasonic anemometer,” *J. Phys. E: Sci. Instrum.*, vol. 18, no. 5, p. 384, 1985.

[100] R. C. Baker, *Flow measurement handbook : industrial designs, operating principles, performance, and applications*. Cambridge: Cambridge University Press, 2000, pp. 24–29.

[101] U. Gessner, “The Performance of the Ultrasonic Flowmeter in Complex Velocity Profiles,” *Biomedical Engineering, IEEE Transactions on*, vol. BME-16, no. 2, pp. 139–142, Apr. 1969.

[102] J. C. Jung and P.-H. Seong, “Estimation of the flow profile correction factor of a transit-time ultrasonic flow meter for the feedwater flow measurement in a nuclear power plant,” *IEEE Trans. Nucl. Sci.*, vol. 52, no. 3, pp. 714–718, Jun. 2005.

[103] B. Mickan, G. Wendt, R. Kramer, and D. Dopheide, “Systematic investigation of flow profiles in pipes and their effects on gas meter behaviour,” *Measurement*, vol. 22, no. 1–2, pp. 1–14, 1997.

[104] P. Lunde, K.-E. Froysa, and M. Vestrheim, *GERG Project on Ultrasonic Gas Flow Meters: Phase II*. VDI Verlag, 2000.

[105] L. Qin, L. Hu, K. Mao, W. Chen, and X. Fu, “Application of extreme learning machine to gas flow measurement with multipath acoustic transducers,” *Flow Measurement and Instrumentation*, vol. 49, pp. 31–39, 2016.

[106] Y. Yu and G. Zong, “Design and simulation of an ultrasonic flow meter for thin pipe,” in *Mechatronics and Automation (ICMA), 2011 International Conference on*, 2011, pp. 1115–1119.

[107] H. . Zhao, L. . Peng, T. . Takahashi, T. . Hayashi, K. . Shimizu, and T. . Yamamoto, “CFD-aided investigation of sound path position and orientation for a dual-path ultrasonic flowmeter with square pipe,” *IEEE Sensors Journal*, vol. 15, no. 1, pp. 128–137, 2015.

[108] D. Zheng, P. Zhang, T. Zhang, and D. Zhao, “A method based on a novel flow pattern model for the flow adaptability study of ultrasonic flowmeter,” *Flow Measurement and Instrumentation*, vol. 29, pp. 25–31, 2013.

[109] W. Frei, “Which Turbulence Model Should I Choose for my CFD Application?.,” [Online]. Available: http://www.comsol.com/blogs/which-turbulence-model-should-choose-cfd-application/. [Accessed: 19 June] (Archived by WebCite® at http://www.webcitation.org/6ZPGz3FAG).

[110] J. G. Drenthen and G. de Boer, “The manufacturing of ultrasonic gas flow meters,” *Flow Measurement and Instrumentation*, vol. 12, no. 2, pp. 89–99, 2001.

[111] M. V. Zagarola and A. J. Smits, “Mean-flow scaling of turbulent pipe flow,” *Journal of Fluid Mechanics*, vol. 373, pp. 33–79, 1998.

[112] *AMCA Publication 611-10 Certified Ratings Program - Product Rating Manual for Airflow Measurement Stations. AMCA Publications & Standards [Online] Available at:http://www.amca.org/store/ (Accessed: 22/04/2015)*. Air Movement and Control Association International, Inc., 2010.

[113] *BS EN 14277:2006 Ventilation for buildings. Air terminal devices. Method for airflow measurement by calibrated sensors in or close to ATD/plenum boxes. British Standards Online [Online] Available at: https://bsol.bsigroup.com/ (Accessed: 21/04/2015)*. British Standards Institution, 2006.

[114] A. Martikainen, H. Dougherty, C. Taylor, and A. Mazzella, "Sonic anemometer airflow monitoring technique for use in underground mines (Archived by WebCite® at http://www.webcitation.org/6idAmHU0T)," in *Proceedings of the 13th US/North American Mine Ventilation Symposium*, 2010, pp. 13–17.

[115] G. Chen, G. Liu, B. Zhu, and W. Tan, "3D Isosceles Triangular Ultrasonic Path of Transit-Time Ultrasonic Flowmeter: Theoretical Design and CFD Simulations," *IEEE Sensors Journal*, vol. 15, no. 9, pp. 4733–4742, 2015.

[116] M. J. Pattison, "Secondary Flows," [Online]. Available: http://www.thermopedia.com [Accessed: 28 April 2015], 2015.

[117] S. Bevan, A. Brown, S. Danaher, J. Perkin, C. Rhodes, T. Sloan, L. Thompson, O. Veledar, and D. Waters, "Study of the acoustic signature of UHE neutrino interactions in water and ice," *Nuclear Instruments and Methods in Physics Research, Section A: Accelerators, Spectrometers, Detectors and Associated Equipment*, vol. 607, no. 2, pp. 398–411, 2009.

[118] A. Murray, "Cheapest energy tariffs tumble from £1,000 to below £750 in two years: our guide to today's cheapest deals," [Online]. Available: http://www.telegraph.co.uk/bills-and-utilities/gas-electric/falling-energy-prices-this-is-the-best-way-to-take-advantage/ [Accessed on 7 June 2016], 2016.

[119] "Pro-Wave Electronics Corp: Selection and use of Ultrasonic Ceramic Transducers," [Online]. Available: http://www.prowave.com.tw/pdf/an0508309.pdf [Accessed: 5 December 2014].

[120] "Quantelec: Selection and use of ultrasonic ceramic transducers," [Online]. Available: http://www.eng.newcastle.edu.au/eecs/fyweb/Archives/2004/c9608650/8576.pdf [Accessed: 12 December 2014].

[121] W. Ooppakaew, "Figure C.6 Schematic of PA94 power amplifier module. [Schematic]. In: Advanced signal processing techniques for underwater acoustic transmission using steerable transducer arrays," [Online]. Available: http://nrl.northumbria.ac.uk/11371/ [Accessed: 3 August 2015], 2012.

Thesis DVD Data Disk